Doctoral Dissertation

Doctoral Program in Electrical, Electronics and Communications Engineering

(33.rd cycle)

Integration of nanotechnologies in microscale invasive *in vivo* brain devices

Vittorino Lanzio

* * * * * *

Supervisors

Prof. A. Lamberti Supervisor

Prof. C. Pirri, Dr. S. Cabrini Co-supervisors

Doctoral Examination Committee:

Prof. M. De Vittorio, Referee, Università del Salento

Dr. A. Angelini, Referee, Istituto Nazionale di Ricerca Metrologica (INRIM)

Dr. J. Villalobos, Bionics Institute of Australia

Dr. R. Rizzoli, Institute for Microelectronics and Microsystems (IMM CNR)

Dr. S. Marasso, Institute of Materials for Electronics and Magnetism (IMEM CNR)

Politecnico di Torino

April 2021

This thesis is licensed under a Creative Commons License, Attribution - Noncommercial-NoDerivative Works 4.0 International: see `www.creativecommons.org`. The text may be reproduced for non-commercial purposes, provided that credit is given to the original author.

I hereby declare that, the contents and organisation of this dissertation constitute my own original work and does not compromise in any way the rights of third parties, including those relating to the security of personal data.

. . . . . .

Vittorino Lanzio

Turin, April 2021

Abstract

The brain is an extremely complex organ whose exploration and understanding requires the use of several different *in vivo* approaches at multiple spatial and temporal ranges; one such approach, developed in the last decades, aims at understanding how neural networks with thousands of neurons process and generate signals at the single neuron and single neural event levels by combining electrical readouts and optical stimulation. However, one major challenge is the creation of devices that enable the implementation of these methods to a high number of neurons in living brain tissue with high precision and accuracy and with minimal tissue damage.

To this end, neurotechnologies represent a great example of the merging of different disciplines, such as microtechnologies and electronics to realize real-world devices able to extract meaningful neuroscientific data. One type of device is the Michigan neural probe, which consist of micrometric sized silicon (or polymeric) cantilever tips (typically 1 to 10 mm long, 100 µm wide, 25 µm thick) embedding micro-scale sensors (such as microelectrodes) for neural activity readout and/or actuators (such as microlight emitting diodes or microwaveguides) for neural activity photostimulation.

While these micrometric scale devices are appropriate for interfacing with neural networks with single to few neuron resolutions, their coupling with microscale sensors and actuators limits their functionality, preventing them from studying neural populations with high degrees of accuracy and functionality. Examples of such limitations include device bulkiness; lack of simultaneous integration of sensors and stimulation sites in high numbers; limited optical functionality – generally allowing for the illumination of the entire population, or localized illumination of parts of the

network, through integration of several light-emitting diode sources, but resulting in excessive heat generation.

To tackle these challenges, which are associated with the use of sensors and stimulation sites based on microtechnologies, we develop and integrate nanotechnologies in minimally perturbative neural probes for simultaneous neural network readout and selective activation and deactivation of neurons. As a first example of nano-circuit integration on microprobes, we validate the use of nanophotonics based on add-drop ring resonators to shine light in the area(s) of interest without any heat generation and resulting in the photoactivation of the desired neurons. Remarkably, these nanophotonics allow for both reducing our device dimensions due to their small footprint and for integrating an arbitrary number of stimulation sites without any significant increase in the device's lateral dimensions. Besides, we demonstrate their use for multi-color illumination, which can be used to stimulate either different types of neurons in the brain or to access different functions (such as activation or inhibition of neural activity). A second example of integration of nanotechnologies in microprobes is the fabrication of chirped nanogrooves to focus the output light to either illuminate single neurons or spread light more efficiently; a final example is the integration of carbon-based nanomaterials on sensing microelectrodes in an effort to improve the microsensor-neuron interface.

This work describes the design, simulation, fabrication, characterization, and *in vivo* validation of these microscale devices integrating nanoscale circuitry and components. We first give an overview of the brain's networks, connectivity and functionality (page 4) of neuroscience methods that measure and manipulate brain activity (page 9), and of state of the art microinvasive tools for high resolution

neural networks studies (page 19). First, we describe the integration of nanotechnologies in microscale devices. in form of nanophotonic circuits embedding optical switches as passive on-demand demultiplexers for area selective illumination (page 45) and directional couplers for multiwavelength illumination for activation or deactivation of neurons (page 46). Their integration, along with arrays of sensors is explained in page 69. Then we illustrate the fabrication processes to realize the nanocircuits, embed them onto microscale probes, and connect them to macroscopic instrumentation (page 99) so to validate both the nanophotonic circuit's capabilities (page 106) and those of the electrical's (page 133). We explore nanoscale carbon-based materials to improve the sensors' interfaces and neural signal readout (page 137). We finally validate the nanocircuit's functionality *in vivo* by measuring both the neural activity (page 150), and the device's capability of exciting neural cells in the area(s) of interest (page 152). As such, we have proven the capability of these nanotechnologies to interface with the brain tissue in a minimally invasive way, and with high degrees of functionality and accuracy.

Acknowledgements

I want to acknowledge my supervisors for their help and support during the development of this thesis' project: Prof. Lambert, Prof. Pirri, and Dr. Cabrini. Each of them brought a different perspective to this work – either from material science or nanofabrication, helped in developing and refining the ideas underlying this thesis.

Ms. West, Mr. Sassolini, and Dr. Koshelev also supervised the project's initial parts and mentored some of my initial work. Dr. Lorenzon helped me analyzing the data and results. Several Master students also helped develop some parts of the work – Gianni Presti, Paolo Micheletti, Elisa D'Arpa, Paolo De Martino, Shervin Vahid. Dr. Denes, Prof. Adesnik, and Dr. Cabrini came up with the initial project idea, and Dr. Adesnik provided help for the in vivo experiments, along with Dr. Telian.

Several more people helped me during these years. I would like to mention: Dr. Scalia, Dr. Zaccagnini, A. Gashi, Dr. Dallorto, F. Riminucci, S. Dhuey, Dr. Schwartzberg, E. Wong, Dr. Barnard, Dr. Altoe, Dr. Bouchard. All the people mentioned here have been – more or less, sometimes with some advice, sometimes with work contribution - contributed to the successful development of the work. Finally, I would like to thank Dr. A. Angelini and Prof. M. De Vittorio for refereeing this doctoral thesis.

Sometimes we think that we achieve our goals only through hard work and self-motivation; in reality, motivations and passion are strengthened by those who support us. Mu, Pu, Zucca, Gian and Joan, as well as my grandparents and family; my friends in Berkeley and in Turin. To all of you: thank you for supporting me. The Ph.D., the pandemic, the nostalgia: you helped me walk through it.

Contents

Integration of nanotechnologies in microscale invasive *in vivo* brain devices

Vittorino Lanzio

Background: brain, analysis techniques and devices

Challenges towards the brain exploration

Can we decipher the meaning of conscience and where or how it arises? Can we read memories and thoughts from other persons' brains and transfer them to computers? Can we cure neurodegenerative disorders? These fundamental questions have interested many generations of scientists and are still sparking a great deal of interest around the world (see for example the brain-related projects across the world [46]). However, these questions are still unanswered due to severe technological challenges brought on by the impossibility of measuring the entire brain and its processes across different spatial and temporal scales. Brain activity ranges from the single synapse and single neuron scales (nm to µm), to the network level (hundreds of µm), and even to the whole brain (mm) and its corresponding temporal scales (from ms to years). Besides, the brain consists of a huge number of neurons ($\sim 10^{11}$) and interconnections ($\sim 10^{14}$), has high interconnectivity between different areas, and is difficult to access without damaging the cells.

In the last century, scientists have made great strides towards these efforts. They engineered and optimized several different methods to analyze and manipulate brain activity at specific length and temporal scales, leading to an increased understanding of some brain functions. For example, recent studies have shown that memories can be implanted and manipulated [67] [111], and that devices can partially correct seizures [58].

One interesting and not yet fully explored area concerns the impact of single

(or a few) neurons in an *in vivo* network: can a few neurons influence the behavior of an entire population, and if so, how? Do they correspond to specific brain functions? To answer these questions it is important to interface neurons with high accuracy (single neuron resolution), multiple functionalities (sensing and manipulation of their activity), high spatiotemporal accuracy (to confine the readout and stimulus), and with a large number of sensors and stimulation sites. This project tackles all of these issues by the integration of nanocircuits onto microdevices; for example, a simultaneous readout of neural activity and its manipulation in areas of interest with high spatial accuracy − providing, for example, the network excitation only on a few neurons instead of an entire network − is obtained by integrating electrical circuits with nanophotonic circuits. But before describing the concept of this thesis, we give an overview of the brain, its organization, and its functionality.

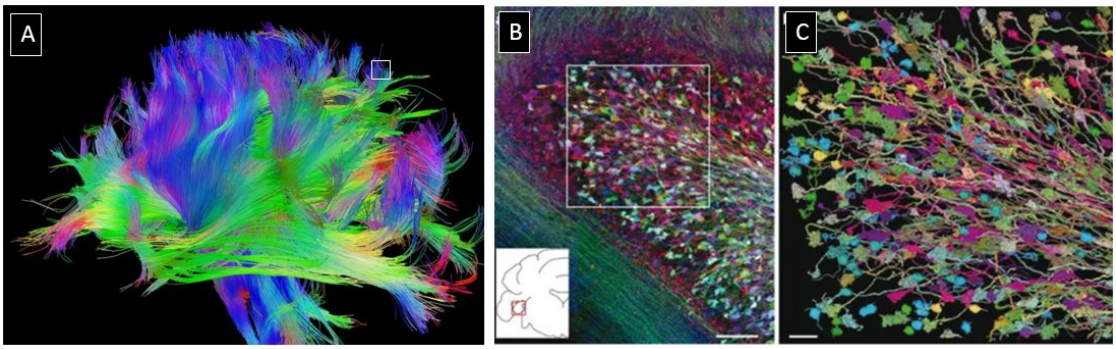

Figure 2.1: The brain and some of its components at different spatial ranges. (a): neural connections across different brain areas. (b): neural network and (c) magnification imaged with optical microscopy after genetic staining [68].

Brain biology

The macroscopic, microscopic, nanoscopic brain structure and function

The brain is part of the nervous system and resides inside the skull, surrounded by the dura mater. It can be divided into gray and white matter, with the former composed mainly of cell (neuron) bodies and their inputs and the latter composed of long-range cell outputs that connect to the different brain areas and the rest of the body. Within the white matter, the cortex is the outer layer of the brain (which is 1 mm thick for mice) and is mainly devoted to the elaboration and processing of the sensory information.

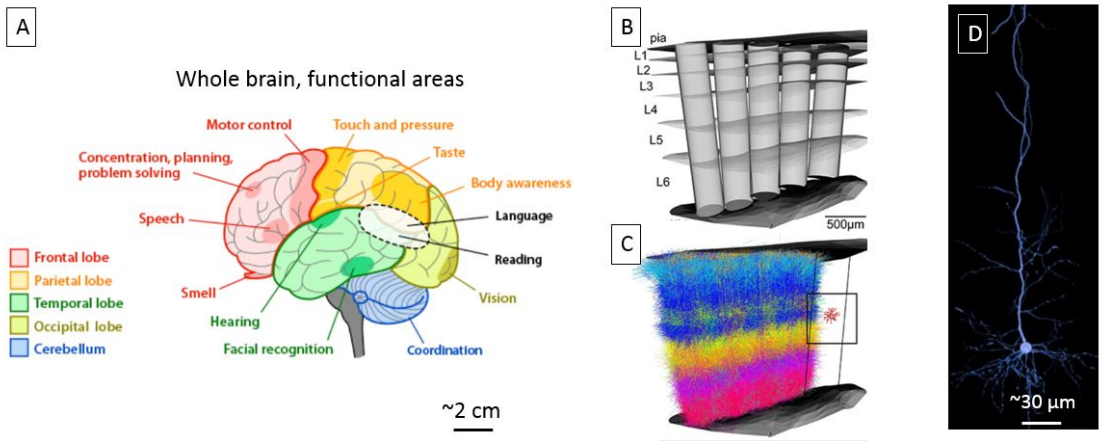

Figure 4.1: the brain and its organization. (a): Networks are arranged and interconnected together across different functional areas of the brain [14]. (b,c): schematic illustration (b) and simulation (c) of a cortical area and its six layers and divided into microcolumns in the vertical direction [30]. (d): microcolumns are composed of interconnected neurons [89] [68].

The cortex, as the whole brain, spans over several functional areas (Figure 4.1 a), each devoted to specific tasks (i.e. vision or motor control) and interlinked with each other. The cortex itself is organized into six layers, formed by different neuron

types (having different morphology, genetic sequences and electrical activity) and density. The layers in several functional areas (such as the visual and motor cortex) are then composed of microcolumns (Figure 4.1 b), which are networks of neurons spanning vertically over the six layers and horizontally by a few tens of micrometers [51][41]. Microcolumns are believed to be the functional unit in the cortex[45][80]: for example in the mouse barrel cortex, each of them is topographically arranged according to the whiskers and assigned to each [100]. However, not all of the cortical areas seem to be arranged in microcolumns, and are rather arranged in sparse networks (or populations) of neurons. Microcolumns and networks are formed by interconnected neurons (4.1 c), which may be the ultimate computational unit: in fact they "respond to a particular feature, or a specific combination of features, of the stimulus, such as position in space, frequency or intensity" [114]. We'll describe neurons in the following pages.

It is worth noting the different spatial and temporal scales of the brain: from the functional areas (mm wide and working at low frequencies, few tens of Hz) to the single neuron ones, spanning $\sim$10 to 20 micrometers horizontally and a few hundred micrometers vertically, operating at the kilohertz frequencies (although different operation frequencies exist inside neural populations [128].

Neurons in a network

The neuron is the basic unit in the brain and is composed of a body called the soma, one - or several - inputs called the dendrites, and one - or several - outputs called the axons (which serve as inputs of other neurons) (Figure 5.1 a). The morphology and the number of inputs and outputs depend on the neuron type, which is defined also based on its genetic code and electrical activity. Neurons

are interconnected between each other and form networks: the axon of a neuron connects to the dendrite of other(s) in a junction called synapsis. All neurons and networks are immersed in a sodium chloride solution, while their soma is filled with potassium, which makes them have a lower potential (the resting potential, ∼-70 mV) with respect to the extracellular medium.

Neurons communicate through electro-chemical signals. Action potentials (electrical signals) start at the soma and transfer through the axon to the synapse, releasing neurotransmitters (that are chemical molecules) that bind to the dendrite of the second neuron and activate the ion pumps in proximity. The ion pumps are channels in the membrane that allow for the exchange of intracellular and extracellular ions to either increase the intracellular potential (excitatory) or decrease it (inhibitory) [8]. If the sum of the synaptic potentials leads to an internal voltage above the neuron's threshold's (∼-55 mV), all the ion pumps on the neuron's soma open, and the neuron fires an action potential. This results in a voltage spike (Figure 5.1 b) consisting of an initial increase and subsequent decrease (corresponding to the opening and closing of the ion pumps) and refractory period (due to the slow kinetics of the potassium's pumps' closure) [18].

Neural networks and signal pathways in the brain

Despite several neuroscientific studies showing the organization and function of neural populations for specific tasks, such as in vision or movement [100], there is still a great number of neural populations that have not been studied in detail and whose functioning and signal processing is not clear. Furthermore, it is difficult to find patterns in neural firings across groups of neurons, networks, and the whole brain, as well as defining the brain computational unit and the role of single neurons

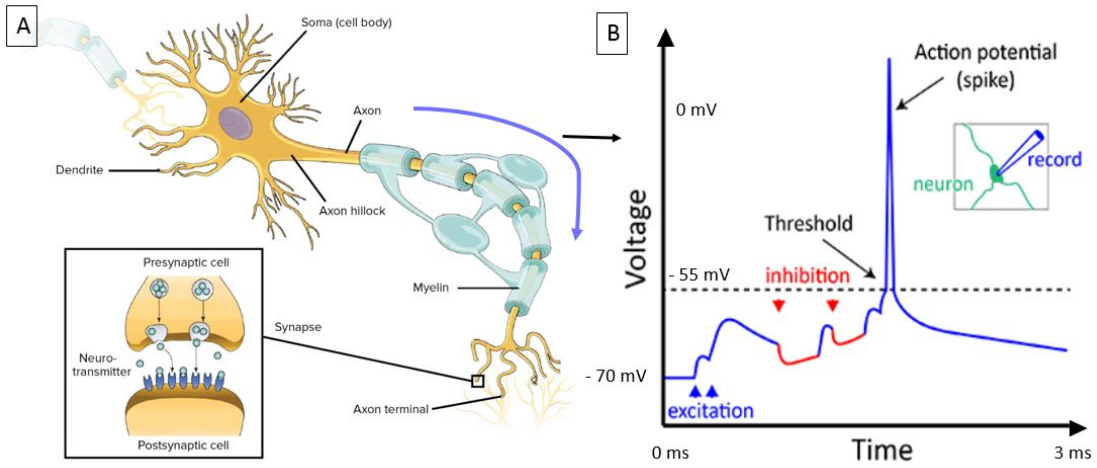

Figure 5.1: example of neuron structure and electrical signal. (a): neuron structure, showing inputs (dendrites), body (soma), and outputs (axons terminated by synapses) [19]. (b): typical neuron action potential spike, happening when the sum of synaptic (excitatory and inhibitory) potentials brings the neuron intracellular voltage above the threshold potential [20].

in the network or minicolumn. For example, detailed studies in the visual cortex (Figure 6.1 a) and in single barrels in the mouse motor cortex show complicated and non-straightforward neural potential pathways between the layers (6.1): signals in the visual cortex layer number four (L4) were found to simultaneously drive L2/3 and suppress L5 [103] and signals in the mouse barrel cortex have different pathways, such as L4→L2/3→L5 , L4→L5 or L4→L6 [6].

The arising challenges are found both in the difficulty of recording a high number of neurons with a high spatial and temporal resolution (ideally below a few tens of microns and milliseconds respectively), and in controlling or silencing (with a similar resolution) parts of the network. The recording allows the experimenter to assess both where the neurons are positioned and how they fire. High resolution is necessary to interface single neurons and single-neuron action potentials and how they spread across different neurons. Silencing single cells or layers would

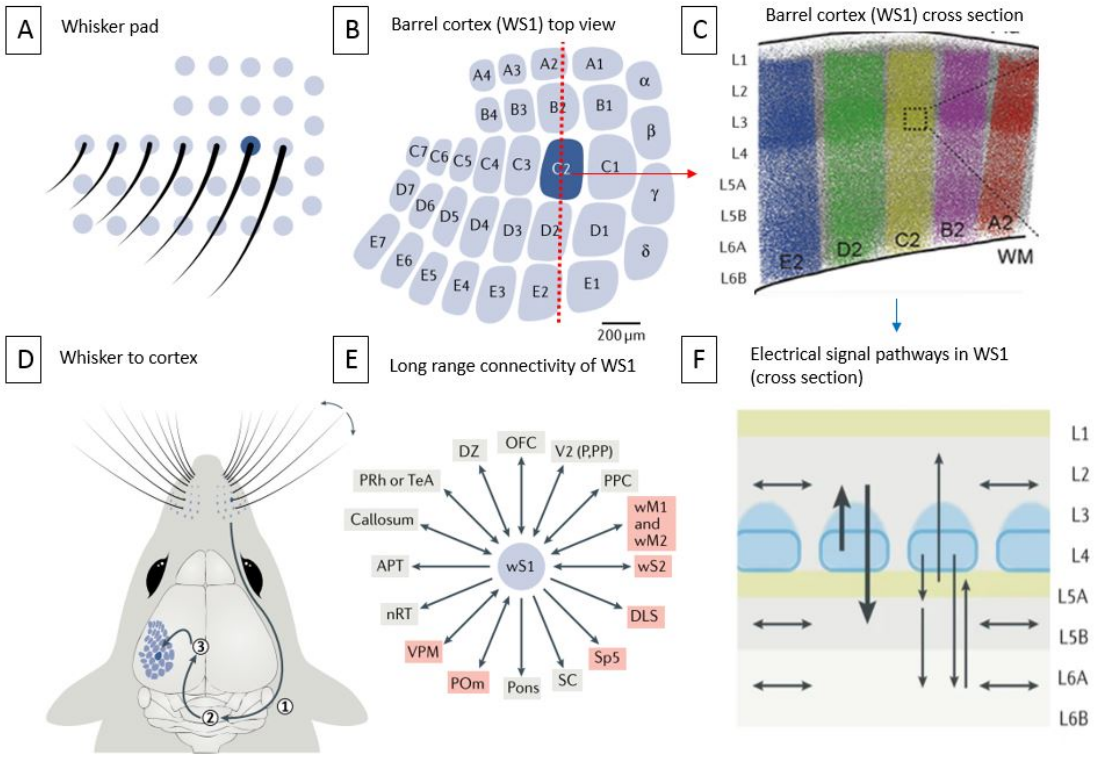

Figure 6.1: Neural network organization and signal pathways. (a) Whisker barrel cortex, where every whisker corresponds to a column ((b): top view; (c): cross section; (d): whole brain representation). Neural signals travel across different brain areas (e) and, in the barrel cortex, different signals travel along different cortical layers (f) [100], [6].

allow for assessing their role in the network by inference and observation of how the signal pathways in the other layers/neurons change. These operations require advancement into two distinct fields, which we'll discuss in the following sections: techniques to record and manipulate neurons and networks (page 9), and devices to implement such techniques (page 20).

Neuroscience methods

General overview: state of the art neuroscience methods

Understanding the brain is an extremely complex task due to the high number of neurons, axons and dendrites, the huge amount of data, and the difficulty in accessing it and the broad spatial and temporal ranges involved, which span respectively from nanometers to millimeters and from milliseconds to seconds. Scientists engineered and optimized several techniques that analyze, image and reconstruct parts of the brain with specific spatiotemporal ranges to understand the individual pieces of the whole puzzle.

Four main ranges of interest exist when studying the brain. The first one is the spatial extent of brain tissue interfaced, which corresponds to the number of neurons and connections the method measures; ideally, it extends to the whole brain. Similarly, the second one is the temporal range, which corresponds to the temporal extent the technique can record and which, ideally, spans from the millisecond (single neural event) to years. The third one is the spatial resolution, which is the minimal spatial feature the technique can resolve (ideally a few nm, to visualize the synapses and their clefts). The Fourth is the temporal resolution, which is the minimal temporal feature the technique can resolve (ideally around one millisecond, so to analyze all of the neural events). Thus, an ideal technique would allow for the spatial interfacing of the entire brain along the temporal scales (ms to years) with high spatiotemporal resolution (nm and ms respectively). However, all of the current methods provide either one or a combination of two of the points listed above: we show a graph of the techniques' spatiotemporal ranges and resolution in (Fig. 8.1), displaying the trade offs in spatiotemporal resolution and ranges of different techniques, but showing that although separately, they are able to cover all of the

brain ranges. In the following, we describe in detail some of these methods, along with their spatiotemporal resolution, benefits, and applications.

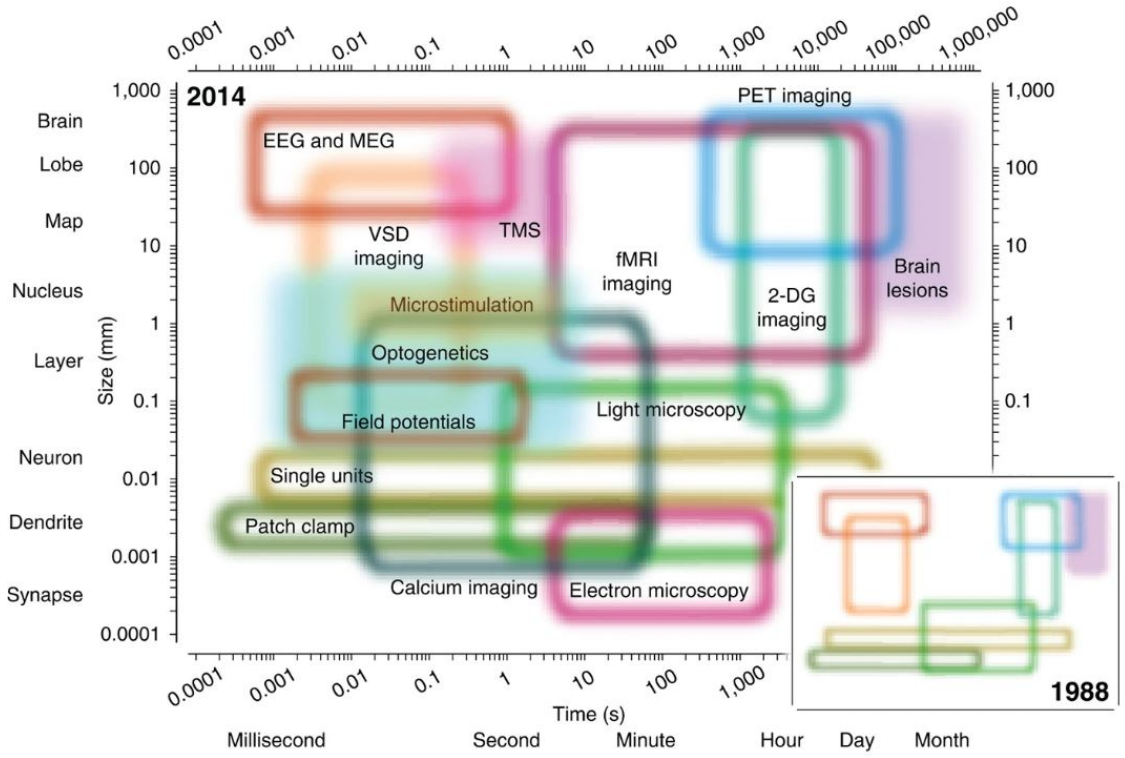

Figure 8.1: Spatiotemporal graph of recent neuroscience methods, highlighting both the tradeoffs of current techniques but showing that together they cover all of the possible ranges and resolutions [118].

Imaging the morphology and activity of the brain

Imaging with light and electrons is a powerful technique used to assess the morphology and activity of an arbitrary number of neurons with high spatial resolution at the expense of the temporal one. Imaging techniques, such as confocal or two-photon microscopy [113], use light to visualize large portions of the brain (mm^2) with a high spatial resolution ($\sim$1 µm) and *in vivo*. They also enable the user to directly visualize neural cells' activity by using Calcium or voltage indicators that transduce the action potentials into photons (but having severe tradeoffs

between the signal to noise ratio and fast, ms, kinetics) [114]. Other indicators allow for coloring different types of cells by their genetic modification so that they fluoresce with different wavelengths and to thus distinguish both their soma, axons and dendrites from the adjacent cells (brainbow [15] [107]). Generally, these techniques work for shallow brain depths [141] – up to around one mm – since visible wavelength light is strongly absorbed in brain tissue (while longer-wavelength infrared light is less absorbed, but yields a lower resolution). Techniques for in vitro brain imaging can overcome the absorption by making the brain transparent either, through immersion in an index matching solution or through substitution of the strongly-scattering lipids on the neurons' somas with hydrogels [37][26]. An even higher resolution (nm) is achieved by visualizing the brain in slices (milled with an ion beam) in electron scanning microscopes [43][138]. Other imaging techniques, such as functional magnetic resonance imaging (fMRI), magnetoencephalography (MEG), or positron emission tomography (PET), use magnetic fields to measure brain activity in the whole brain and for long periods of time, but have a poor spatial resolution ($\sim$0.5 mm^2) [78]. These latter methods are useful in assessing the activation of functional brain areas related to different behavioral tasks [78], [47]

Electrophysiology: readout of electrical neural signals

Electrophysiology refers to the measurement of voltage changes associated with action potentials and allows for a fast (ms) and high spatial resolution (up to the single neural cell) of neural activity for up to hundreds of neurons in a population and for a wide temporal range (ms to months). *"The primary strength of electrophysiology is its combination of time resolution and sensitivity, allowing the precise*

determination of the temporal pattern of neuronal signals over many orders of magnitude, with high signal-to-noise ratio" [114]. The electrical activity of neurons can be measured with arrays of sensors either above the skull (electroencephalography) or above the brain surface (using multi-electrode arrays), or by implanting them inside the brain tissue (using implanted microwires or microelectrodes) [78]. Such readouts allow for reading the neurons' activity and triangulating their position over hundreds of neurons. The benefit of this technique, as mentioned earlier, is that it allows for a high resolution (single neuron) readout of each neuron's event, which takes place in the ms time scale (while calcium imaging techniques and magnetic recordings are much slower, on the order of a few hundreds of ms to s) and allowing, for example, to record the sequence of temporal events between adjacent neurons. The drawback is that there is not a direct visualization of the cells and their connections: neuron somas' positions are inferred from the triangulation of the electric measurements. We describe this technique in the following paragraphs.

Optogenetics: manipulation of neural cell activity

Similarly to the readout of electric activity, it is possible to modulate neuron activity by delivering pulses of current, in a process called deep brain stimulation. However, there are some severe drawbacks: damage to the cells due to the need to apply large voltages and the impossibility of coupling it with the readout, since the stimulation fields will overwrite the neural fields [18]. An alternative recent technique for studying the brain, optogenetics [11], allows for manipulating neural cell activity of genetically modified neurons by illuminating them. The main benefit of this technique is that it allows the user to control the neural activity of specific cell types at the millisecond timescale, with minimal brain damage, and can be coupled

to electrical readouts. We describe this technique in the following paragraphs.

Computation: simulating brain circuits

Finally, brain activity can be simulated in supercomputers (*'in silico'*) once the typical response of a neural cell has been mathematically recorded and modeled [127]. Simulations allow for studying the network behavior [54], the relationships between the different neurons [12], the connectome [106], and the electrical signal propagation in large networks with thousands of neurons, and for different choices of inputs.

Electrophysiology for neural readout and triangulation

The electrophysiology technique consists of the voltage measurement of neural activity as a change in the local electric field due to charge redistribution when a neuron reaches its threshold voltage; it is measured through electrical sensors (metal wires or electrodes) either inside the cell membrane or outside of it (intracellular and extracellular recordings respectively). Extracellular and intracellular recordings yield similar features [42], although intracellular ones have a higher signal to noise ratio. Extracellular recordings measure either the low frequency (<500Hz) - local neural field potentials arising from the contributions of several neurons (multi-unit recordings) [31] - or single neuron action potentials (single-unit recordings) at higher frequencies ($\sim$ 1000 Hz), depending on whether the size of the sensor is (respectively) much larger or similar to that of a neural cell soma ($\sim$tens of µms). Even when reading single-neuron action potentials, signals from further neurons are read by the sensor; these signals are smaller in amplitude (due to the electric field decrease as a function of the distance from the neuron) and time shifted [14] (Fig.

10.1 a,b). Considering the amplitude, time differences, action potential waveforms, and the use of dedicated algorithms, it is possible to discern the closest neuron and its action potentials for each sensor in an array. This operation is called spike sorting [110] and yields, along with the neural activity readout, the triangulation of the neurons' positions (Fig. 10.1 c).

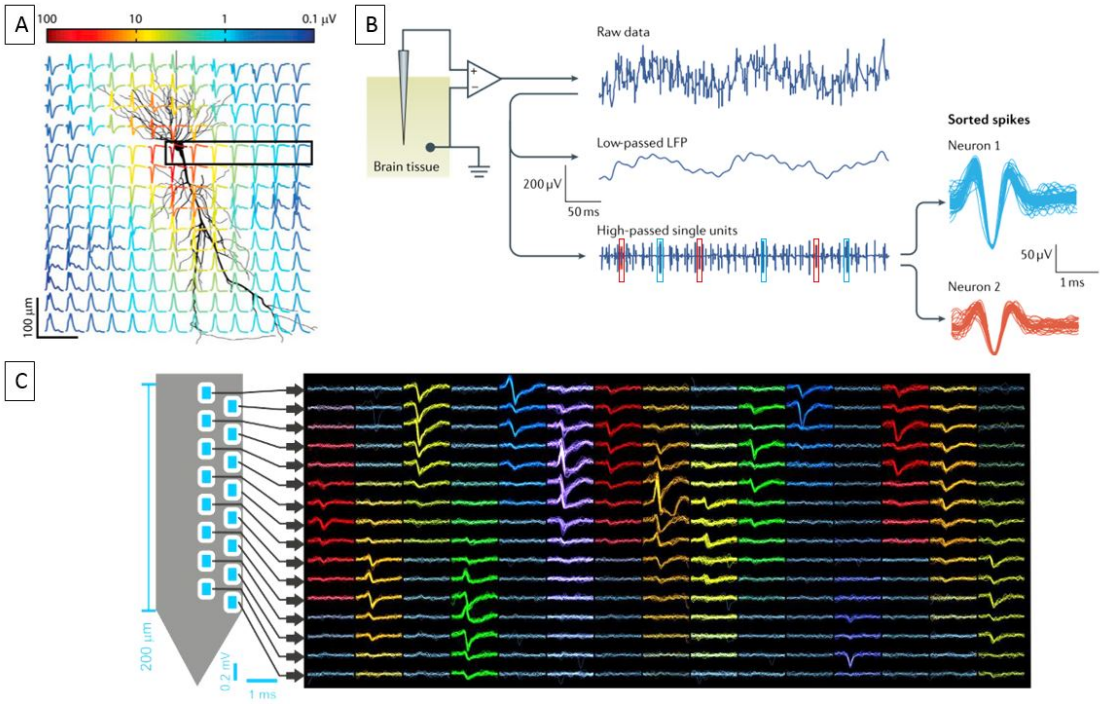

Figure 10.1: electrophysiology measurements of multiple neurons with single neuron resolution. (a): action potentials measured at different locations around a neuron, showing the recorded waveform amplitude decreasing as the distance from the neuron increases [42]. (b,c): examples of *in vivo* electrophysiology measurements with multiple sensors and post processing [43]. (b): single sensor recording raw data, and after low frequency filtering, showing that multiple neurons are recorded onto the same channel. (c): data post processing after recording with an array of sensors, showing individual neural waveforms assigned to each neuron and to the corresponding closest electrode.

Optogenetics for fast neural activity manipulation

Optogenetics [11] allows for fast (milliseconds) and neuron-type selective manipulation of brain activity without the use of high electrical voltages. This technique consists of the excitation or inhibition of neural cell activity through their illumination and requires the genetic modification of neurons so to attach light-sensitive proteins – called opsins – on their membranes. This modification is obtained either through in utero electroporation or by delivering the opsin through a viral vector (i.e. injection with a syringe); attachment to the neuron type of interest is obtained by specific genetic promoters for the opsin of interest, such as the Cre (while in a non modified mouse all of the neurons are targeted) [38] (Fig. 11.1 a). Once the opsin is transferred to the neurons, their activation requires both a correct illumination wavelength, which depends on the opsin type and its absorption spectra – residing in the visible wavelength range, 400 nm to 700 nm – and a threshold optical power density, which is typically around 1 mW/mm^2 [38] (Fig. 11.1 b). Several types of opsins and corresponding variants have been engineered [56] [65], each having a well-defined absorption spectrum and differing by function (neural network excitation or inhibition), and time response (ms to tens of minutes). Some examples of opsins are the (blue-activated) channelrhodopsins for neural activity excitation or the (yellow-activated) halorhodopsins for inhibition (peak wavelength: 473 nm and 570 nm respectively) [65].

The use of a single type of opsin enables the experimenter to manipulate brain activity either by silencing or exciting it at a fast temporal scale (on the order of neural events). The combination of two or more opsins allows for the combination of their different dynamics for experiments with higher degrees of freedom (i.e. for example to both silence and excite neurons [57]). Finally, optogenetic stimulation

of neural cells is damage less for short illumination periods (<500 ms) – meaning that it does not cause significant tissue heating (∼0.5°C [4]) due to light absorption [122]. As an example, there are no observed neural behavior changes at high optical fiber light output powers of 5-10 mW (corresponding to power densities of ∼300 mW/mm^2) [38]. In general, shorter (few ms) and lower power (by at least one order of magnitude) light pulses are sufficient to elicit single neural action potentials [56].

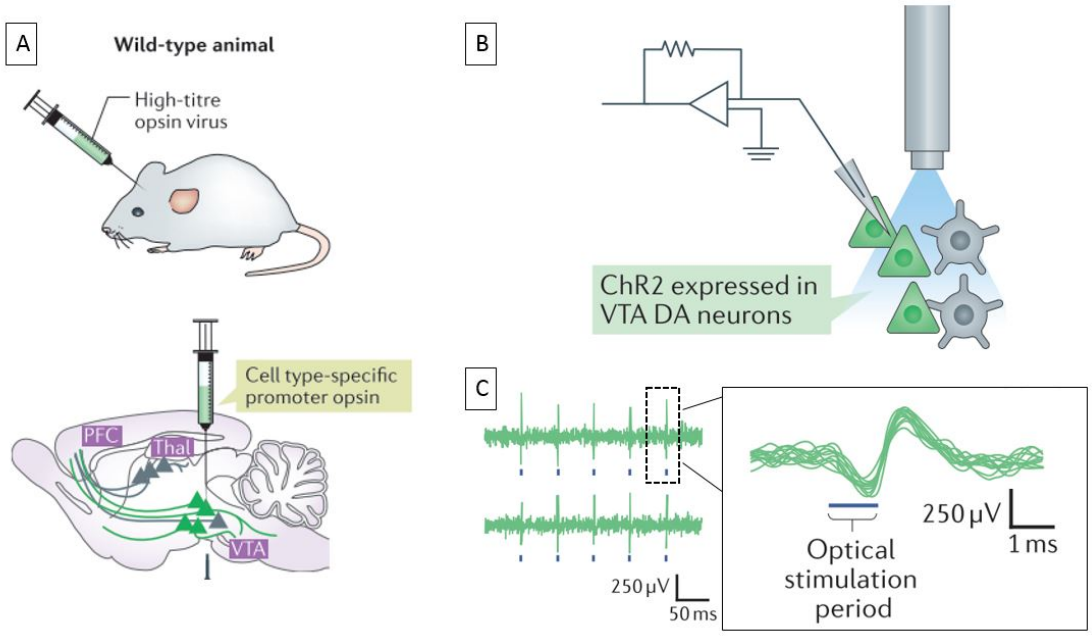

Figure 11.1: optogenetic technique for the fast manipulation of neural cell activity. (a): wild type mouse, in which a virus with opsins and cell-specific promoters is injected, resulting in specific light sensitive neurons (represented by the green triangles). (b): illumination of the neurons and simultaneous recording. (c): recorded signals, showing the neuron excitation (green spikes) during optical stimulation (blue lines) [56].

Combination of electrophysyology and optogenetics

The combination of optogenetics and electrophysiology is of great interest to neuroscience research, since it combines the simultaneous readout and stimulation

(or inhibition) of neural cell activity. This allows for many new applications. For example, we can study neural behavior in the presence or absence of precise stimuli [36], feedback loops, and phototagging [18]. The first application refers to the optogenetic manipulation of the areas of interest and the analysis of the changes in electrical activity (i.e. in the electrical signal pathways). This is done at the population level, either by targeting axonal projections to silence distant areas, [117], by targeting entire neural populations directly, or by focusing on selected spatial areas, such as single cortical layers, to infer their functions. For example, Petersen et al. [100] describe the optogenetic activity suppression of different areas associated with whisker movement (somatosensory cortex WS1 and motor cortex WM1 (Fig. 12.1 a) to determine the role of WS1 as negative feedback to suppress its neural activity, which is driven by WM1. As another example, Pluta et al. [21] describe the optogenetic deactivation of layer number four in the mouse barrel cortex to determine its role in the suppression of the neurons in layer five (Fig. 12.1 b).

Feedback loops implement a sensing part (the electrophysiology measurements) and an acting part (the optogenetic stimulation). Several applications were demonstrated in humans to recover impaired motor abilities, speech, or vision using feedback loops that implement both electrical readouts and electrical stimulation. Feedback loops that implement optogenetics as the stimulation technique in mice allow for fast network manipulation, and have allowed, for example, for the inhibition of seizures [58] or the inception of a false fear memory [67].

Phototagging [56] exploits the cell-type specificity of opsins to determine the type of neurons measured by electrophysiological techniques through the illumination of an entire population and the observation of which neurons and associated

waveforms are (de)activated.

In conclusion, the simultaneous readout of neural networks with the combination of electrophysiology and optogenetic tools allows for fast and neuron-type selective analysis and control. The studies described above were all performed on large brain areas (i.e. the somatosensory cortex) or in specific cortical layers (i.e. layer 4), but they do not allow wider flexibility in terms of the chosen area. For example, it would be useful to assess the contribution of the various layers by selectively silencing each of them in the same experiment (while in [103] only layer four can be optogenetically manipulated due to the virus injection happening in the area). In the following sections, we will describe both the tools that implement high resolution techniques (namely electrophysiology and optogenetics) and how our device, along with the integration of nanotechnologies, could be used to analyze neural networks with high flexibility – i.e. suppressing the desired layers in the same experiment – while providing minimal brain tissue damage.

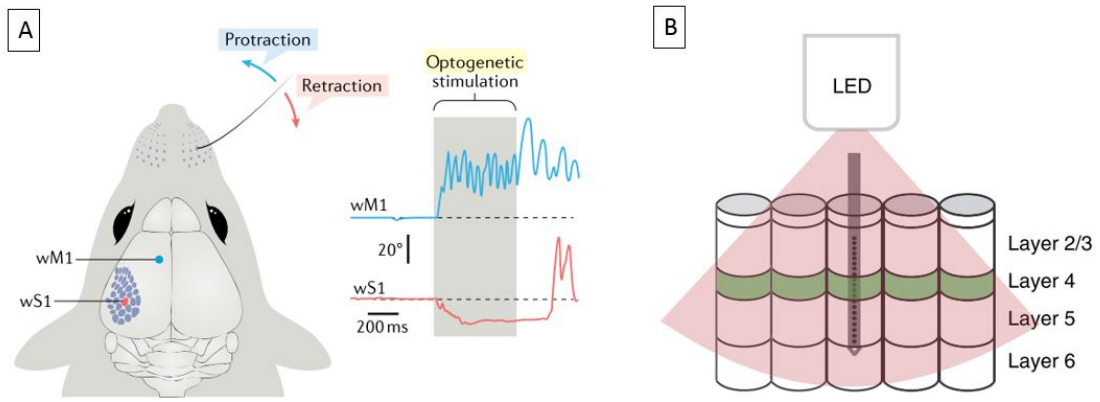

Figure 12.1: Experiments combining electrophysiology and optogenetics for neural activity readout and simultaneous manipulation. (a): optogenetic stimulation of motor barrel cortex simultaneous to readout of sensor cortex assigned to a whisker [11]. (b): simultaneous optogenetic manipulation of layer four and readout of the entire barrel cortex microcolumn [21].

Probes: invasive microdevices for brain interfacing

As we mentioned in the previous sections, scientists engineered several techniques to explore the brain at different spatial and temporal ranges and resolutions; this section describes the devices that allow the implementation of electrophysiology and optogenetic techniques, since they enable a high spatiotemporal resolution *in vivo* readout and manipulation of networks and neural cells. High resolution electrophysiology and optogenetics at different brain depths require the use of invasive devices – ones that are inserted into the brain of a living animal – so to position the sensors as close to the neurons as possible. For example, electrophysiological recordings of neural activity with noninvasive devices (electroencephalography) yield a poor spatial resolution. Other non-invasive techniques, such as magnetic recordings or brain imaging, suffer from poor spatial or temporal resolution. Semi-invasive devices, which are placed on the surface of the brain, such as multi-electrode arrays [94], can record single-unit activity but only near the brain surface. Despite their high spatiotemporal resolution, invasive devices have two main drawbacks: damage to the brain tissue, which limits their application to chronic (short term) studies and the small volume of interaction, limited by the fact that only neurons adjacent to the device are recorded and the limit on the implantation of multiple devices, which would result in excessive brain damage. Thus, invasive devices are suited for a high spatiotemporal resolution and short term interrogation of neural networks (few hundreds of neurons) with single neuron and single neural event resolutions ($\sim$few µm and ms respectively). These studies yield a great amount of information on how neural processes are orchestrated at the neuron and network level. As an example, invasive devices are used to analyze single cortical barrels in the mouse somatosensory cortex and extract the neural signal pathway and the role of single

cortical layers. In the following sections, we will describe major classes of invasive devices and their integrated sensors and stimulation sites for electrophysiology and optogenetics.

Microdevices: Fibers, Utah and Michigan neural probes

In this section, we describe three of the main types of invasive microdevices for neuroscience: Utah neural probes, Michigan neural probes, and fiber probes, all of which consist of a silicon or polymeric substrate integrating a variety of microscale sensors and stimulation sites for, respectively, neural activity recording and manipulation. These devices are composed of an insertion part (the tip), which is fabricated to be small, while at the same time embedding as many sensors and stimulation sites as possible. There is also a device connection area to connect the device tip to the printed circuit board external and the external instrumentation (electronics or lasers) (Fig. 13.1 a).

Utah neural probes [32] (Fig. 13.1 c) are fabricated by wafer micromachining directly through the wafer and yielding multiple tips with a low density of sensors (one per tip) and lengths limited to the wafer thickness. On the other hand, Michigan neural probes (Fig. 13.1 b) are silicon or polymeric cantilevers microfabricated in-plane on the wafer surface; sensors and stimulation sites are integrated on the cantilever surface, thus allowing their high-density integration, corresponding to their number increase with a simultaneous decrease of the tip lateral dimension, in long tips (10 mm) [32]. Fiber probes (figure 13.1 d) are polymeric fibers that are fabricated by thermal drawing processes, where "macroscopic materials are heated and stretched to wires and sheets with greatly reduced thickness" [44]. Fiber probes integrate a limited number of sensors and stimulation sites, but they benefit from

high flexibility and compliance to the brain tissue.

This thesis focuses on the *Michigan neural probes* (which we will call 'neural probes') because they allow us to integrate nanocircuits due to their in-plane fabrication, allowing for the interfacing of a higher number of neurons and increased accuracy in the spatiotemporal analysis of the neural networks. Furthermore, Michigan probes can be fabricated on polymers rather than on silicon, so to be more compliant to brain tissue [20]. Michigan probes are used to investigate the behavior of high numbers of neural cells (10 to 1000) with high spatial and temporal resolutions – around 5 µm and 1 ms respectively, which is on the order of single neural cells and single neural events – in a tissue radius of 200 µm around the probe tip [28]. Thus, typical neural probes interface a volume around 0.4 mm_3 if we consider a 10 mm long tip; using several tips (for example 16), only a small portion of the total mouse brain, around 1.2%, can be interfaced (where the mouse brain volume is around 500 mm^3 [130] [75]). Typical neural probes integrate multiple tips (generally one to four), each tip having 1 to 10 mm length (where 1 mm is the thickness of the mouse cortex), ∼100 µm lateral width and ∼30 µm thickness and integrating between 8 to 1000 microsensors and a few microstimulation sites, as we describe in the following sections. Microsensor dimensions for electrophysiological recordings are on the order of the neural cells' soma having a square or circular shape (with lateral size or diameter around 10-20 µm) so to achieve single-neuron resolution; their spacing (center to center) is around 30-50 µm. Microstimulation sites for optogenetics deliver light to illuminate as more neurons as possible. We will detail both in the following section.

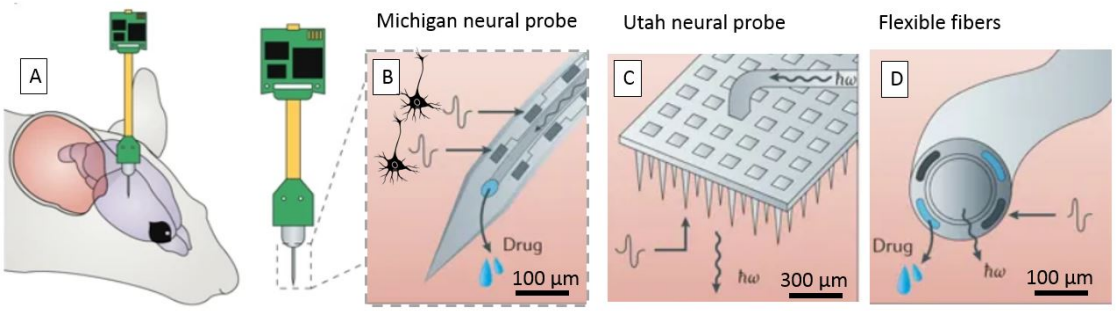

Figure 13.1: schematic illustrations of the probes for interfacing neural populations with high spatiotemporal resolution. (a): the neural probes consist of a tip area, which is inserted in the mouse brain to record or stimulate neurons, and a device interfacing area to connect the tip to the printed circuit board and external instrumentation [44]. (b-d): [20]; (b): Michigan type neural probe and neuron sketch [90] scaled to its approximate dimensions to the probe tip; (c): Utah neural probe and (d): fiber probe.

Integration of microsensors in Michigan probes for electrophysiology

Neural probes integrate microelectrode sensors for detecting *in vivo* neural action potentials from several neurons in a network. Design considerations for these passive readout sensors are based on the average neuron arrangement, density, and spacing in the areas of interest of the brain. Microelectrodes are square or circular-shaped metal areas on the probe's surface with lateral dimensions (or diameters) comparable to single neural cells, therefore making them able to triangulate their position with a 5 µm resolution (Fig. 14.1 a,b). Bundles of wires run from the electrodes on the tip of the probe to the ones on the probe interfacing area so to connect them to the PCB and to the external electronics, which embed frequency filters and amplifiers. Electrodes measure neurons' activity within the detectable radius range r (∼50-200 µm, since signal amplitudes decay with an inverse relationship with respect to the distance) and with a low yield (around 10%) since the majority of the neurons (>90-95%) are silent. A neuron is considered silent if it does not fire action potentials at a high enough frequency to be detected by spike

sorting algorithms [120]. The yield number does not count the neurons displaced or killed by the probe insertion, which are far lower than the silent ones [28]. Thus, it can be estimated that a 10 mm long tip should record from ∼500 (out of ∼10000) neurons, while a 1 mm long one should record from ∼50 neurons (out of ∼1000) in the cases where the number of integrated electrodes are at least 500 and 50, respectively. Thus, considering the number of detectable neurons, 1 mm long neural probes should have at least 50 electrodes with size and spacing comparable to neural cells. Wider spacing or fewer electrodes detect a reduced number of neurons, while smaller, closer packed electrodes (such as 9 µm size square electrodes with 10 µm center-center spacing) yield neuron oversampling (recording on multiple electrodes from the same neuron).

State of the art neural probes integrate massive numbers of electrodes to allow recording from as many neurons and different areas as possible; their integration happens either in a single tip, such as for the Neuropixel and Neuroseeker probes [84] [105] [52], or in several tips arranged in three-dimensional arrays [32], [108]. These probes yield the monitoring of massive numbers of neurons: for example, the insertion of 2 Neuropixel probes has detected >700 neurons [44] (Fig. 14.1 c,d).

Few bottlenecks restrict an increased integration of even higher numbers of electrodes: first, the tip lateral dimensions cannot be increased too much, as this will cause excessive brain damage. Second, a limited number of wires can be placed in the given tip space. For example, only up to ∼150 wires with 100 nm width and 300 nm spacing would fit in a 70 µm wide tip (considering that ∼20 µm of lateral space are already occupied by the electrodes). One solution is to use a limited number of wires to programmably address all of the electrodes [52]. The third limitation towards a further scaling is that electrode dimensions cannot be

reduced since they lead to neural oversampling, and, as we explain in the following section, their signal to noise ratio (SNR) decreases as a function of the dimensions, preventing the detection of action potentials. The SNR decreases with smaller electrodes: typical amplitudes of detected signals in electrophysiology extracellular measurements are on the order of a few tens of µV (out of the actual 70 mV) [42] and the noise level can reach similar values when the electrode lateral sizes are smaller than a few tens of microns.

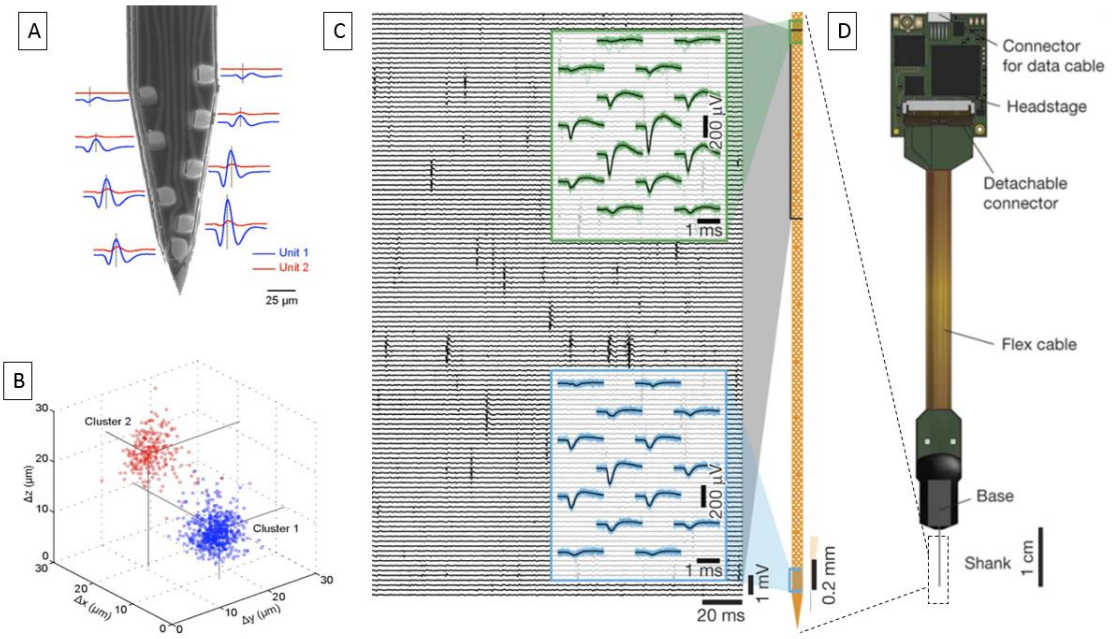

Figure 14.1: Michigan neural probes integrating electrodes for neural activity read-out. (a): neural probe tip integrating 8 electrodes and measured waveforms corresponding to two different neurons (blue and red colored) [28]. (b): triangulation of the two neurons' position in space with respect to the tip. (c,d): Neuropixel probe recordings from 900 electrodes (left) and insets showing two distinct neurons on a few electrodes [52] and a probe (right).

To further explore this concept, it is necessary to investigate how electrodes in the brain read extracellular voltage variations. With this information, we can understand the readout limitations relative to the electrode parameters (such as material, area, surface topology. . .). An electrode in the extracellular medium and adjacent to a neuron can be modeled as an electrode in solution (Fig. 15.1); several electrical parameters model the transduction of the electric field variation into electrical current when the neuron membrane channel opens [121]. The main contribution is a double layer capacitance, Ce, that forms at the electrode-solution interface and that polarizes the electrode. Further elements are the electrode resistance, Re, which can be reduced by using metals such as Au, Pt or Ir, and the extracellular medium resistance (Rseal); the resistance of the wires connecting the electrode to the PCB and the external amplifier impedance can be neglected [18]. Altogether, these elements are modeled as a Randless cell circuit (figure) [22] [62], where the main contribution arises from the parallel of the electrode resistance and the double layer capacitance, thus an impedance (Z). This impedance is largely dominated by the contribution of the electrode surface area [18], [109]; a small area results in a large impedance value and thus in a low signal to noise ratio (SNR), preventing the readout of single-neuron action potentials. Strategies to decrease the electrode impedance were developed in the last few decades and involve the decrease of Z of one to two orders of magnitude by increasing the electrode surface micro-roughness. Such roughening does not increase the electrode lateral dimensions, allowing for reduction of the electrode lateral footprint up to the single neural cell dimension ($\sim$10-20 µm) and thus, reading single-neuron action potentials; it can be achieved through electrodeposition of metallic nanoparticles

(named electroplating) [23] or by electrode roughening by chemical/physical etching [22]. Electrodeposition is not sufficient to overcome the SNR issue for further scaled down electrodes, which could prove useful to increase the available space on the probe tip. Ongoing efforts targeting the electrode scale down involve the use of active sensors, such as field-effect transistors [44].

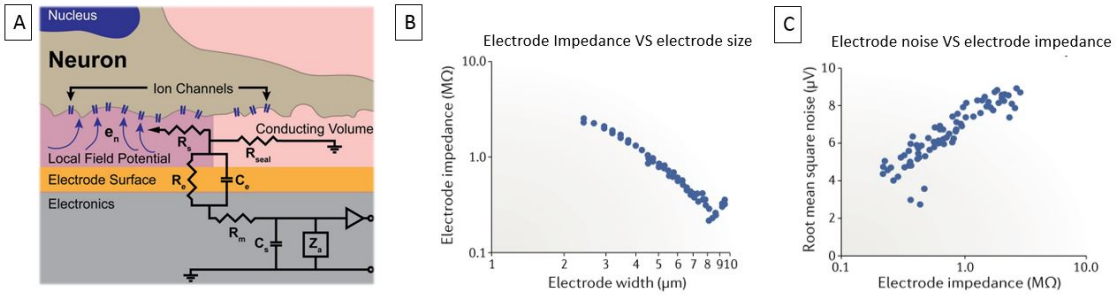

Figure 15.1: Neural activity recording with electrodes. (a): electrode-neuron electrical equivalent (Randless cell), where the electrode is modeled as an RC circuit with material resistance R and double layer capacitance at the metal-extracellular medium resistance C [18]. (b,c): [44]: the electrode impedance is the main factor influencing the signal to noise ratio of detected signals, where a low impedance is desired. (b): The impedance decays with the electrode area and (c) the noise increases for higher electrode impedance values.

Impedance characterization

The electrodes' impedances are estimated by electrochemical impedance spectroscopy (EIS) (15.2), which is a technique that measures the frequency response in terms of voltage and phase delay of the electrochemical system (an electrode in solution) to a small (5 mV) sinusoidal applied input current [17]. The probe tip is immersed in a phosphate-buffered saline solution, which mimics the brain extracellular environment, while the PCB probe is connected to the voltage measurement and current generator; a counter electrode and a Ag/AgCl reference electrode close the circuit. Measured data is displayed either with a Nyquist plot (y-axis: Z imaginary part; x-axis: Z real part) or a Bode plot (y-axis: logarithm of the magnitude

of Z or phase; x-axis: frequency). Nyquist plots asses if undesired electrochemical reactions at the electrode-liquid interface take place (such as, for example, electrode corrosion). Bode plots display the electrodes' impedance magnitude value and are used to assess the electrode yield, which is the number of working electrodes, whereas high impedance values (above 10 MΩ for square electrodes with size ∼10 µm) are nonfunctioning electrodes (having open wire connections). The same setup allows for electroplating the working electrodes by using a solution containing nanoparticles as the electrolyte. Typical resulting values for square electrodes with 10 µm size are (at 1 KHz) around 5 MΩ before electroplating and around 0.2 MΩ after electroplating.

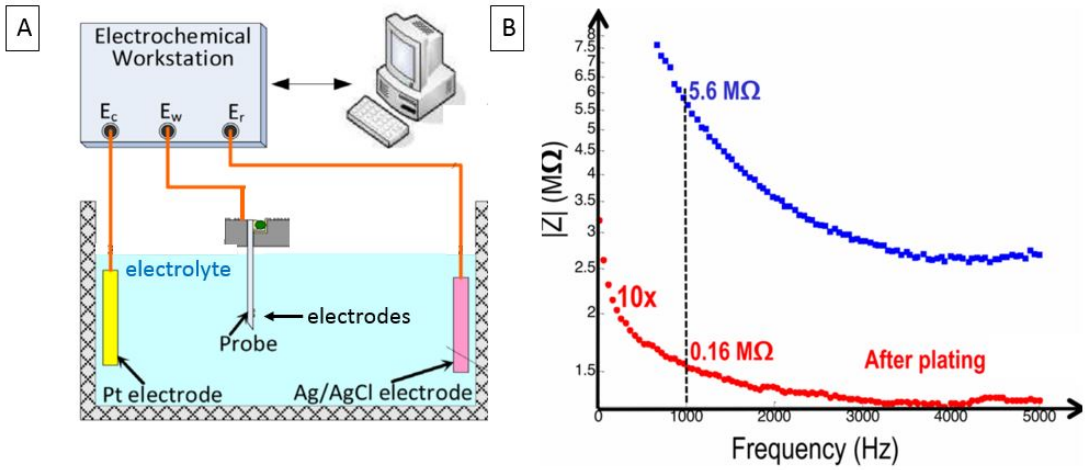

Figure 15.2: electrochemical impedance spectroscopy and electrode impedance. (a): electrochemical impedance spectroscopy setup for measuring the electrode impedance: a small current in solution is applied in between a counter electrode and the probe electrode and the voltage amplitude and phase are measured; (b): Electrode impedance as a function of the frequency for electrodes before electroplating (blue points) and after electroplating (red points, 10 times the actual value) [16].

Electrode materials and impedance

Common electrode materials include metals such as gold, platinum, iridium oxide, and titanium nitride, which are employed due to their chemical inertness and high electrical conductivity [18]. Platinum black or gold nanoparticles can be electrodeposited on the electrodes' interfaces to create nanostructures in the ∼100 nm range dimension, with the result of an improved signal to noise ratio. However, these materials read neural activity by means of faradaic reactions, which involve the reduction of chemical reactions at their interface and subsequent release of metal nanoparticles in brain tissue [19]. In addition, several of these plated nanoparticles (such as platinum black ones) have poor mechanical stability on the electrode's surface and tend to delaminate.

Electrodes made of (or coated with) non-metallic materials, such as polymeric or carbon-based materials, are gaining an increased interest for their increased compliance, chemical stability and multifunctionality. For example, they allow both for the detection of neural activity and of chemical activity associated with neurotransmitter release. Several of these materials can also be functionalized to release chemical molecules, such as the PEDOT polymer [18].

Carbon-based materials can have several different forms and electrochemical and optical properties depending on their atom arrangement and overall morphology. Several materials were engineered and optimized for neural interfaces, such as carbon nanotubes, graphene, glassy carbon, diamond, and laser induced porous graphene, with each having unique sets of benefits. Due to their high biocompatibility, and high electrical conductivity and chemical sensitivity, these materials are well suited for neural interfaces and will thus be discussed in section 23, page 67.

Integration of microstimulation sites in Michigan probes for optogenetics

Neural probes use different strategies to deliver light for optogenetic manipulation of neural activity. A first strategy is to integrate light sources such as micro light-emitting diodes (µLEDs) on the neural probes (Fig. 16.1 a), placing them either on the tip or on the probe interfacing area and, for this last case, coupling them to waveguides so to bring light to the tip. A second strategy makes use of external light sources, such as lasers or diodes, and couples them to waveguides on the probe interfacing area (Fig. 16.1 b). Waveguides can then be terminated by a grating, for light extraction perpendicularly to the tip, or light can be output directly from the waveguide's facet. Typical µLEDs are square (or circular) shaped with lateral dimensions (or diameter) of 30-50 µm and require an electrical connection for their activation, while waveguides can have lateral widths and thicknesses anywhere in between a few hundred nm to few tens of µm, depending on the material they are made of. For example, polymeric waveguides, such as silicon oxynitride-silicon dioxide, or polyimide ones are rather wide and thick (∼20 X 30 µm) due to their low light confinement capabilities (due to their low refractive index contrast, ∼ 0.01). On the other hand, silicon nitride-silicon dioxide ones are two orders of magnitude smaller (∼0.2 X 0.3 µm) due to their high refractive index contrast (∼0.5). Although they have wider dimensions, polymeric waveguides are also of interest because they are flexible (and can thus be integrated onto polymeric substrates). Silicon is not used as waveguiding material since it absorbs light in the visible wavelengths (400-700 nm) where the opsin activation takes place. Coupling of light from a light source to a waveguide can be achieved either by aligning the light source beam or optical fiber laterally to the waveguide edge (butt or edge coupling) or from the top by integrating a grating as the waveguide input (grating

coupling). Examples of state of the art probes integrate a high number of µLEDs in the tip [81] or several waveguides (one for each output) in the probe interfacing area (to which a µLED can be selectively coupled to [63] (Fig. 16.1 c) or use external tunable laser sources coupled to arrayed waveguides having a single input and multiple waveguides as outputs [117]. Besides, several of these devices integrate electrodes for neural activity readout alongside with the light stimulation.

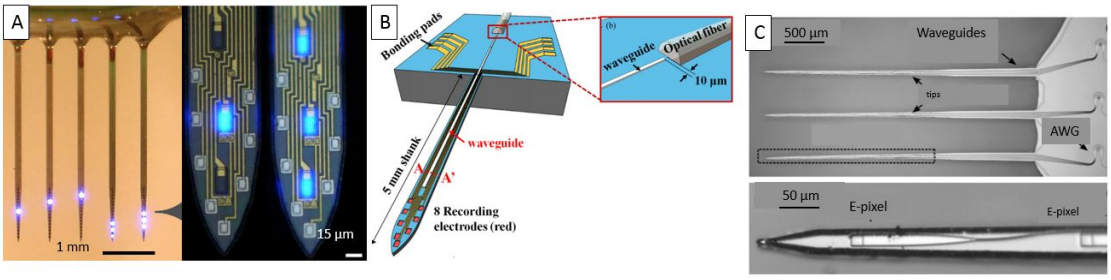

Figure 16.1: State of the art neural probes with different light delivery strategies. (q): integration of µLEDs on the probe tip [115] [134]; (b): use of an external light source by coupling of an optical fiber to the waveguide on the probe [134]; (c): state of the art probe with arrayed waveguide gratings (single waveguide input, multiple waveguide outputs on the tip) able to deliver light on demand in the area of interest [117].

Microstimulation sites characteristics

The three light source configurations (on the tip, on the probe interface, or external coupling) have different benefits and drawbacks in terms of thermal management (amount of heat delivered to the brain tissue), light spatial shape control and localization, wavelength selection and scalability.

Heat management

With respects to the heat management, it must be considered that one of the

main drawbacks of µLEDs is that their activation requires high currents that result in a significant heat generation and a consequent tissue heating above the safe limit (∼0.5 °C temperature, which was shown to change neurons' behavior [4]). This poses stringent limitations on their pulse duration and repetition rate, which should be kept below 10 ms and 10 Hz respectively (depending also on their output power) [81], [27] (Fig. 17.1 a). It should be considered that these studies highlight the heat directly released to the tissue, whereas the probe (which absorbs ∼4 times the heat due to a higher thermal conductivity than brain tissue) is at an even higher temperature [81]; furthermore, in the case in which more than one µLED is activated, the thermal constraints are even higher. This heat sums up to the heat generated by light scattering and absorption into neural tissue, which is a fraction of the one generated by the µLEDs [122]. For example, we can compare the the case of heating by continuous light illumination provided by a microLED [81] and the one simulated for an optical fiber [122]. While the microLED at an optical output power of around 600 mW/mm^2 results in a tissue heating of 1°C after 200 ms (Fig. 17.1 e), a similar amount of output power (500 mW/mm^2, calculated from the fiber's core dimension) takes more than 5 seconds to result in a 1°C increase of temperature in brain tissue. Thus, one benefit of integrating light sources externally to the probes' tips is that the heat generation associated with the µLED activation is far from the brain. Waveguides and several nanophotonic circuits can be designed to be entirely passive, meaning that they do not rely on any electrical elements that can generate heat.

Light spatial shape control

The spatial shape of the light beam has a direct relation to the amount of illuminated brain tissue. µLEDs illuminate broad areas, since their emission has a Lambertian shaped profile with a nearly isotropic angle and illuminating 100-200 µm of tissue around the probe tip [81] [27] (Fig. 17.1 b). This type of emission profile is useful for illuminating all of the cells close to the tip, but suffers both from poor spatial depth reach and directionality (lateral areas are illuminated, which may be a problem if a restricted illumination area is preferred). Instead, waveguides can be terminated by gratings which allow the user to spatially collimate [117] (Fig. 17.1 c) or focus [60] the output beam (or even to steer it [112]) with an angle almost perpendicular to the tip (depending on the initial grating design), thus allowing for a higher spatial depth reach and directionality, but with a poorer lateral reach. This last limitation can be partially overcome by the integration of multiple outputs. However, it is of great interest to have site-selective (or on-demand) illumination, meaning single illumination sites that can be activated or deactivated as desired; this allows for selective manipulation of single cortical layers or desired groups of neurons in a network. µLEDs allow for this by sending seperate currents to every individual site, while waveguides need specific structures for demultiplexing light, such as arrayed waveguide gratings, which consist of a single waveguide input with multiple addressable output waveguides [117]. They can also use multiple waveguide inputs, one for each output waveguide [63].

Wavelength selection

The capability to accomodate wavelengths (or colors) that are tens of nm apart (such as blue or green ones) enables the illumination of different opsins. One of the main limitations of µLEDs is that their output wavelength is fixed by the material

[101]. One solution to address this has been proposed by Kampasi et al. [53], which integrate red and blue diodes in the probe interface area to combine the two-color into the same output waveguide and thus, succeed at both exciting and inhibiting an entire neural population by activating multiple opsins. Nanophotonic circuits using waveguides, such as silicon nitride ones, allow, instead, for the use of multiple wavelengths, ultimately depending on the external laser source, which has fewer constraints with respect to µLEDs in terms of coherence, wavelength selection, and tunability. Demultiplexing structures for light on-demand delivery are however designed to work for a limited set of wavelengths encompassing a single color (maximum around 100 nm bandwidth).

Scalability

Few bottlenecks restrict an increased integration of even higher numbers of stimulation sites on the tip. µLEDs can be integrated into high number arrays due to their small diameters and need only thin electrical connections [115], but further scaling below a diameter of ∼25 µm results in their efficiency dropping [27]. This results in higher drive currents and thus, an even more pronounced heat generation. Silicon nitride-silicon dioxide waveguides can have extremely small lateral dimensions (∼300 nm), but to ensure that their evanescent tail does not optically interact with nearby structures, their lateral ridges (empty regions of cladding) should at least extend for ∼2.5 µm all around the waveguide, thus giving the single waveguide dimension a lateral footprint of around 5 µm. Thus, multiple output waveguides can fit in the tip, such as the ones in [117] [63]. However, this strategy prevents a further scaling above around ten waveguides for a tip width ∼50-70 µm. An additional challenge is the integration of electrodes, which take

additional space and thus, result in a low number of electrodes (or their absence), which we can see from several works [117] [81], [135] [134] [53]. One strategy consists of separating the optical and electrical circuits into two vertically stacked layers, whereas it is preferable to integrate the electrodes above the waveguides (electrodes cannot be covered by waveguides since their surface needs to be exposed to the extracellular medium, while waveguides can be covered by electrodes, except for the gratings).

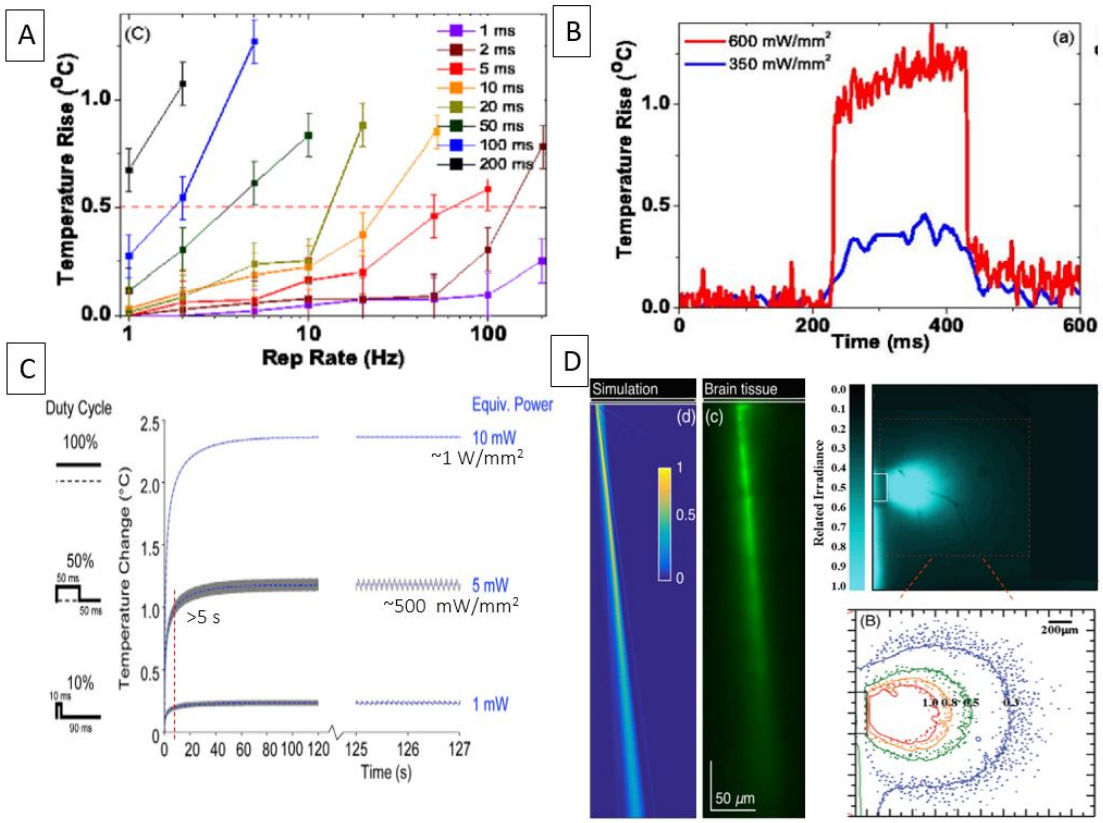

Figure 17.1: Characterization of µLEDs and waveguide gratings. (a,b): significant heat generation in the brain tissue associated with the µLED illumination [81] with (a) repetitive pulses and (b) a continuous 200 ms-long pulse. (c): Heat in brain tissue due to light scattering from an optical fiber, showing that continuous heating results in a 1°C temperature increase in brain tissue for long (5 seconds) illumination times (while in (b) for only 200 ms). (d): Grating beam output shape, where light is collimated in a parallel fashion (top: imaged; bottom: simulation) [117]. (e): µLED output beam shape (top: imaged; bottom: corresponding data plot), which is in the form of a Lambertian shape (thus almost isotropic) [134].

Optical losses

Finally, it is necessary to consider the optical losses related to the light delivery system, since the opsin activation requires a minimum output power of around 1 mW/mm^2. µLEDs have poor current to light transduction efficiency [27] but

even small drive currents result in a high enough output power. The same situation is true for optical waveguide systems, where several sources of loss exist (external source-waveguide coupling, waveguide propagation, and absorption losses...), but their careful design and optimization yield relatively high output powers (∼thousands of mW/mm^2). Furthermore, power densities for waveguides are high compared to optical fibers, since collimated beams have a size comparable to the grating (∼10 µm X 10 µm). Thus, even low output powers (on the order of µW) result in high power densities (on the order of hundreds of mW/mm^2).

Probe's scaling: Moore's Law-like integration and minimization for biocompatibility

To achieve higher numbers of electrodes and stimulation sites, with the final goal of recording and manipulating all of the neurons in the brain with single-neuron resolution, Moore's Law-like trends were proposed for both neural probes integrating electrodes and stimulation sites. These trends are just intended as guidelines to push research towards higher integrational densities on neural probes, and they do not take into account other factors, such as brain damage. For published probes integrating electrodes, a doubling of recording sites every 7 years was found (in comparison with the doubling of transistors every two years for the microelectronic industry) [44] (Fig. 18.1 a). The current constraints towards curve advancement include the electrode size scalability and the packing of wire traces in the probe tip, as mentioned earlier. Once the maximal number of electrodes with a size comparable to that of the neuron is achieved, scaling down of the electrode size only leads to oversampling of the same neuron onto different electrodes; the number of sensors can then be increased by using multiple tips (however, at the cost of increased

brain tissue damage). For published probes integrating both electrodes and light delivery sources for optogenetics, a cross-sectional area coefficient was established as the tip cross-section value (lateral width times thickness in μm^2) divided by the sum of recording and stimulating sites [63] (Fig. 18.1 b). The current constraints for these devices are the scalability limitations of the µLEDs' size and the number of output waveguides that can be accommodated on the tip, along with the combined integration of electrodes and wires onto these structures. In this frame, nanotechnologies and nanocircuits can help advance this trend (similarly as for the transistors' case) thanks to their reduced dimensions and increased integration.

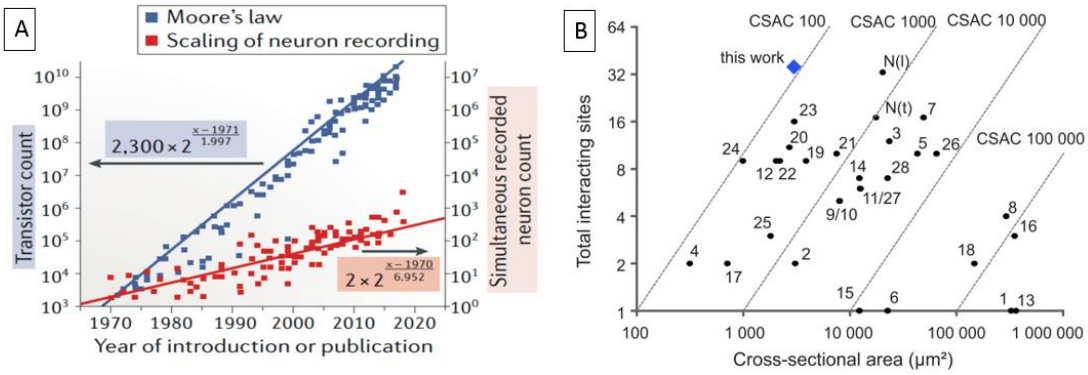

Figure 18.1: Moore's laws for neural probes. (a): Moore's law for recording electrodes [44] and (b) cross sectional area coefficient (tip cross section divided by number of sensors and stimulation sites) for probes combining both electrodes and light delivery sites [63].

Another important challenge that neural probes face is the brain tissue damage due to the probe's invasive nature (Fig. 18.2 a), which takes place with different mechanisms and time scales [61]. The neural probes' tips must penetrate through the dura mater without much tissue compression (which can be achieved using sharp tips [29]) and slide inside the brain cortex, causing the tissue to tear, and killing some neural cells on their path. The volume of damaged tissue for short

periods after implantation (< 1 week) is proportional to the tip's cross-section [61]. Thus, especially for chronic studies, small tip widths and thicknesses are preferred. On longer time-scale, tissue inflammation can elicit a brain response resulting in the encapsulation of the inserted device with microglial cells [124], and consequent signal to noise ratio decrease for the recording electrodes. Besides, brain micro-movements occur naturally and result in tissue displacement on the order of tens of microns [61] and consequent laceration in the presence of a stiff probe. Damage for neural probes is unavoidable; however, there are strategies that can minimize it. The first one (as mentioned earlier) is to keep the tip dimensions –width and thickness - as small as possible; for example, studies use the Euler's buckling force to describe the probe's compliance to deflect under the tissue's movements [61]:

$$F_b \propto \frac{I * E}{L^2}$$

where F_b is the buckling force on the probe under tissue micromotion, E is the probe's Young modulus, L the tip's length, and

$$I = \frac{a * b^3}{12}$$

where b is the probe's thickness or width (along the buckling's force direction) and a is the width or thickness in the direction perpendicular to the force. Thus, decresing the tip's cross-section (width times thickness) reduces the tissue laceration.

A second technique is to use flexible probes, having a low Young modulus value (E) that approach the brain's. This is achieved by using flexible probes fabricated onto polymeric materials (such as polyimide or SU-8) as substrate instead of silicon (Fig. 18.2 b,c) Extremely flexible materials do not, however, address the initial penetration damage since they need temporary stiff carriers (such as tungsten

microwires) to penetrate through the dura. Furthermore, these materials cannot always be used since they cannot withstand high temperature (>250°C) processes which may be useful for some applications, such as the deposition of silicon oxide and nitride with optical quality for the integration of high-density nanophotonic circuits.

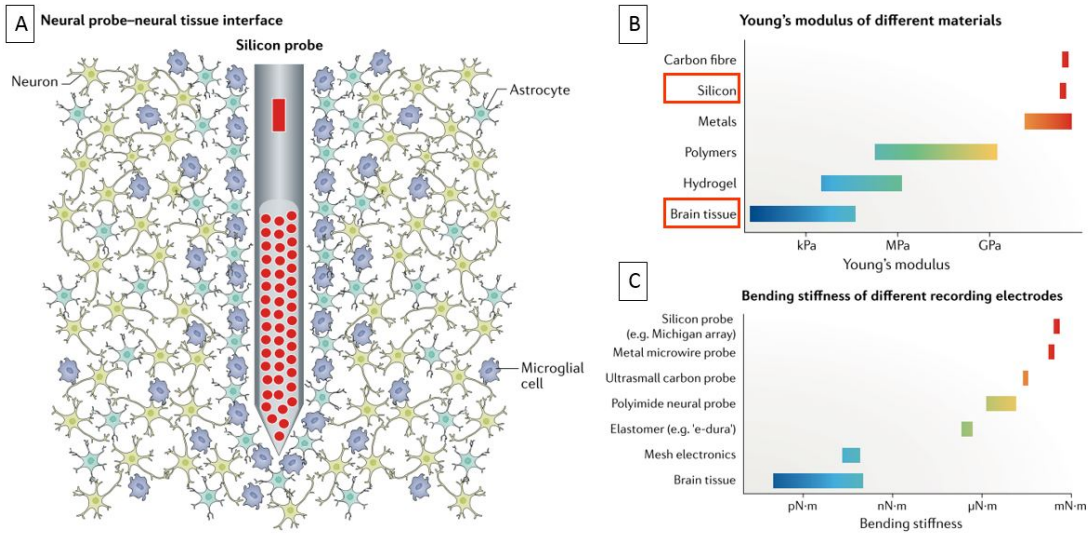

Figure 18.2: brain tissue damage for different neural probes [44]. (a): neural probe tip inserted in the brain and causing tissue laceration and eliciting an inflammatory response from the brain tissue, resulting in the probe encapsulation by the glia cell proteins. (b,c): young's modulus and bending stiffness of different substrate materials compared to brain tissue.

A third strategy is to use coatings that are released upon insertion and that can mitigate the tissue inflammatory response. Probes should not cause any secondary effect when they are used in experiments, such as the generation of heat when using probes that embed µLEDs. Altogether, careful designs encompassing ultra flexible probes with a small tip form factor and biocompatible materials have shown to yield no significant tissue damage (i.e. no response from the brain tissue) over the period of months studied [44]. A final consideration concerns whether the probe

presence changes the recorded electrical signals. A study from Buccino et al. [13] shows that the presence of the probe into the neural tissue acts as a barrier for the extracellular potential, thus increasing their signal strength in proximity to the electrodes (thus electrodes read higher action potential), but show no effect on waveform or timing.

Integration of nanotechnologies in micro brain devices

In this thesis, we analyze the integration and functionality of nanotechnologies in microprobes in the form of nanocircuits or nanomaterials embedded in microsensors, with the aim of providing a more accurate and less invasive *in vivo* neural network interrogation and analysis. We first describe the implementation of nanophotonic circuits into the neural probe, which allows for increasing the number of light outputs and introduces multiple functionalities, such as the capability of delivering light in the location of interest for multiple wavelengths without resulting in heat generation from electrical components. These features allow for the manipulation of spatially clustered neuronal activity and neuron subtypes, as well as the ability to silence and excite selected groups of neurons inside neural networks. By integrating a high number of microsensors with nanophotonics to measure neural activity across the network, this combination of both circuits allows coupling of well-defined stimuli with a high-resolution readout and inferral of excited (or inhibited) neural units. We also describe how the design of chirped nano grooves in micro gratings acts as lenses that spatially focus the output beam, with the aim of either illuminating single neurons or spreading the illumination point to a wider area. We then analyze carbon-based materials and their contributions to neural microelectrodes due to their superior electrical and chemical properties; in particular, we analyze the use of graphene due to its high electrical conductivity and transparency, as well as the use of carbon nanoonions, which have a high surface area to volume ratio. These properties make them promising candidates to achieve low electrode impedance. Some of these concepts are schematically illustrated in Fig. 19.1.

In conclusion, this project demonstrates, through all of these examples, the feasibility of integrating nanotechnologies for the reduction of implant size, maximization of number of sensors and stimulation sites, and importantly, the implementation and combination of new functionabilities that achieve greater accuracy for interface with *in vivo* neural networks.

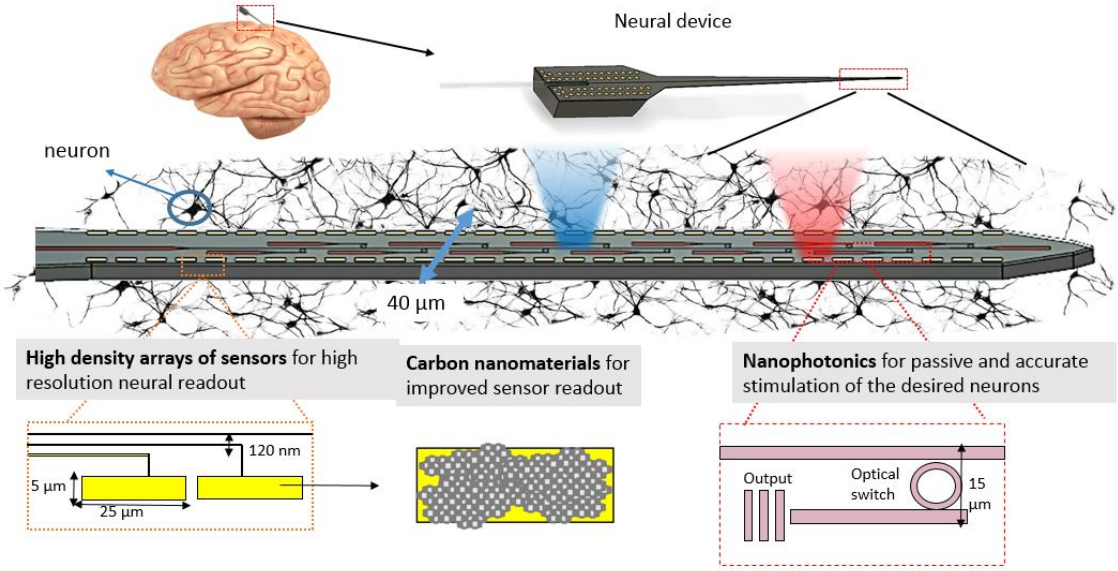

Figure 19.1: Integration of nanotechnologies in micro invasive brain devices. Top: schematic of the device and magnification on the tip. We integrate high density arrays of sensors for massive neural readout, and analyze the contribution of carbon based nanomaterials on their surface. Besides, we embed nanophotonics for accurate stimulation of the desired neurons.

Nanophotonics for micro brain devices

Optogenetic techniques allow for fast and less damageable neuron sub-type specific manipulation; electrophysiology allows for high spatiotemporal resolution readout of neural networks. Several works have described the combination of the illumination of entire populations and simultaneous readout to infer their function.

However, it is challenging to disentangle the role of neurons in well-defined spatial locations from neurons of well-defined type, while simultaneously achieving minimal tissue damage and perturbation. One goal of this project is to develop nanotechnological tools to interrogate *in vivo* neural networks with high spatiotemporal resolution and minimal perturbation under well-defined optogenetic stimuli, which allows for selectively activating (or deactivating) spatially clustered neurons and defined neuron subtypes in a population. Simultaneous electrophysiological readouts allow for monitoring the signal propagation in the network to analyze the role of the stimulated cells. An example application of on-demand light delivery (illumination of selectable areas of interest) is the study of the cortical layers in the mouse barrel cortex, where selective silencing or excitation of one layer at a time can help to determine their function and possible different signal pathways. Multicolor illumination relies on the capability of either transfecting different neuron sub-types with different opsins (that respond to a different color) or transfecting a network with two different opsins such that it can be excited or silenced under different color illumination. By adding the capability of using different wavelengths to on-demand light, we aim at either manipulating neuron subtypes to determine their function or selectively inhibit or excite areas of a neural population. Thus, we optogenetically stimulate neurons by integrating nanophotonic circuits that deliver, under the experimenter's selection, light in the area(s) of interest and for different colors. We show a schematic example of different light patterns achieved with the probe in Fig. 20.1 a,b, along with an example of an experiment, in which the light of different colors is delivered to different cortical areas to selectively inhibit neural signals for specific neuron sub-types and in spatially defined areas. The electrodes simultaneously monitor the signals. Nanophotonic circuits are entirely passive since

they rely solely on the selection of the external laser's input wavelength and do not rely on any electrical element for their functioning, which would result in excessive heat generation. On-demand light delivery is obtained by employing arrays of ring resonators, which are used as passive optical switches that can be selected (along with their grating output) by matching the laser's wavelength to its specific resonance wavelength. Multicolor illumination is achieved with directional couplers that, for a single input with mixed wavelengths, splits far colors (for example blue at 450 nm and red at 650 nm) such that they are coupled to rings which are optimized for each of the coupler's output wavelengths. We describe their functioning concept and simulations in (page 45 - 48).

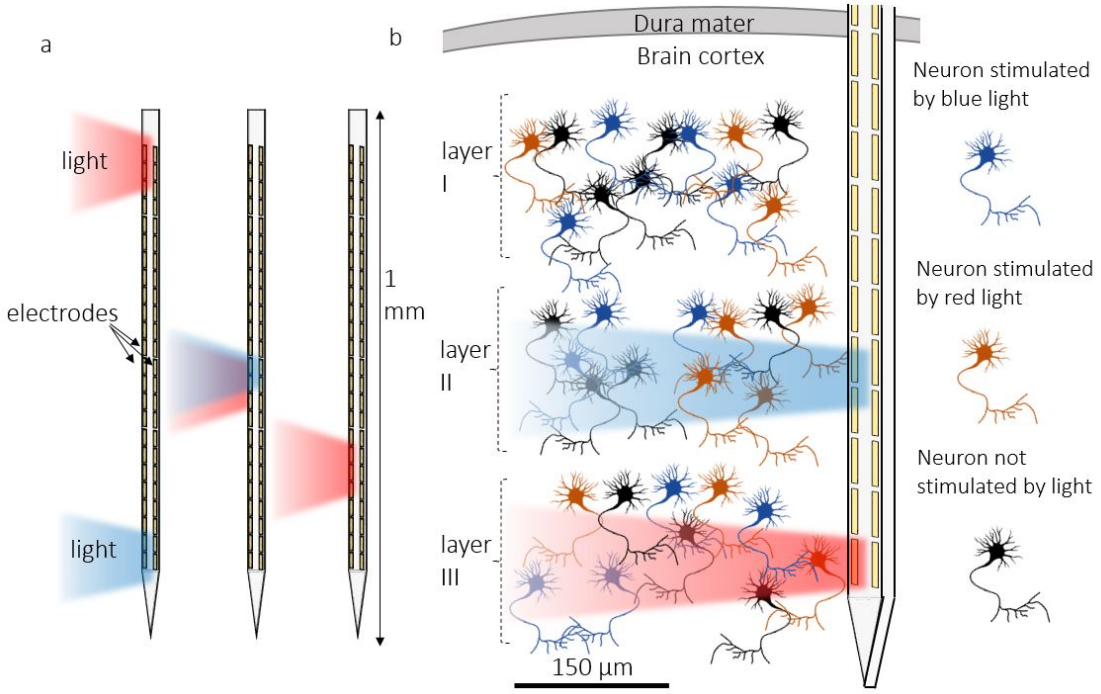

Figure 20.1: Nanophotonic circuits are used for manipulation (activation and/or deactivation) of groups of neurons inside a neural network. (a): The device tip delivers light in the area of interest and for different colors. (b): The schematic illustrates the simultaneous readout and manipulation of defined neuron subtypes in distinct cortical layers as well as recorded neural traces.

Nanophotonics for passive, on-demand light delivery for local neuron stimulation

Nanophotonic circuits allow for shining light in areas of interest to illuminate specific locations along the tip length, thus only exciting and activating desired portions of the neural network. This selection of the light output location is achieved by using ring resonators, which act as passive optical switches and are simply selected by tuning laser input wavelength, to route the light confined in nanophotonic circuits. Our nanophotonic circuit consists of the main waveguide (also called bus waveguide) that transfers light from the external laser to the probe tip, and of several ring resonators, which we place along the length of the tip at an optimized distance from the bus. A sketch of the nanophotonic circuit is shown in Fig. 20.2 a. We choose ring resonators as passive optical switches since they enable us to select the light location by inducing small shifts in the input laser wavelength (<1nm). Since there is no need for electrical current flowing through the optical elements, issues regarding heat generation will not occur. In addition, rings have a low footprint, since only one bus waveguide is needed to interface all of the ring resonators. We describe the ring resonators in detail in page 55. By comparison, other designs, such as the ones described in [117], make use of arrayed waveguide grating purposes and require multiple waveguides for light routing (specifically, one for each output). With this strategy, we can choose the light output location to illuminate the desired neurons by tuning the external laser's wavelength, as sketched in Fig. 20.2 b. Notably, all of the ring resonances fit well within the opsin's absorption peak (Fig. 20.2 c [69]), thus different resonators can be selected by small wavelengths shifts to activate the opsin with similar sensitivity.

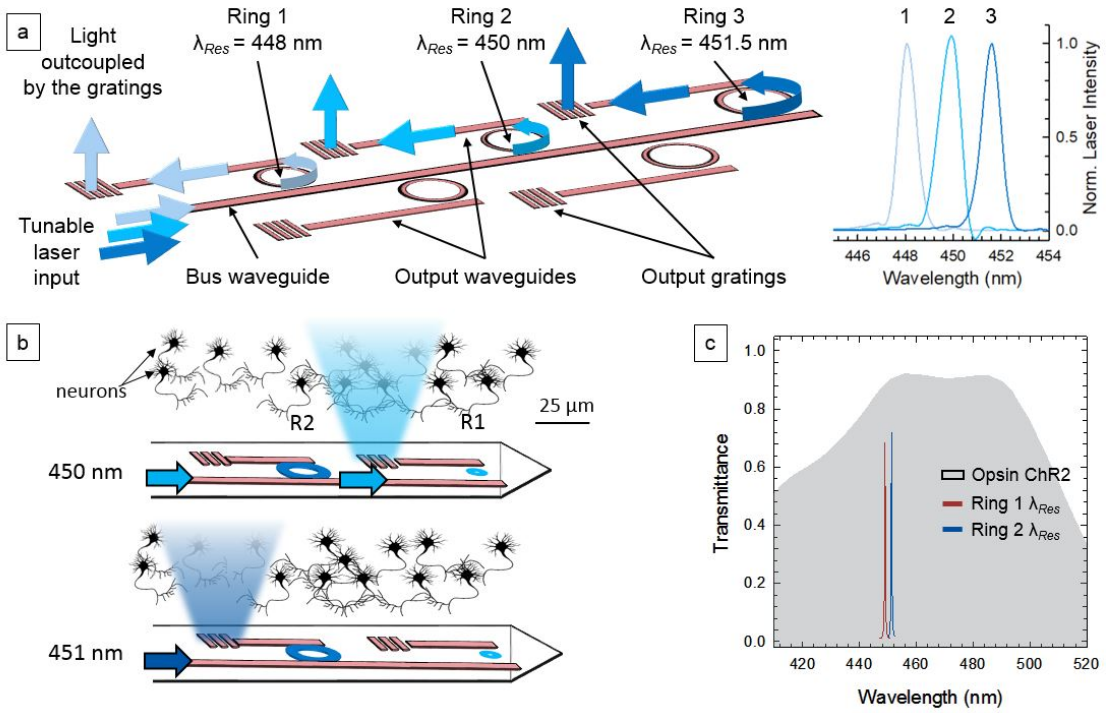

Figure 20.2: Ring resonators are integrated into the probe's nanophotonic circuits for passive and on-demand light delivery in area(s) of interest to optically stimulate the neurons of interest. (a): This schematic illustrates several rings, each with a well-defined radius corresponding to a different resonance wavelength, and their on-demand selection (and thus light output selection) through the external laser's wavelength tuning (on the right). (b): Schematic of the light output location selection along the probe tip. (c): All of the ring resonances (i.e. ring number 1 and 4) fit well within the opsin's absorption spectra (grey curve).

Integration of nanophotonic elements for multicolor illumination

To activate distinct neural groups in a population with two different opsins, our neural probe delivers on-demand illumination in the area of interest and independently for each of the two wavelengths pertaining to different opsins. We separate two wavelengths of different opsins to control them independently by integrating directional couplers [116] in the nanophotonic circuit, as schematically illustrated in Fig. 21.1. The directional coupler acts as a broad wavelength splitter (∼100 nm) having two single color outputs for a single mixed-color input. The broad

spectrum wavelength splitting allows for introducing additional nanophotonic elements, designed for each wavelength, to further manipulate the light within each of the two opsin absorption spectra, since ring resonators designed for blue wavelengths would not work correctly for red ones(see section 21, page 48). We select the light output location in the tip for each of the two wavelengths by integrating arrays of ring resonators close to each coupler output. The arrays consist of several ring resonators with different radii, each corresponding to a narrow (0.1 to 1 nm) resonance wavelength that is designed to work within the corresponding coupler's output wavelength range. By matching the input wavelength to the desired ring, we can select its corresponding output and therefore its location, as described in the previous section. Due to its broad wavelength band, the directional coupler splitting is insensitive to small wavelength variations (on the order of nanometers) used to interface between different ring resonators. Therefore, the combination of directional couplers and ring resonators in the nanophotonic circuit allows us to select the light output location for any of the two desired colors by matching the laser input wavelengths to the rings corresponding to the desired outputs. Additionally, the directional coupler has a small lateral footprint (<5µm), thus not exceeding the other nanophotonics' space.

Directional couplers consist of one input and two output waveguides (with width W), in which the lower output matches the input, and the upper output is a waveguide that runs parallel to the input for a well-defined coupling length L_c and gap G. The coupler mechanism relies on the light coupling and transfer between the input waveguide and the upper output, which is faster for longer wavelengths; based on this principle, we optimize the coupler to transfer the longer wavelength (i.e. 650 nm) while leaving the lower wavelength (i.e. 450 nm) in the lower output, as shown

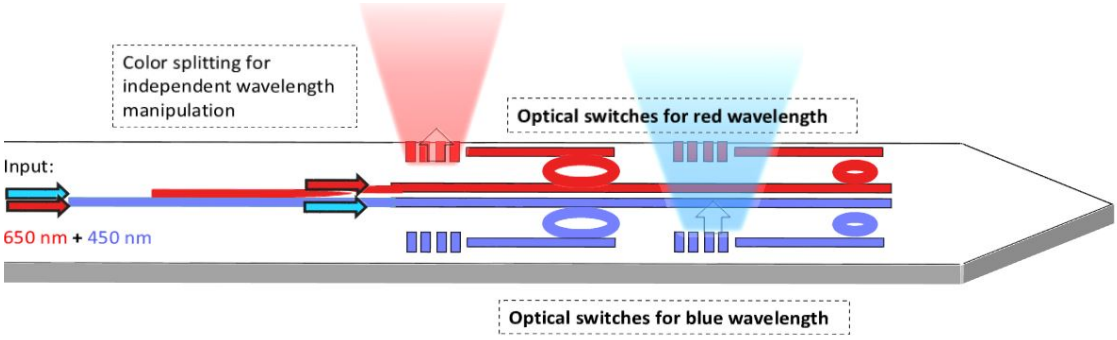

Figure 21.1: This schematic illustrates the integration of the nanophotonic circuit into the neural probe tip for simultaneous control of the light output location for two independent wavelengths (450 nm and 650 nm). For the single waveguide input, we integrate a directional coupler that splits the two wavelengths (based on their color) into two output waveguides. Each output embeds several ring resonators with different radii, allowing for selection of the light output location for each of the two wavelengths.

in Fig. 21.1. For each output, as a figure of merit, we define its corresponding transmission (T) as the output amount of light with respect to the input.

Simulations of nanophotonics

This section describes the simulations aimed at optimizing the various elements integrated into the nanophotonic circuit.

Simulation environment

We use Lumerical finite time difference domain (*FDTD*) - both two and three dimensional (2D and 3D) - to perform simulations of nanophotonic components [87]. FDTD Simulations [1] solve finite-difference approximations of Maxwell's equations in every given point of a two or three-dimensional grid to compute, for every time step, the electric and magnetic field in the simulation area. This process results in accurate calculations but requires long computation times [129].

Simulation parameters

We initially define the materials, refractive index (n), and extinction coefficients (k) either from ellipsometry data or from predefined software data. We design the structure, set an input source with the fundamental TE mode for the wavelength range of 400 nm – 700 nm, and collect the output data using transmission monitors, which returns the amount of transmitted light through or outside of the waveguiding element. We optimize the structure, based on the figures of merit, by performing geometrical parameters sweeps (i.e. the ring's gap value).

Choice of materials and material characterization

We use Si_3N_4 (core) and SiO_2 (cladding) as waveguiding materials due to their low absorption in the visible spectrum [40], which is the region of absorption for opsins [38]. A schematic illustration of the stack is shown in Fig. 22.1 a. We chose the thickness of the SiO_2 to be 2.5 µm, based on the tradeoff between the minimum thickness that would prevent light leakages from the Si_3N_4 nanophotonic circuit to the silicon substrate (which has to be $>$ 2 um [123]) and the maximum thickness that can be feasibly etched during the integration of nanophotonic circuits in the probe. We chose the Si_3N_4 waveguide thickness to be 160 nm since thinner waveguides provide lower optical propagation losses in straight waveguides − which is useful when starting from scratch the fabrication of photonic circuits −, although they provide higher bending losses [39][40]. We use commercially available wafers that have high optical quality for these two layers, measure their refractive index using ellipsometry, and obtain refractive indices around 2.05 and 1.47 and thicknesses around 160 nm and 2.5 µm for Si_3N_4 and SiO_2 respectively, as we show in

Fig. 22.1 b.

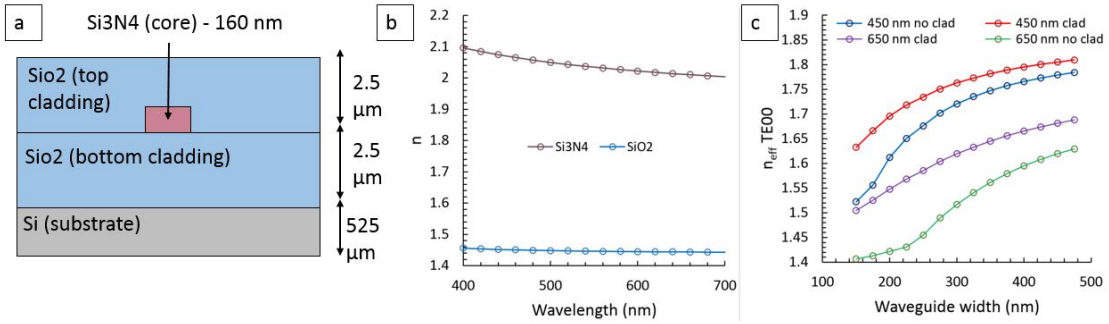

Figure 22.1: Waveguiding materials and characterization, (a): a waveguide stack made of Si_3N_4 (core) and SiO_2 (top and bottom clad) and (b): ellipsometry measurements of the refractive index for both materials are presented. (c): Effective index of fundamental mode TE00 for both top cladded and non top cladded waveguides as function of the waveguide width.

Waveguide simulations

Given these materials and waveguide thickness (160 nm), we use FDTD to simulate single-mode wire (or strip) waveguides, which are structures capable of confining and guiding light from the laser input to the tip of the device and rings. From the simulations, shown in Fig. 22.1 c, we define the waveguide's width to be ∼250 nm for blue wavelengths (450 nm) such that the waveguide propagates only the fundamental mode which, given our geometry, is quasi-transverse electric (TE00). Single-mode operation is necessary, since several nanophotonic structures that we integrate into the probe are designed to work for only one mode [7]; additionally, we chose a TE mode instead of a TM mode since the former results in lower bend losses due to a higher effective index and thus a higher mode confinment [24].

Fiber-waveguide coupling simulations

To couple light from the laser's output optical fiber to the waveguide, we simulate and optimize both edge *(butt) coupling* [86]] and *grating coupling* [5] structures. Edge coupling consists of the alignment of the fiber to the (cleaved or etched) input cross-section of the waveguide. By comparison, grating coupling consists of the alignment of the fiber to a grating structure which is fabricated in the same waveguide's plane (Fig. 22.2 a,b).

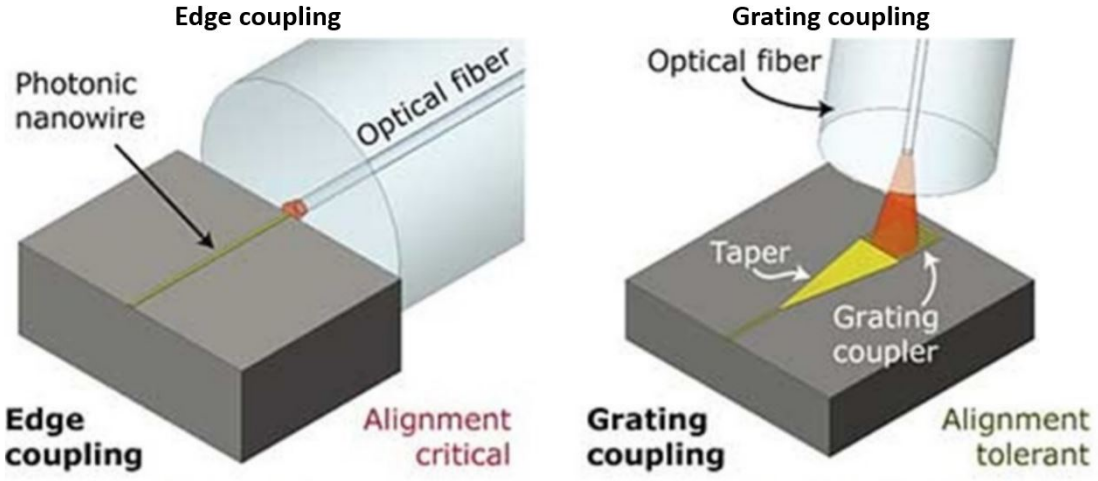

Figure 22.2: These schematic representations of the coupling between the laser's optical fiber and the nanophotonic circuit . (a): edge coupling and (b): grating coupling [93]

Edge coupling

Based on the input optical fiber, modeled as a gaussian input beam with a waist comparable to the fiber's (∼3 µm for fiber SM400 from Thorlabs), as well as the choice of materials and waveguide thickness (160 nm), we optimize the waveguide width to maximize the edge coupling efficiency. Due to the poor mode mismatch in the vertical direction, we achieve a maximum coupling efficiency of 12% for a waveguide width of 4 µm and 3 dB misalignment (the amount of fiber misalignment to reduce the coupling of 50%) of 2.5 µm and 500 nm (in the width and height

directions respectively), as shown in Table 22.1. Several strategies could be implemented to further maximize the coupling efficiency and the 3 dB misalignment, such as tapers [140], multiple tip tapers [95], and spot size converters [85] (which allow mode matching to the fiber's modeand a slow conversion to the waveguide's one) [76].

Grating coupling

In comparison to the edge coupling, gratings are used to couple light from the optical fiber to the nanophotonic circuit. Gratings have several benefits, namely the capability of matching the fiber's mode since they are fabricated in the plane; as a result, a higher coupling efficiency and larger misalignment tolerances can be achieved. Potential drawbacks are the narrow coupling 3 dB bandwidth (∼20 nm) and larger vertical footprint (although additional elements, such as micro prisms, can mitigate this last issue [117]). We simulate grating couplers by using 3D FDTD and an input Gaussian source with beam waist comparable to our fiber's (∼3 um) as well as collecting the light coupled in the TE00 mode into the waveguide. We simulate both square and horn-shaped gratings and obtain similar results for both. We sweep the groove pitch (adjacent groove distance), duty cycle (DC, amount of groove versus SiO_2), fiber angle, and misalignment parameters. Furthermore, we obtain a coupling efficiency (at 450 nm input wavelength) of 32% (with 3 dB band of 17 nm) for pitch 315 nm, DC = 0.5 and fiber angle 13° (in the direction of the waveguide) and tolerance misalignments larger than for edge coupling, as displayed by Table 22.1.

Our Implementation

Coupling method, FDTD simulation	Coupling efficiency (%)	Maximum experimental output power(mW)	simulated 3dB misalingment in X (nm)	simulated 3dB misalingment in Y (nm)	simulated 3dB misalingment in Z (nm)	simulated 3dB misalingment tilting (degrees)
Grating coupling	32%	9.46E-3	3.3	3	>50	1.6
Edge coupling	11.5%	2.71E-3	2.5	0.5	25	2.2

Table 22.1: Comparison between simulations for edge coupling and grating coupling methods.

Although grating coupling is more efficient than edge coupling, we chose the edge coupling method due to its broadband coupling efficiency that allows for the use of nanophotonic structures that deliver multicolor illumination, such as directional couplers. In addition, edge coupling results in a lower footprint since it does not require extra vertical space to fit the fiber. The edge input, designed to maximize coupling efficiency, is 160 nm thick and 4 µm wide. We use an adiabatic taper (a gradual waveguide tapering) to convert its mode to one of the single-mode waveguide (160 nm thick and 250 nm wide) in the tip area. The taper is 150 um long since our 2D FDTD simulations show that it must be longer than 50 µm to convert all of the light to the fundamental mode.

Background: waveguide coupling and resonance

The fundamental mode of two parallel waveguides close to each other (i.e., with a distance < 1 µm) is a superposition of a symmetric and an antisymmetric mode spread across the two waveguide's cross section (Fig. 22.3 a) [21]. The two modes have a different effective index (whose difference increases as the gap between the two waveguides decreases) and phase (the antisymmetric mode in waveguide B has a π phase difference with respect to waveguide A) (Fig. 22.3 b). Given the two modes' effective index difference - and thus propagation velocity - the modes will

accumulate a phase difference. After a π phase difference, the mode will cancel in the first waveguide (waveguide A) and will constructively interfere in the second (waveguide B). Thus, light transfers back and forth for two adjacent waveguides; the power transfer from waveguide A to waveguide B (k^2) is described by:

$$k^2 = sin^2(\frac{\pi * \delta n * L}{\lambda})$$

with λ the wavelength and δn the effective index difference between symmetric and antysimmetric mode (which can be calculated with FDTD), L the coupling length (length at which the two waveguides run close to each other). A total transfer of light happens at a length $L = L_c$ (the cross-over length), which is equal to:

$$L_c = \frac{\lambda}{2 * \delta n}$$

As mentioned above, the coupling coefficient C = π*$\delta n/\lambda$ depends strongly on the gap between the two waveguides, with an inverse exponential dependence [21]:

$$C \sim e^{-A*G}$$

with A equal to a constant dependent on the waveguide geometry and G the waveguide gap. It's also important to notice that, once the mode transfers from waveguide A to B, the phase will have a $\pi/2$ shift due to the negative component of the antisymmetric mode profile in waveguide B.

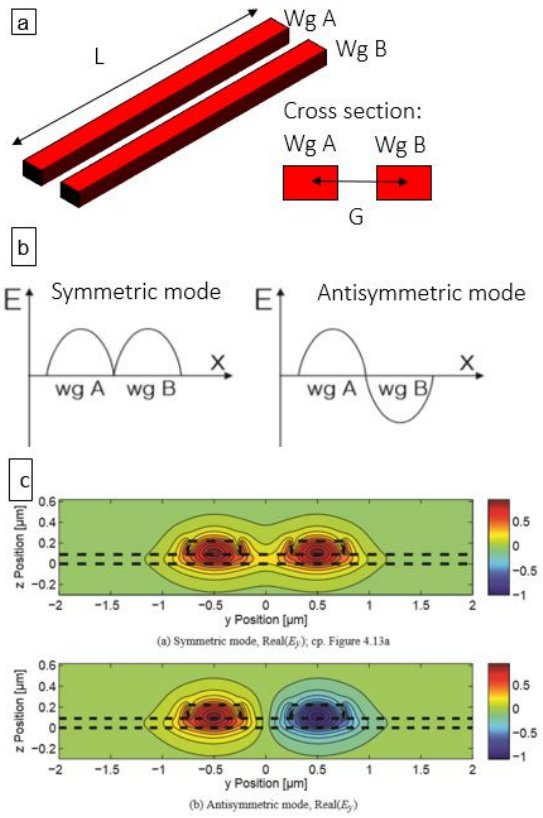

Figure 22.3: Modes of two adjacent waveguides from [21]. (a): schematic representation of the two waveguides (wg A and wg B) and their cross section. (b): schematic of the electric field value for both the symmetric and the antisymmetyric modes. (c): Mode plot for the symmetric (top) and antisymmetric (bottom) modes.

Add-drop ring resonator simulations

We use ring resonators as passive optical switches to select the light output location. Each ring has a specific and well-defined radius, which is designed to resonate at a specific wavelength and is coupled to an output waveguide, terminated by a grating for light extraction (Fig. 22.4 a). The whole process of light transfer from the bus waveguide to the grating of interest relies on the evanescent light coupling between adjacent optical elements, due to their close spatial proximity, as well as on the light resonance inside the ring [10]. When the input laser wavelength, transferred from the bus to the ring, matches the ring's resonance frequency (a multiple

of the cavity length), light resonates in the ring due to constructive interferences. This is described by the formula:

$$\lambda = n_e * L * m$$

Where λ = resonance wavelength of the ring, n_e= effective refractive index, L = ring circumference, m=mode number This resonating light, in turn, couples to the ring's output waveguide and is finally extracted perpendicularly by its grating. Wavelengths that are resonant in the ring experience in fact a total round-trip phase of 360°. Besides, light experiences a 90° phase shift when coupling from the input to the ring and an additional 90° phase shift when coupling from the ring to the input waveguide. Thus, resonant light in the ring interferes destructively with light in the input waveguide. Conversely, if there is no match between the input wavelength and the ring's resonance frequency, light experiences a phase different than 360° inside the ring and does not destructively interfere with the light in the input waveguide. As a result, non-resonant light couples back to the bus waveguide, where it can eventually resonates with rings having different resonance frequencies.

We optimize the design of ring resonators based on the light delivery spatial pattern of interest, external laser characteristics (see page 67), and the target opsin using FDTD simulations, in which we vary the ring parameters – namely the waveguide and ring widths W, their gap G, and the radius R – and analyze their resulting trends on the figures of merit in the wavelengths around the opsin absorption peak (±10 nm). The figures of merit are the free spectral range (FSR), the full width at half maximum (FWHM), Q factor, and Finesse F which are, respectively, the wavelength spacing between different resonance modes of a ring, the half-power bandwidth at resonance, the peak resonance wavelength divided by the FWHM,

and the ratio between FSR and FWHM that corresponds to the number of independently addressable rings [2]. Fig. 22.4 2 displays a false-color scanning electron microscopy (SEM) image of a fabricated ring resonator and its components: bus waveguide, ring and output waveguide. In the FDTD simulations, we vary the waveguide and ring width (W) for values between 200 nm (below which the light is not confined) and 300 nm (above which the waveguide is not single-mode), the gap (G) between 40 nm (for fabrication practicality) and 110 nm (very low coupling), and the radius (R) between 2 µm (below which there are high curvature losses) and 5.5 µm (to limit the structure lateral footprint). For the parameters sweeps we perform two-dimensional simulations (which are comparably faster than 3D ones) that well reproduce both the rings' transmission and FSR, but underestimate the Q factor (Fig. 22.4, Table 22.2).

Simulation type	FSR [nm]	T [%]	Q	FWHM [nm]	Finesse
2D	4.406	74	3001.8	0.1499	29.39
3D, 160 nm thickness	4.402	77.1	1771.2	0.254	17.32
3D, 250 nm thickness	4.318	75.8	2230.4	0.201	21.42

Table 22.2: Comparison between simulations for edge coupling and grating coupling methods.

We display the resulting figure of merit trends in (Fig. 22.4 c-e). The transmission increases for smaller gaps (since more light is coupled in the ring) and widths and decreases for smaller radii (due to higher curvature losses). The Q factor increases for larger W, G and R (that corresponds to a longer round-trip length of light in the ring [2]). The FSR is constant for variations of W and G but increases for smaller R. From these results, we extrapolate that it is necessary for a balance between a small enough G value and large enough Q and R values, such that a sufficiently high T and FSR can be achieved.

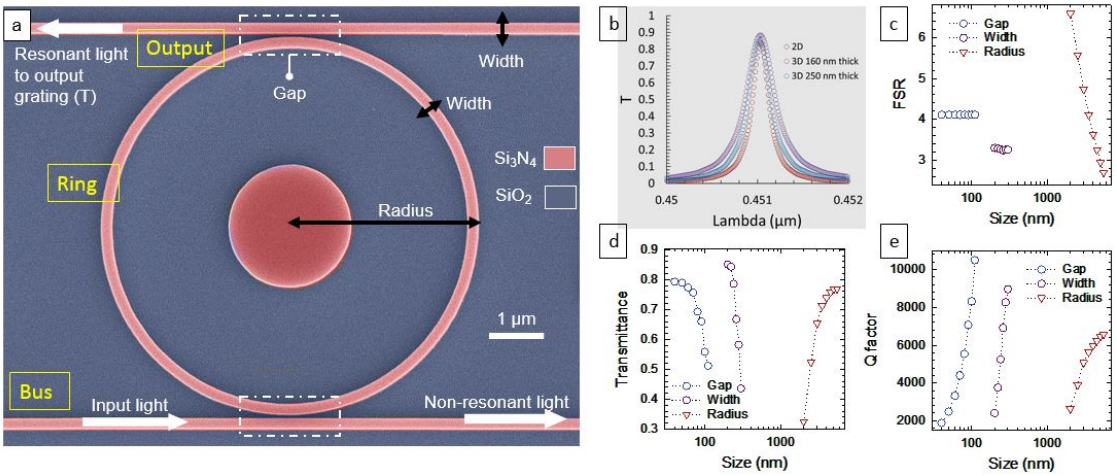

Figure 22.4: Ring resonator simulations. (a): false color SEM of an add-drop ring resonator, highlighting the light propagation direction (white arrows) and some geometrical parameters (gap, width and radius). We calculate the ring's transmittance at the output (drop) port. (b):Comparison of two dimensional (red) and three dimensional (blue for 160 nm thick Si_3N_4 and violet for 250 nm thick Si_3N_4) FDTD simulations of a ring resonator for a given W, G and R value demonstrate that similar results (except for the larger FWHM) are obtained. (c-e): 2D FDTD simulation of ring resonators shows trends of transmission, Q factor, and free spectral range versus variations of the width, gap and radius.

Once we define the desired rings' FSR, FWHM and T, we calculate the ring's radii such that their resonance wavelengths equally distribute within the input laser's tunability range, taking into account the FWHM, by linearly extrapolating their values as shown in Fig. 22.5 a. After the extraction of the rings' geometrical parameters (based on the 2D FDTD simulations), we validate the results with 3D simulations.

For the first application, we aim at delivering light in four different areas along the tip (according to our laser's model) to activate the channelrhodopsin ChR2. Therefore, we set the initial wavelength range for the rings' resonance frequencies according to the maximum absorptance of the ChR2 (centered at 450 nm) and then restrict it according to our laser's tunability range, which is 3.4 nm for the selected

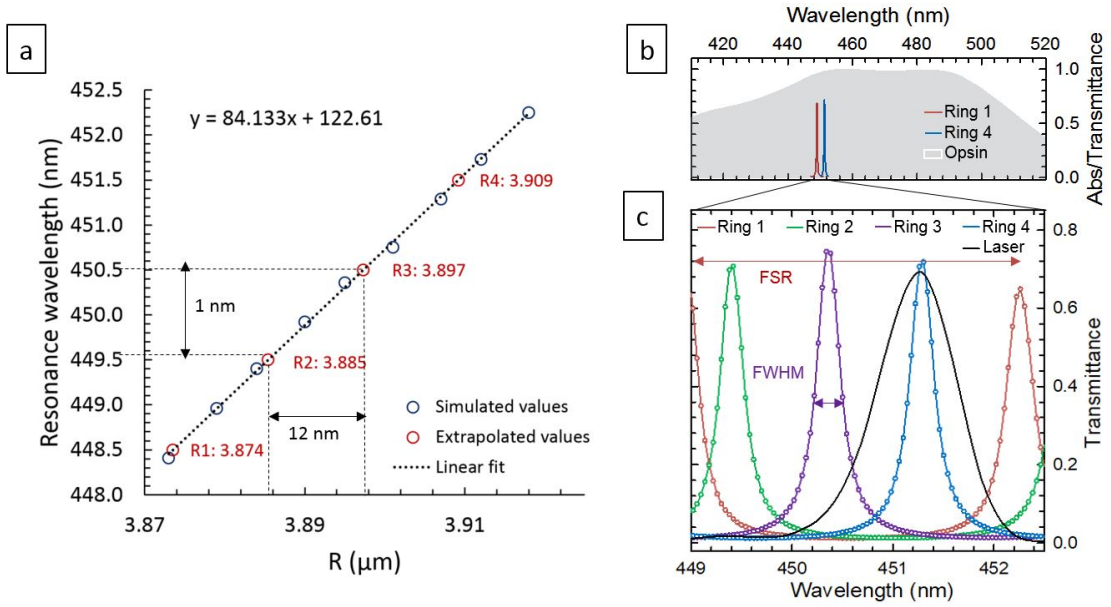

Figure 22.5: simulated ring resonance frequencies as a function of the ring radius (Gap=80 nm, Waveguide width=250 nm) (blue points) and linearly extrapolated radii (red points) for equal spacing of the ring's resonances within the laser's tunability range, taking into consideration its FWHM. (b): First and last ring resonance peaks and opsin normalized absorption [69] (in grey), which is almost unitary for all the ring resonances. (c): 3D FDTD simulation of ring resonators for four point on-demand illumination along the probe tip. The rings are optimized according to the laser's tunability range and FWHM (black curve).

laser model (QFLD-450-10S from QPhotonics, see more detail in page 67).

We choose the ring free spectral range (FSR) to be close to the laser's tunability range to maximize the number of rings within this range. The resulting ring activation wavelength range (449nm-452.5 nm) fits within the maximum ChR2 opsin absorption (Fig. 22.5 b): therefore, we do not expect a significant variation in the opsin sensitivity at the different grating sites [57] [69]. We choose the ring's Q factor ($\sim$1600) to be on the same order of the laser's one (860$\pm$20), such that it absorbs all of the laser's energy and maximizes the percentage of light transferred from the bus to the output waveguide at the resonance frequency (called transmittance). The Q factor is slightly higher to accommodate for fabrication shifts (which will

tend to reduce it). Given the chosen ring FSR and Q factor, we chose four rings, whose transmittance (on average 69.5 ± 2.9 %) is displayed in Fig. 22.5 c, along with the laser spectrum (black curve). The rings' radii, resonance wavelengths and Q factors are reported in Table 22.4.

Finally, we calculate the resonance curves overlap, which results in light leaking into non selected rings. We calculate a 6% overlap between resonance curves, which results in an on/off ratio (the amount of grating output power for the selected ring versus the non selected one) of 12.2 dB. This value is comparable with other nanophotonic technologies [83], and it ensures a sufficient gap between the output power at the desired grating versus the non-selected gratings. As a result, once chosen the proper range for the system under study, the leaking light will not activate unwanted neurons.

Ring number	Radius [µm]	Resonance [nm]	Q factor	FWHM [nm]
1	3.873	448.5, 452.26	1500	0.281
2	3.885	449.4	1610	0.301
3	3.897	450.6	1550	0.26
4	3.909	451.5	1120	0.301

Table 22.3: Simulated ring resonator parameters for a fixed gap and width of (respectively) 80 nm and 250 nm.

Rings designed for blue (450 nm) wavelengths do not work well for longer wavelengths (650 nm) due to modal dispersion (difference in effective refractive index as a function of the wavelength). Red wavelength are useful to activate different opsins. Thus, it is not possible to use a single array of ring resonators to work on wavelengths of tens of nanometers apart. This concept is illustrated in Fig. 22.6 a,b, where we simulate (2D FDTD) a ring designed for blue wavelengths and the results demonstrate that while expected optical performance for 80 nm of gap

(T∼70%, FWHM∼0.3) is achieved, there is poorer performance at the wavelength of 650 nm (T>90% at resonance but >8% far from resonance, FWHM∼2 nm). Furthermore, tradeoffs for the two wavelengths do not work. For instance, increasing the gap above 140 nm leads to improved ring performance at 650 nm but drastically decreased ring performance at 450 nm (T<0.3). By comparison, designing rings specifically for red wavelengths enables the possibility in obtaining good ring performance (T= 90 ± 0.5 %) as displayed in Fig. 22.6 c, along with the laser (QPhotonics, model QFLD-450-10S) spectra.

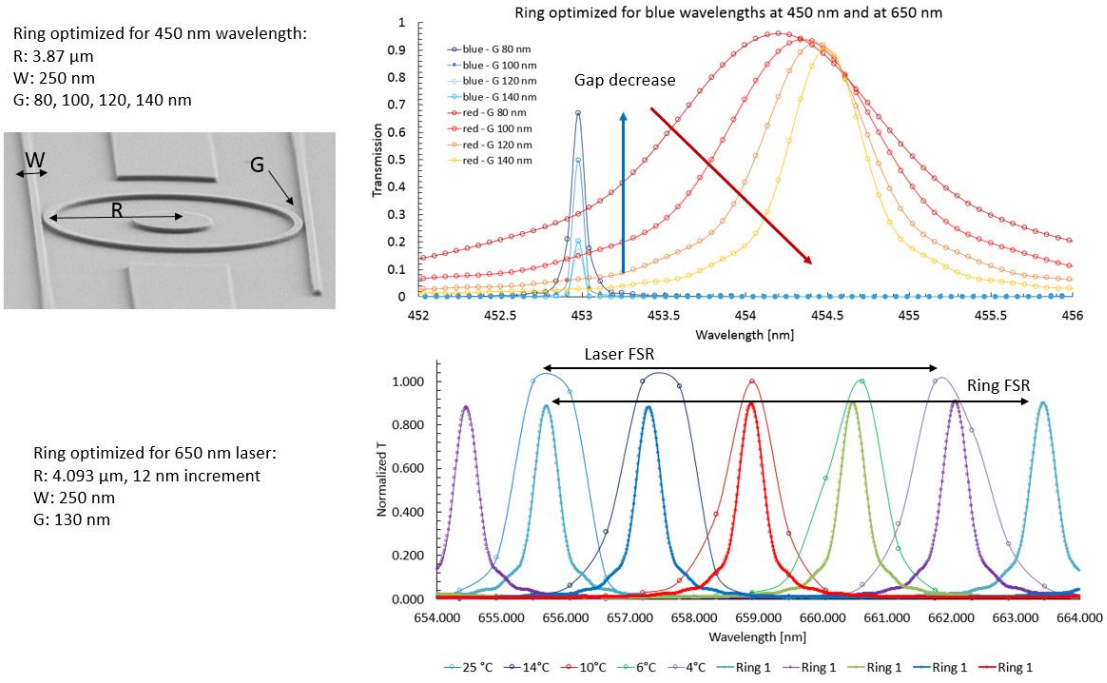

Figure 22.6: This shows ring resonators for red wavelengths. (a): Simulation geometrical parameters of a ring are optimized for blue wavelengths. (b) Comparison of results for a blue source input (blue curves) and red source input (yellow-red curves) demonstrate that rings designed for blue wavelengths do not work well for longer wavelengths. (c): Rings are optimized specifically for red wavelengths and are compared with our red-wavelength laser model spectra at different temperatures (thus, wavelengths).

Outcoupling grating

We simulate gratings with the objective of optimizing the amount of light extracted from the waveguide to the brain tissue as well as obtaining the desired beam shape and angle. Given our material and thickness (Si_3N_4, 160 nm), we sweep the outcoupling grating parameters (pitch, duty cycle,..) and design, which are identical for coupling grating, to optimize the emission efficiency (amount of light outcoupled), emission angle, and output beam shape (that depend on the illumination of interest). We design both regular gratings, which have rectangular-shaped grooves and collimate output light (with a slight divergent angle), and focusing gratings, which have chirped grooves to focus or spread light more efficiently, as schematically shown in Fig. 22.7. For the simulations of both, we set the input as TE00 mode source in the waveguide and collect the light transmitted above the grating plane.

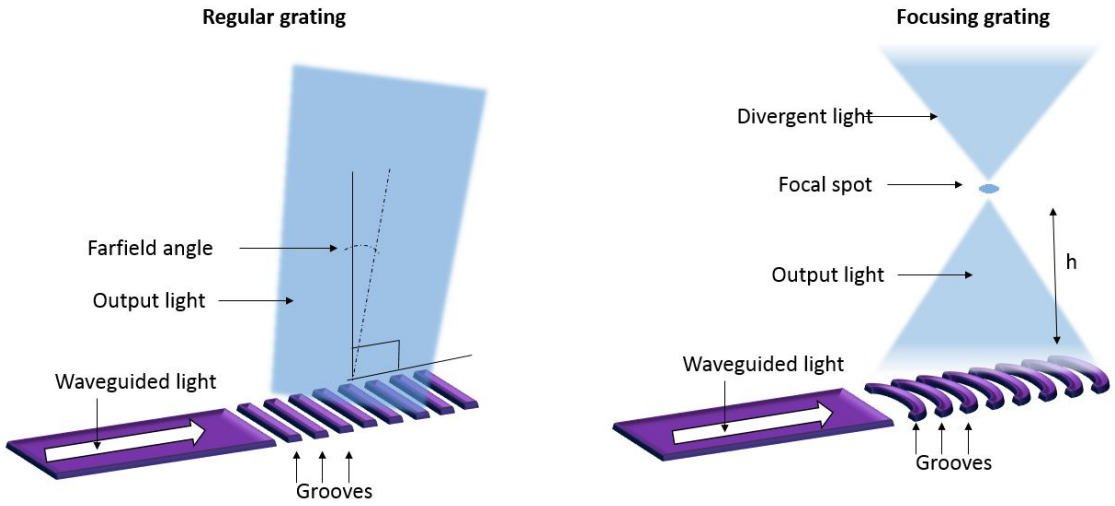

Figure 22.7: schematic illustration of outcoupling gratings that extract light from the waveguide into brain tissue. (a): regular grating and (b): focusing grating

Optimized square-shaped regular grating outcouplers are 4 µm wide and 15 µm long, with either 365 nm or 280 nm pitch (for emission angle of -16° and 0° respectively), have 0.5 duty cycle, and result in almost 70% outcoupling efficiency

(with oscillations due to back reflections from the silicon substrate [21]). Wider gratings do not increase efficiency while longer ones (> 30 µm) only increase the efficiency marginally (5% increase) but take up more space in the tip (where we place the electrodes).

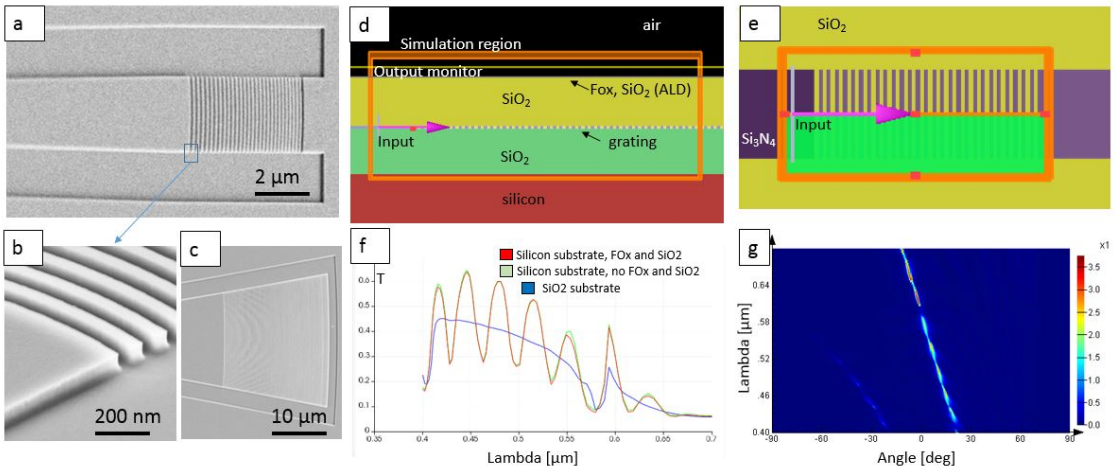

Figure 22.8: regular grating fabrication and simulation results. (a-c): SEM images of fabricated grating for light outcoupling from the waveguide (b,c) and light coupling from the fiber to the nanophotonic circuit (c). (d,e): lateral view (d) and top view (e) of the simulated grating. (f): Outcoupling transmission in the visible wavelength and (g): farfield value of the grating output angle at different wavelengths are shown.

Focusing gratings are scripted in Matlab according to the formula in [24], which calculates the groove shape such that all the rays are diffracted into the same spot (the focal height h) with the same path length and no destructive interferences occur:

$$\sqrt[2]{x^2 + y^2 + h^2} + x * \frac{n_e f f}{n_m} = m * \frac{\lambda}{n_m}$$

Where x, y are in-planecoordinates, h is the focal height, n_m is the refractive index of the medium (saline, n_m= 1.33), $n_e f f$ is the effective refractive index of our photonics (1.71), and m is the number of grooves. The script provides an output *.CIF* file which can be exported in both L-Edit (for electron beam lithography mask

exposure) and Lumerical (for simulations). Simulations are performed similarly to the regular outcoupling grating, wih the exception that the output electric fields are both monitored at the grating cross-section(Fig. 22.9 a,b) and on relevant planes (at focus and above focus, Fig. 20.1 c-e).

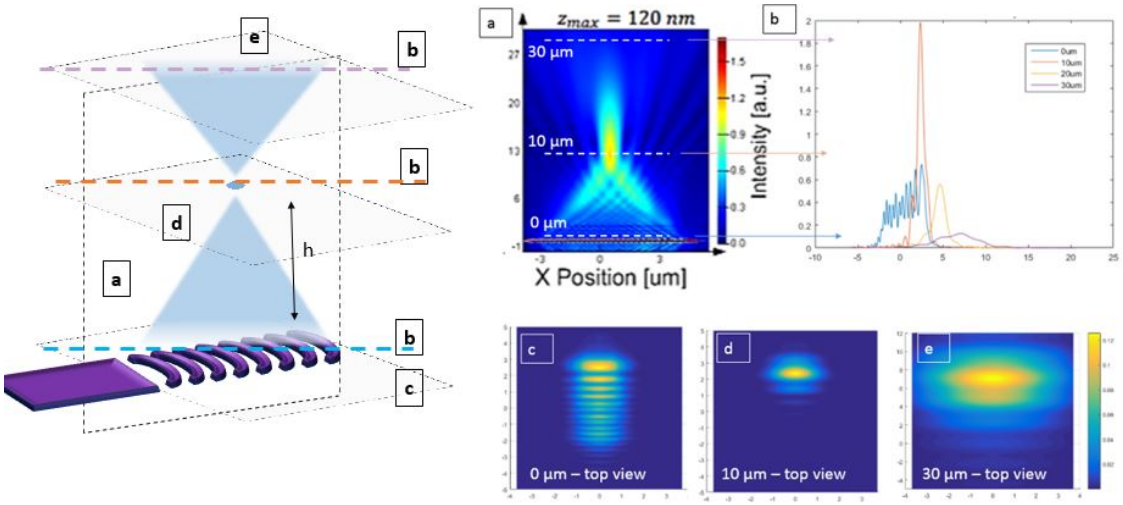

Figure 22.9: focusing grating simulation results. (Left): Schematic shows the grating and various monitor planes (letters correspond to figures on the right). (a): Cross section monitor displays the electric field and its focusing 10 µm above the plane. (b) Corresponding line plots are at different heights and (c-e).

Directional couplers

Next, we simulate the directional coupler with the goal of achieving high transmission for the wavelengths of 450 nm and 650 nm, which were shown to independently drive responses from different opsins (i.e. Chronos and Chrimson [57]). We simulate and optimize for our two wavelengths of interest two types of coupler design (Fig. 22.10 a,b): short couplers, which do not transfer the blue light to the adjacent output but transfer red light once (configuration 1) and long couplers, which transfer blue and red light multiple times between the two output waveguides. Configuration 1 has a coupling length L_c equal to 4 µm, a waveguide width

W of 275 nm and a gap G of 240 nm; configuration 2 has L_c equal to 19 µm, W 250 nm and G 170 nm. Their output transmission is plotted in Fig. 22.10 c,d and the values in Table 22.4 and shows high transmission (>90%) and small values of cross talk for both configurations, but slightly better for configuration 2; however, configuration 1 is more robust towards waveguide width variations that can occur during the coupler fabrication. Since the 1 dB wavelength band (corresponding to 10% coupler transmission loss) is around 71 and 33 nm for (respectively) configuration 1 and 2 and the rings' FSR is around 3-6 nm, we do not expect to have any influence of the coupler presence on the rings' functioning.

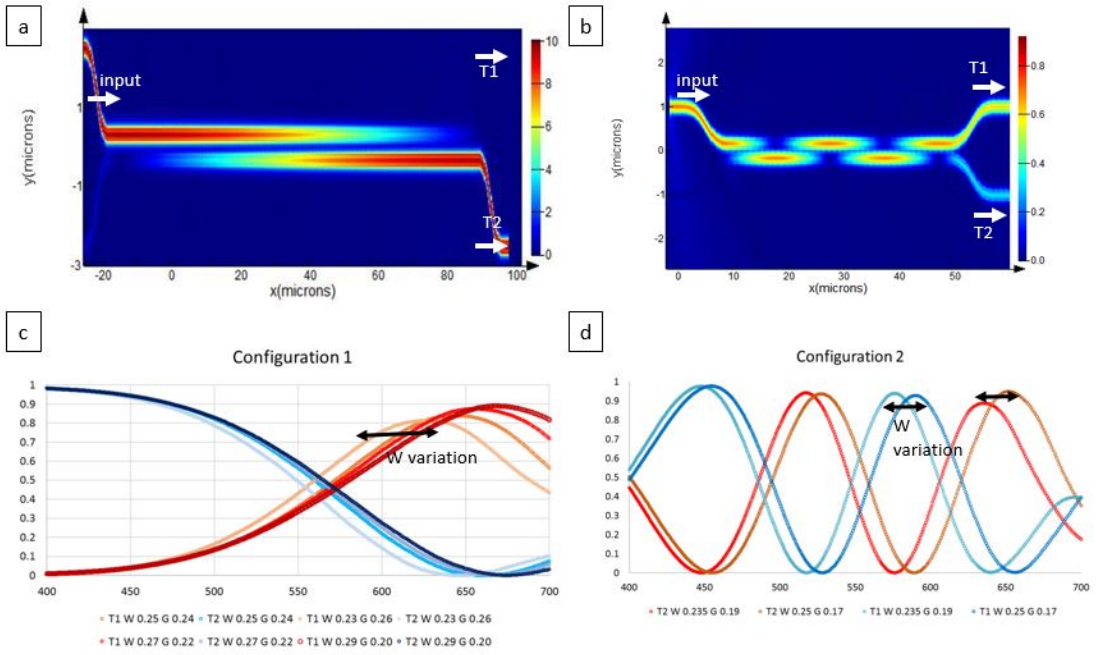

Figure 22.10: directional coupler 3D simulations. (a): Three-dimensional simulation of the electric field inside the directional coupler for a fixed wavelength. The coupler can transmit light in two distinct configurations: either the light is split once (a) or multiple times (b). (c,d): (trasnmission) for the two configurations of (a) and (b) designed to split the 450 nm and 650 nm wavelength and for different variations of the waveguide width that could result as during the fabrication.

Combination of light location and opsin-type control

Parameter	Configuration 1	Configuration 2
T 450 nm	93%	97.6%
T 650 nm	89%	94.8%
Cross talk 450 nm	4.1%	1%
Cross talk 650 nm	0.17%	0.2%
1 dB band 450 nm	88.97 nm	35.03 nm
1 dB band 650 nm	71.847 nm	33.61 nm
Loss 10 nm W variation, 450 nm	0 %	2.02 %
Loss 10 nm W variationn, 650 nm	0.03%	16.3%
Cross talk from 10 nm width variation at 450 nm	4.1%	1.55%
Cross talk from 10 nm width variation at 650 nm	0.22%	4.64%

Table 22.4: Simulated ring resonator parameters for a fixed gap and width of (respectively) 80 nm and 250 nm.

We combine both the directional couplers and ring resonators into the nanophotonic circuit to independently control each color's output location(s). We simulate such nanophotonic circuit embedding both couplers and rings and obtain similar results to those for the two separate optical elements, as shown in Fig. 22.11 a,b.

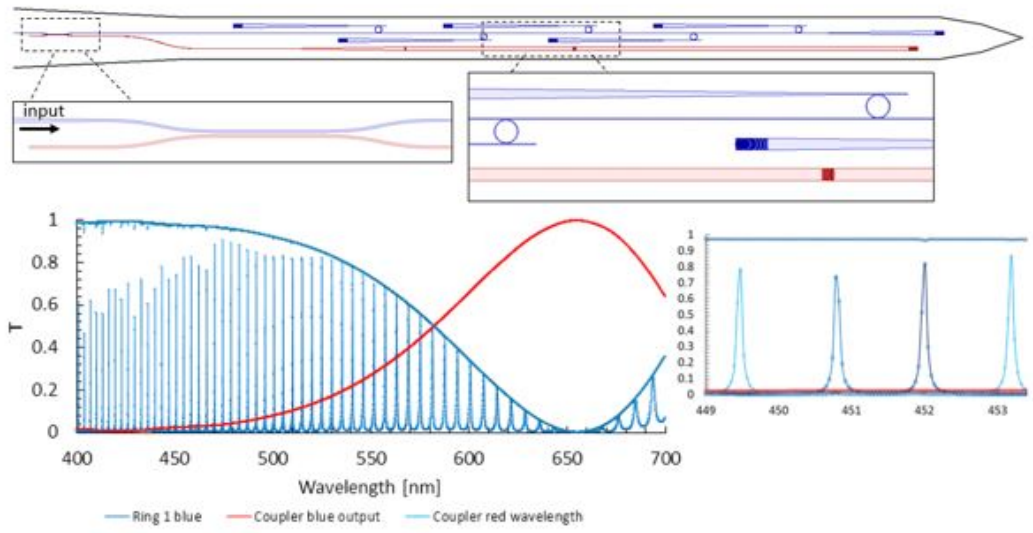

Figure 22.11: combination of the directional coupler and ring resonators is designed for both blue and red wavelengths. (a): 2D FDTD simulation results and (b) magnification around the 650 nm wavelength

Laser characterization

We design our nanophotonic circuits based on chosen laser and its output wavelength and power characteristics. We use a small laser diode (model QFLD-450-10S, from QPhotonics) as a convenient proof-of-concept test of our probe. We measure the laser's output power using a powermeter (PM 100 from Thorlabs) and its wavelength with a spectrometer (AvaSpec-ULS2048) and extract all the data through automatic Matlab scripts. In particular, given our spectrometer's low resolution (0.5 nm), we fit its measured data points with a Gaussian curve and extract the peak wavelength, obtaining a measurement resolution well below 0.1 nm. First, we obtain our laser's central wavelength (450 nm) and Q factor (860) (Fig. 23.1 a). Next, we tune the laser's temperature from 8°C to 65°C (through its temperature-controlled mount) to change the wavelength and obtain a tunability range of 3.21 nm (Fig. 23.1 b). By cycling up the laser with 0.1°C increase and 1 s pause time between each, we repeatably obtain the same wavelengths (Fig. b). By tuning the temperature by small increments (0.1 °C), we vary the wavelength by 0.04 +- 0.02 nm, demonstrating that our laser can precisely be tuned to the desired wavelengths to select the corresponding resonators.

Carbon nanomaterials for microsensors

As mentioned in section 15 (page 28), several materials were explored in various literature to improve the electrode-tissue interface, signal to noise ratio, and biocompatibility. Carbon based materials are of particular interest because of their unique combinations of electrical, chemical, and optical properties. In addition, Graphene and CNT are capacitive materials, as opposed to Au, Pt, and IrOx (faradaic materials) and thus are 'safer', since they do not produce any chemical

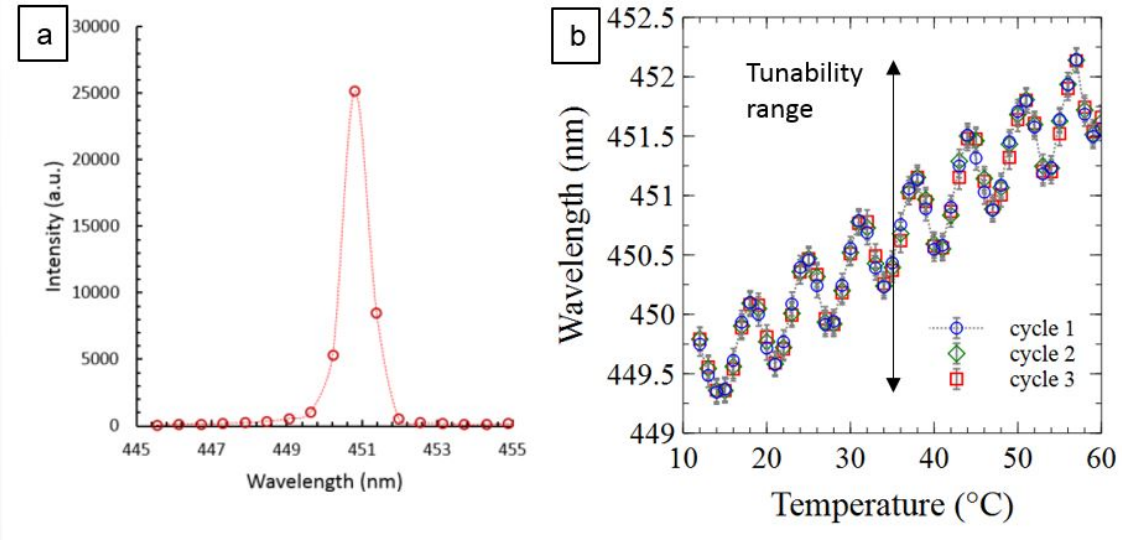

Figure 23.1: Laser characterization. (a): Laser spectrum and (b) temperature-wavelength curve for several cycles, showing high repeatability and precise wavelength selection.

reactions with the ionic environment [19]; *'' carbon is a chemically stable element and one of the fundamental compositions in the body, the toxicity of carbon is minimal compared to metallic materials which may release harmful metallic deposits in the body"* [19]. Carbon atoms can be arranged in different forms and result in different properties. The first example are carbon nanotubes [104], which consist of carbon atoms arranged in cylinders of a few nm in diameter and which, when coated on electrodes, decrease impedance and increase charge transfer (amount of current that can be delivered by unit area) due to the high surface to volume area [55]. Carbon nanotubes can either be plated on microsensors [139] [73] [48] [133] [72] or aligned vertically on them [64], [92]. Random arrangements of carbon nanotubes were also used as transparent and stretchable electrodes [136]. However, there are studies that highlight the citotoxicity of carbon nanotubes [137]. A more inert and biocompatible material is diamond, which was also shown to have a high chemical sensitivity [33]. Another material of interest is Glassy carbon, which is

comparable to platinum electrodes and shows a half signal to noise ratio, 70% wider electrochemical window, high adhesion to delamination [131]. An interesting family of carbon based materials is graphene (a two dimensional arrangement of carbon atoms in hexagonal cells) and its derivates (porous graphene [71] and graphene oxide [25] [91] [126] [74] [66]). Monolayer graphene presents excellent electrical (high electrical conductivity), mechanical, and optical properties (> 97% transmission), combined with a high biocompatibility. The combination of electrical and optical properties were studied in multi electrode array electrodes for simultaneous electrophysiology and optical (2 photon) imaging [70] [96] [125] [59] [97]. We thus studied a fabrication process to integrate graphene at the wafer scale on our neural probes' electrodes, which we describe in section 137. Other carbon based materials that may be of interest for neural applications are active carbons [98] and carbon nanoonions [26]. The first are highly porous, micrometric-sized particles obtained from physical or chemical activation of carbonaceous materials (i.e. coal), while the second are nanoparticles made of concentric shells and obtained from the detonation of nanodiamonds [26]; both have a high surface to volume ratio (area 3000 m2/g [98] and 500 m2/g [26], (respectively) and such, have the potential to decrease the electrode's signal to noise ratio. We study their electrodeposition in page 141.

Device design, integration of nanoscale circuits in the microprobe

Once we define the main concepts and geometrical parameters of nanophotonic and electrical circuits, we design the microprobe and the integration stacking of circuits to achieve maximum reduction of the insertion area without sacrificing the circuit's performance. The probe consists of three parts: (i) the tip, which is

the only recording and manipulating area that is inserted into the mouse's cortex, (ii) the interface, which is an area that connects the tip's circuits to the external laser's optical fiber and the printed circuit board (PCB) and electronics, and (iii) a connecting area, which brings the electrical and optical signals from the tip to the interface area and vice-versa (Fig. 24.1 a,b). The interfacing area is 525 um thick and has dimensions of 1.5 mm x 2mm such that the groove can be embedded for connecting the laser's optical fiber and pads for the PCB-probe electrical connection. The connecting area is 20 um thick and gradually tapers towards the tip. The tip dimensions are minimized (compatibly with the lateral footprint of the circuitss we integrate) to reduce the potential of damaging brain tissue. We obtain a tip that is 900 µm long, 45 µm wide, and 20 µm thick. The tip is terminated by a sharp taper (with one µm curvature radius) to facilitate the device penetration through the dura mater.

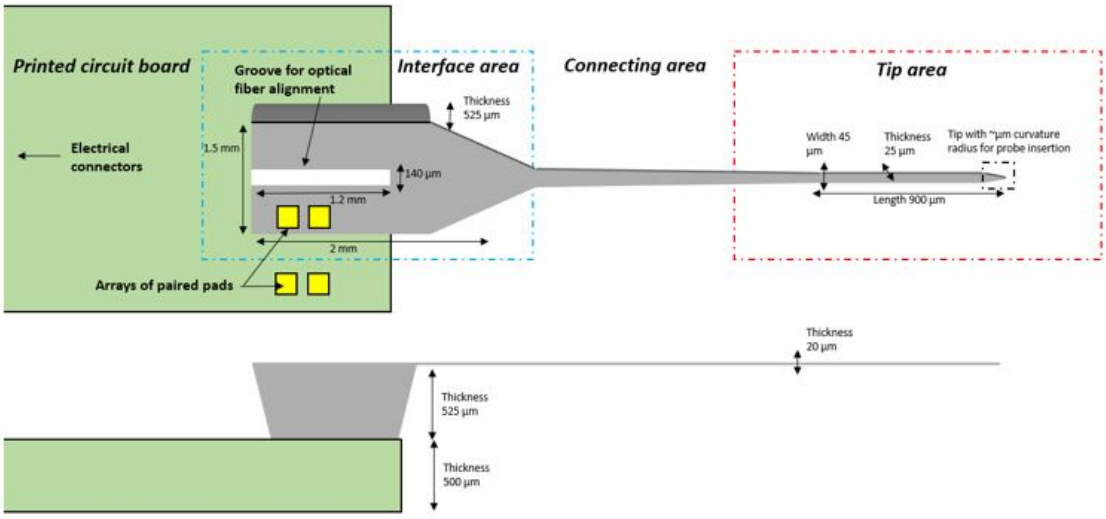

Figure 24.1: probe schematic design. top view (top image) and lateral view (bottom image) of the device, which is composed of a thin tip (brain insertion area), an area to connect the tip's sensors and stimulation sites to the interfacing area (embedding a groove to host the external laser's optical fiber), and a PCB on which the device is mounted and electrically connected to.

The entire device embeds three different levels, which is schematically illustrated in (Fig. 24.2) for the tip area. The bottom level consists of a 15 µm thick silicon layer that provides mechanical stability for the tip. On top of the silicon, we fabricate the level embedding the nanophotonic circuit, which is composed of patterned silicon nitride, sandwiched between two optically isolating silicon dioxide layers (SiO_2: 2.5 µm bottom and 3 µm top cladding). The purpose of these nanophotonic circuits is to deliver on-demand light to specific locations along the tip length. The nanophotonic circuit integrates several elements. The edge coupler in the probe's interfacing area inputs light from the laser's optical fiber to the nanophotonic circuit's waveguide, which confines and propagates light from the coupling region to the probe's tip. Additional optical elements in the probe's tip, such as color-based demultiplexers or optical switches, deliver light of a specific color to the locations of interest. Output waveguides and grating outcouplers terminate these optical elements to deliver the confined light into the brain tissue. Notably, such circuits have a lateral footprint below 20 µm for several addressable outputs.

Above the nanophotonic circuit, we fabricate the level embedding the electrical circuit, which is made of titanium and gold. This layer is comprised of open electrodes for reading neural activity as well as SiO_2-passivated wires for transferring the signal from the electrodes to the probe interface area. The tip embeds 64 closely packed titanium/gold electrodes with dimensions of 5 µm x 25 µm and pitch 27.5 µm. Electrode dimensions are on the same order of the neural cell soma such that they record with single-neuron resolution. 64 corresponding electrodes with dimensions of 100 µm x 100 µm and 175 pitch µm are hosted on the probe interfacing area. We connect pairs of electrodes at the two ends of the device with SiO_2 passivated wires, which are 120 nm wide and have 450 nm pitch in the tip area,

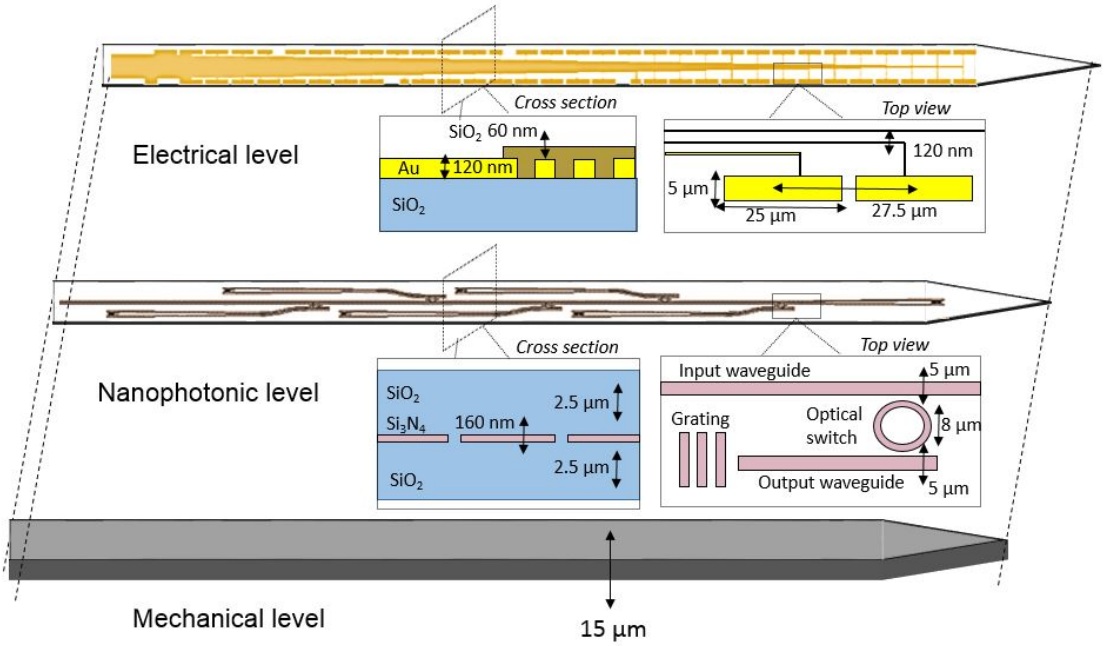

Figure 24.2: The probe is fabricated onto three levels: mechanical (for tip stability), nanophotonic (for light delivery), and electrical (for electrical readout).

such that they fit in the tip space of ∼30 um between two electrode rows. Wires are gradually widened to 1 µm wide as they approach the wire bonding area, since larger wires reduce their chances of malfunctioning (open circuit) due to greater tolerance to submicrometric defects.

We chose to sandwich the nanophotonic level beneath the electrical level to maximize density integration for both of their components; the nanophotonic circuits (excluding gratings) can be completely covered by the electrical ones. Furthermore, the deposition of high optical quality nanophotonic layers requires high annealing temperatures (800°C-1100°C), which are incompatible with metal lines and result in metal migration.

Hybrid fabrication of nanocircuits in microscale devices

Device fabrication

Overview

In order to optimize device reproducibility and achieve high throughput and scalability, we combine micro and nanofabrication techniques within the neural probe design. As a result, fabricating the nanophotonic and electrical circuits on wafers and integrating them on the tips of the neural probes allowed us to obtain around 200 devices per wafer. The device fabrication process, outlined in Fig. 25.1, begins from a commercial 4 inch silicon wafer with SiO_2 and Si_3N_4 optical quality layers [94] (i). We pattern the nanophotonic circuits with electron beam lithography and dry etching, followed by cladding with 2.7 µm of SiO_2 (ii). Subsequently, we spin and bake a 350 nm thick flowable oxide [108] to planarize the substrate. We then align and pattern the electronic circuits (iii) with electron beam lithography, titanium/gold evaporation, and liftoff. We proceed with the wires passivation by depositing 60 nm of SiO_2 using the atomic layer deposition tool. We then remove the passivation layer from the electrodes by means of another electron beam lithography step and dry etching (iii), thus leaving only SiO_2 on the wires. Next, we pattern the device shapes and grooves for the alignment of the optical fiber from the wafer frontside (iv) by using optical lithography and dry etching, and finally, release the devices from the wafer by using backside wet etching in potassium hydroxide solution (v). We describe several of these fabrication procedures in [107].

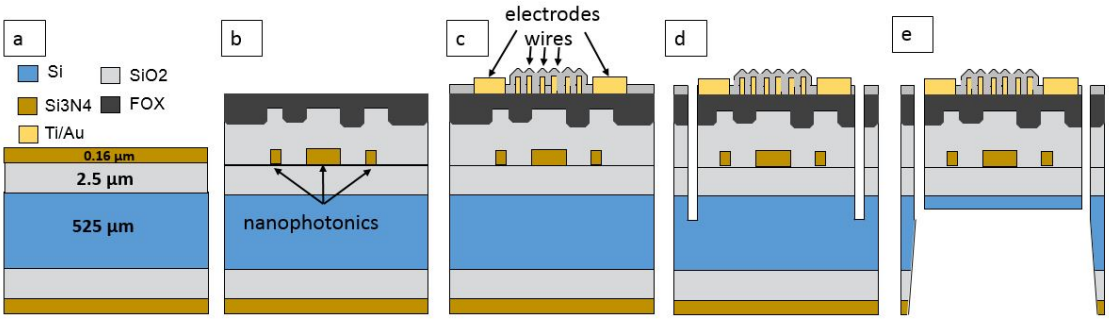

Figure 25.1: sketch of the neural probes' fabrication process, showing (i): the substrate wafer with SiO_2 and Si_3N_4 optical layers, (ii): patterning of nanophotonic circuits, optical insulation and planarization, (iii): integration of electronic circuits above nanophotonic ones, (iv): patterning of device shape, and (v): release of the device by backside etching.

Nanophotonic circuit patterning

Introduction

We describe the fabrication steps, such as patterning, optically insulating, and planarizing the nanophotonic circuits on a silicon wafer.

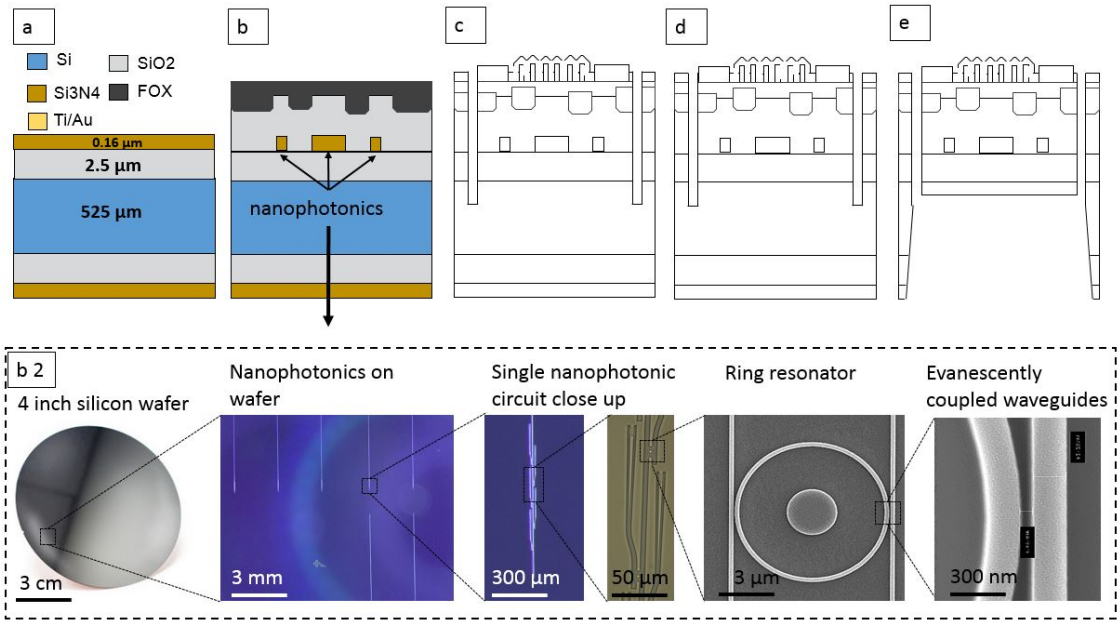

Figure 26.1: Nanophotonic circuits are fabricated at the wafer scale. Here we show several magnifications of the nanophotonic components.

Circuit and pattern design at the wafer level

All nanophotonic and electrical circuits, trenches that define the probes' shapes, and areas where silicon was removed from the wafer's backside and the printed circuit board are designed using a commercial software (L-Edit). Nanophotonic circuits are designed based on the simulations and account for reduced linewidth during fabrication; the same applies for the electrical circuits. Although around 300 probes could be placed in the wafer area, we design and fabricate around 200 probes per wafer for reduced electron beam lithography processing times.

Starting wafer

We use Lionix TripleX wafers, which are silicon wafers (525 ± 25) µm with 2.5 µm low pressure chemical vapor deposition (LPCVD) deposited SiO_2 and 160 nm Si_3N_4 layers that have low optical absorption in the visible to infrared spectrum [94]. These layers are the materials that compose the nanophotonic circuits and are deposited and patterned before the electrical ones. Such configuration allows for a higher sensor and stimulation site density on the tip, as well as an easier fabrication process (as we explained in Section 23, page 69) since the nanophotonic layers require high temperature depositions (>800°C), which are incompatible with the electrical circuit materials (Ti and Au).

Alignment marks patterning

We pattern titanium and gold (Ti/Au) alignment marks onto the Lionix wafer for alignment in subsequent electron beam exposures (for the nanophotonic circuit, electrical circuit, and electrode passivation opening) and in optical lithography exposures (for the wafer frontside and backside patterning). Their patterning is

achieved with electron beam lithography (using PMMA C4 resist spun at 2000 rpm and aquasave at 2000 rpm), 20 s oxygen descum in a reactive ion etching tool (RIE), followed by electron beam evaporation of titanium and gold (10 nm and 100 nm respectively), and solvent liftoff (1 hour in Remover PG at 80°C). We use electron beam lithography instead of optical lithography because the latter technique yields marks with rounded corners and consequently misalignment (by tens of µm) due to erroneous readings by the electron beam lithography software during the following exposures.

Nanophotonic circuit patterning

The nanophotonic circuits are aligned to the marks and patterned with electron beam lithography (using ZEP 520A resist diluted at 50% and aquasave) and reactive ion etching (RIE, using CHF_3/O_2 chemistry with 48:2 gas ratio and forward power RF of 40 W). In the following we detail some of these processes.

Electron beam lithography mask patterning and development

We pattern the resist mask with electron beam lithography due to the small feature size of the nanophotonic elements (such as 80 nm ring-waveguide gap and 250 nm waveguide widths, as explained in the previous section 21, page 48). For this process we use 50% diluted ZEP502A (a positive, high contrast and low dose, electron beam resist) spun at 1000 rpm and baked for 5 min at 180°C (for 230 nm thickness) and aquasave spun at 2000 rpm and baked at 100°C for 1 min, which prevents charge buildup during the resist exposure. We expose the resist in 2.5 µm wide areas around the designed nanophotonic elements with the goal of removing them. The trench width is determined by considering tradeoffs regarding electron

beam exposure time and good optical insulation between the nanophotonic elements and the bulk Si_3N_4 layer. For the exposure process, we ran several dose tests to determine the desired exposure dose: resist underexposure yields incomplete trench removal, while resist overexposure yields both feature roughness and decreased linewidth that result in poor circuit optical performance. We start at 200 µC/cm^2 with increments of 1.05, develop the sample in amyl acetate (1 m, no ultrasonication), and image with the scanning electron microscope (SEM) (Fig. 26.2) following 5 nm Ti/Pd sputtering. We obtain the correct dose at 225 µC/cm^2. Notably, we do not use ultrasonication during the development step since the thinner resist results in complete mask consumption during the following etching process.

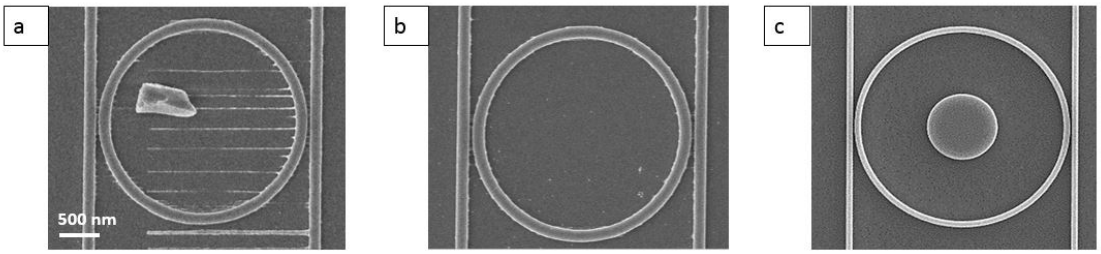

Figure 26.2: Electron beam resist dose exposure tests for nanophotonic circuits are shown: (a) underdosed waveguide curve and (b) grating are corrected for dosage in (c,d)

Pattern transfer with dry etching

Once we defined the nanophotonic elements' mask in form of resist trenches around its elements, we transfer the pattern with a RIE etching step. After a 15 s long O_2 descum (100 sccm and 40 W forward power RF), we use a CHF_3/O_2 chemistry [109], [110] with 48:2 sccm flow, 55 mTorr of pressure, 20°C table temperature, and 40 W RF for the first 7 m 30 s followed by 100 W RF for 1 m 30 s. We fine-tune the etching step based on the nanophotonic circuit optical performance, which is dependent on nanometric scale roughness (that cannot be easily observed

in the SEM) and is described in details in 33, page 107.

Nanophotonic circuit optical insulation with an oxide capping layer

Once the nanophotonic circuit is patterned, we deposit a thick oxide layer to optically insulate it from the electrical circuit above. This SiO_2 layer is deposited with a plasma enhanced chemical vapor deposition (PECVD) [111], which allows deposition of thick films at low deposition temperatures (< 350 °C) and therefore reduces thermal induced stress on the other layers. We deposit a 2.7 µm thick film at 150°C with low SiH_4 to N_2O ratio to decrease the film absorption of the nanophotonic circuit's confined light. As for the previous etching process, the layer's impact on the optical performance of the circuit can be measured with an optical setup (since there was no availability for the use of an FTIR spectrometer [112]); we describe the rationale for this process in the 33, page 107. This layer deposition results in both a long scale (µm) roughness (on the order of 160 nm) stemming from the presence of the underneath nanophotonic circuit as well as a short scale one (few tens of nm) that is due to the high material porosity resulting from the low deposition temperature (Fig. 26.3).

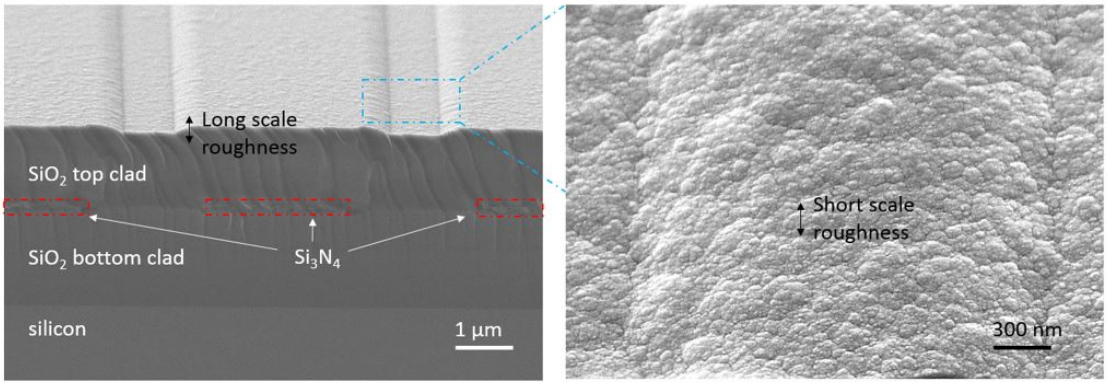

Figure 26.3: SEM of a cross section of nanophotonic circuits after top cladding deposition (SiO_2 shows both the long scale and short scale roughness stemming from (respectively) the waveguide shape and porosity of the SiO_2.

Top cladding planarization

To prevent the PECVD SiO_2 long scale roughness that impacts the functionality of the electrical circuit by creating openings in the wires, we planarize (flatten) the wafer by spinning and baking a flowable oxide.

These materials are used as planarization layers [113], [114] thanks to their superior gap filling properties [108] as an alternative to chemical mechanical polishing. These materials are initially at liquid state and diluted in solvent; once spun and baked, these materials turn into a porous oxide (with around 20% porosity) at low temperatures (<200°C) and become less porous with greater similarity to stoichiometric oxides (at 650°C) as the baking temperature increases [115]. We spin FOx 15 (from Dow Corning) at 3500 rpm for 350 nm thickness, which is thick enough to compensate for long scale roughness (resulting in a smooth and gradual slope of 40 nm over 1µm) and thin enough to prevent this layer from cracking during the baking step due to induced stress (Fig. 26.4). The FOx refractive index (measured with an ellipsometer at the wavelength of 450 nm) is 1.42 (close to measurement of 1.47 for thermal oxide). We measure the impact of this layer on the nanophotonic

circuit's optical properties in page 107.

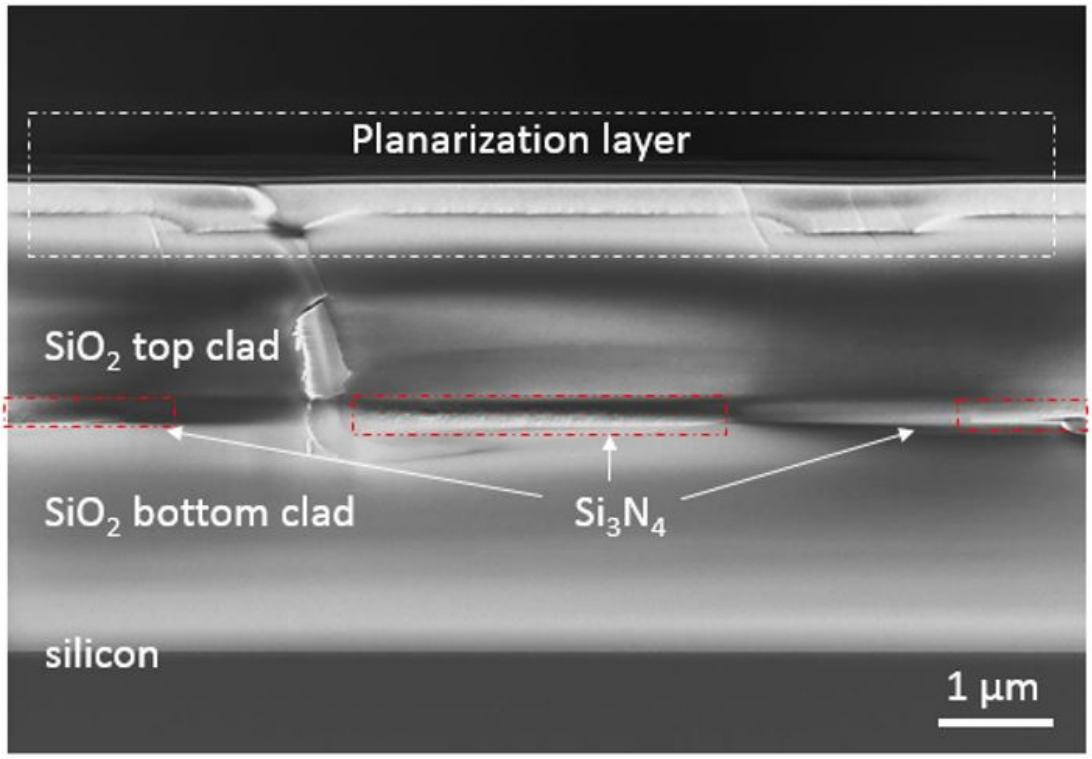

Figure 26.4: SEM cross section of the same circuits is shown in 26.3 after planarization with a flowable oxide.

Electrical circuit patterning

Introduction

We describe the fabrication steps for the alignment and integration of the electrical circuits above the nanophotonic ones as well as the electrical insulation of non-recording areas (wires for carrying the electrical signal).

Electrical circuits are patterned with electron beam lithography, metal evaporation, and liftoff. Electron beam lithography is key to achieving wires with small widths and spacing (120 and 450 nm) with a high density of electrodes in the tip area. 100% ZEP 502A is spun at 3000 rpm and baked at 180°C for 5 min, followed

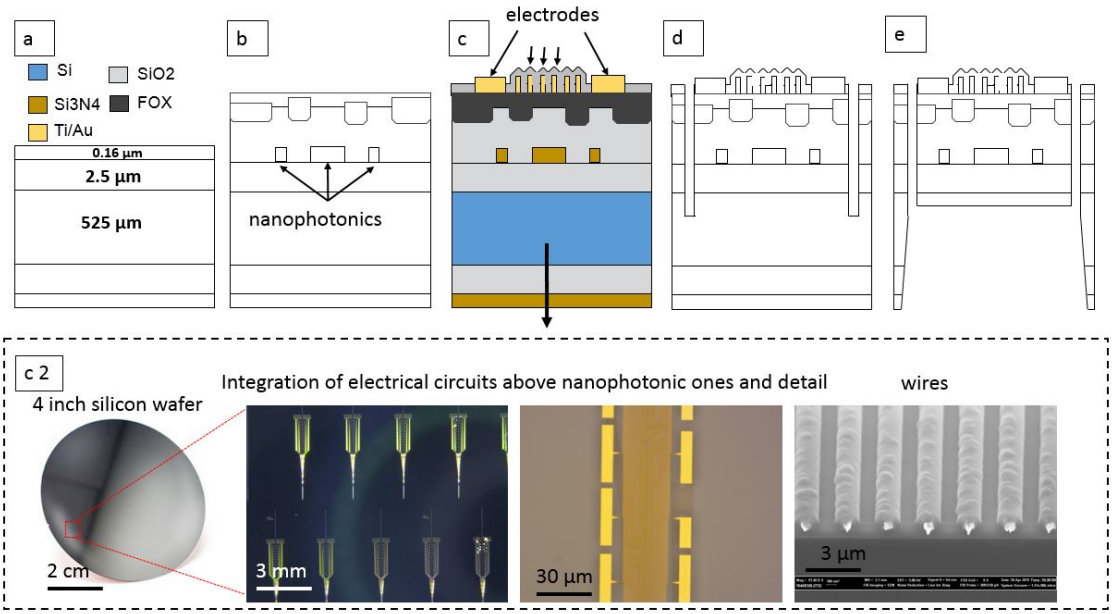

Figure 27.1: Schematic of the fabrication process described in this section, where we (a) pattern and passivate the arrays of electrodes and wires and (b) images of various components in the wafer are shown.

with aquasave spun at 2000 rpm and baked at 100°C for 1 min. The resist is exposed with a dose of 282 µC/cm^2, which is optimized by SEM visual inspection to obtain the desired feature size and minimize defects (where underexposure leads to poor removal of resist in between wires lines and overexposure leads to resist collapse and consequently line short circuit). We develop the exposed wafer for 1 minute in amyl acetate without ultrasonication (which would increase the line collapse). We then perform a descum step in the RIE (20 s, 100 sccm O_2 at 40 RF), which is essential to removing scum and improving the wires' adhesion onto the substrate, followed by a titanium adhesion layer (10 nm) and gold electrical conduction layer (100 nm) electron beam evaporation; (Fig. 27.1 shows an SEM cross section of this fabrication step).

We then remove the gold from the non-patterned areas by means of a liftoff process, which dissolves the ZEP (and therefore removes the metal above it) in a

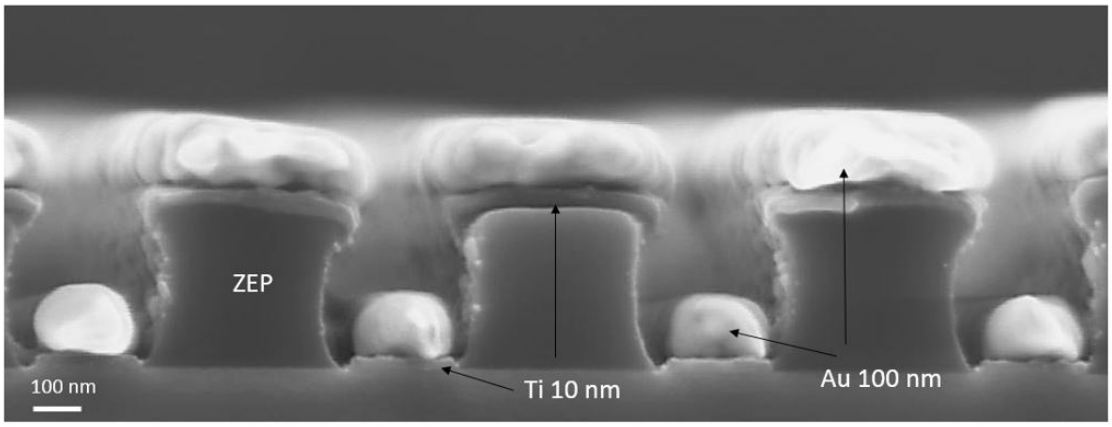

Figure 27.2: The SEM cross section of the wires on the wafer is imaged before liftoff and after electron beam exposure and Ti/Au evaporation.

hot solvent (Remover PG at 80°C). The process is optimized based on electrical resistance measurements to estimate the number of working lines (which do not have open or short circuits). Fig. 27.3 shows the results (top view and cross section) of the electrical circuit integration above both non-planarized and planarized nanophotonic circuits, demonstrating lower defectivity of the latter. We describe the optimization of the electrical circuit's yield in page 130

Wire passivation

We passivate the wires in order to electrically insulate them so that they do not contribute to the neuron's signal readout; this is obtained by first depositing an SiO_2 passivation layer on all of the wafer and then removing it from the electrodes.

Deposition

A thin (60 nm) SiO_2 passivation layer is deposited by means of atomic layer deposition at a low temperature (40°C) to prevent further induced stress on the other layers.

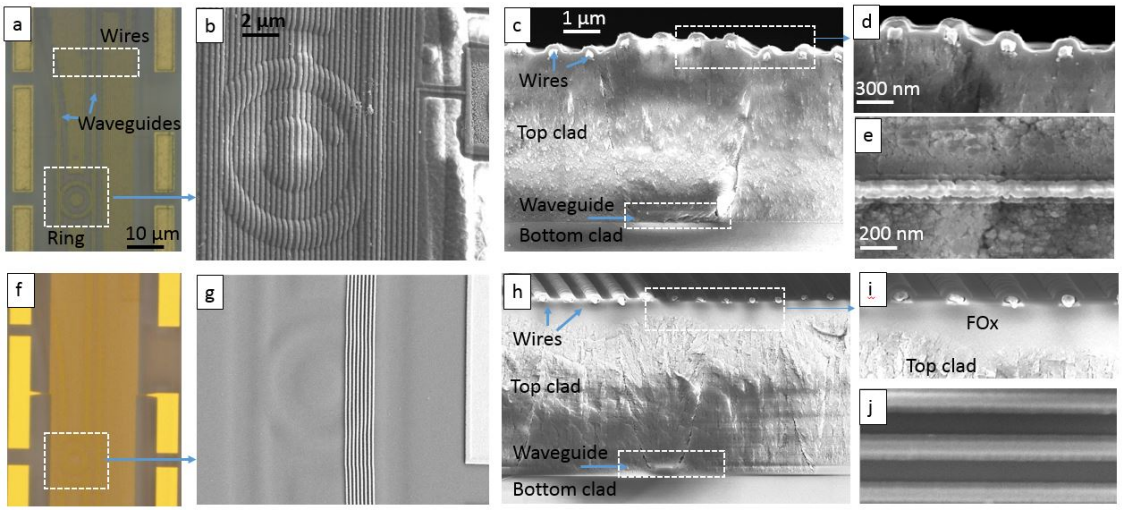

Figure 27.3: Comparison images between the arrays of sensors and wires without (top) and with (bottom) planarization at the (a,b) electrode array scale, (c,d) wire scale, and (d,e) relative cross sections. (f-i): Magnifications on a few wires, cross section (f,h) and top view (g,i) are shown.

Mask patterning

An electron beam exposure, aligned to the previous one, defines the mask for the underneath passivation layer over the wires. ZEP 502 A is spun with the same parameters as those for the electrical circuits' exposure; it is then exposed with the same dose as for the electrodes' one and developed for 1 minute in amyl acetate with ultrasonication. The mask opening for the etching of the SiO_2 above the electrodes consists of openings which are 500 nm smaller than the electrode's dimensions to compensate for exposure misalignment, which would lead to damaging the wires, as we show in Fig. 27.4.

Passivation layer etching

Once the resist mask has been defined, the SiO_2 is etched in the RIE tool with a CF_4/O_2. The SiO_2 is slightly etched, resulting in the etch of the top 20 nm of Au from the electrodes; this compensates for shifts in the etching rate (since even a few

nm of unremoved SiO_2 above the electrode may prevent it from reading electrical signals). SEM characterizations of these steps are shown in Fig. 27.5.

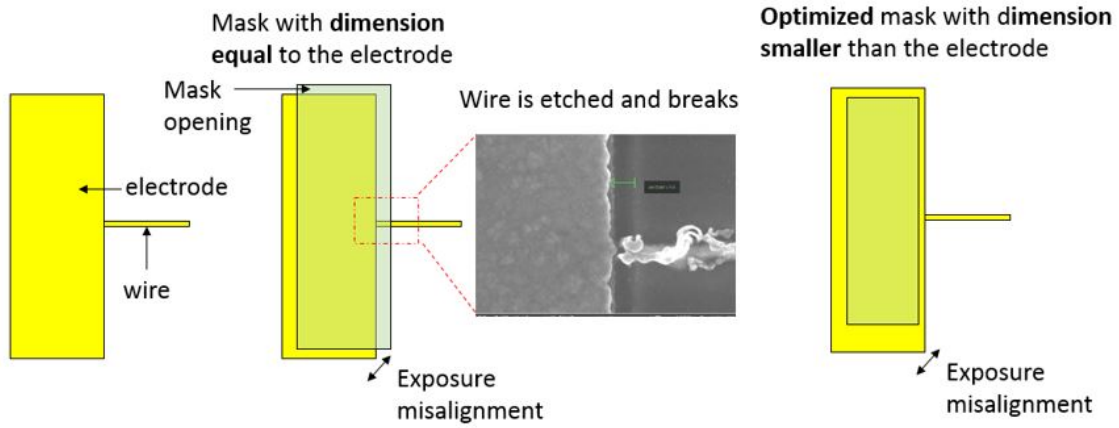

Figure 27.4: Mask opening design before and after optimization that took into account the electron beam exposure misalignment.

Backside optical lithography

After the electrode passivation layer opening, the silicon nitride on the wafer backside is patterned as preparation for the final wet etching step for the SiO_2 and bulk silicon removal (with potassium hydroxide) underneath the tip; this is described in the next section. The nitride is a masking layer for this process (since its etching rate in potassium hydroxide is zero [116]) and is designed to mask the probe interfacing area - such that it remains as thick as the wafer for probe handling - and accounts for convex corner compensations [117] as well as mesh-like areas around the probes for wafer stability and handling. After an initial resist spin (2000 rpm, 1000 rpm/s, 45 s and bake at 100°C for 2 m) on the wafer frontside to protect the electrical circuits from scratches, the nitride mask patterning is obtained by optical lithography onto the wafer backside. After spinning the adhesion layer (HMDS at 2000 rpm, 1000 rpm/s, 45 s with 5 min bake at 100°C onto silicon pieces

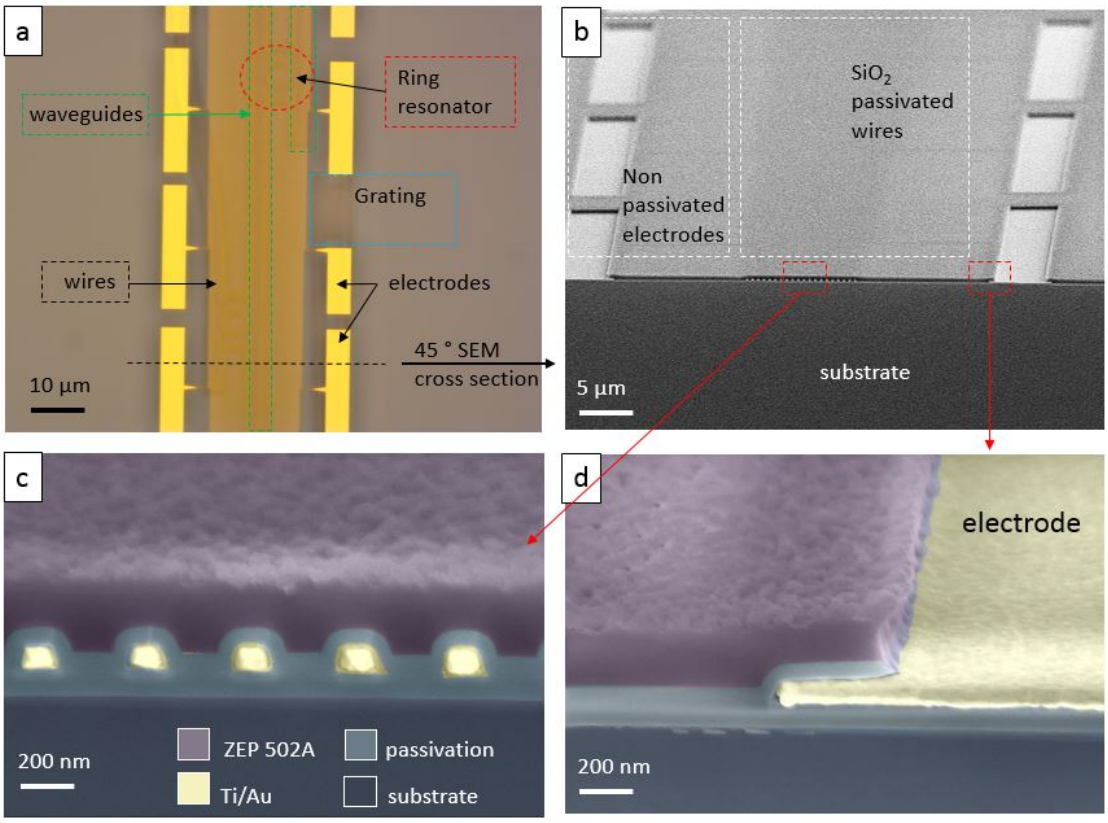

Figure 27.5: Arrays of sensors and wires after fabrication onto the wafer, (a) top view, (b) cross section, and magnification onto the (c) wires and (d) electrode are shown.

to raise the wafer above the hotplate), resist MAP1215 is spun (same parameters as those for HMDS), followed by alignment to the marks for UV exposure (14 mW/cm^2, 5 s) and development for 60 s in ma-D 331 solution. The pattern is then transferred to the wafer by a dry etch with the RIE tool (CHF_3 48 sccm, O_2 2 sccm, 50 W RF, 55 mTorr, 20°C) and the resist is removed by a 30 min soak in acetone.

Integration of nanocircuits on microprobe

Introduction

Trenches are etched around the nanophotonic and electrical circuits to define the probes' shape as well as the grooves for the optical fibers. To accomplish this, we spin an optical lithography resist to mask the probe regions and use dry etching processes to etch both the layers above the silicon (5.5 µm of SiO_2 and 160 nm of Si3N) and 15 µm of silicon.

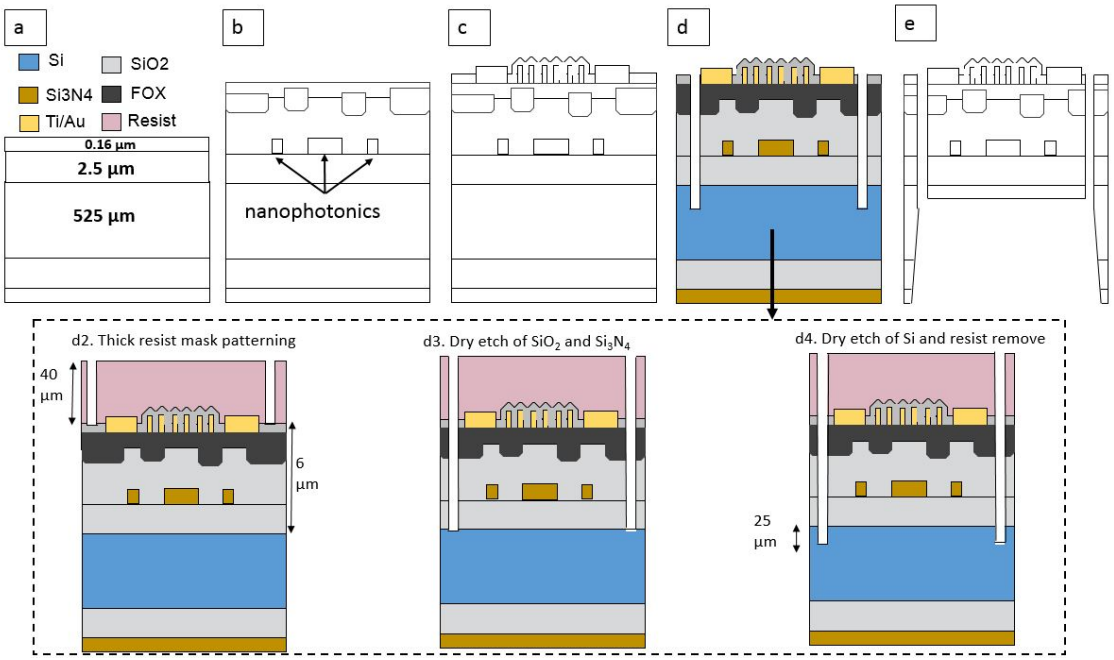

Figure 28.1: The fabrication process described into this section is outlined: (a) patterning of the device shape onto the wafer and (b) detailed processes.

Mask patterning

We use a thick photoresist mask (>40 µm of resist AZ 40 XT-11D) on the wafer frontside - where the circuits have been integrated - to protect the probes during the subsequent etching steps. We choose a resist instead of a hard mask (such as chromium) to avoid issues with redeposition in the trenches during etching. The exposed areas of resist consist of 100 µm wide trenches to minimize the amount of silicon etched in the chamber and associated loading effects [118] (smaller widths may lead to gas limited transport) and 140 µm wide grooves for the optical fiber.

The resist is spun, on top of an adhesion promoting layer (HDMS), at 1750 rpm and 5000 rpm/s for 20 s for a thickness of (40 ± 2) µm. We perform a slow ramp softbake step on a hotplate by placing the wafer on glass slides (1 min every 5°C from 20°C to 60°C, 20 m 60°C, 20 m 80°C, 10 m 100°C, 10 m 125°C) to avoid the quick formation of nitrogen bubbles. After the baking, the wafer sits on the hotplate until it reaches room temperature to avoid resist cracking. The resist is removed from the wafer's edges (10 mm), since the thickness (tens of µms) prevents the photolithography mask from contacting the wafer during the following step. This is achieved by exposing the edges with UV light (at 14.5 mW/cm^2 for 12 s) followed by a post-exposure bake (with slow heat and cooldown ramps) and a development in MF26A (2% tetramethyl ammonium hydroxide) for 8 min.

Once the edges have been removed, the mask patterned with the probe shapes is aligned to the wafer and the UV light is activated with an intensity of 14.5 mW/cm^{2}for 12 s. The wafer is then developed in MF26A for 4 m 45 s. The resist optimal exposure dose is found by varying it between 50% - 200% of the datasheet suggested value and is optimized for a fully developed trench to maximize the tip linewidth and compensate for subsequent etching variations that result in silicon undercut. Given the final resist thickness (around 42 µm) and the initial designed tip width (50 µm), the patterned resist width at the tip was determined as 48 µm.

SiO_2-Si_3N_4-SiO_2 etching

After the mask definition, the pattern is transferred by etching, into the same tool (Oxford Plasma lab 100 Viper) for a one-step process, resulting in the etching of the following layers: 60 nm SiO_2, 350 nm FOx, 2.7 µm SiO_2, 160 nm Si_3N_4, 2.5 µm SiO_2. We perform the etching at room temperature (due to cooling provided by the wafer chuck) to avoid the resist burning (at high temperatures) or cracking

(at temperature <10°C,). Before starting the etching, a long descum step (10 m of O_2, resulting in a loss of 4 µm of resist) removes all the resist residues in the trenches , which (from optical microscope characterization) are more prominent in the proximity of the probes' tips and grooves (whereas longer development in solution yields linewidth enlargement). We then perform the etching using the following parameters: gas chemistry and flowrates of CF_4, Ar and O_2 (35, 15, 10 sccm respectively), RF of 150 W, very high-frequency power of 400 W (similar to the inductively coupled power), 10 mTorr, and a table temperature of 20°C. The 4 inch wafer is loaded on an 8 inch carrier (the tool has an 8 inch automatic transfer system from the loadlock to the main chamber) and temporarily bonded by fomblin (a thermally conductive oil).

As mentioned in the previous paragraphs, a resist mask was chosen instead of a hard one (such as chromium mask) since the latter resulted in its resputtering inside the trenches during etching and consequently the etching stop before reaching the silicon. The etching stop was characterized at the SEM (Figure), while the presence of resputtered chromium at the bottom of the trench was confirmed by XPS measurements (Figure) for a recipe using SF_6/Ar chemistry at cryogenic temperatures (-100°C). The same measurement also showed the presence of Aluminum in the trench, which assumedly resulted from the bonding (and etching) of the SF_6/O_2 plasma volatile byproducts (SiFOx) formed at the wafer interface with the Al chamber walls. This was confirmed by using the resist mask ; in fact, after changing the mask to resist, the formation of pillars in the trench resulting in the etching stop could still be observed (Fig. 25.1 a) even at various temperatures, RF powers and pressures. Thus, gas chemistries with a different carbon (C) to fluorine (F) ratio, such as C_4F_8/O_2 and CF_4/O_2, were tested and the best result

(determined by minimal pillar formation that result in the etching of layers up to silicon, Fig. 25.1 b) was found with CF_4/O_2, as the XPS measurement (Fig. 25.1 c) demonstrates little Al presence in the trench.

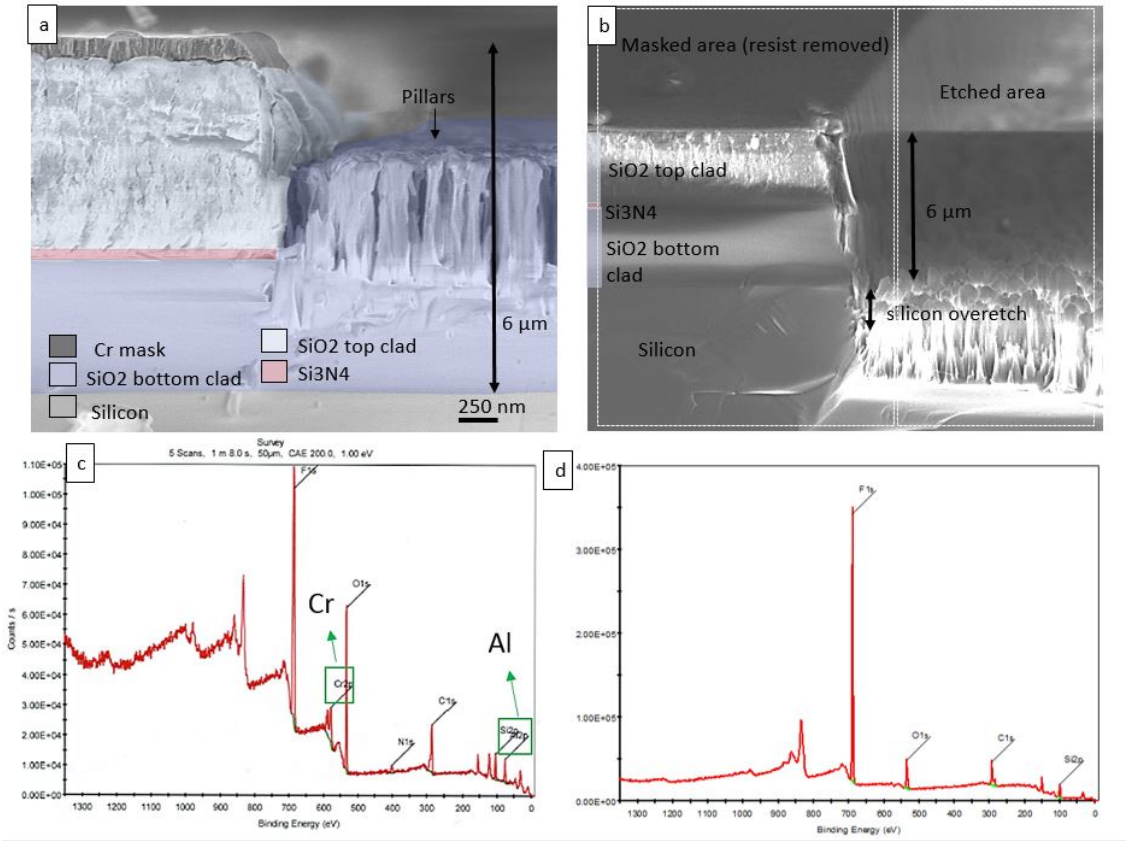

Figure 28.2: Etching of the SiO_2 to define the device shape. (a) etching with a chrome mask and using SF_6/O_2 chemistry that formed pillars which prevented the etching for all of the SiO_2 due to the resputtering of chrome inside the trenches and the deposition of aluminum from the tool chamber walls, as shown in the XPS measurement (b). (c): SiO_2 etching with CF_4/O_2 chemistry and resist mask (image taken after the resist removal) and (d) corresponding XPS spectrum showing minimum presence of aluminum are shown.

Silicon etching

After the frontside SiO_2 etching, 15 µm of silicon are etched using the same tool to define the tip and groove thickness. This process requires precise sidewall etching control since it defines the tip structure as support for the nanophotonic and electrical circuits: we thus aim at straight sidewalls and avoid an excessive (>10 µm) undercut. The recipe is initially optimized based on etching tests conducted using the Oxford ICP Fluorine tool for 1 cm^2 wafer pieces mounted on 4 inch silicon wafers with a 100 nm evaporated chromium layer. Such layer avoids the severe underestimation of the sidewall undercut arising from loading effects involving differences between the large silicon area exposed during the tests (and in the absence of the chromium layer) and the 4 inch wafer (Fig. 28.3).

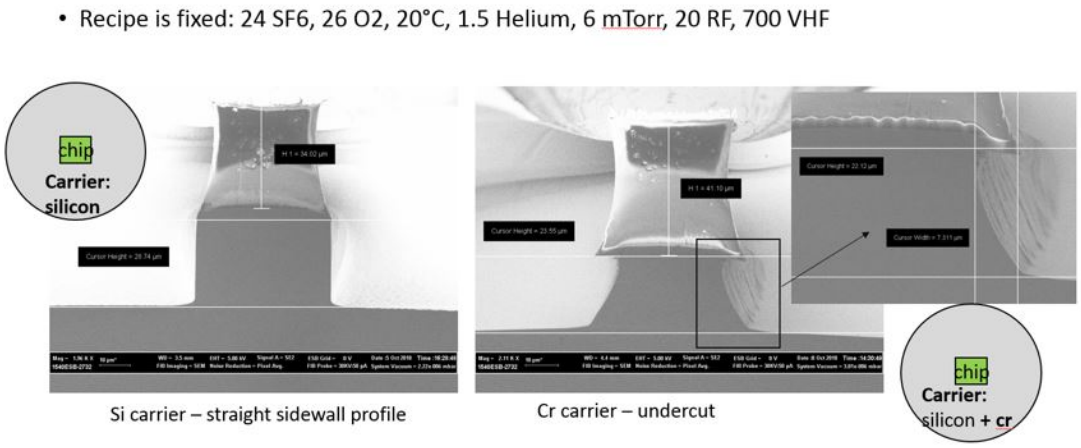

Figure 28.3: Loading effects during the silicon etching result in straight sidewalls when using a silicon carrier wafer during tests on the chip (a) and in a high undercut when using a chromium-covered carrier wafer (b).

Continuous RF etching processes (meaning there is no alternation of gases but their continuous flow) were performed using two different gas chemistries and tuning their ratios: percentage of SF_6 in O_2 [119], [120] and of SF_6 in C_4F_8 [121]. The results are displayed in Fig. 28.4 a and provide a study of their undercut ratio, which

we calculate by dividing the µm of sidewall undercut by the µm of etching depth (perfect sidewalls have an undercut ratio of 0). The undercut ratio should be well below 0.2 (resulting in 8 µm total undercut for a 20 µm deep etch) to accommodate for experimental variations - such as temperature shifts - during the wafer etching process. These data show that the C_4F_8/SF_6 gas chemistry results in appreciably lower undercut rates in comparison with the SF_6/O_2 ones. Importantly, comparing between the test and full wafer (for a fixed gas ratio) a lower variation is observed for the C_4F_8/SF_6 chemistry, resulting in a smaller process sensitivity to either gas ratio changes (the C_4F_8/SF_6 curve has a smaller slope) or to temperature changes (not measured for C_4F_8/SF_6). Fig. 28.4 a shows an SEM cross section of a probe tip resulting from the silicon etching process, having straight sidewalls, and a small undercut value (1.5 µm) and rate (0.06).

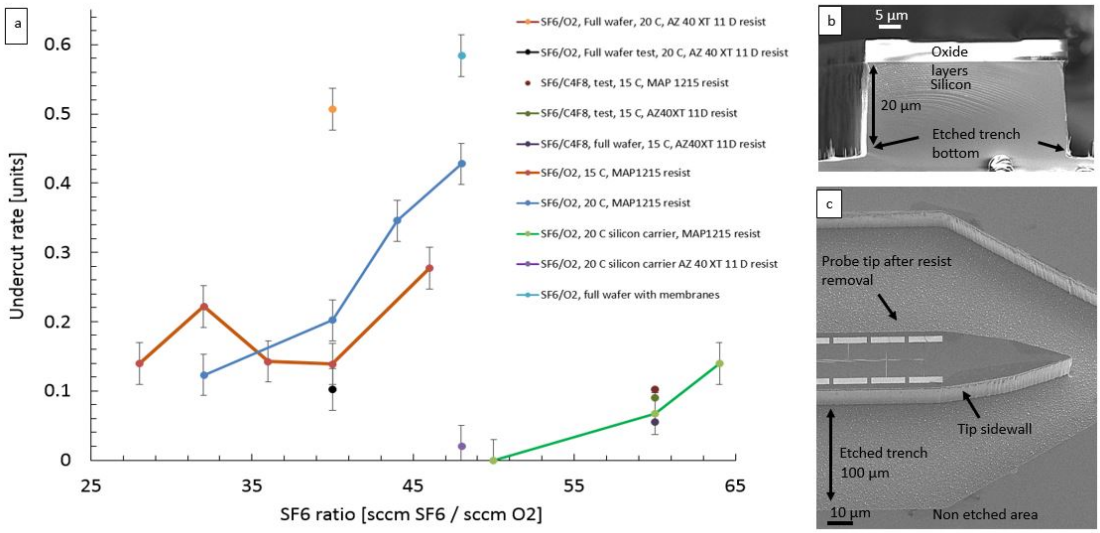

Figure 28.4: Silicon etching is used to define the probes' shapes. (a): The undercut ratio (µm of undercut per µm of trench etching depth) is a function of different gas chemistries and ratios and masking materials. (b): Tip SEM cross section after etching with low undercut ratio (<0.1) and (c) tilted top view of the probe tip after etching with straight sidewalls and resist removal are depicted.

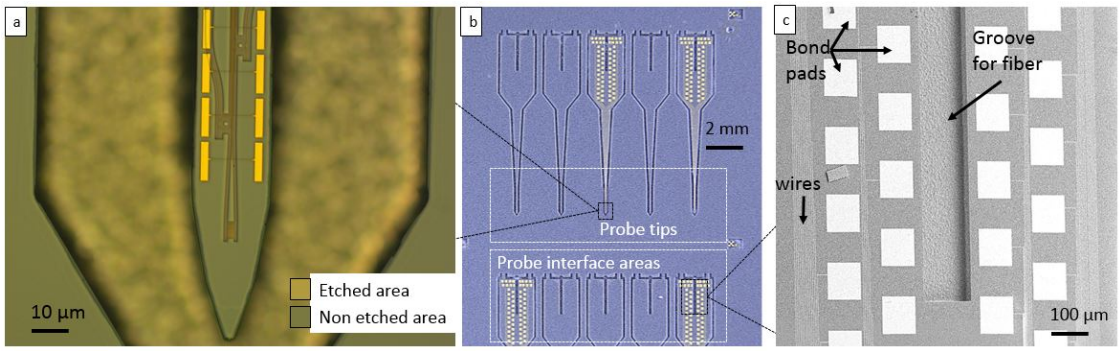

Figure 28.5: Probe shapes etched at the wafer scale and magnification on the tip part and the interfacing area are shown.

After the silicon etching process, the resist is heavily crosslinked and cannot be removed by standard solvents such as acetone, dichloromethane, n-methyl pyrrolidone; we found that AZ400T (2% TMAH + n-methyl pyrrolidone) lifts the resist after a relatively long soak (30 min) at 80°C, leaving most of the probes clean and without residues (95% for test wafer made of silicon with top 2.5 µm PECVD SiO_2, 80% for the probes' wafer).

Backside bulk teching: introduction

After the patterning of the nanophotonic and electrical circuits and having defined the probes' shapes, the silicon underneath the tip areas is removed to make them thin (20 µm), while leaving the silicon underneath the probes' interfacing areas. To achieve this, the silicon nitride on the wafer's backside is patterned with optical lithography (using resist MAP-1215) and RIE etching (same parameters as for the etching of the nanophotonic circuits). Most of the silicon (480 µm) is removed from the previously nitride-etched areas on the wafer backside using potassium hydroxide (KOH) after a protective polymer coating on the circuits (Protek B3), as we describe in [81]. Besides, during the KOH etching we protect the wafer circuits by placing it in a wafer chuck (from AMMT). After the KOH etch, we

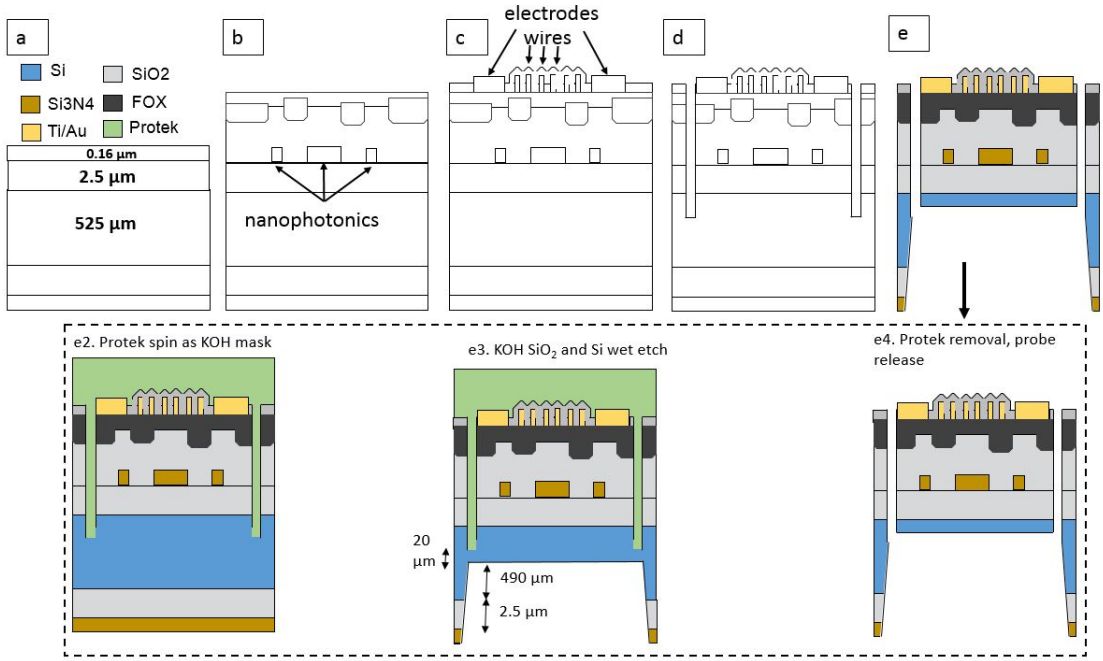

Figure 28.6: Schematic illustration of the fabrication process to remove the bulk silicon (a) and detail on the process steps (b).

remove the last few remaining µm of silicon with a dry etching step in the VIPER tool (using SF_6 and O_2 chemistry). As a result, free standing optoelectrical neural probes are obtained.

Protek

A protective polymer (Protek B3, from Brewer Sciences [122]) is spun and baked onto the wafer frontside to protect the electrical and nanophotonic circuits during the following backside wet etching step. After the Protek Primer adhesion layer is spun (1500 rpm, 1000 rpm/s, 60s and 1 min baking on hotplate at 205°C), the protek primer is spun twice at 1000 rpm, 5000 rpm/s, 60 s and baked 2 min at 110 °C on a hotplate; a final 1 min baking at 205°C is then performed. Fig. 28.7 displays an optical microscope image of a wafer cross section highlighting the Protek coverage of the wafer frontside trenches. Finally, as additional protection to the

circuits, the wafer is clamped inside a KOH chuck (from AMMT), which creates a dry enclosure for the frontside while leaving the backside exposed to the chemical.

KOH etch

Once the wafer frontside is protected, a wet chemical etch in postassium hydroxide (KOH) removes, from the nitride unmasked areas, the backside SiO_2 (2.5 µm) and most of the silicon (480 µm). A silicon layer is left unetched such that the KOH does not leak at the bottom of the trench, peeling off the Protek layer. The wafer holder is soaked vertically in a 2.5 L bath composed of 25% KOH (in the form of dissolvable pellets) in water, heated at 85°C, and stirred with a magnetic stir bar at 800 rpm. During the etching process, the etch rate and depth is monitored with a profilometer (Veeco Dektac) after soaking the wafer in water and a nitrogen dry. The etch rate of the SiO_2 is around 500 nm/hour while the Si one is 1.8 µm/min, depending on the exact bath temperature and KOH concentration. The profilometer measurements show that the stirring avoids temperature gradients across the bath that would result in measured etching depth variations across the wafer as high as 25 um (Table). We found that keeping the wafer in a horizontal position (with its surface facing the stirbar) yields less variation with respect to a vertical one (Table 28.1), though we use the latter because of the geometry of the wafer chuck. Furthermore, after having etched the 480 µm of silicon, we notice an increased etch depth (20 µm) near the edges (with an extent of 1 mm) of the large etched areas, which does not represent a significant issue since it is far from the probe trenches.

Protek remove and dry etching to release the devices After the etching is completed and the wafer is soaked in water and dried with nitrogen, the Protek layer

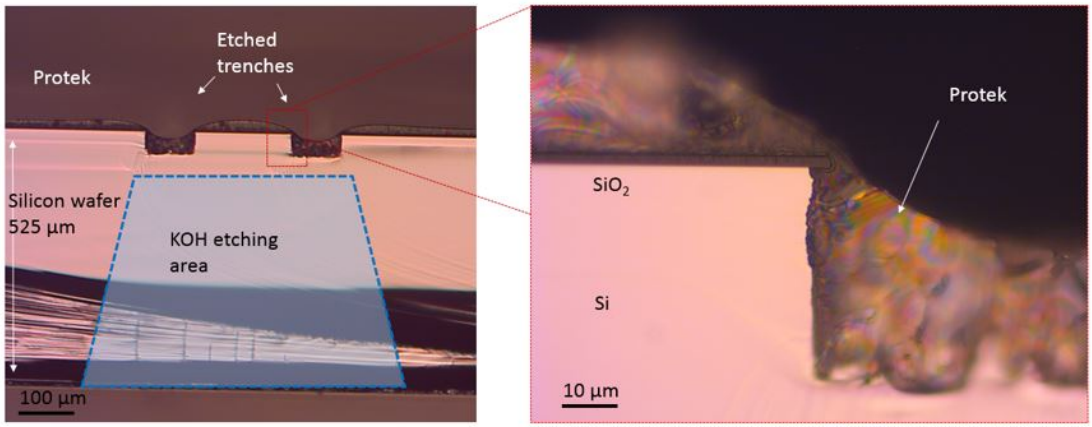

Figure 28.7: Optical microscope's cross section image (a) and magnification (b) of a probe's tip before bulk backside silicon etching and covered by Protek polymer.

Method	Stirring, [rpm]	T bath, [°C]	Max thickness variation, [µm]
Wafer on bottom beaker	0	80	25
Wafer horizontal on holder, 1 L solution	300	85	5
Wafer vertical on AMMT holder, 2.5 L solution	800	85	12

Table 28.1: Comparison between different KOH etch methods.

is removed by soaking the wafer into three different baths of Protek remover 100 (after 45 m, after 10 m, the last 5 m) and rising with isopropanol in between the transfers. The use of multiple solvent baths reduces the redeposition of protek particles onto the wafer.

The remaining 20 µm of silicon at the trench bottoms are dry etched in the VIPER tool at 20°C using 180 sccm SF_6, 20 sccm O_2, 20 W RF, and 10 mTorr pressure. After this process, the trenches are opened and the probes are attached to the wafer solely by 20 µm thick bridge holders (Fig. 28.8), which can be broken with the help of tweezers to separate the neural probes from the wafer.

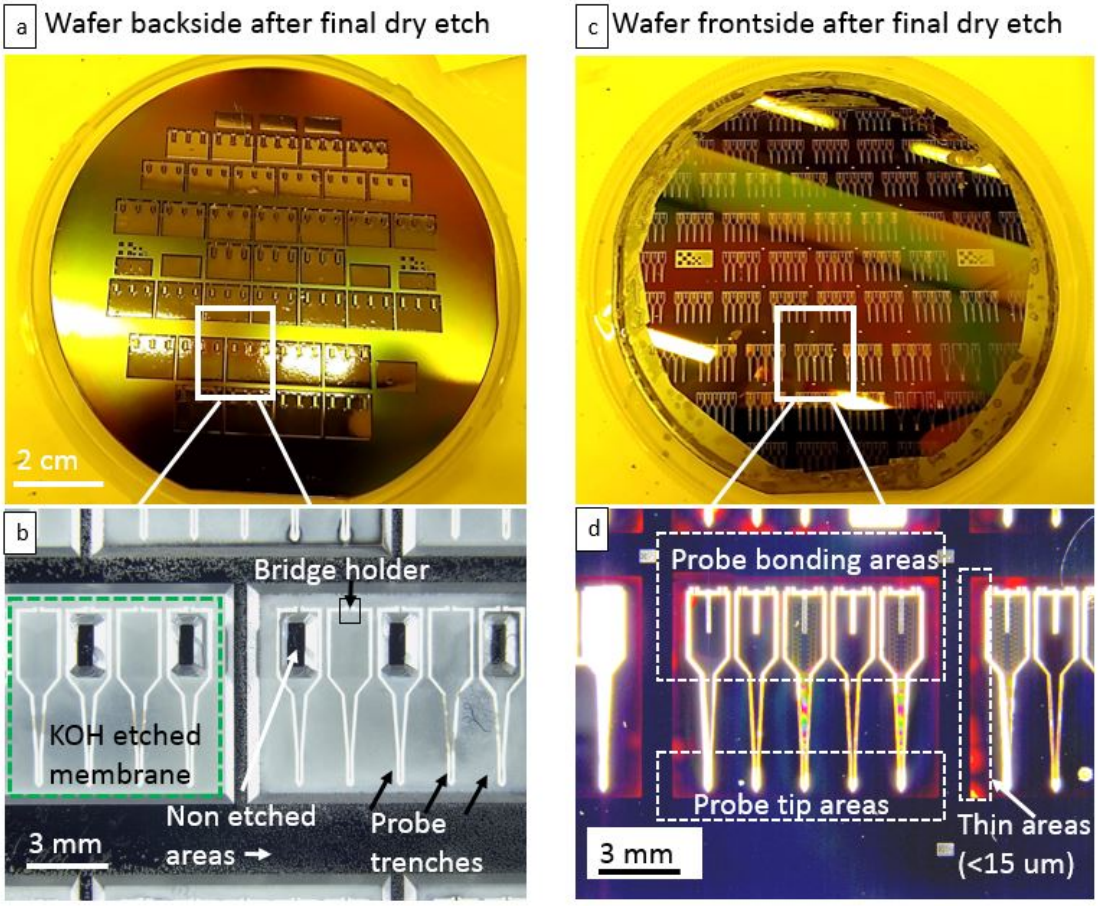

Figure 28.8: Wafer images after bulk silicon etching show both the wafer's backside and (a) magnification as well as the (b) wafer's frontside (c) and magnification (d).

Fabrication results: fabricated optoelectrical probes

The wafer batch fabrication yields around 200 optoelectrical probes, which we initially visually characterize by optical microscope and SEM and from which we estimate that more than 90% of them have no visible defects that would completely impair the probe's capabilities (i.e. broken tips). Resulting probes have a 900 µm long tip, 45 µm width, and 15-25 µm thickness; we show examples of false-color SEM images of a probe in Fig. 29.1 a, highlighting the integration of electrical and nanophotonic circuits, as well as the reduced dimensions and straight sidewalls.

Nanophotonic elements such as rings, grating and waveguides can be observed in detail (Fig. 29.1 b), as well as the wires and electrodes that are part of the electrical circuit. The circuits' stacking is shown in (Fig. 29.2 a,b), which shows an SEM cross section of the tip, with false colors highlighting the layer by layer integration of the nanophotonic and the electrical circuits, as well as the planarization layer above the nanophotonic circuit's cladding.

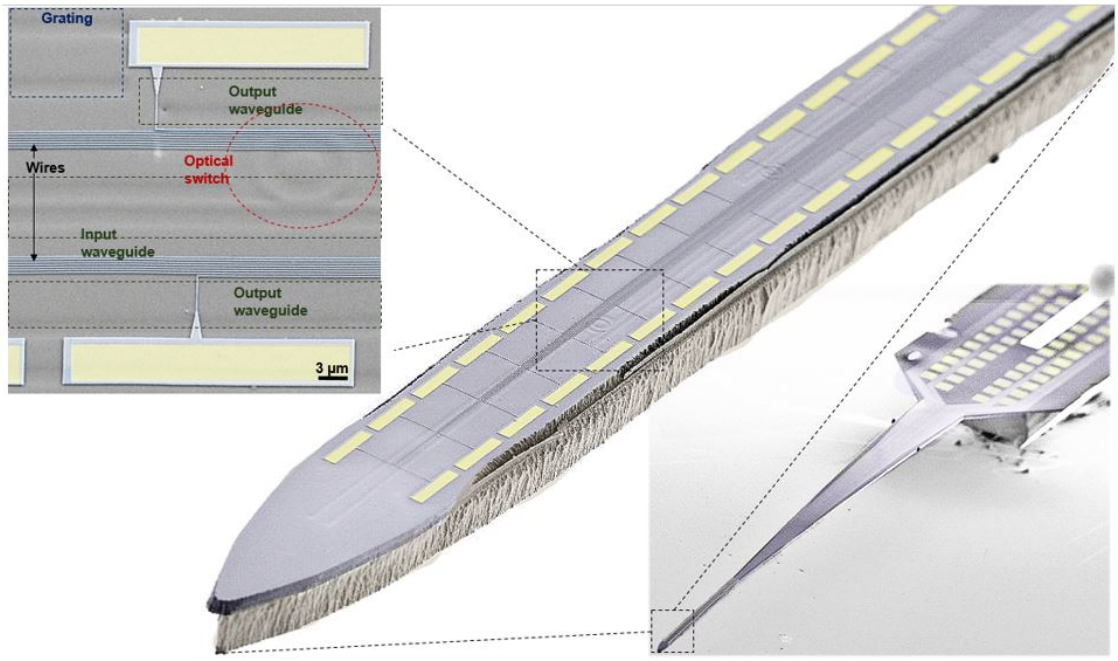

Figure 29.1: False color SEM image of a fabricated optoelectrode after release from the wafer.

Device packaging, connection: from macroscale to nanoscale

Overview

In order to be able to access the tip circuits and use their relative functions, we connect it to external electrical instrumentation (amplifiers, filters...) and to our external laser. We achieve the electrical connection by gluing and wire bonding our

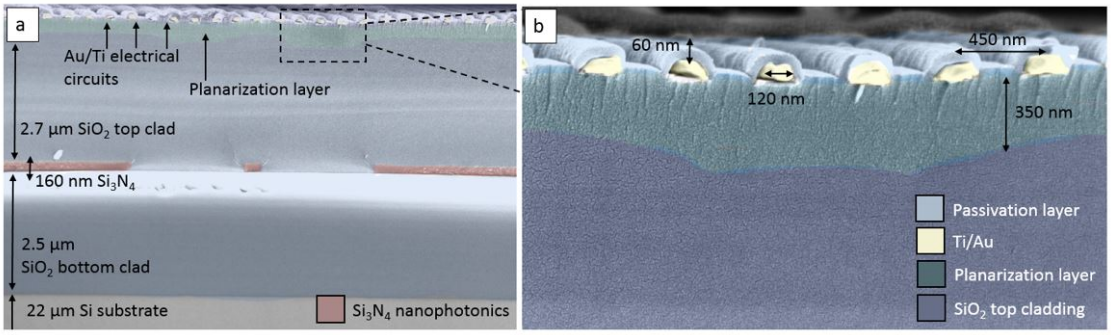

Figure 29.2: False color scanning electron microscope (SEM) images of a cross section of the upper layers of the tip show (a) the integrated Si_3N_4 nanophotonics and Ti/Au electrical circuits, separated by the 3 µm thick SiO_2 optically insulating layer, and (b) a close-up of the SiO_2 passivated wires, which we pattern above the SiO_2 top cladding, planarized by a flowable oxide layer.

probe on a custom-made printed circuit board (PCB), having on one side electrodes for wire bonding and on the other side electrical connectors. Moreover, we obtain the optical connection by coupling the laser's single-mode optical fiber to the edge of the bus waveguide. We align the two parts and glue them together such that they remain securely in place. We describe in detail the electrical and optical assemblies in section 30, page 69 and section 31, page 100 respectively.

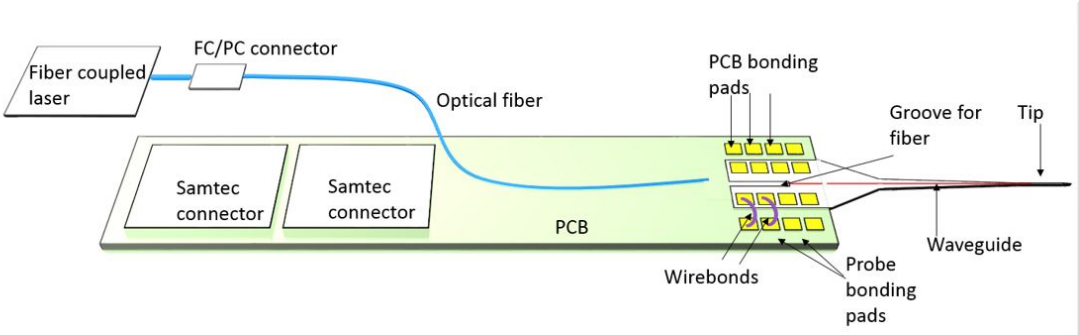

Figure 30.1: This schematic illustrates the connection of the optoelectrode to external electronics by wire bonding and laser by optical fiber alignment and gluing.

Device electrical connection

We design a printed circuit board as the interface between the neural probe and the experiment connector. The PCB design is obtained with L-Edit and comprises a set of 64 pads (75 µm x 75 µm) for wire bonding, a set of 80 pads on the opposite side of the PCB for connector surface mount soldering (2 Samtec MOLC with 40 pins), and 75 µm wide traces to connect the two (the lower level is connected to the upper one by electroplated VIAs). PCBs are commercially manufactured by SF Circuits. We designed connector maps to assign each electrode on the neural probe to its corresponding Samtec connector pin and readout channel. We then glue the probe on the PCB gluing area (UV curable glue OP-67-LS from Dymax) and wirebond it with an automatic machine with assisted ultrasonication and no stage heating.

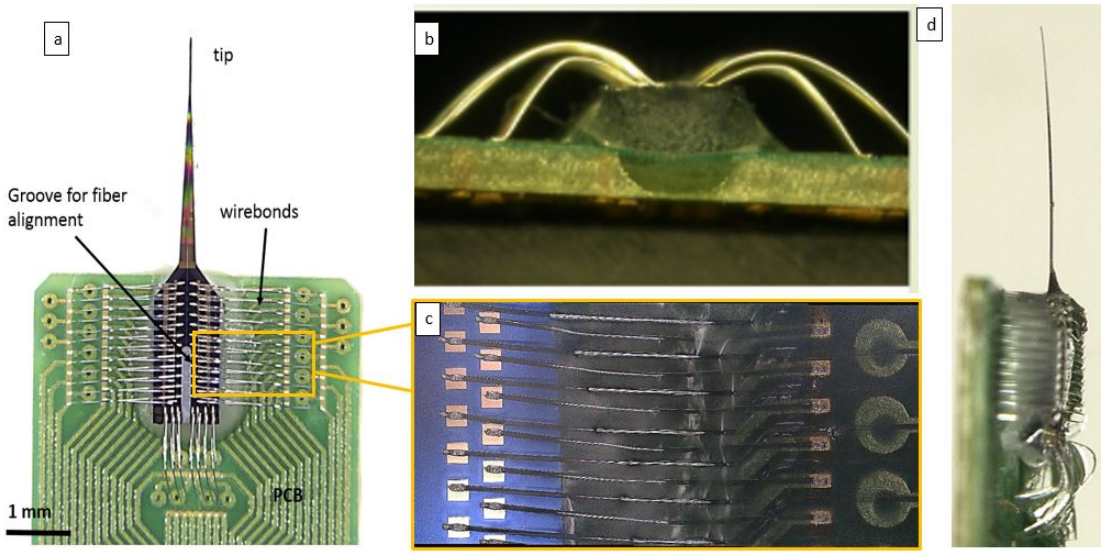

Figure 31.1: Connection of the optoelectrode to the printed circuit board by wire bonding is depicted in the (a) top view and (b) magnification, (c) front view showing the rows of wires, and (d) lateral view with a comparison to an optical fiber.

Device optical assembly: optical fiber preparation

We obtain the connection between our fiber coupled single-mode laser diode (model QFLD-450-10S, from QPhotonics) and the nanophotonic circuit by aligning and gluing an optical fiber to its input.

Fiber preparation Fiber connectorization. We use single mode optical fibers at the wavelength of 450 nm (model SM 400, from Thorlabs) with dimensions of 125 µm (cladding) and 3 µm (core). We cut them from the bundle and cleave the two ends to obtain a well-defined interface (to avoid any irregular light scattering). We splice one end of the fiber to a fiber patch cord (an SM 400 fiber whose end has a FC/PC connector) using a fusion splicer (with loss between 0 to 2 dB) so that the fiber can be readily connected to the laser's one. We mechanically stabilize the splicing region with a fiber splice joint (from Thorlabs). Fiber thinning During the frontside etching fabrication step, we etch a groove region on the probe wire bonding area having a width of 140 µm (to compensate for optical lithography misalignments between the groove and the waveguide input) and 25 µm thickness (depth of the SiO_2 and Si etching). Such a groove mechanically stabilizes the fiber to the probe when glued (since gluing only the fiber tip to the probe edge without the groove will result in poor attachment). The limited groove depth results in the necessity of thinning the fiber diameter, as schematically illustrated in Fig. 32.1, which is obtained either by mechanical polishing or by chemical etching in hydrogen fluoride (HF).

Mechanical polishing consists of removing fiber material by mechanical abrasion using a high speed spinning wheel with polishing paper. We created a tool (Fig. 32.2), inspired by [123], [124], in which two clamps are used to hold the fiber and a rotating disk and mounted on a DC motor with optical polishing paper (1 µm

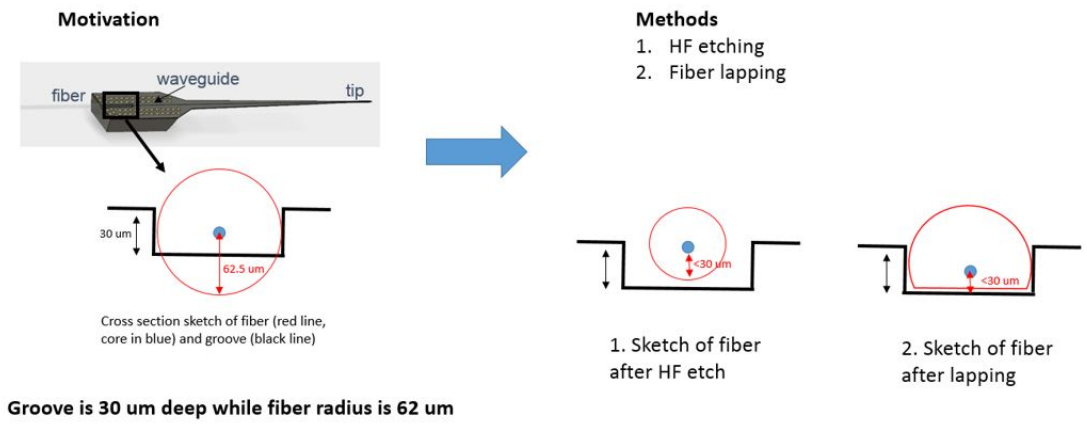

Figure 32.1: Schematic illustration of the optical fiber alignment in the probe's groove and highlights methods to reduce its diameter.

roughness). We monitor the amount of material removed from the fiber under an optical microscope while using micromanipulators to adjust the distance between the fiber and polishing wheel as well as the tension of the fiber. The main drawback of this operation is the poor reproducibility due to its nature of manual control (nonautomated setup) leading to a removal variation of 5 um between samples and low throughput (only one fiber is processed at a time). After the polishing, the fiber is cleaved and ready to be optically aligned.

HF etching involves chemically removing material from the optical fiber using $>$ 40% HF (etch rate: 2 µm/min) for 42 m to obtain a fiber diameter of 44 µm. We chose to implement this process because of its benefits over mechanical polishing in terms of repeatability (the etching is precisely controlled by the soaking time in acid with submicrometric precision) and the setup throughput (10 fibers can be processed at the same time, and the setup can be easily scaled to larger numbers). We build a custom-made optical setup to align and glue the fiber to the probe's (or test structure's) waveguide input for their optical characterization. The setup (schematic in Fig. 32.3 a,b) is an enclosed space with an optical table

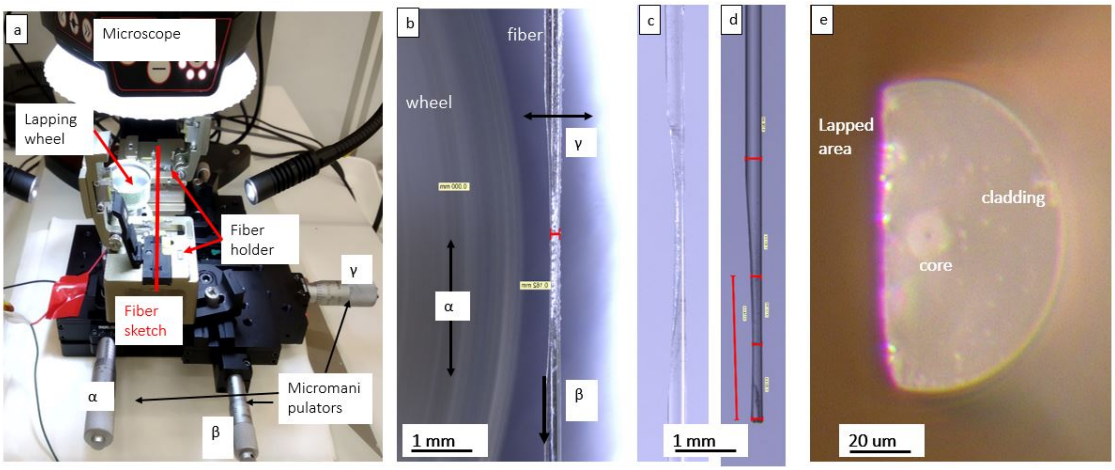

Figure 32.2: (a): Setup for mechanical polishing of an optical fiber [2]; top view image of the fiber (b) during and (c) after lapping, (d) after cleaving and (e) cross section of lapped optical fiber.

mounting a sample stage (that fixes the probe or test structure) and a fiber holder stage (that fixes the fiber), both of which are moved by microstepper motors (from Newport), connected to external controllers. The fiber is connected to the lasers of interest through the FC/PC connector and multiple lasers can be coupled into the same fiber using fiber combiners; the fiber output light is linearly polarized and its angle can be rotated using a Thorlabs manual paddle controller. A microscope and CCD camera, connected to a computer, provide real time monitoring of the fiber-waveguide alignment and light output gratings. We designed the optical setup to provide mechanical stability and submicron-precise alignment. Mechanical stability is obtained by carefully securing all the components of the setup (the fiber and sample/probe on their respective holders); submicrometric precision is essential to achieve the precise alignment necessary for edge coupling (0.5 µm) and is achieved using microstepper motors (with a smallest step of 20 nm). In addition, the setup's microscope and camera allow for real time monitoring and feedback to monitor possible misalignment. We complete the setup with additional metrology

components, such as a powermeter to measure the fiber's output power before its alignment to the sample and a spectrometer for real time monitoring of the laser's output wavelength.

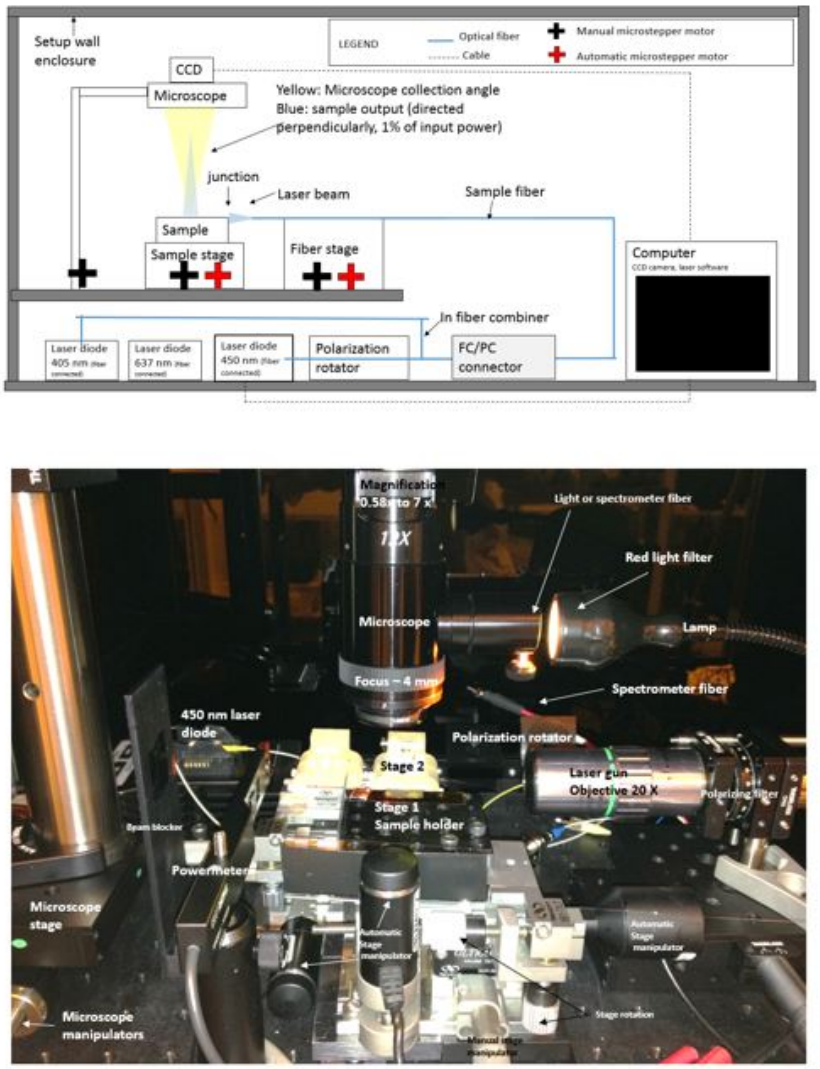

Figure 32.3: The custom-made optical setup for fiber alignment to the probe's (or test chip's) nanophotonic circuits is depicted by the (a) schematic illustration of the setup's component and (b) setup image.

We align the thinned fiber to the probe waveguide in the optical setup with the

aim of maximizing the light coupling by minimizing the fiber-waveguide misalignment; by gluing the two parts together, they are secured during the in vitro and in vivo experiments. Fiber-waveguide alignment We initially combine the 450 nm and the 637 nm laser into the same fiber and connect it to the thinned fiber, mounted on a holder; we then secure the wirebonded probe and its PCB onto the sample stage, activate the 450 nm laser, and align the fiber to the probe's waveguide input. After the initial alignment, we shift the microscope field of view onto the probe's output gratings and maximize the fiber coupling by monitoring their output intensities.

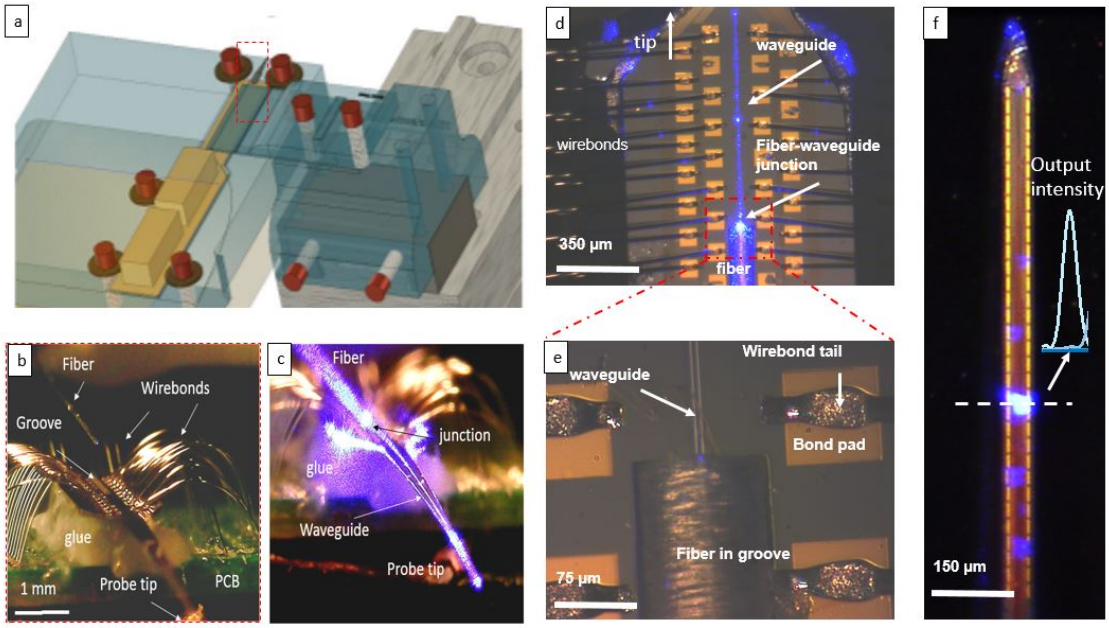

Figure 32.4: Optical fiber alignment to the probe is depicted in the (a) 3D model of the setup and (b,c) front camera images of fiber alignment (b) before and (c) after aligning the fiber and turning the laser on. Images displaying the top view camera at the (e,f) fiber-waveguide junction and magnification after fiber alignment with the laser on, and (f) top view at the tip are shown.

Fiber gluing Once we obtain the alignment, we secure the two parts to prevent misalignment by gluing them together. To achieve this, we turn off the 450 nm laser and turn on the 637 nm one to check the alignment while dispensing

the glue without curing it. We chose ultraviolet (UV) curable glues (rather than heat curing glues or two part mixing glues) to achieve quick curing (seconds) and low glue shrinkage values (<1%, since they have no solvents), both of which are essential to minimizing part misalignments and decreased coupling efficiency. We manually dispense the glue on the probe wire bonding area (glue OP-4-20632 from Angstrongbond, having linear shrinkage of 0.39% and transmission > 85% at 450 nm) to cover both the groove and fiber waveguide junction but not the probe tip. If misalignments occur during this step, we realign the fiber with the 637 nm laser, turn on the 450 nm laser at low power (< 100 µW), and finely tune the alignment before turning it on at higher power (1 mW) for 5 m to complete the cure. We then add some glue around the fiber, the fiber holder, and the PCB for increased mechanical stability. We dispense and cure some black glue to cover the light scattering at the waveguide junction and cure everything with the UV lamp for 60 s.

In vitro validation of nanocircuits integrated in microprobe

Probe experimental characterizations in air and in saline solution, which mimics the brain's ionic environment, allow for validation and optimization of functionality for the nanophotonic and the electrical circuits prior to inserting the tip into the mouse brain. The process of nanophotonic circuit validation involves monitoring the probe's grating outputs for different laser input wavelengths to estimate the circuit's optical losses as well as the ring's and directional coupler's frequency responses. We aim at minimizing optical losses and at reproducing the nanophotonic elements' simulated figures of merit for functioning design and performance. The process for electrical circuit characterization involves measuring the impedance of each electrode to assess functionality and lowering the impedance of the working electrode. We aim to achieve high circuit yield (at least 95% of working electrodes) and minimal impedance - to this end, we carry out electrodeposition for high surface area to volume ratio of carbon-based materials, such as nano-onions.

In vitro validation of nanophotonics

Introduction

Optical characterizations in air are achieved after aligning (and gluing) the laser's fiber to the nanophotonic circuit input and monitoring the grating outputs. These operations are performed in the setup described in page 100.

Characterization of the probe output power and device optical loss

We initially evaluate the tip output power which, for a given laser input power, is limited by the device losses. Such losses can be ascribed to several sources (scattering, fiber-waveguide coupling, absorption, outcoupling, etc). Minimization of system loss is crucial for sufficient output of light power to activate the opsins, which has been estimated as 0.1 mW/mm^2 [38]. Our 450 nm wavelength centered laser diode has a maximum output power of around 10 mW, while the total system losses amount to ∼30 dB, leaving total output power to be around 5 to 10 µW. Considering a light output spot on the order of the grating dimensions, 5 µm x10 µm, this total output power corresponds to a power density of ∼ 1 W/mm^2; such indicates that the system can achieve greater than necessary light output for opsin activation, as demonstrated by the *in vivo* experiment (see 47, page 152).

Probe's output power estimation

We estimate the probe's output grating power by comparison with a known source and converting the intensity of the microscope images into power (mW). We initially assume that the microscope objective can collect all the light extracted by the gratings (for this purpose, we use a high numerical aperture objective, 0.75). To this end, we initially use the powermeter to measure the laser fiber's output intensity (P) for a well-defined laser input current; we then image its output (Fig. 34.1), from which we analyze its intensity (K_f) defined as the area of the bright spot (A) times the difference of light intensity and background noise (I_s-I_n) divided by the camera exposure time (t_e):

$$K_f = A * \frac{I_s - I_n}{t_e}$$

We then connect the laser's fiber to the probe's input fiber and image the probe tip, while maintaining the same laser input current. For each output grating's image we obtain the relative intensity K_g in a similar manner as above:

$$K_g = A * \frac{I_s - I_n}{t_e}$$

The ratio between K_g and K_f in decibels (dB) yields the total optical losses from the fiber's laser to the grating output:

$$Losses[dB] = 10 * log_{10} K_g K_f$$

The corresponding probe's grating output power is obtained as the ratio between the two values times the fiber output intensity (in mW) which is measured by the powermeter:

$$Output[mW] = P * \frac{K_g}{K_f}$$

This measure is an estimate of the probe's losses and output power; thus for our purposes, this is a sufficient approximation to determine if our probe reaches the activation threshold of the brain opsins.

Once we have estimated the total losses, which amount to around 30 dB, we separate its various contributions to optimize them individually. (Fig. 34.2):

- Laser fiber-probe fiber FC/PC connection: 1 to 2 dB
- Edge coupling: 10 dB

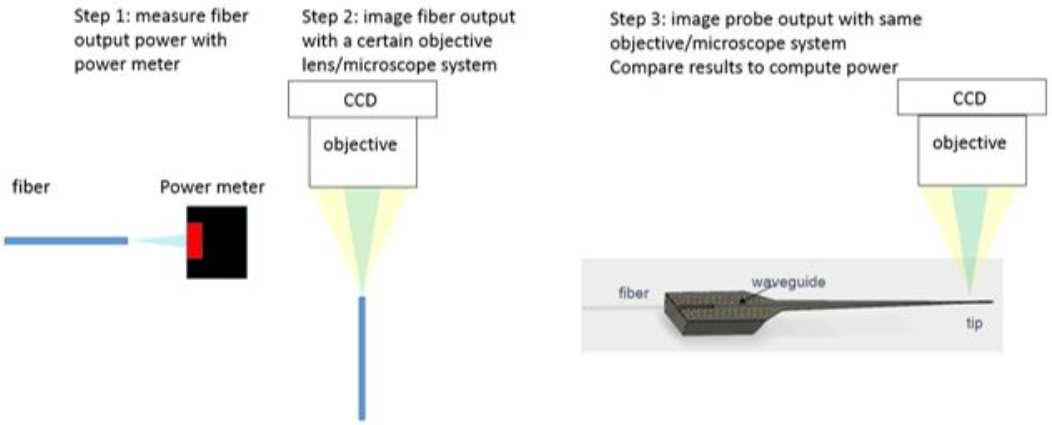

Figure 34.1: This diagram outlines the experimental process flow, in which the probe's output power is measured following laser input and camera calibration for subsequent imaging of the probe's output light.

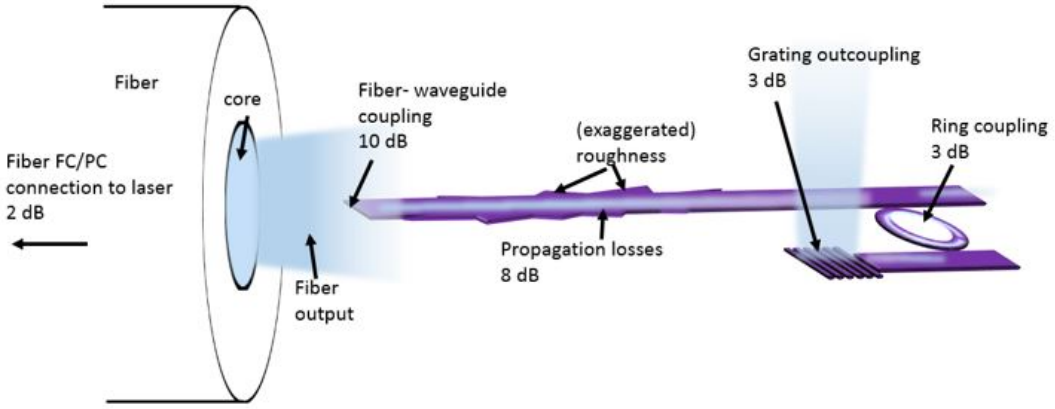

Figure 34.2: This schematic illustrates the system's optical losses.

- Fiber gluing: around 5 dB

- Waveguide propagation: 6-8 dB

- Grating outcoupling: 3 dB

- Ring transmission: 3 dB

In the following, we describe the corresponding losses and measurements in greater detail.

Laser fiber-probe fiber FC/PC connection

The FC/PC connection loss (typically 3 dB) results from non-perfect concentricity of the fibers inside the ceramic patch cord terminations that lead to the cores' misalignment. This can be minimized by using low insertion loss patch cords which typically result in 1 dB loss.

Waveguide propagation losses

Waveguide propagation losses arise from two main factors: absorption losses and scattering losses; here we describe the scattering losses, while we describe the absorption losses in the next section.

Scattering losses are ascribed to waveguide roughness, which can be measured on the top waveguide surface or on sidewalls; small roughness values (standard deviation of even a few nm) with small correlation lengths (<50 nm) can introduce large scattering losses (>10 dB/cm) for submicrometric-sized waveguides [39], [35]. Small roughness values are difficult to characterize by SEM, and although some alternative techniques have been used [49], we use waveguiding test structures for their estimation. We can neglect the top waveguide roughness since the Si_3N_4 layer is chemical-mechanically polished to a roughness below 1 nm [40]. Notably, sidewall roughness is assumed to be the main contributor to scattering losses due to waveguide fabrication variations, namely the electron beam resist patterning and pattern transfer during dry etching. Thus, we measure the waveguide's scattering losses using test structures fabricated on Lionix TripleX wafer pieces, in which the design that splits one input waveguide into two pairs of waveguides (A and B), each with one short and one longer waveguide outputs (A1, A2 and B1,B2), as described in [119]. Pairs of waveguides differ only in the waveguide width; they have

a fixed height of 160nm, while the the widths are 300 nm and 4 um for the first and second pair respectively. This allows comparison of the propagation losses for two differently confined fields. The path difference of every pair of waveguides allows for measuring the losses by comparing their output intensities. Using a common waveguide input for both waveguide outputs rules out fiber coupling losses. We cleave the input and output sections of the test chip and couple a fiber to the input waveguide, while the microscope and CCD camera monitors the cross section of the latter (output gratings are not used to avoid introducing their outcoupling losses), from which we extract their intensities Ai or Bi (as described in the previous Section):

$$Ai(orBi) = Area * \frac{I_s}{I_n}$$

Taking the logarithm of their ratio and dividing by the path difference (in cm), we obtain their losses (in dB):

$$Losses[dB/cm] = 10 * log_{10}(\frac{A_1}{A_2} * \frac{1}{Path})$$

This amounts to 5.6 and 8 dB/cm for 4 µm waveguides at the wavelengths of 650 nm and 450 nm respectively and to 12 dB/cm at 450 nm for 300 nm wide waveguides due to their higher mode overlap with the sidewalls [132].

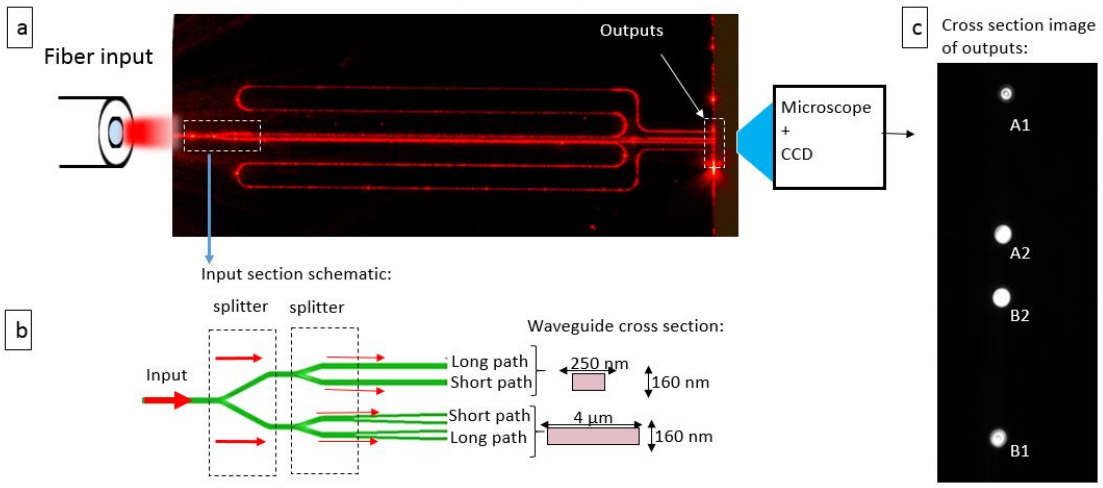

Figure 34.3: Waveguide propagation losses can be estimated by subjecting (a) the waveguide under a 650 nm (or 450 nm) wavelength laser input (the bright waveguide coloration is due to sidewall scattering) and examining the waveguide cross section output with a microscope and CCD camera. (b): For qa common waveguide input, we have two splitters for long and short waveguides with different cross sections. (c): Example of CCD output image; we estimate the waveguide propagation losses from the output spots' intensity ratios.

Absorption losses

Absorption losses are associated with material defects; given the high optical quality of the bottom SiO_2 and the Si_3N_4 layers, we focus on optimizing the top cladding SiO_2, which is deposited using PECVD. Several studies mentioned localized impurities, such as OH, SiH, and NH from PECVD depositions of SiO_2 layers with their corresponding optical absorptions [79], [99], [3]; these defects can be measured by Fourier Transform Infrared Spectroscopy (FTIR), which measures light absorption in the presence of vibrational modes associated with defects at well-defined wavelengths. Following these studies and considering the unavailability of an FTIR spectrometer, we minimize the oxide absorption by measuring the oxide refractive index and compare waveguide losses to uncladded waveguides. We proceed by testing different oxides on different Lionix chips (patterned with the

same parameters), each containing arrays of waveguides for measurement averaging. Different oxides are obtained by varying the PECVD gas ratios (N_2O and SiH_4) and temperature at a fixed chamber pressure (1000 mTorr) and RF power (20 W). Results of ellipsometry, plotted in Fig. 34.4 a, show a high refractive index (>1.47 at 450 nm) for low N_2O/SiH_4 ratio (below 50) – this is due to the silicon richness in the film (associated with high absorption losses) [99] – and a lower refractive index for higher ratios, with the lower bound being 1.47 at the wavelength of 450 nm for thermal oxide. Given the chamber's maximum temperature at the fixed N_2O/SiH_4 ratio, the measurements indicated decreasing refractive index as a function of increasing temperature (and subsequent decrease in Si-OH incorporation) until a high temperature of 375°C (due to N-H incorporation); this is in well agreement with previous studies [99]. However, a low refractive index is obtained for low temperatures (150°C) which is due to high porosity of the material (Fig. 34.4 e,f). Optical absorption in the film is analyzed in terms of propagation losses for the different claddings, indicating their decrease for increased N_2O/SiH_4 ratio (Fig. 34.4 b) and, for a fixed gas ratio, their decrease at lower temperatures (Fig. 34.4 c). About 20% of these results are attributed with uncertainties that arise from different parameter variations, but primarily the fiber-waveguide alignment accuracy. From these results, we choose to combine a high N_2O/SiH_4 ratio of 1440 (50 sccm SiH_4 is diluted at 1% in Ar, 720 sccm N_2O, 162 sccm N2) with a low temperature (150°C), resulting in small waveguide losses (3 dB at 450 nm).

Given the top cladding deposition parameters, we then analyze absorption losses associated with the presence of flowable oxide (FOx planarizes waveguide top cladding) for different SiO_2 layer thicknesses. The results, plotted in Fig. 34.5 a, suggest that using a waveguide top cladding thickness that is greater than 2.5

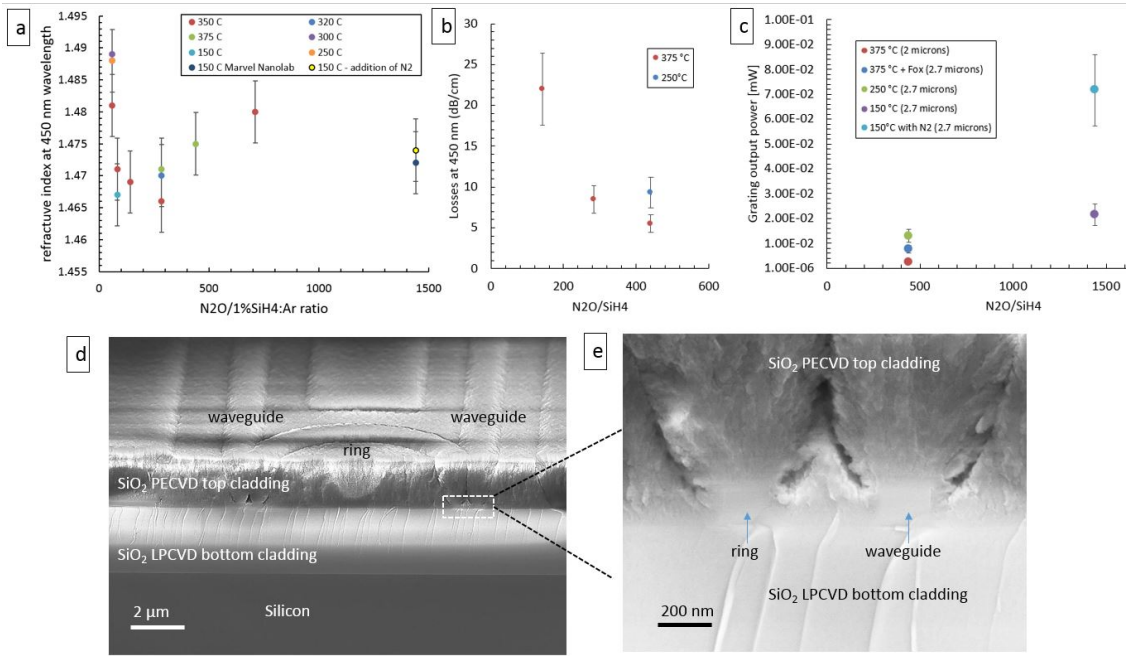

Figure 34.4: The waveguide absorption losses are characterized by (a): refractive index measurements, (b) absorption losses, and (c) probe optical output power for SiO_2 cladding deposited with different N_2O/SiH_4 ratios. (d,e): SEM micrographs of the waveguide cross section with top cladding deposited at 150°C and 1440 of N_2O/SiH_4 ratio.

µm avoids introducing losses related to the presence of the FOX layer; therefore, we chose to deposit 2.75 µm of SiO_2 PECVD top cladding (0.55 to 1.25 dB).

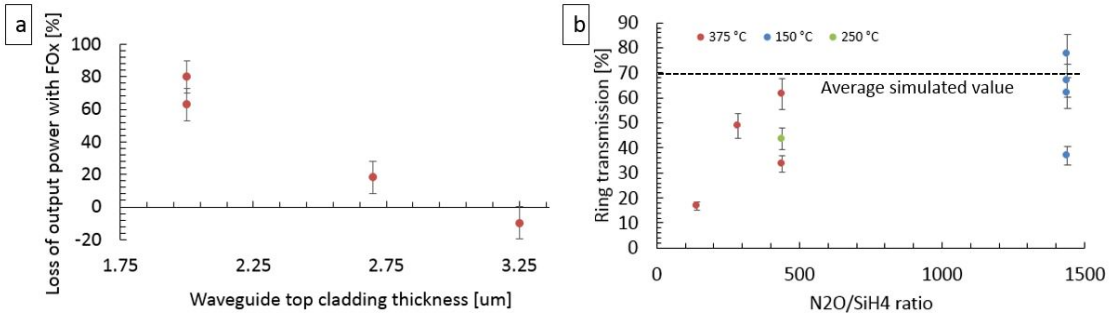

Figure 34.5: (a): Experimental measurements of the waveguide's power loss at different top cladding thicknesses and after the flowable oxide deposition. (b): Experimental ring coupling efficiency is a function of top cladding oxides deposited with different N_2O/SiH_4 ratios and at different temperatures.

Ring transmission

The ring transmission is the percentage of the total input power (defined by proximity of the ring) transmitted to the waveguide output at the ring's peak resonance, which we match by tuning the laser polarization and wavelength. Ring transmission efficiencies, displayed in Fig. 34.5 b, are calculated as an average of every ring's output grating intensity at resonance divided by the total intensity of all the gratings. For our ring design, whose simulation showed an efficiency of around 70%, we obtain a transmission of 60.75 ± 17.35 % (or 68.76 ± 8.13 % if not considering the low-efficiency measurement), corresponding to 1.67 ± 0.36 dB losses. Non-coupled light in the ring is mostly emitted by a final grating, with other rings emitting just a fraction of the light (<1-5% for every other ring).

For our given ring design and simulation, we obtain an average transmission of around 70 % (1.55 dB); we thus analyze the fabrication process for patterning the resist ZEP 502 A and transferring it with an RIE dry etch with the aim of optimizing both the waveguide transmission and coupling efficiency to obtain values similar to those from the simulation. The dose of the first step is fine-tuned, while the second step is performed at a fixed RIE pressure (55 mTorr), table temperature (20 °C), and total gas flow (50 sccm) with variations in the gas chemistry CHF_3/O_2 ratio and RF power. We design a variety of test structures with different ring gaps (ranging from 20 to 100 nm with 5 nm increments) and waveguide widths (ranging from 200 to 300 nm with 10 nm increments) to find the resulting optimized combination from the two processing steps; this evaluation takes into account propagation loss, coupling efficiency optical measurements, and visual measurements using the SEM. We perform 7 dose variations starting at 225 $\mu C/cm^2$ with 5% increments; as shown in Fig. 34.6 a,b, while the difference between the designed and fabricated gaps is

not significant (<10 ±5 nm for highest doses), the waveguide difference can be significant (56 ± 5 nm), both of which can be accounted for in the initial design.

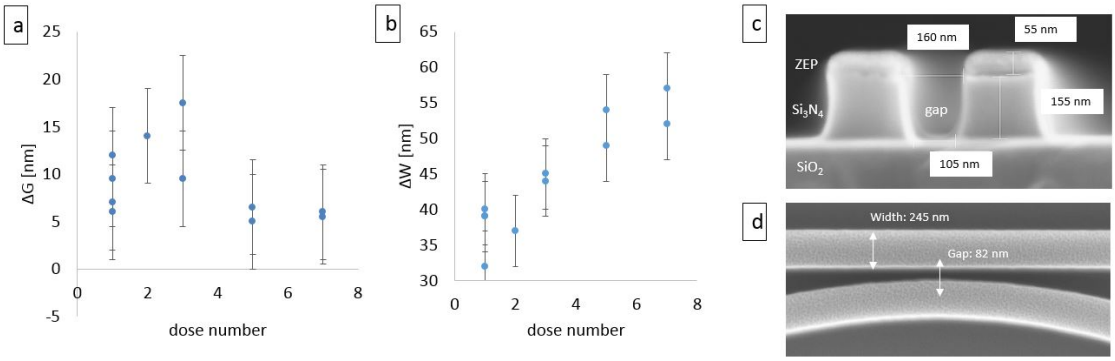

Figure 34.6: A comparison of the fabricated and designed ring resonators is characterized by (a) gap and (b) width. SEM images of (c): the cross section of the ring-waveguide gap for non optimized etching recipe and (d) top view of the ring-waveguide gap (as small as 80 nm) after recipe optimization are depicted.

During the dry etching process, the CHF_3 gas is responsible for both the chemical removal of the Si_3N_4 and the polymer formation at the bottom trench and sidewall; the resulting passivation layer creates a vertical sidewall profile, which is essential for achieving the correct ring-waveguide gap dimensions such that an undercut will not result, but also introduces additional roughness (and scattering losses) [50]. The presence of O_2 reduces polymer roughness (since it reacts with carbon polymer resulting in CO or CO_2) while maintaining the vertical sidewall angle, but decreases the resist ZEP 502A selectivity (we did not optimize for a hard mask such as Nickel). Initial experiments were conducted for 10-12 minutes, flowrates of 48 sccm CHF_3 and 2 sccm O_2, and at RF = 40, demonstrating waveguide propagation loss around 8 dB/cm (at 450 nm wavelength) but the wide waveguide-ring gap as depicted in the SEM images (>120 nm, Fig. 34.6 c) results in low simulated ring coupling efficiency (25.7%, 10.4%, 6.1% for gaps respectively of 120, 140, 150 nm) and close to zero for the experimentally measured efficiency. We modified the

recipe accordingly by increasing RF power (100 W) to achieve greater directional etching; this step was implemented for 1 m 30 s and followed by the original 7 m 30 s etch step at 40 RF. The longer high power etching step resulted in complete resist degradation and waveguide etching. The smallest gap is 82 ± 5 nm for a designed gap of 30 nm, Fig. 34.6 d. We also modified the CHF_3/O_2 ratio from 48:2 to 45:5 (maximum amount of O_2 allows complete etching of the Si_3N_4 without full resist degradation) and decreased the pressure to 30 mTorr (longer ion mean free path leads to increased directionality); however, the optical tests demonstrated poor ring coupling efficiency (<20%).

Grating outcoupling losses

As discussed previously, we consider the grating outcoupling efficiency based on their simulation (2-3 dB non outcoupled light). When measuring gratings, we use high numerical aperture objectives to collect all of the light. This is particularly important for gratings that do not extract light perpendicularly for the input wavelength in use. Fig. compares measurements between a low (0.2) and a high (0.8) numerical aperture objective, suggesting no significant difference (∼50%) of light collected for gratings that are optimized for perpendicular light extraction, but a significant difference (∼3400%) for gratings that are not optimized for perpendicular extraction (out grating design which outputs the wavelength of 450 nm at an angle of 16°).

Fiber-waveguide coupling losses

We estimate the waveguide propagation losses, and assuming the grating losses are similar to the simulated ones (2-3 dB), we estimate the fiber-waveguide coupling

efficiency by comparing the maximum grating output power obtained from the best achievable fiber alignment with the fiber output power. We compare both edge coupling and grating coupling structures and obtain 10 ± 2 dB (around 10% coupling efficiency) and 7 ± 1.4 dB (around 30% coupling efficiency) respectively, which are in good agreement with the simulation results. Images of the optical fiber aligned to these two structures are shown in Fig. 34.7.

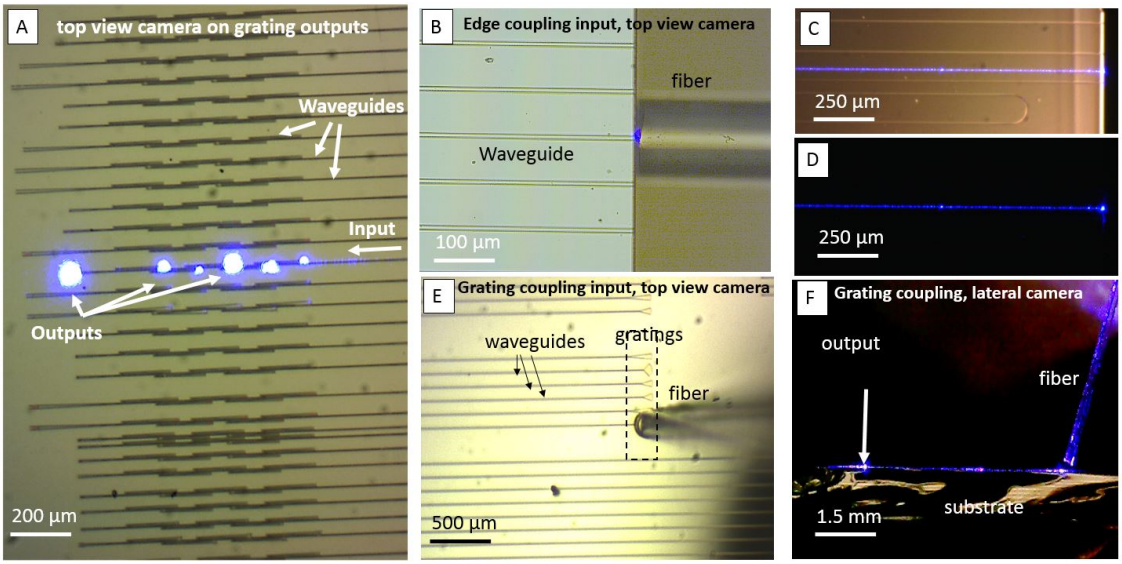

Figure 34.7: Fiber coupling is shown by (a): an image of test waveguides on the chip after fiber alignment with the laser on, showing the grating output light, (b-d): fiber-waveguide edge coupling, and (e-f) top view and lateral images of fiber-grating coupling.

Fiber gluing losses

We glue the optical fiber after it is aligned to the waveguide input edge for a mechanically fixed system such that there are no movable parts. The gluing procedures result in a range of losses approximated between 1 to 5 dB; this is attributed to misalignment of the fiber during glue curing and consequent shrinkage. From these values, we can estimate a misalignment below 1 µm in the vertical direction. After gluing, the fiber-waveguide junction stops working after a few minutes if we use high laser powers (>= 1.5 mW, although, as described in 47, page 152, a high power is unnecessary) and short wavelengths (< 500 nm); this can possibly be attributed to glue overcuring in the fiber's core region, leading to glue ambering. This effect shown in Fig. 34.8 occurs after we glue a fiber to a glass slide, leave the laser on at 1.5 mW, and detach the fiber afterwards. One option to overcome this issue (apart from using a laser power <1.5 mW) is to dispense a high viscosity opaque glue (OP 61 LS from Angstrongbond with a linear shrinkage of 0.03%) on the groove's back component such that the glue does not flow to the fiber-waveguide junction. The resulting gluing did not present losses related to glue darkening in the junction area for the 450 nm laser at high power (>= 1.5 mW); however, the wire bonding area is not covered with dark glue (to limit the amount of light scattering to the tip) and this could increase the photoelectric artifact on the electrodes.

Grating nanogroove design for output beam focusing

We characterize the focusing gratings' output beam shape and height of focus by observing their output at different heights, starting from the in-plane (h=0) and moving the objective with microstepper motors by the desired increment (e.g. h= 5

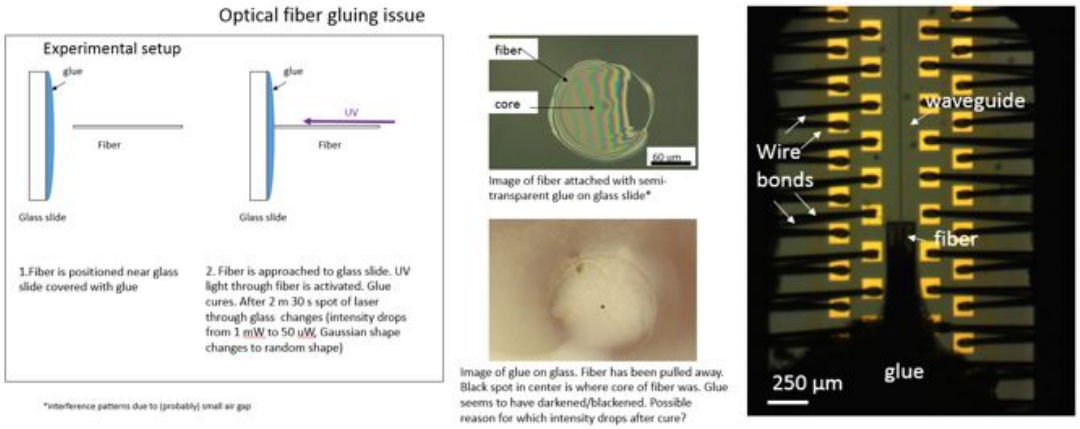

Figure 34.8: The losses associated with fiber gluing were determined through (a): the experiment that measures glue darkening after prolonged laser light illumination. The following images depict (b): the fiber glued onto the glass slide after glue curing, (c) the darkened glue in proximity to the fiber core after fiber removal, and (e): the optical fiber edge coupled to the probe's waveguide and glued far from their junction.

um, h=20 µm,...) to the focal point and beyond. We show the results for a grating designed for an input wavelength of 450 nm with a focusing height of 20 µm and a focusing grating designed for 650 nm with h = 10 µm Fig. 35.1. As we described in [60], wavelengths that are different from the designed one still focus but at a slightly different height Fig. 35.1. For the first grating, the resulting output spot is close to the simulated focal height (with a difference of a few µm) and its diffraction limited FWHM is 2.35 µm.

In vitro on-demand light delivery and localized illumination

Once we have fabricated, assembled and optically characterized the neural probe's optical losses, we proceed by testing its nanophotonic's circuit capability of spatially addressing the light output location. After fixing the sample onto the optical setup, connecting its fiber to the laser's, and adjusting its polarization

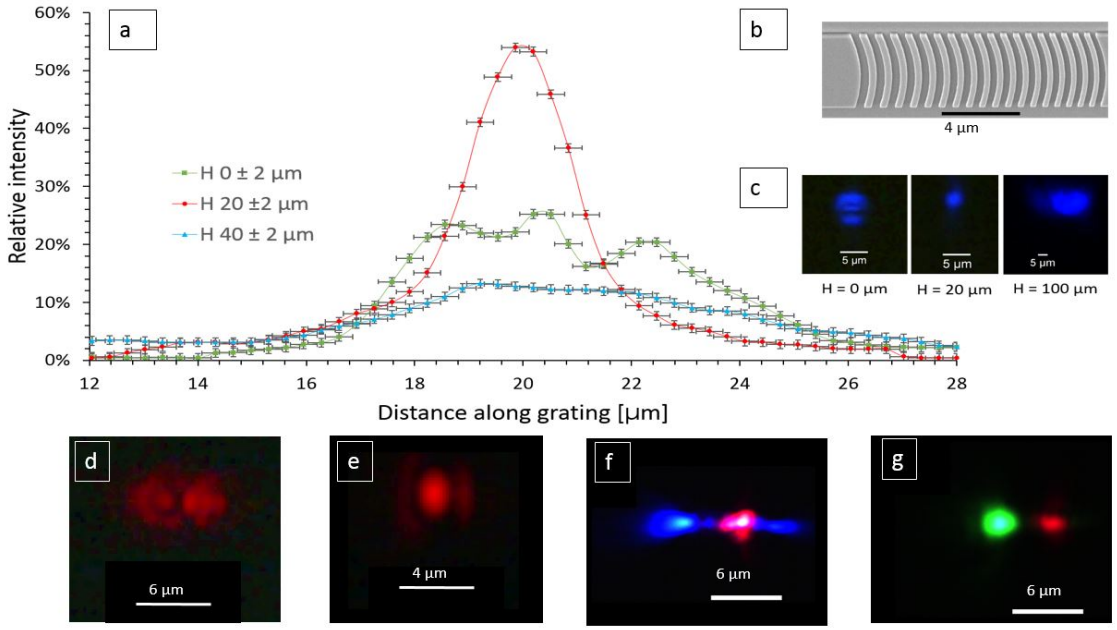

Figure 35.1: The following is an optical characterization of the focusing grating at different heights with respect to the grating's (h=0). (a): A line plot of grating outputs measured at different heights above the grating (b) and corresponding light spots (c) are shown. (d,e) Focusing gratings designed to focus light at the wavelength of 650 nm and (g,f) use of different wavelengths onto the same gratings are depicted.

by means of the paddle controller to match the TE fundamental mode, we tune the laser's wavelength (within a range of 3.4nm) as a function of temperature (10°C to 62°C) and observe the output gratings. Since the laser's wavelength is a nonlinear function of temperature and its output power varies for different temperatures, we implement a feedback loop with a Matlab script that adjusts the desired wavelength (by fine-tuning temperature) and holds the laser output power at a constant value across varying wavelengths (by changing its input current).

The program (Fig. 36.1) scans the laser's wavelength at defined values by tuning the laser at different temperatures while monitoring the different grating outputs on the probe tip to measure their intensity as a function of wavelength.

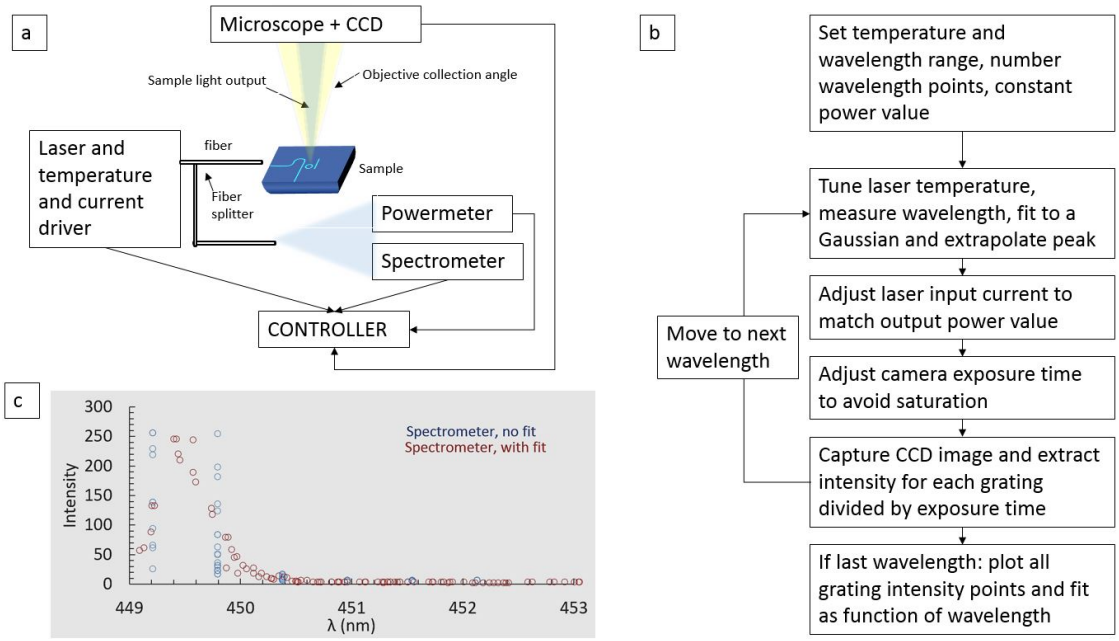

Figure 36.1: experimental setup to take automatic measurements of the ring resonators.

The wavelength is monitored with a spectrometer (whose exposure time is adjusted by the script to avoid saturation) and extrapolated by a gaussian fit to compensate for poor spectrometer resolution. Once the desired wavelength is reached, the power (measured with a powermeter) is kept constant by modifying the laser input current. The camera exposure time is adjusted to avoid saturation and an image is taken, from which each grating's intensity is measured. The program then moves to the next wavelength and restarts the loop.

We report an example of such a test in Fig. 36.2 which shows a tip with five ring resonators. Light spatial localization, as shown in (Fig. a-d), is demonstrated after we turn on the laser at wavelengths corresponding to the first four ring resonances; this is plotted in Fig. 36.2 e, along with the laser spectrum. From this measurement, we extract the experimental ring Q factor (on average: 861 $\pm$ 127) which closely matches that of the laser (860 $\pm$ 20). As an example, we plot the rings' experimental

and simulated transmittances along with the laser's spectrum in Fig. 36.3 a. The ring's coupling efficiency was measured in the previous Section with an average of 60.75 ± 17.35 % (out of resonance rings' efficiency of < 5%). Notably, the ring's FSR is not available since it is wider than our laser's tunability range. Numerical comparisons between the simulated and experimental resonance wavelengths are displayed in Fig. 36.3 b. Finally, we evaluate the tip output power with the methods described in 33, page 107; our laser diode has a maximum output power of ∼10 mW, while the total system losses amounts to ∼30 dB, leaving the total output power to be around 5 to 10 µW. This output power value corresponds to a power density of ∼1 W/mm^2 (considering a light output spot on the order of the grating dimensions, 5 um x 10 um), thereby showing that our system can output more than enough light for opsin activation, as validated during the *in vivo* experiment (see 47, page 152).

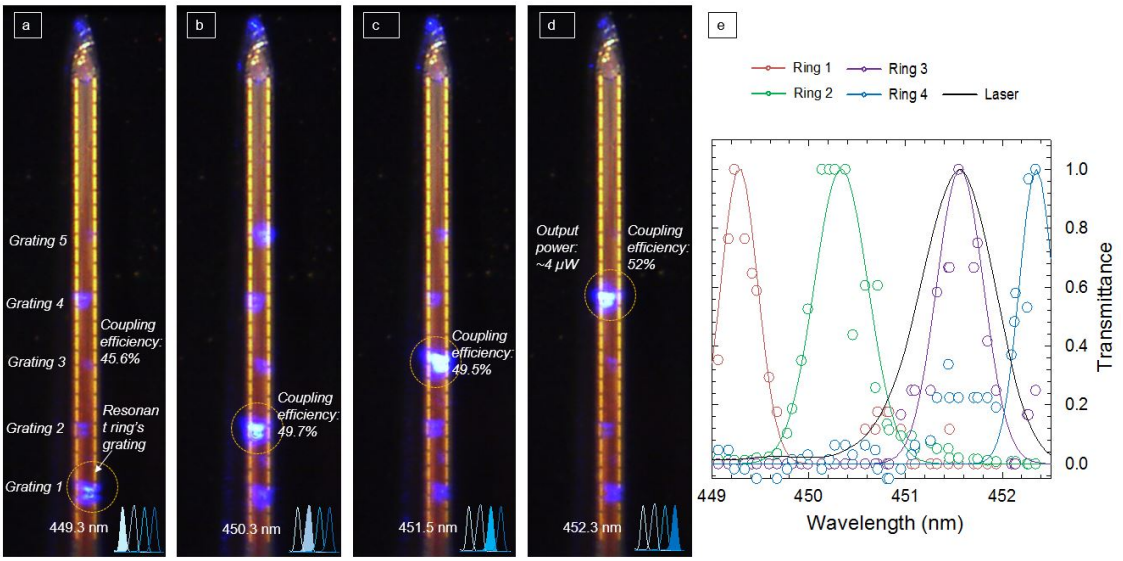

Figure 36.2: Experimental measurements of the ring's outputs at (a-d) different input wavelengths show the capability of spatially locating the light output along the probe's tip. (e) Normalized intensity plots as a function of the input wavelength for the ring resonators are depicted.

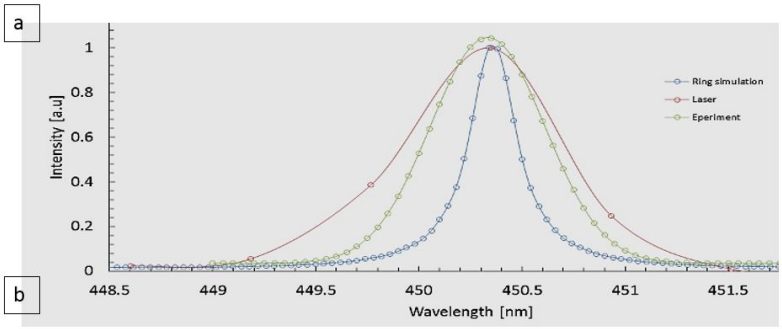

Ring	Radius [μm]	Experimental $\lambda_{resonance}$ [nm]	Simulated $\lambda_{resonance}$ [nm]
Ring 1	3.869	449.3	449.4
Ring 2	3.881	450.34	450.6
Ring 3	3.905	451.6	451.5
Ring 4	3.917	452.4	452.26

Figure 36.3: comparison of a single ring's simulated and experimental resonance with respect to the laser's spectra.

On-demand light delivery and localized illumination in saline solution

After validating the probe's capability to deliver light in the area(s) of interest by selecting the desired ring resonators in air, we repeat the experiment by immersing the probe's tip in saline solution (PBS saline, pH 7.4, by ThermoFischer). In Fig. 37.1 we compare the ring resonances before and after immersion in saline solution. We notice the peaks shift (red arrow in figure) by a value of 0.59 $\pm$ 0.05 nm, which we associate with some leaking of saline solution inside the top cladding oxide (which is porous since deposited at low temperatures, see Section 33). Ring Q factors do not change significantly (variation of around 80). Although ring resonance show an initial shift, we do not observe resonance variations after the probe immersion in saline for times of 15 m, 90 m and 150 m demonstrating that, once we characterize the ring resonances in saline, we can select the desired ring resonators without any visual feedback from a microscope. This is an essential step during the probe's implantation in mouse brain, where we have no visual feedback

on the selected rings.

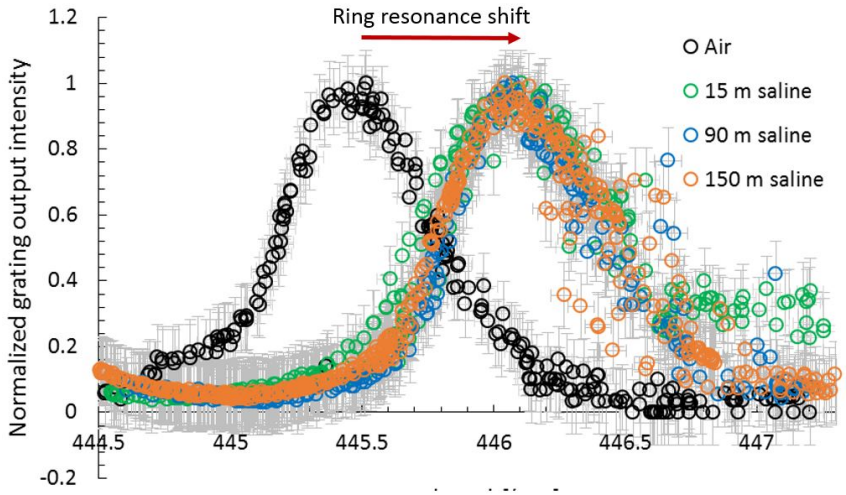

Figure 37.1: Measurement example of a ring resonance before and after saline immersion, showing that, after an initial shift, the rings' resonances do not change over time.

Polarization

We perform optical tests at different input polarizations to verify the correct ring's working for the designed polarization (TE, or 90°). We select the desired polarization by rotating a polarization grid (which transmits only one polarization angle) and by maximizing the transmitted intensity (thus, matching the grid's angle) by rotating the polarization in the laser's fiber with the paddle controller. First, we measure the grating's output intensity as a function of the wavelength for both the TE and TM polarizations (Fig. 37.2 a). For the TE polarization, the ring is working as expected, while for the TM one the ring does not resonate. Next, we monitor the same ring's output grating intensity with different input polarizations (Fig. 37.2 b); we obtain a maximum grating output intensity (and thus, ring coupling) for a polarization angle of 90° (corresponding to the TE mode)

and low coupling values for the other polarization angles, which well agrees with the values simulated with FDTD (red points).

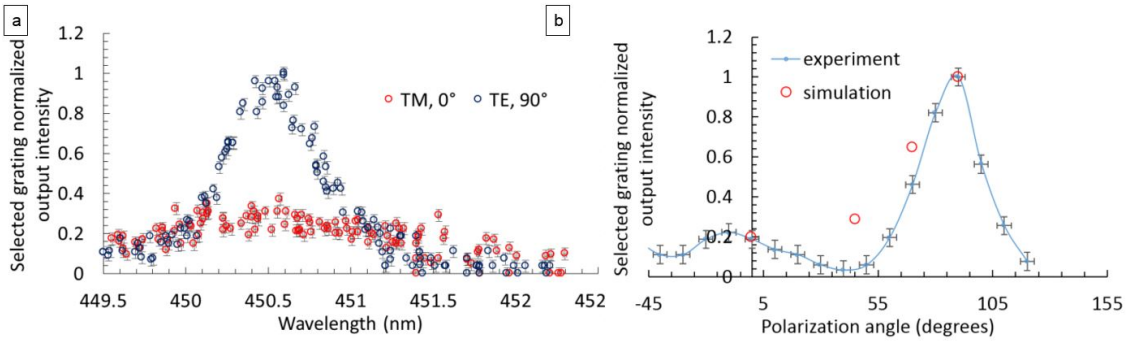

Figure 37.2: Ring's grating output intensity for different input polarizations. (a): Simulated and experimental data of a grating output intensity at the ring's resonance wavelength for different polarization angles.(b): Experimental ring resonance curve for TE and TM input polarization.

Multicolor illumination

To deliver multi-color, on-demand illumination in the areas of interest, we design a nanophotonic circuit (38.1) that combines two key elements, namely: i) an optical directional coupler, for the independent selection of two wavelengths that can optically excite two different opsins and ii) ring resonators, to address a specific light output location for any of the two desired wavelengths. We thus describe the implementation of the coupler with rings specifically designed for each opsin activation wavelength (450 nm and 650 nm).

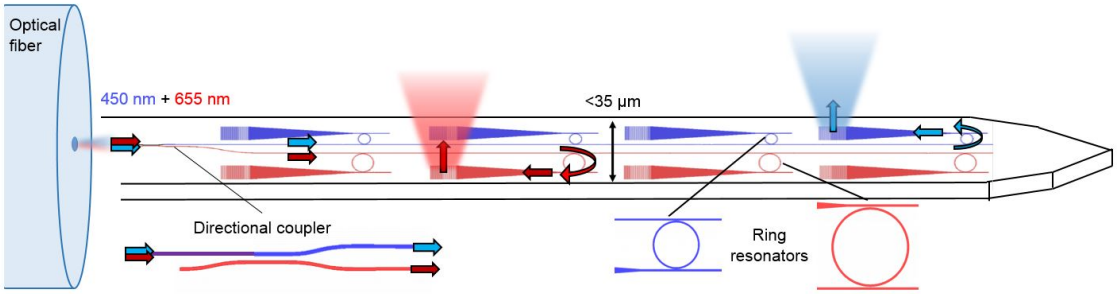

Figure 38.1: schematic illustration of the nanophotonic circuit integrated into the neural probe tip for simultaneous control of the light output location for two independent wavelengths (450 nm and 650 nm). For the single waveguide input, we integrate a directional coupler that splits the two wavelengths (based on their color) in two output waveguides. Each output can embed several ring resonators with different radii allowing for selecting the light output location for each of the two wavelengths.

Experimental validation of coupler

Optical directional coupler are passive switches [116] that allow for independently controlling two input wavelengths coming from the same input waveguide by assigning them to separate outputs. We simulate and fabricate the directional coupler with the goal of achieving high transmission for 450 nm and 650 nm, which were shown to independently drive responses from different opsins (i.e. Chronos and Chrimson [57]). We implement a broad-spectrum wavelength splitting, which allows for introducing additional nanophotonic elements - such as ring resonators for light location selection, in order to finely control the light delivery within each of the two opsin absorption spectra. Our coupler consists of an input waveguide and of an upper and lower output waveguides that confine and guide the 655 nm and 450 nm light wavelengths respectively. We fabricate a stand-alone directional coupler (Fig. 38.2 a-c), where the two output waveguides are terminated with gratings to provide a straightforward characterization of this optical element; we report the simulation and fabrication details in the Methods section. We then validate

the coupler by comparing the experimental optical transmission with the simulated one, as we show in Fig. 38.2 d. The simulated transmission is 97.8% for 655 nm and 95.2% for the 450nm waveguide, with low cross-talk values (the percentage of red light going in the blue waveguide and viceversa) of 0.13% and 4.2% for 655 and 450 nm; for both outputs, the transmission is within a 10% value of the peak one in a range >70 nm around the maximum (that is, much larger than our rings' bandwidth). Accordingly, the measured transmission for a 655nm and 450 nm laser are, respectively, around 99.64 ± 0.3 %, and 96.3 ± 0.38 % and the cross-talk is 0.36% and 3.7 %.

Combination of directional coupler and ring resonators

To deliver light of different colors in the location of interest along the probe's tip to activate distinct neurons we integrate, for each coupler's output waveguides, arrays of ring resonators optimized for each two colors (blue at 450 nm and red at 655 nm, (Fig. 38.3 a) and select the desired ring and its corresponding grating by tuning the input lasers' wavelengths. We aim at maximizing both the amount of light delivered in the brain tissue and the number of independently selectable outputs while minimizing channel cross talk, which could result in the spurious activation of opsins near non-selected gratings. We thus optimize each ring's transmission – that is the amount of light transferred to the ring's output - at selected resonance wavelengths and the number of channels with a minimum cross-talk by matching our input laser model tunability range and bandwidth. In Fig. 38.3 b,c we show the simulation and optical test of 3 rings at the wavelength of 448-452 nm and 3 rings at the wavelength of 654-658 nm that fit within the coupler's bandwidth and with, respectively, radius 4/ 7 μm (with 12/ 18 nm increments), ring-waveguide

gap 80/ 130 nm and waveguide width 250/ 375 nm. Rings show high simulated and experimental transmission (>50%) at their peak wavelengths and low channel cross talk (<5% for both simulation and experiment) for both coupler's colors. We design three outputs for each color because we use narrow-tuning lasers and wide bandwidth laser (<6 nm and around 1.2 nm respectively) and because of the same ring's resonance repetition across the wavelength (the free spectral range FSR).

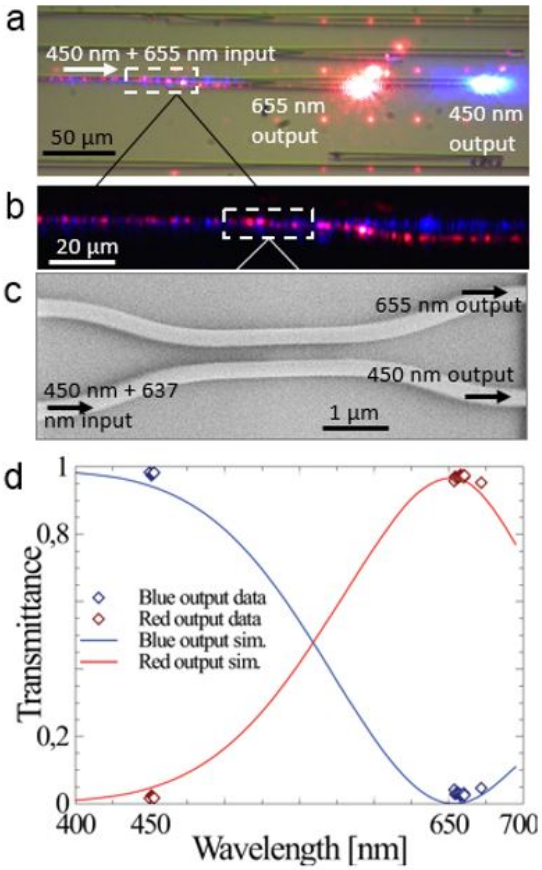

Figure 38.2: directional coupler simulation and experimental characterization. (a): directional coupler simulation and experimental characterization. (a): we fabricate a coupler terminated by gratings and edge-couple laser light (450 nm + 655 nm) at its input. (b) shows a magnification around the coupler area, highlighting the splitting of red and blue light. (c): micrograph of the directional coupler. (d): coupler's simulated (line) and experimental (squares) transmittance, showing high transmission and low cross-talk values.

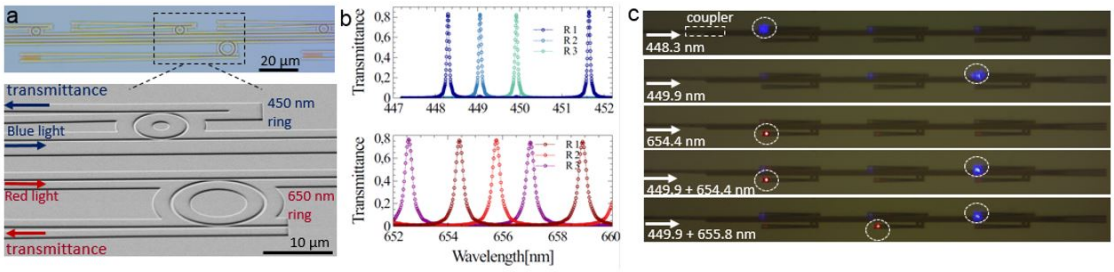

Figure 38.3: fabrication and test of ring resonator for blue and red wavelengths. (a): optical microscope image showing the red and blue rings. (b): simulated ring transmission as a function of the wavelength. (c): experimental characterization, showing the activation of different rings by the laser's wavelength tuning.

Integration of multicolor and on demand nanophotonics with sensing electrodes

Once optimized both the directional coupler and the ring resonators, we integrate arrays of electrodes for electrophysiology sensing simultaneous to the optogenetic stimulation (Fig. 38.4 a,b). We fabricate the 64 electrodes, having 10 X 8.5 µm dimension and 30 µm pitch and integrate them in a separate layer above the nanophotonics so to maximize the probe tip area for both. In Fig. 38.4 c-f we show the activation of the desired gratings, placed between the electrodes, by the selection of the blue and red laser specific wavelengths. Given the tip lateral width and thickness (45 µm and 15 µm respectively) and the number of sensors and output gratings (64 and 6) we obtain a cross sectional area coefficient [63] $<$ 10, which is one order of magnitude smaller than the current state of the art.

In vitro validation of electrical circuits

Electrode yield testing and optimization

Given the difficulty of establishing the number of defects in the electrical circuit using visual (SEM) characterization (defects are too small and sparse to be precisely

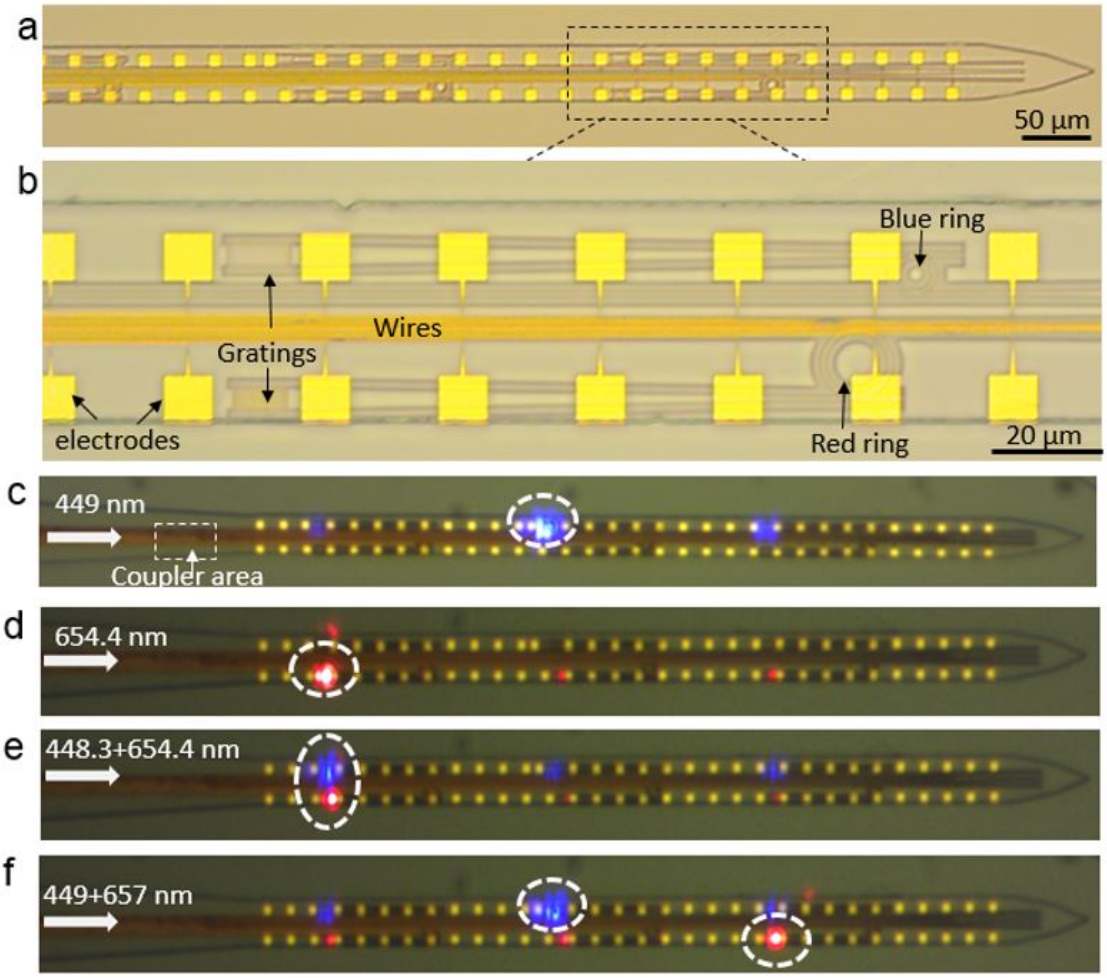

Figure 38.4: integration of electrodes above the multicolor nanophotonics. (a,b): resulting probe tip, integrating 64 electrodes above the nanophotonic directional coupler and the ring resonators. (c-f): selection of the desired gratings for each color corresponding to a distinct opsin (blue or red) in the area(s) of interest.

estimated), we test the electrical circuit functionality (number of working, open or short circuited wires) after the liftoff and several following fabrication processes with resistance measurements. We use the manual probe station, which consists of metallic tips, moves by micromanipulators, and monitors by a microscope to measure the resistance between the electrodes in the probe tip and the ones in the interfacing area (Fig. 39.1). We design probes at the center of the wafer and at

its edges having electrodes in their tip areas with dimensions 45 µm x 45 µm to ease their interfacing. Typical resistance measurements for working electrodes are in the range 5 KΩ - 10 KΩ (while open circuit electrodes have values within the range of GΩ). Short circuits are checked by measuring pairs of adjacent electrodes in one probe area for a single electrode in the other area. Following resistance measurements, we optimize the liftoff process, where we find that sonication in solvent (i.e. acetone or dichloromethane) results in a high number of defects, no working electrodes, (likely due to the movement of lifted gold particles scratching the wires), and solution stirring (70-80% yield). Using PG remover at 80°C and no form of bath agitation, we obtain yields > 90%.

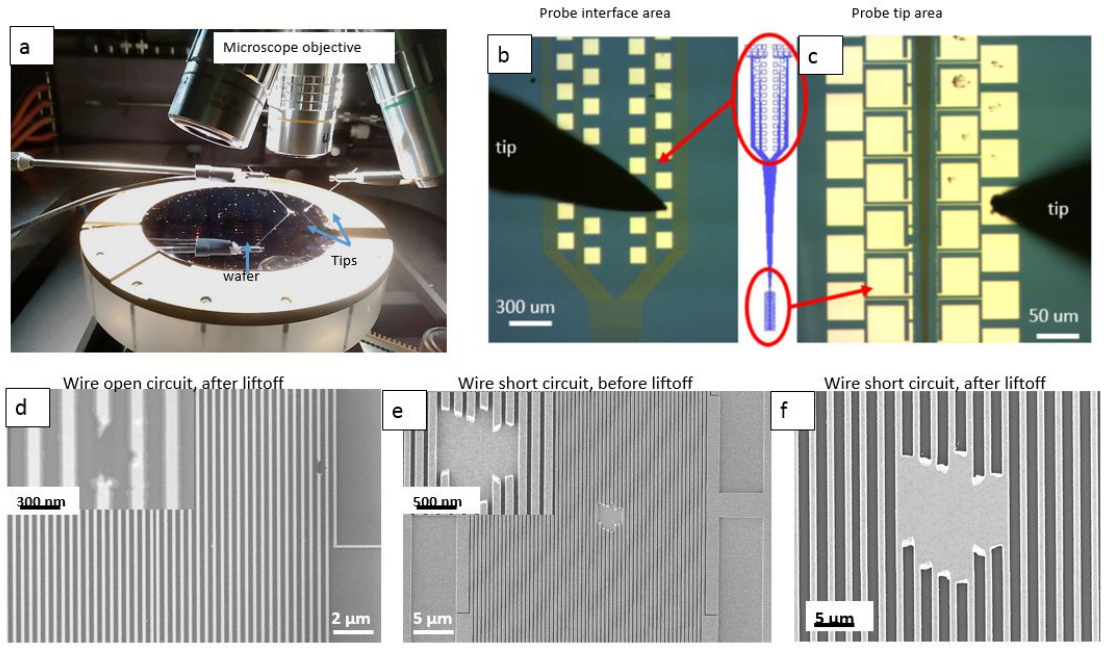

Figure 39.1: Resistance measurements of the arrays of sensors, (a) probe station setup, and (b,c) microscope image of the station's tips interfacing with the probe's electrodes are shown. The (d): results of electrode yield measured at the probe station after liftoff with different procedures and (e-g) defects on wires limiting the yield are also shown: (e) open circuits, (f) short circuits before metal deposition and (g) after liftoff.

These values do not take into account the number of short circuited wires (15-30% of the electrodes). We analyze the short circuits with visual SEM inspections, from which we deduce that they arise from resist line collapse during its development due to a high dose (more resist undercut) and the use of ultrasonication (better contrast but higher collapse probablity). Furthermore, we design a new layout which increases wire spacing in the tip as more electrodes are connected towards the probe tip's end. We confirm these hypotheses with probe station measurements in (Fig. 39.2), where we find that lower doses and no use of ultrasonication lead to a high yield (>95%) and lower dose sensitivity for the new layout.

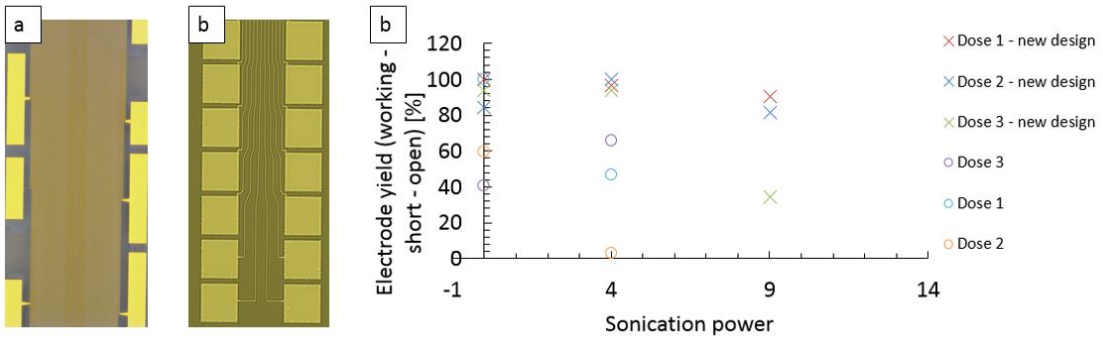

Figure 39.2: Electron beam dose study and effect on electrode yield: (a,b) first layout and new layout with higher spacing in between wires and (c) electrode yield measurements for the two layouts at different doses and sonication powers are shown.

Electrical characterization in saline: impedance and electroplating

Introduction

We test the electrical circuits in saline solution to measure the electrodes' impedance and yield (number of functioning electrodes). We use electrochemical impedance spectroscopy techniques to measure each electrode's impedance, which

is a measure of the system's capacity of recording an external time-variant voltage in the ionic environment (see 14, page 25). We then decrease the functioning electrodes' impedances by increasing their surface area through the deposition of metallic nanoparticles, such as gold (Au) and platinum black (Pt). We immerse the probe's tip in phosphate buffered saline solution (Thermofischer) and connect its Samtec connectors to the NanoZ toolkit [88], which applies a 5 mV AC sinusoidal signal to each electrode at the desired frequency (200 Hz- 10 KHz) to retrieve the voltage and phase values; we connect a Platinum counterelectrode between the solution and the Nanoz' ground pin. The average impedance value at 1000 Hz for working electrodes (size 5 µm x 25 µm) is 5.18 ± 0.87 MΩ (averaged over 95 electrodes), while open electrodes have impedances above 10 MΩ. An example of impedance measurements of a neural probe is shown in Fig. 40.1 a (impedance module at 1000 Hz), and the average value of impedance at varying frequencies (1 Hz-2000 Hz) is shown in Fig. 40.1 b.

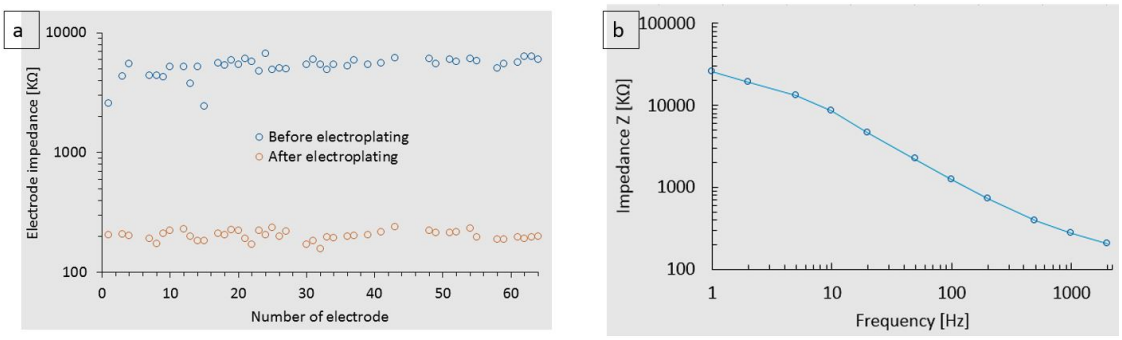

Figure 40.1: Probe in vitro electrical measurements in saline, showing (a) the electrodes' impedances before and after electroplating and (b): the impedance at different frequencies are depicted.

Electroplating

As expected, the first *in vivo* measurements with flat gold electrodes did not yield any neural signal readout due to the low signal to noise ratio associated with

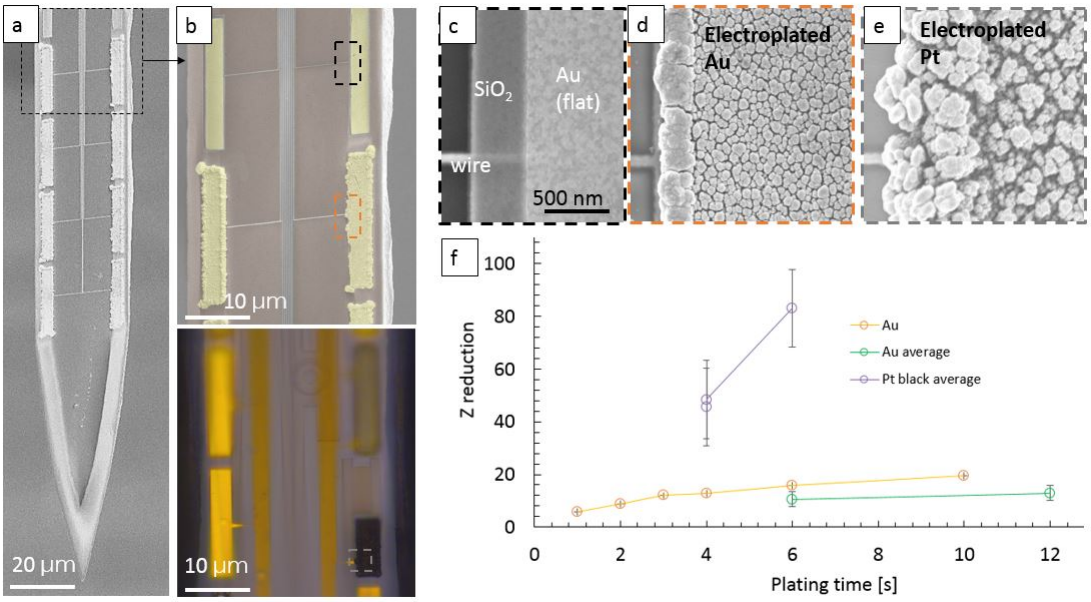

Figure 40.2: Results of probe electroplating is depicted by (a): the SEM top view image of the probe tip and magnifications of electrodes plated with (b, top) gold and (b, bottom) platinum black and corresponding magnifications (c: no plating; d: gold plating; e: platinum black plating). (e) Comparison of impedance decrease after electroplating with gold and platinum black for different plating times.

high electrode impedance (see page 25). To lower impedance, we electroplated with gold nanoparticles or platinum black nanoparticles (Neuralynx [102],[34]) and substituted with saline solution. Three dimensional structured electrode surfaces for both materials are shown in Fig. 40.2 a-c. Plating was achieved using different combinations of currents (100 nA to 3 µA) and deposition times (1 s – 20 s); The average impedance of > 100 electrodes decreased for all tested combinations of varied times and currents. Plating of Au and Pt black nanoparticles lowers the average impedance value from 5.18 ± 0.87 MΩ to 0.32 ± 0.2 MΩ (12.7 ± 6 times impedance reduction, 73 electrode sample) and 0.138 ± 0.09 MΩ (55.6 ± 27.14 times impedance reduction, 97 electrode sample) respectively, demonstrating a significantly higher impedance reduction for platinum black (Fig. 40.2 d-e). We

plate with the lowest available current in the NanoZ (100 nA) for short times (4 s – 8 s) since higher currents and longer deposition times lead to an excessive growth of material without a significant impedance reduction (maximum Z reduction for Au: 18.9 ± 4.3; for Pt black: 96.3 ± 23.9) and often result in the shortcircuiting of adjacent electrodes.

We measured impedance variations in saline a few days after electroplating the pads assuming we have a similar situation when performing the experiment (i.e. we implant probes a few days after plating) and found that the impedance increases noticeably up to around 1 MΩ. From these probes, we measure the corresponding electrode noise in saline, which is within the range (5-16 µV) at 1 KHz frequency.

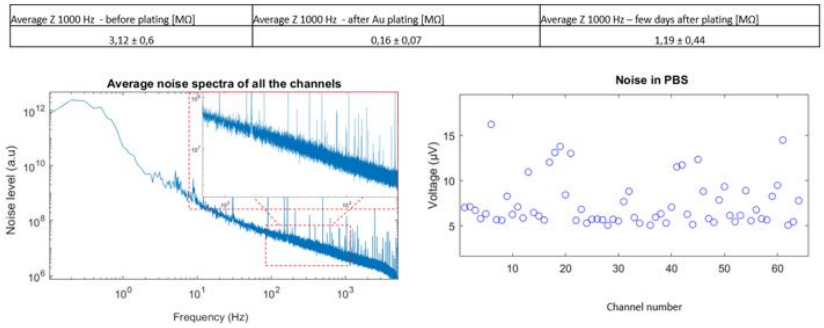

Figure 40.3: This depicts the electrode noise in saline solution after electroplating.

Photoelectric artifacts

Photoelectric artifacts are voltage artifacts measured on microelectrodes due to fast light onset/ offset. The photoelectric artifacts arise from the interaction of light with both the electrode and molecules surrounding the electrode. For example, light-induced photovoltaic effects can excite electrons in the microelectrode's conduction band, thus changing the double layer capacitance at the electrode-brain interface. Furthermore, light can interact with molecules in the brain and generate

electrical charges [82]. The microelectrode records these changes with an amplitude (>100 µV) and time duration (ms) comparable to neural waveforms. Since photoelectric artifacts arise in concurrence with light, they can be manually removed from post-processing analysis by merely discarding any time interval within ±1 ms around the laser onset/offset. However, these artifacts can be of great importance when performing fast (ms) optogenetic stimulation of neural activity since they may mask the real neurons' voltage signal. In our experiments (see Section 47), we perform 1-second prolonged stimuli, such that we can discard any photoelectric artifact and distinguish it from the optogenetic stimulation of opsins.

For our probes, we measure the photoelectric artifact and display it in Fig. 41.1, where we show a real neuron waveform (no light) in comparison to the photoinduced artifacts at different laser powers. We measure a very large (mV) but short (ms) signal, which we attribute to the fiber-waveguide junction's closeness to the bonding pads. Future probe designs for fast (ms) optogenetic experiments will minimize these artifacts by distancing the fiber-waveguide junction to the bonding pads and covering the latter in dark epoxy.

Integration of carbon nanomaterials on microsensors

We study the coating of carbon based nanomaterials on our microelectrodes to improve their biocompatibility and signal to noise ratio readout; specifically, we explore graphene on gold and carbon nano-onions on gold.

Graphene

Fabrication

We developed a wafer-scale process to integrate graphene on the microelectrodes

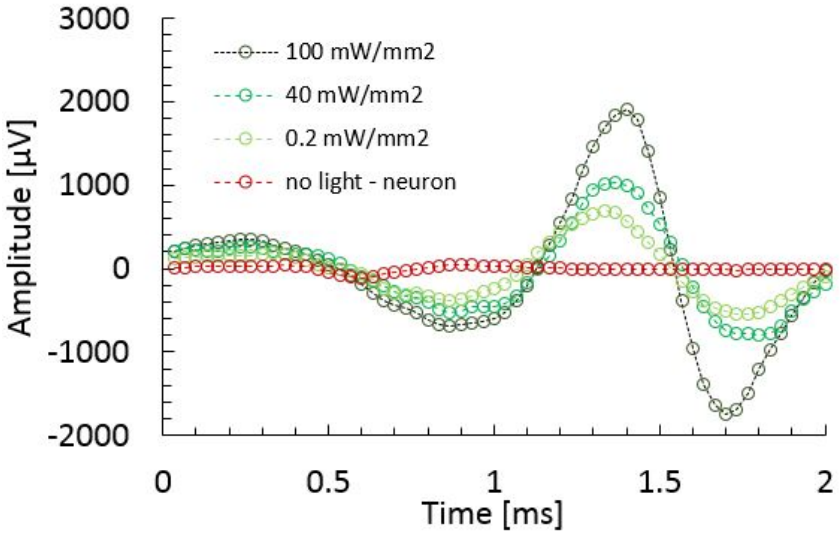

Figure 41.1: Comparison between neuron waveform and induced photoelectric artifacts.

by means of transfer process in solution. At the Molecular Foundry (on a Aixtron Black Magic CVD) and ChiLab (nanoCVD, Moorfield Nanotechnology, UK) monolayer graphene was grown on copper foils through the decomposition of methane at high temperatures (>900°C). After the growth on the copper foil, we verify the material quality and monolayer of graphene by Raman spectroscopy, which confirmed that the 2D peak (at 2700 cm^{-1}) is twice the height of the G peak (at 1585 cm^{-1}).

After spinning on the copper supporting PMMA C4 layer at 3000 rpm, 1000 rpm/s, 60s for mechanical support in solution, the graphene is transferred into a copper etchant solution, where the copper foil is etched. The PMMA-graphene stack is transferred to water and then scooped onto the wafer integrating passivated wires and exposed electrodes. After two hours of drying, in which the graphene adheres to our substrate, we remove the PMMA C4 layer by an acetone soak. Since the resulting graphene covers all of the wafer, this would short circuit the

non passivated electrodes (42.1 i, ii). To electrically insulate the electrodes, we remove a 1 µm wide frame of graphene from the electrodes by means of an electron beam exposure with ZEP 502 A (similar to the one for the electrode passivation layer opening) and oxygen etching in an RIE tool (2 min, 80 W, 100 sccm O_2) (42.1 iii). The ZEP layer is finally removed by a dichloromethane soak (30 m) (42.1 iv). As a result, we obtain microsensors at the wafer level coated with graphene.

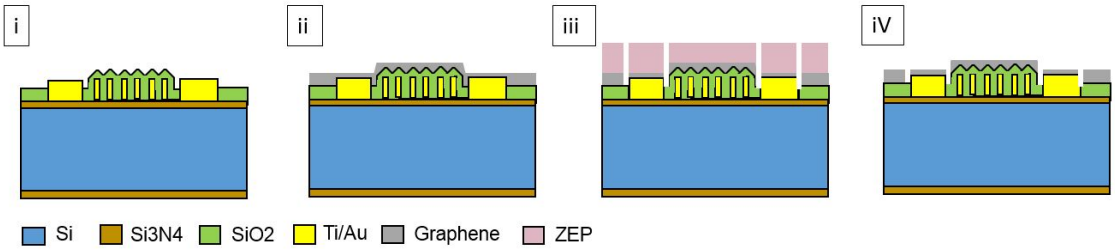

Figure 42.1: Schematic illustration of the fabrication process to integrate graphene on electrodes. (i): Starting wafer with arrays of electrodes and wires is covered by (ii) the deposition of a graphene foil (transferred from solution). The resulting electrodes are short circuited. We then (iii) expose the electrode's outer rim by means of an electron beam exposure and (iv) dry etch the graphene in the resist unmasked regions.

Measurement

Through this fabrication process, we manage to transfer graphene onto the microelectrodes and onto the whole probe at the wafer level. Once we transferred the graphene, we perform Raman measurements and SEM characterization on several electrodes to confirm its presence and material quality, as shown in Figure 42.2 a-d. We then analyzed its impedance and found a value of around 2.25 ± 0.6 MΩ. This is about half the impedance of the unplated gold (5.18 ± 0.87 MΩ) but may still be insufficient for high signal to noise ratio neural readout. The high electrode impedance is due to the high flatness of the graphene layer; several techniques to further decrease the impedance were also described in literature

contributions and involve either graphene doping, which reduces the impedance by a factor of two [76], or electroplating of metallic nanoparticles which decreases the graphene's impedance by one order of magnitude while preserving high transparency (transmission of around 80%) [77]. Furthermore, graphene can be used as channel material for field-effect transistors integrated on neural probes [78] and to map neural activity [79] [80].

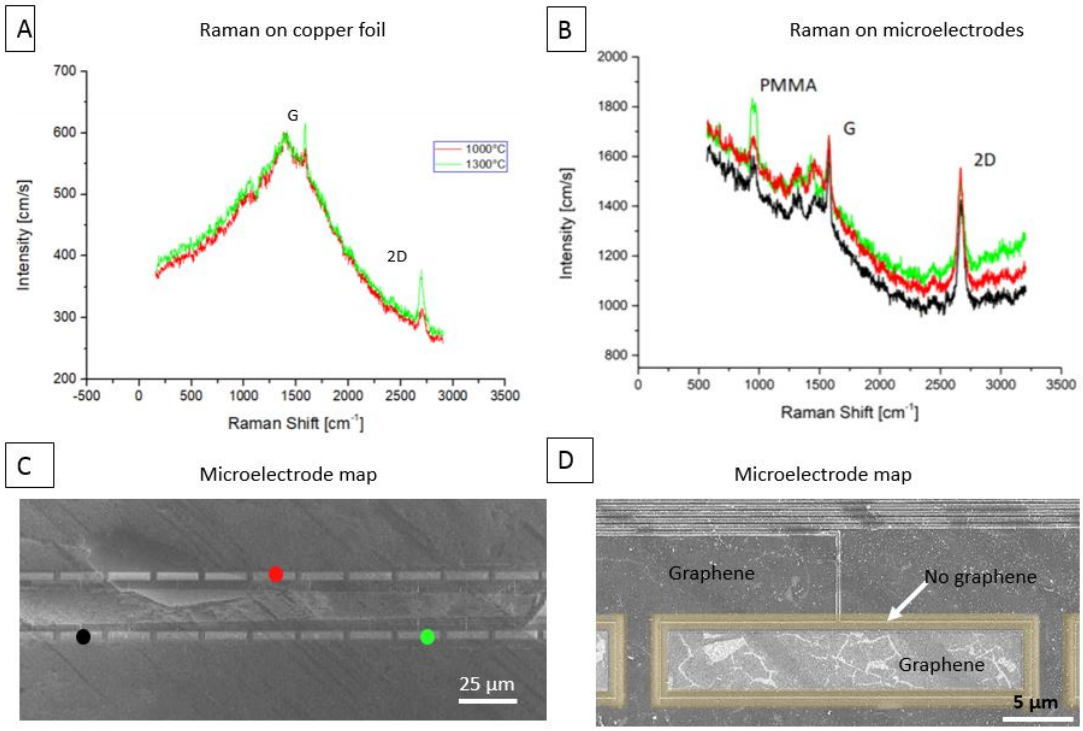

Figure 42.2: Characterization of graphene on microelectrodes. (a): the Raman spectra on copper foil, in which the 2D peak has double the size of the G peak, confirming that the graphene is monolayer, (b): Raman measurements on microelectrodes shown in the SEM figure in (c), and (d): SEM magnification, showing that the graphene layer coats both the electrode and passivated wires with the exception of a 1 µm-wide frame around the electrode.

Electrodeposition of active carbons and carbon nanoonions

Active carbon and carbon nano-onions were plated on 150 µm wide gold traces for supercapacitive applications in [48]. Here, we tried to apply these materials, which benefit both from their carbon composition that could result in high biocompatibility and from their high surface area to volume ratio that could benefit the signal to noise ratio readout of the microelectrode. We thus followed the procedure outlined in [48], in which we prepared a 95%-5% ethanol water colloidal solution with 0.3 wt % of activated carbons (and carbon nano-onions) and stabilized with 0.03 wt % of MgCl2 (since the Mg reacts with the OH2 to form Mg(OH)2 which acts as inorganic binder for the particles on the electrode.) The resulting solution had a conductivity = 38 µS/cm and pH of 6.3 at 19°C.

Active carbons

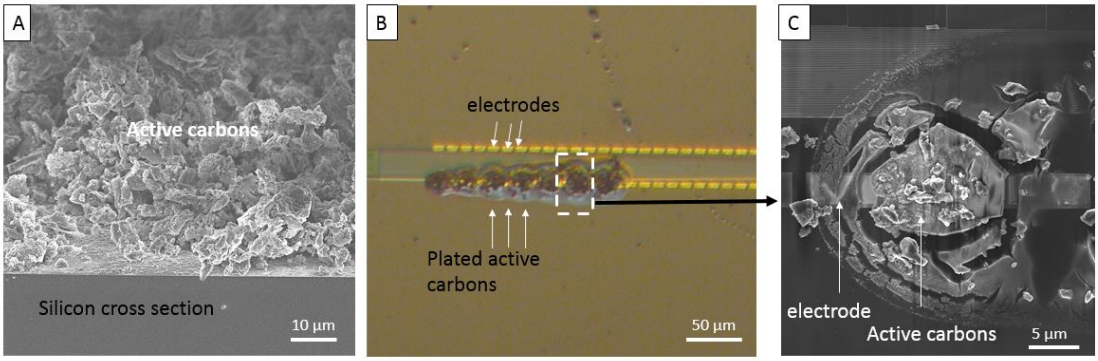

Figure 43.1: Electrodeposition of active carbons on microelectrodes.

We performed intial tests using the active carbon solution on 1 cm x 1 cm silicon substrates coated with Ti (10 nm) and gold (100 nm); for optimal results we use an input with a square shaped pulsed voltage, duty cycle of 70%, and frequency of 100 Hz for 30 to 60 s, resulting in a measured current of 2 mA (with distance

substrate-counter electrode ∼0.5 mm). However, as shown in the cross section SEM image in Figure 43.1 a, even the optimized deposition is not uniform, as indicated by the presence of many voids on the substrate. We then scaled the deposition to 75 µm x 75 µm electrodes and, for an input current of 10 µA with the same parameters described above, we had decreased the electrode impedance from 100 – 300 kΩ at 1 kHz to 30 – 60 kΩ at 1 kHz. However, the deposition on our probe's electrodes, which have dimensions of 5 µm x 25 µm and pitch of 27.5 µm, resulted in short circuits; this is likely due to the micrometric size of the active carbons . In addition, there was a high amount of residues outside of the electrode (Figure 43.1 b,c), which may be contamination from solution.

Carbon nanoonions

Since active carbon have size comparable to the electrodes, we test carbon nano onions, whose diameters are below 100 nm. We electroplate them by imposing a 4 V to 10 V negative voltage on the electrodes with respect to the counter electrode, with 1 s period and 50% duty cycle; during this operation, we monitor the electrical current. Initial plating tests are performed on round electrodes with 10 to 15 µm diameter and 30 µm pitch and show an effective deposition of the nanoonions onto the electrodes, as we show in Fig. 43.2. Once we obtain the plating of nanoonions, we test different combinations of current (controlled by voltage) and deposition time, as we show in Fig. 43.3. For high currents (tens of mA) we deposit a high amount of material and shortcircuit nearby electrodes even if we deposit for short times (10 seconds). We decrease the current to few hundred of µA and notice the deposition of large (µm) size particles onto the electrodes. We obtain the best result for lower currents (40 µA) and times between 15 s to 50 s and we can notice

a uniform deposition of nanoparticles onto the electrodes. Future tests will aim at testing the resulting electrode's impedance decrease.

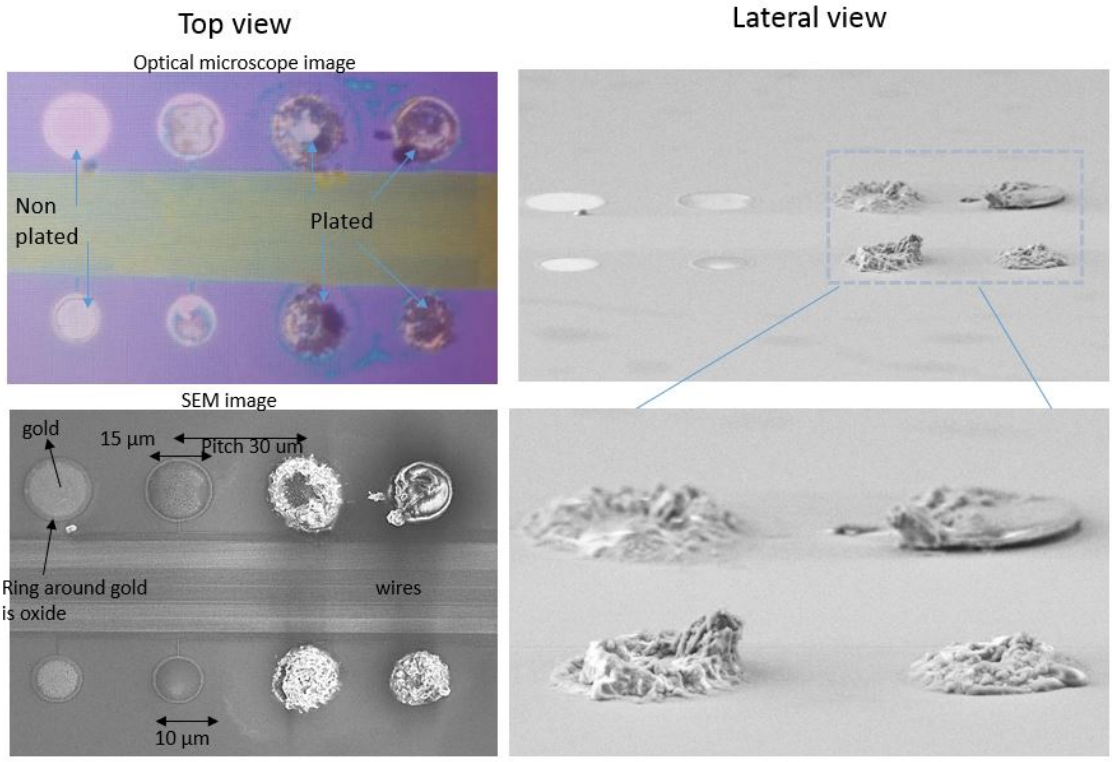

Figure 43.2: Electroplating of carbon nano onions on round shaped electrodes, top view optical microscope and SEM images, and lateral view SEM images.

Decreasing the probe invasiveness: ultrathin oxide tips

We aim at reducing the probe insertion damage by decreasing further the tip's cross section, defined as the lateral width times the thickness. In the previous sections we fabricated and validated neural probes with reduced lateral dimensions: 45 µm width, 20 µm thickness and a resulting cross section equal to 900 μm^2. We achieved such small values thanks to the three dimensional integration of small lateral footprint nanophotonic circuits and high-density wires. Starting from this

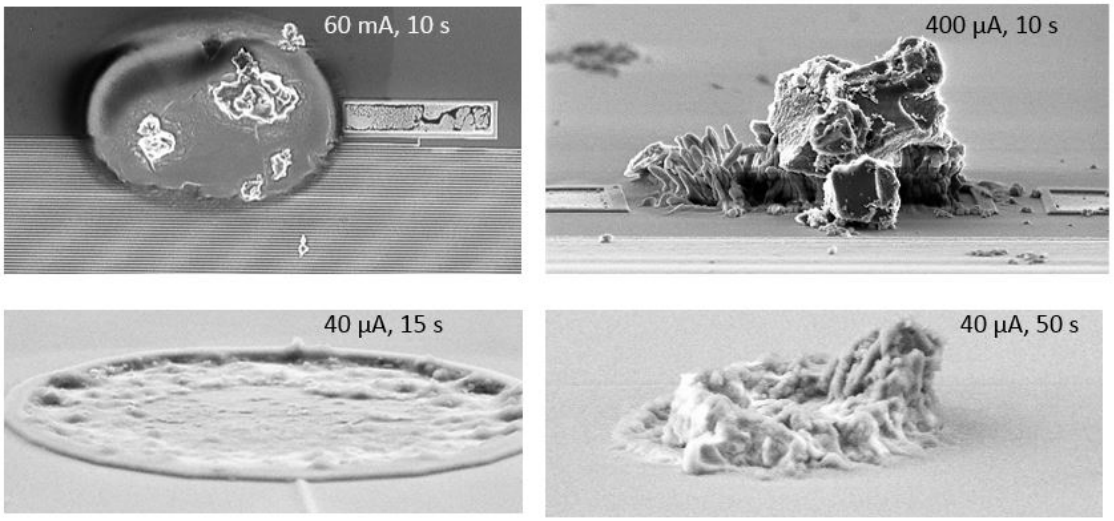

Figure 43.3: Deposition of carbon nano onions at different plating currents and times.

device, we decrease the probe thickness further by etching all of the silicon mechanical layer and leaving only the SiO_2-Si_3N_4-SiO_2 stack that embeds the nanophotonic and the electrical circuits and whose total thickness is 5.2 µm (cross section: 234 μm^2). By integrating the same nanophotonic and electrical circuits (6 light outputs, 64 electrodes) we obtain a cross sectional area coefficient (cross section divided by sum of sensors and stimulation sites, see 17, page 36) of 3.34, which is almost two orders of magnitude with respect to other state of the art optoelectrical devices and thus showing the probe's unique scalability as combination of high density of sensors and stimulation sites and small invasiveness. We develop a fabrication recipe which allows for removing the silicon only underneath the tip (the last mm) while leaving it in the interfacing and connecting areas (see 23, page 69), thus preserving the probe's mechanical backbone. This recipe uses similar fabrication processes described in the previous sections but with a different order; in brief, it consists in five main steps, schematized in (Fig. 44.1). We use the same substrate (Lionix TripleX) (i) on which we pattern, clad and planarize the nanophotonic circuits (ii)

and integrate the electrical ones (iii). Instead of defining the probe's shapes from the wafer's frontside, we etch the bulk silicon in KOH (while protecting the circuits with Protek) so to obtain circuits onto 25 µm thin membranes (iv). We then pattern the probes' shapes by first etching the SiO_2-Si_3N_4-SiO_2 stack and then by using an isotropic silicon etching step so to remove 25 µm of silicon underneath the probe's masked area and thus removing all of the silicon underneath the tip while leaving it underneath the connecting and interfacing areas, since they are laterally much wider. (v).

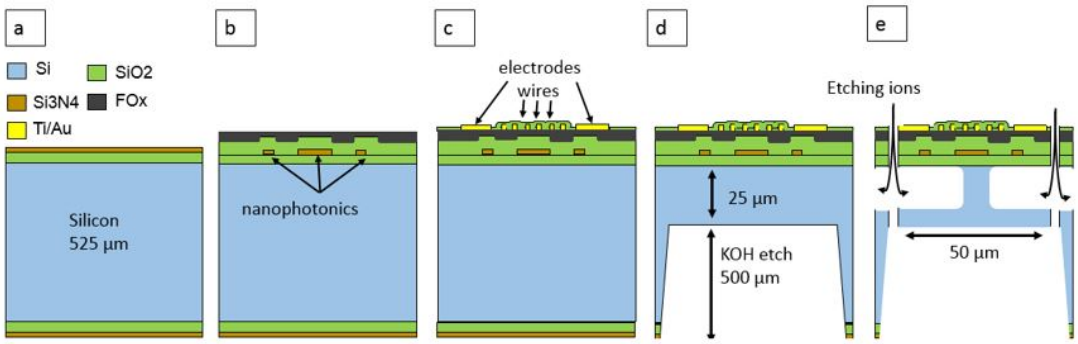

Figure 44.1: Fabrication schematics of the ultra thin neural probes.

We show the resulting devices, microscope magnifications showing the tip from a lateral and top view perspectives Fig. 44.2 and compared to a single mode optical fiber (with 125 µm of diameter). SEM comparisons with the 20 µm thick optoelectrical probe are shown in Fig. 44.2. We obtain tips which are mechanically stable but which tend to curl over time due to the residual compressive stress from the oxide layers. A careful balancing of all the stress could overcome such issue. We perform optical tests in air and obtain similar results to when we leave the silicon underneath the tip (as we expected, since the nanophotonic circuits are optically insulated by the cladding). Several literature works show minimally invasive polymeric probes but their insertion into the animal's brain requires the

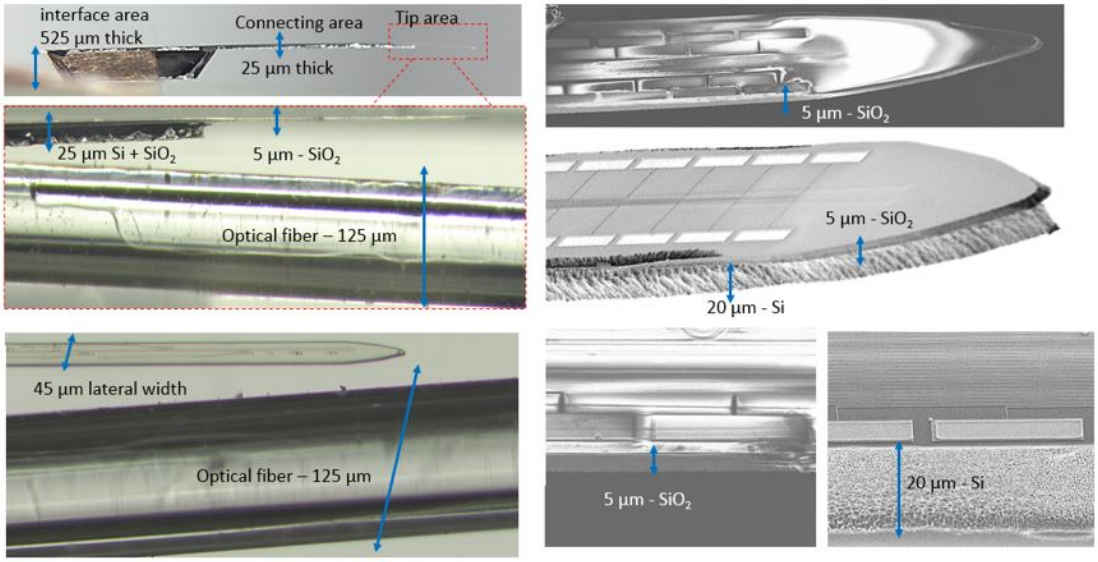

Figure 44.2: Fabricated ultra thin neural probes, where the silicon underneath the tip area is completely removed, leaving only the oxide and nitride layers.Top left: lateral view of the neural probe with lateral view and top view magnifications on the tip area, compared with an optical fiber. Right: SEM images for comparison between the silicon probe and the ultrathin one.

use of vessels due to their inability of sustaining high buckling forces during the dura mater's piercing [61]. We show that our ultrathin probes do not need any secondary carrier by performing a mechanical *in vivo* test and inserting the probe's tips through the craniotomy. We find that in two insertion out of three the tips pierce through the dura and remain intact upon extraction, thus validating the probe's capability of insertion into the brain.

In vivo validation

With the *in vivo* experiment, which consists of inserting the probe's tip in the mouse' barrel cortex to readout and manipulate neurons, we validate our neural probe capability of simultaneously readout neurons while stimulating the ones in the areas of interest.

Characterization of the optical stimulus

We characterize our laser model to have a well-defined optical stimulus during the *in vivo* experiments. We use a 450 nm wavelength-centered laser (model QFLD-450-10S, from QPhotonics) as a convenient proof-of-concept test of our probe. We connect the laser's output fiber to a splitter having one end (99% of the power) connected to our probe and the other end (1% of the power) connected to the spectrometer (AvaSpec-ULS2048) and power meter (Thorlabs PM 100). Specifically, we implement Matlab script to both extract the data and to adjust for the laser parameters in case any shifts are recorded during the *in vivo* experiment.

We described our laser's central wavelength (450 nm), Q factor (820), tunability range (3.21 nm) and temperature − wavelength characteristic in a previous chapter (see page 67). Here, we calibrate the laser's parameters to obtain power and wavelength temporal stability, particularly for on/off modulations, which are used to compare the optical stimulus's effect (and its absence) on the recorded neural activity.

We modulate the laser on and off by changing its input current from low to high levels; we choose a value of low current (corresponding to low laser output power) equal to 22 mA, which is close to the laser threshold's current (26 mA) and which avoids wavelength and power shifts during the laser on/off modulation

(see Fig. 45.1 b-d). We choose a high level current between 28 to 43 mA. Given our slow laser rise time (time to reach the maximum laser output power at a fixed current) of 40 ms, we choose a 1-s long pulse duration for our *in vivo* experiment. Once we fix the desired temperature and wavelength, we monitor their stability over several pulses; we record no shifts for times longer than 300s, which are more extended than each experiment's trial duration (where every trial corresponds to a well-defined temperature and output power). More reliable lasers with fast (ms) wavelength switching capabilities will be used in the future to allow for fast (ms) optogenetic stimulation.

Mouse preparation

We perform all of the *in vivo* experimentys in the Adesnik Lab at UC Berkeley on wild-type mice (CD-1, Charles River Laboratories) and following the regulations and guidelines of the Animal Care and Use Committee (Protocol AUP-2014-10-6832-1). Similar experiments were performed at Litke's Lab

The mice used in these experiments were wild type and underwent two surgical procedures in preparation for the *in vivo* optoelectrode tests. Briefly, in the first procedure mice were anesthetized using 2% isoflurane and head-fixed to a stereotax using proper aseptic technique. The scalp and the underlying fascia were removed to expose the dorsal part of the skull. Two small craniotomies were made using a dental drill, one over vibrissae primary somatosensory cortex (vS1) and the other over vibrissae motor cortex (vM1). A microinjector was used to inject 400uL of an adeno-associated virus (AAV), carrying a genetic payload that causes infected neurons to produce Cre-recombinase (Cre), into vS1. An additional injection of 400uL of a second AAV carrying a payload that causes neurons to express the

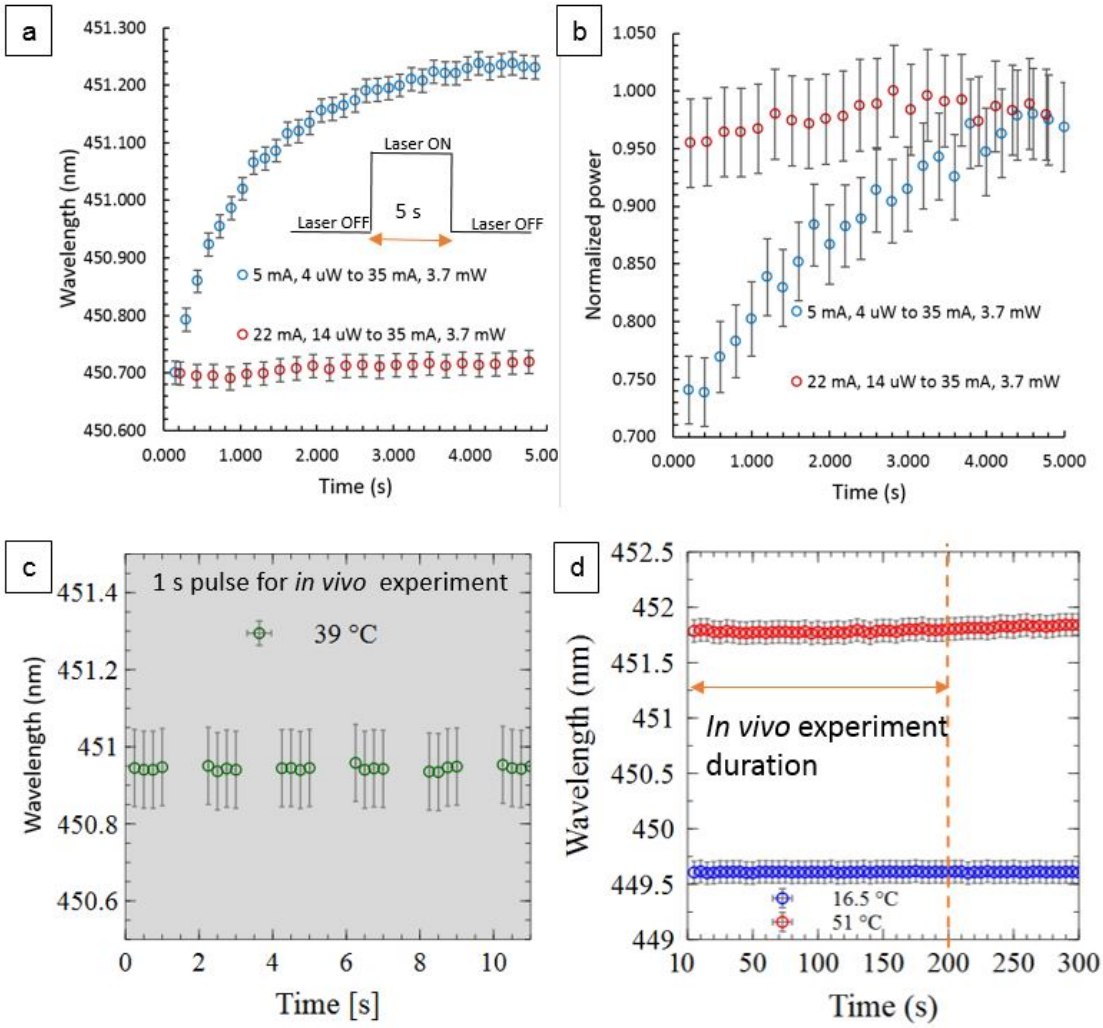

Figure 45.1: Use of a well-defined stimulus during the in vivo experiment.(a,b): We modulate the laser output power from low output to high output current. By using near-treshold current for the low power output we achieve both wavelength (a) and intensity (b) stability over high output current times. (c): We use 1-s long pulses as optical stimulation for the in vivo experiment. (d):During these pulses the Wavelength is stable for times longer than each in vivo trial duration (200 s).

excitatory ion channel Channelrhodopsin (ChR2) in neurons that also contain Cre was injected into vM1. These two brain regions share many reciprocal connections giving us a large target area to test the probes. Once the injections were complete the entire skull was covered in Vetbond (3M) to seal the wound margins and protect

the skull. A custom aluminum headplate was attached to the skull using dental acrylic (Metabond). The mice were then taken off isoflurane and allowed to recover. These mice were given a week to acclimatize to the new headplate as well as being head-fixed to the rotary treadmill where the experiments would take place. The second procedure was conducted on the day of the experiment. Here, previously injected and heaplated mice that showed good expression of the excitatory opsin were anesthetized using 2% isoflurane. A small dental drill was used to thin the skull over the region of the brightest expression. After thinning a 27g needle was used to lift a small flap of the skull to expose the brain. Mice were recovered from anesthesia and placed on the rotary treadmill in the electrophysiology rig.

Neural readout

In vivo readout experiments allow for validating the probe's capability of detecting neural signals and of assigning waveforms to different electrodes [110]. We connect the probe's PCB to a micromanipulator (Sensapex) and lower the tip 1000 µm inside the mouse's barrel cortex, assigned to whisker detection (3, 11, page 4, 16). Once the probe is inserted, neural recordings are performed with SpikeGadgets hardware and software at a sampling rate of 30 KHz; we show non-processed *in vivo* sensing data for one and multiple electrodes in Fig. 47.1 a. Neural action potentials are clearly detected with an amplitude of 500 µV – 1 mV, while noise levels are on the order of ∼200 µV (which are much higher than the ones detected in saline, ∼5 - 15 µV - see 39, page 133). We assign waveforms to particular neurons using the open source algorithm Klusta [110], which considers the electrode's positions to identify spike times associated with specific units (Fig. 47.1 b,c) and postprocess data with custom Python and Matlab programs [60].

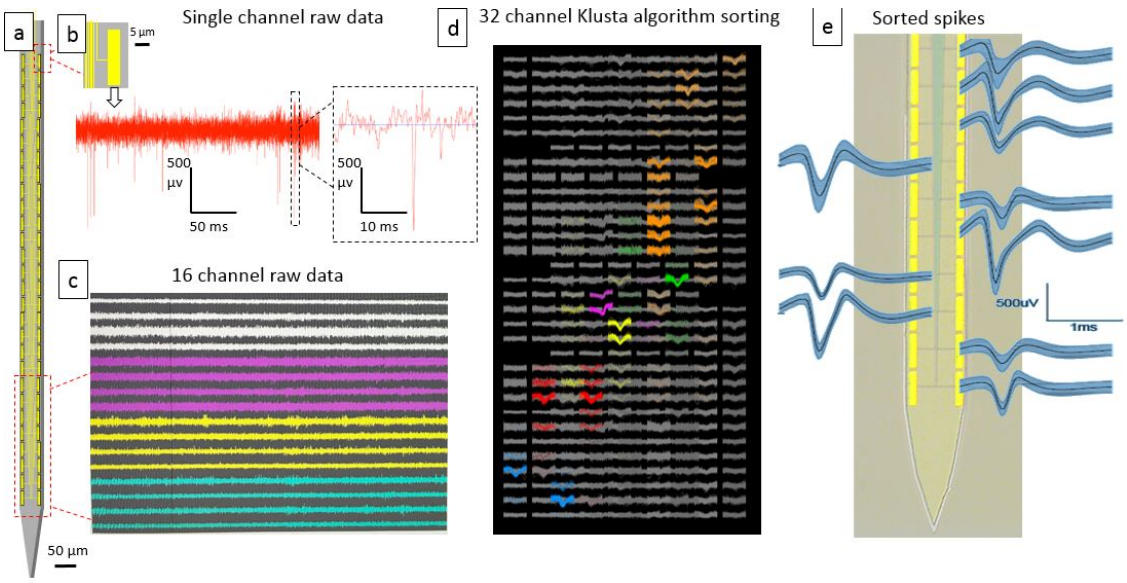

Figure 47.1: Neural readout experiment with probes integrating electrical circuits. (a): schematic of the neural probe, with (b) single electrode measurement and (c) 16-channel measurement. (d): neural spike sorting of 32 channels, showing the detection of single neurons (each one associated to a different color) across multiple electrodes. (e): microscope image of the probe tip with measured and spike sorted neural data; each waveform corresponds to a neuron and is assigned to the closest electrode.

During the *in vivo* measurements we stimulate neural activity with a bar, as we schematically show in Fig. 47.2 a, and measure a strong neural response from several units as we show in Fig. 47.2 b, which is a raster plot of 20 electrodes (with every point corresponding to a detected action potential). A response of a neuron to the bar stimulus in terms of firing rate (number of spikes per second) is shown in Fig. 47.2 c. Finally, we qualitatively compare the response of a neuron unit to the bar position (blue trace), superimposed to an example neural trace plotted in [103].

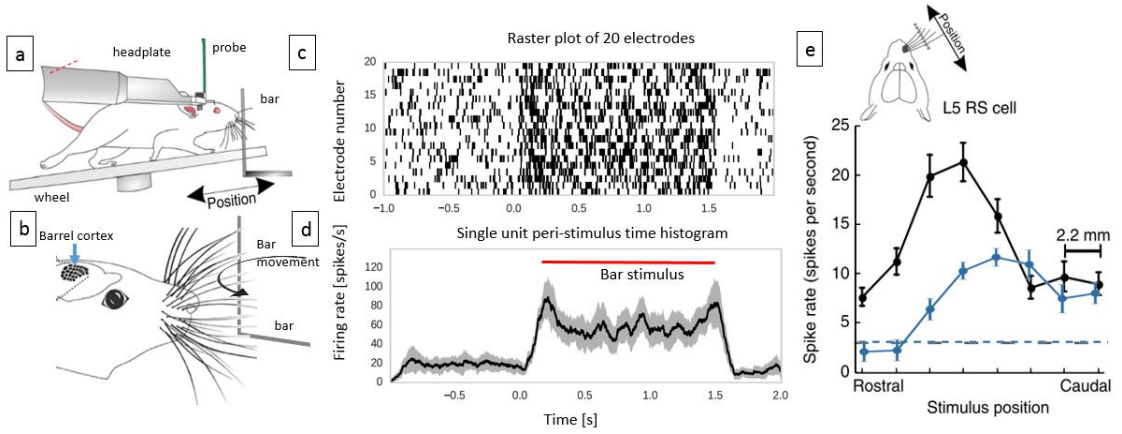

Figure 47.2: Neural readout experiment with 64 electrode probe. (a): experiment setup schematic: the mouse is head fixed and the probe is inserted in the Vibrissae somatosensory cortex area (readapted from [103] [6]). (c): peristimulus histogram of 20 electrodes and (d) single unit peristimulus histogram. (e): single unit spike rate for different bar positions (blue trace), showing its similarity to the one recorded in [103].

Simultaneous manipulation of neurons of interest and readout

Next, we perform a preliminary in vivo test to demonstrate the probe's proof-of-concept, which is to verify that we can simultaneously read neural activity across the entire tip and optically stimulate neurons in selected vertical areas of interest. We select specific areas of interest by choosing specific output grating(s) and matching the input laser wavelength to the corresponding ring's resonance. A mouse that had been previously implanted with a headplate and that showed good viral expression of the light-sensitive opsin ChR2 was selected for the in vivo characterization experiment. Cells expressing ChR2 simultaneously expressed TdTomato, a red fluorophore, allowing us to easily target the region with the brightest expression as our recording area. We recorded from the vibrissae Somatosensory cortex as our

desired recording area and inserted the probe through a small (< 200 µm) craniotomy, lowered it to 1000 µm into the brain, and let the electrode settle for five minutes before beginning our experiment. Throughout the experiment, we record neural activity simultaneously across multiple electrodes from which we identify and distinguish individual units (presumptive neurons) as well as estimate their vertical positions along the probe (using data post-processing algorithms [110]).

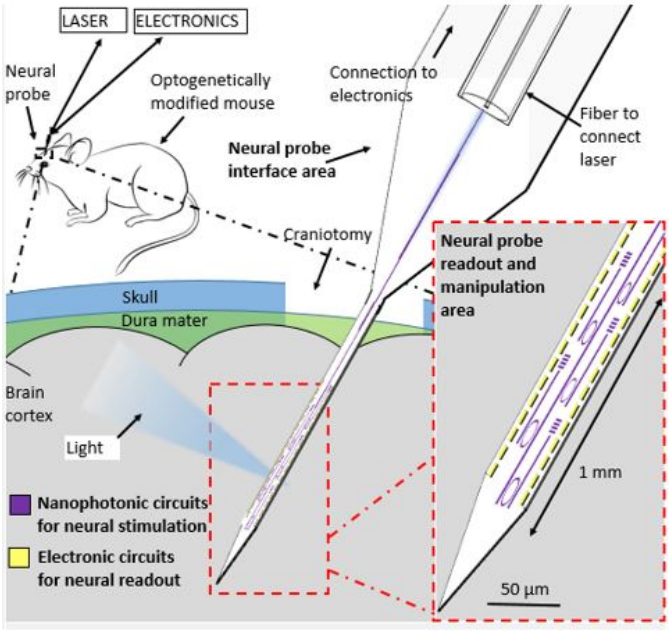

Figure 48.1: Schematic of the optoelectrode implantation in the mouse Somatosensory cortex. After connecting the probe's PCB to the external laser and electronics, we insert the tip inside the mouse cortex and simultaneously record and optogenetically stimulate neural activity.

Specifically, we divide the experiment into 14 blocks, each composed of 100 trials that are two seconds long, in which the laser is turned off for one second and on the next second. We grouped the blocks into subgroups, each corresponding to a fixed laser temperature/wavelength and corresponding to one of the output gratings. By selecting a fixed laser temperature and short experiment duration (200 s), we ensured our laser's wavelength's stability (see page 147). However,

our nanophotonic design can be used for fast (ms) stimulation experiments since ring resonators operate at sub-µs timescales [77]. This requires the use of a more reliable and fast switching tunable laser (such as, for example, the one described in [117]) to enable long-term recordings and/or fast (ms) optogenetic stimulation. We begin our experiments by sending light with increasing power. We choose a different input power for each block in a subgroup, spanning over 3 orders of magnitude. The grating's output power changes accordingly, from 0.2mW/mm^2 to 100mW/mm^2. Within each subgroup, we observe that increasing the laser input power increases the neurons' firing rates (number of action potentials over time, Fig. 6a,b). Importantly, we notice that the firing rates increase when the light output of a specific grating is above a critical threshold. Specifically, we observe neural activity excitation for a laser input value of 0.5 mW, corresponding to a grating output power of ∼0.28 µW and a power density of approximately 5.7 mW/mm^2.

We compare and report in Figure 6c the mean waveforms of the same neuron of Fig. 6a,b before and after the laser pulse (1 s time) and at each reported power densities. The waveform's amplitude does not change as a function of light power, as indicated by the small standard deviation; this shows that the detected neurons' firing rate increases due to the optical stimulation of ChR2 rather than due to photoelectric artifacts. Next, we investigate whether we can modulate the units' firing rates by selecting different gratings. As shown in Figure 6d-g, by selecting different optical gratings, we cause the units' firing rates to change dramatically; the units increase or decrease their rate likely as a function of their relative spatial position around the probe. Specifically, in Figure 6d, we report two neurons' firing rates, one close to the activated grating (neuron near grating 1) and one positioned far from the grating (neuron near grating 4). The traces are calculated from the raster plots

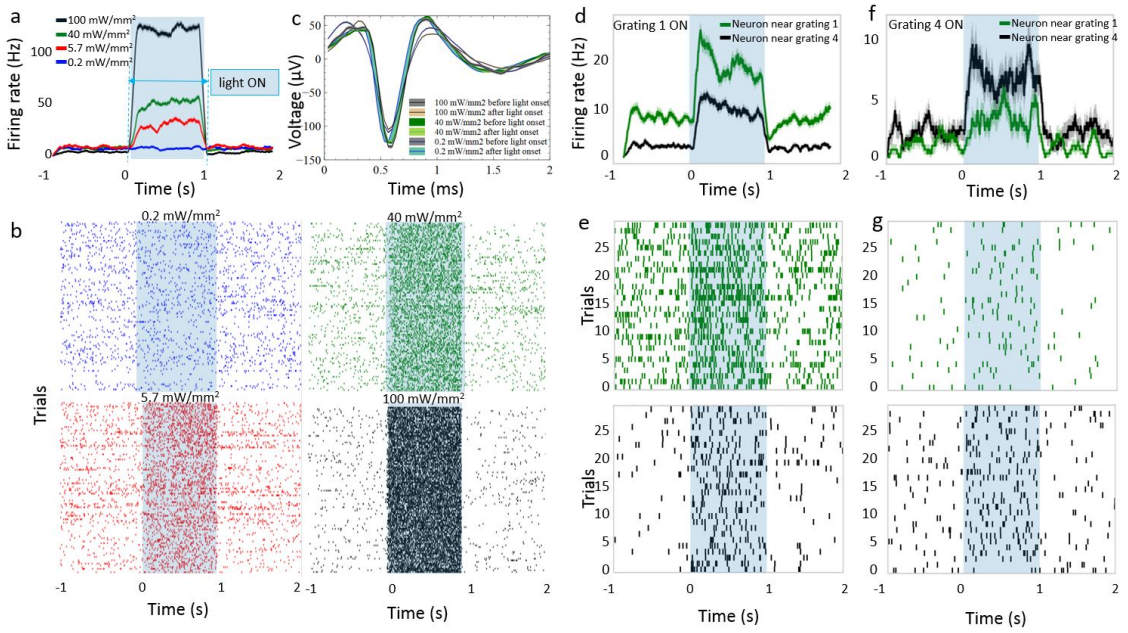

Figure 48.2: Preliminary results of the in vivo recording and simultaneous optogenetic excitation experiment performed in a mouse expressing the ChR2 opsin. (a): firing rate of a neuron before, during, and after light excitation at different intensities and (b) corresponding raster plots. The firing rate increases proportionally for intensities around 5.7 mW/mm^2 (n=50 trials, mean +/- sem). (c) Mean waveforms of the neuron of Fig. 6a,b before and after light onset and for different grating output intensities, showing no changes in the waveform amplitude or shape. (d-f) Excitation of neurons in different spatial locations based on the activated light output grating. Firing rates of two units (d,f) and corresponding raster plots (e,g) when either grating 1 or grating 4 is on (n=30 trials, mean +/- sem).

in Figure 6e and show a stronger activation of the neuron close to the activated grating (grating 1). By comparison, the opposite effect is recorded when grating 4 is activated (Figure 6f,g), in which only the neuron close to grating 4 is activated while the neuron close to grating 1 remains unaffected. While these in vivo tests are only preliminary measurements, we confirm the ring's proof of concept capability to activate only neighboring neurons and, therefore, our strategy to achieve passive and selective neural activity stimulation with low footprint optoelectrodes.

Conclusions

In this thesis, we discussed the integration of nanotechnologies in micrometric-size invasive neural devices to increase neural recording and stimulation capabilities. In this particular section, we describe the achieved advancements and frame their current and future scopes.

Summary of results

Neural probes integrating micrometric sensors and stimulation sites have been studied extensively in the literature and were used to both record and stimulate *in vivo* neural activity. Despite their rapid progress in the last few decades, they have reached scalability and functionality bottlenecks that are inherent to the micrometric sized technologies they integrate.

Scalability concerns both the tip dimensions, which should be minimized to reduce the tissue damage, and the number of sensors and stimulation sites, which should be increased to maximize the number of measured and stimulated neurons.

By functionality, we mean both the capability of providing different *in vivo* interrogation modalities − such as both the readout and manipulation of neural activity − and the ability to deliver light of different colors at desired locations without generating heat to manipulate the desired neurons. By the integration of nanotechnologies in the form of nanocircuits, nanofabrication, and nanomaterials, we overcame these technological challenges, as we describe in the following sections.

Low footprint, passive nanophotonics for light delivery in brain tissue

The first example of nanotechnologies is the integration of nanophotonics embedding ring resonators, which allow for the stimulation of neurons of interest by illuminating the desired areas around the device tip, thus overcoming the constraints associated with other technologies − such as LEDs − that are not easily scalable, bulky, and generate heat. Our approach integrates, along a bus waveguide, ring resonators that act as passive optical switches to enable light location selection (Fig. 47.2 a,b) within a single opsin absorption spectra. We select the desired output gratings along the probe's tip by fine-tuning the external laser's wavelength, thus overcoming any need of electrical currents flowing through the nanophotonic circuit which would result in heat generation. By avoiding a significant heat generation, neuroscience experiments are not limited to short (ms) pulse durations [135] [122].

In comparison with other passive nanophotonic approaches that were developed over the last few years, such as the use of arrayed waveguide gratings [117] or electro-optic switches [83], our strategy benefits from increased scalability, − allowing for the placement of several dozens of optical switches in the probe tip −, since it requires only one input waveguide for multiple outputs (conversely, the other approaches require one waveguide for each output, limiting their total number). Our nanophotonics thus result in a lateral footprint smaller than 20 μm, without any increase in the lateral dimensions as more rings and output sites are added. This is of paramount importance towards the integration of dozens of light outputs in neural probes, which could allow for manipulating independently a corresponding number of neurons. We describe our nanophotonics' scalability to dozens of rings in page 163. On the other hand, our devices are limited to the use in head-fixed animals or caged animals since our nanophotonic circuits require a fiber connection

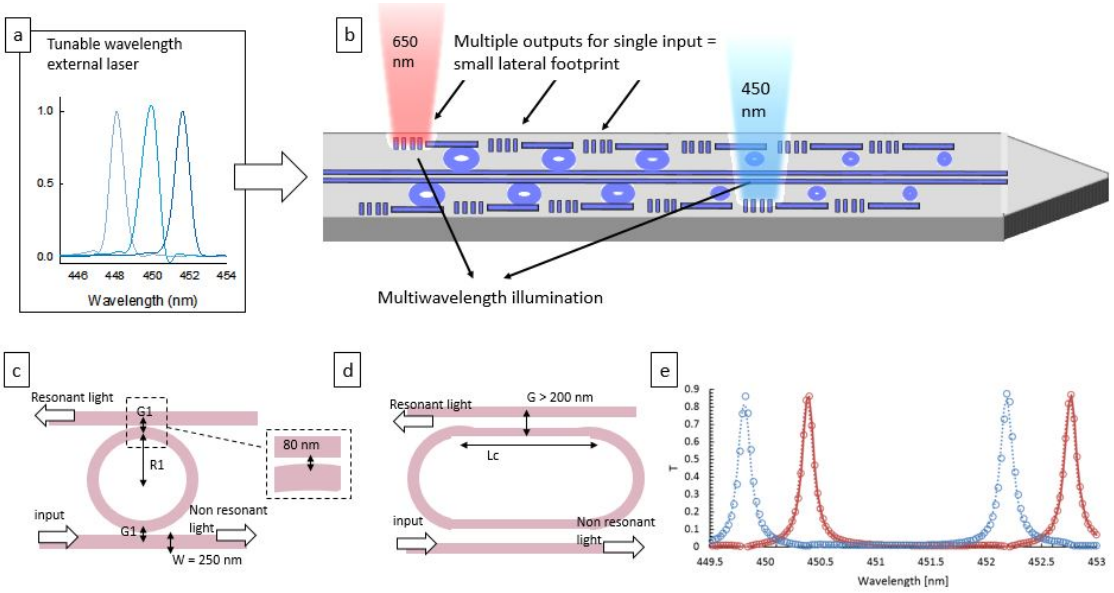

Figure 49.1: Schematic of the nanophotonic circuits and some of its components. (a,b): the light output location is based on the matching of the external laser's wavelength to the desired ring resonator. The nanophotonic circuit requires only one bus waveguide for multiple outputs, which can thus be integrated into high numbers. (c-e): ring resonator future design for fabrication with high throughput lithography. (c): a regular ring resonator, as explained in previous chapters; (d): a racetrack ring resonator, which has a wider gap and with (e): similar lateral footprint and optical performance to the ring of (c).

with a laser. Ideally, a narrow-band (0.3−1 nm) and widely tunable (10−20 nm) laser laser woul de be used, however in this study we used a small laser diode as an initial, quick, and inexpensive proof of concept. Our diode is limited in tunability range (3.4 nm) − and thus, limits the number of light outputs in our probe −, temporal switching (40 ms), and stability over time, which limit the experiment pulse duration above tens of ms. To overcome this issue, supercontinuum lasers properly filtered in wavelength (see for example [117]) will be used in future studies. Furthermore, it is worth noting that the electrode-optic switch technology presented in [83] could be integrated together with our system. For example, each electro-optic switch output could correspond to a different tip in a multi-shank probe;

within each tip and along each electro-optic switch output waveguide, several rings would allow then to choose the precise light output location.

Finally, another example of nanofabrication applied to neural probes is the development of light-focusing output gratings at the end side of the ring resonators. These gratings consist of chirped nanogrooves that focus the light in brain tissue – so to either illuminate single neurons, or to spread it more efficiently. We validated their functionality *in vitro* and for multiple wavelengths (blue, green and red) but future *in vivo* experiment will validate their use.

Low footprint, passive nanophotonics for multicolor illumination

One goal of neuroscience is to define the role of specific neuron types inside neural circuits. Different neuron types can be excite by distinct opsins in the brain, such as the blue-activated Chronos and the red-activated Chrimson [57]. However, light delivery of different colors inside brain tissue is not a straightforward task; in particular, the delivery in the location(s) of interest along a probe and for different wavelengths pertaining to distinct opsins is unachieved. Here, we overcome this technological challenge by integrating directional couplers into our nanophotonic circuit, and rings specifically optimized for each coupler's output waveguide.
By tuning both the external red and blue lasers' wavelengths, we choose the output location of light for both colors. Importantly, these additional elements do not require a significant increase in the tip's lateral space, since they are <35 μm wide. Furthermore, the number of distinct colors can be increased by integrating in series several couplers; this could be of significant importance in case in the future opsins with narrow-band absorption spectra are engineered [57]. The *in vivo* applications of this design will allow us to manipulate the desired neuron types in the

locations of interest along the probe tip simultaneous to the neural network readout.

Electrical circuits

We applied nanofabrication techniques such as electron beam lithography to achieve a high density array of sensors for increased detection of the number of neurons. In comparison with other optoelectrodes, we achieved a much higher number of recording sites (64) by fabricating thin interconnections (120 nm width, 450 nm pitch) with electron beam lithpography and by integrating these circuits in a three-dimensional stacking (we placed the arrays of sensors and wires above the nanophotonics). This type of stacking allowed for maximizing the number of components of both the electrical and nanophotonic circuits in the given tip space. With respect to the electrodes, as we described in page 22, their smallest dimension is limited to few microns per size due to the increase of the signal to noise ratio as a function of the electrode are decrease; we thus designed 5 X 25 μm wide electrodes, which are compatible both with neural readout (page 150) and minimization of their footprint. Future studies will minimize the photoelectric effect, which is the generation of an artifact current in arising from the interaction of light with the electrode; such artifact precludes the readout of neural waveforms in the first milliseconds after the light is turned on, thus preventing the use of our device to fats (ms) optogenetic experiments. The reduction of the photoelectric artifact is mainly a matter of electrode design optimization.

Carbon based nanomaterials Another example of integration of nanotechnologies for microprobes concerns the integration of carbon-based nanomaterials on the

metal electrodes' surfaces to increase their signal to noise ratio during neural activity readout and biocompatibility. Graphene is biocompatible, transparent and has a high electrical conductivity. We developed a process for the wafer-level integration of graphene on gold microelectrodes and decreased its impedance (which is inversely proportional to the signal to noise ratio) by a factor of two. Although the electrode impedance remains high due to its atomic flatness, techniques were developed in the literature to decrease it (see page 137); ultimately graphene was used in other literature studies as a field-effect transistor channel for measuring neural activity.

We then analysed the electrodeposition of active carbons and carbon nano onions, since these materials have a high surface to volume ratio, which could further decrease electrode impedance. Their electrodeposition in 150 μm wide traces for supercapacitive applications was developed in [98]; here we deposited both materials on 5 X 25 μm wide electrodes with 2.5 μm spacing. From this ongoing work, we were able to assess that active carbons (having particles with 2-5 μm average size) are too wide for our electrode dimensions (thus shortcircuiting them). Carbon nano onions, with their smaller sizes (<100 nm), were then effectively deposited onto the neural probes electrodes with different current and time deposition conditions.

Reducing the tip dimensions

A final example of the work we developed was an effort to further decrease the tip cross-section dimensions by drastically reducing the tip's thickness. We developed a wafer-level fabrication process to completely remove the silicon underneath the tip's area, resulting in a 5μm thick tip made of oxide and nitride and embedding the nanophotonic and electrical circuits. Such a process retains all of the nanophotonic

and electrical components, resulting in a high density and a cross-sectional area [63] (the device cross-section divided by the sum of sensors and stimulation sites) of around 3, which is two orders of magnitude smaller than the state of the art optoelectrodes. In comparison with other ultrathin probes, our device does not need a carrier during insertion, as we validated by insertion through the mice's dura mater. On the other hand, it does not provide the flexibility and low Young's modulus of polymeric probes, which are incompatible with high-quality optical materials required for our nanophotonic circuit.

Future optimization

Although we achieved several advancements in the neurotechnology field, some more detailed analysis is required to extensively validate our technologies.
First, some additional fabrication optimization is required to increase the fabrication throughput.
Second, the scaling of nanophotonic circuits to dozens of light outputs requires some design optimization and further validation.
Third, the validation of carbon-based materials must be studied more in detail, both from a scalability point of view (how small an area they can be deposited onto) and from the material properties (i.e. impedance, biocompatibility, mechanical adhesion to the electrode, signal to noise ratio...).
In the following paragraphs, we detail these future improvements.

Increasing the fabrication throughput

The fabrication throughput is mainly limited by the use of the four electron

beam lithography steps for the exposure of alignment marks, nanophotonic circuits, arrays of electrodes and wires, and electrode passivation opening.

All of these processes could be replaced by higher throughput lithography techniques: alignment marks and electrode passivation openings could be defined by standard optical lithography. Electrodes and wires could be exposed by 193 nm lithography by slightly enlarging the wires in the device tip. The most challenging exposure in terms of resolution is the nanophotonic circuits' one since rings were designed with a gap of 80 nm (see Fig. 47.2 c). By changing the design of the ring to a racetrack resonator [10], where the coupling region consists of a straight waveguide, gaps of up to a few hundred nm, which are compatible with other lithographic techniques, can be achieved. The lateral footprint and the optical performance of this design is similar to the rings without the straight coupling section, as we show in Fig. 47.2 d,e.

Another low throughput step is the backside bulk silicon etching, which at the moment is performed with a combination of wet and dry etching, and which could be replaced by a deep reactive ion etching process, as used in several other works [117][63][83].

Scaling of nanophotonics to dozens of sources

Increasing the number of independently addressable outputs on the probe's tip may be beneficial to either increase their density in a given area, or to have several sources along long tips (i.e. 10 mm long tips would require 100 light sources to have an illumination point every 100 um). A high number of light sources is incompatible both with microLED technology due to scalability limits and with other nanophotonic approaches (since they require one waveguide for every output).

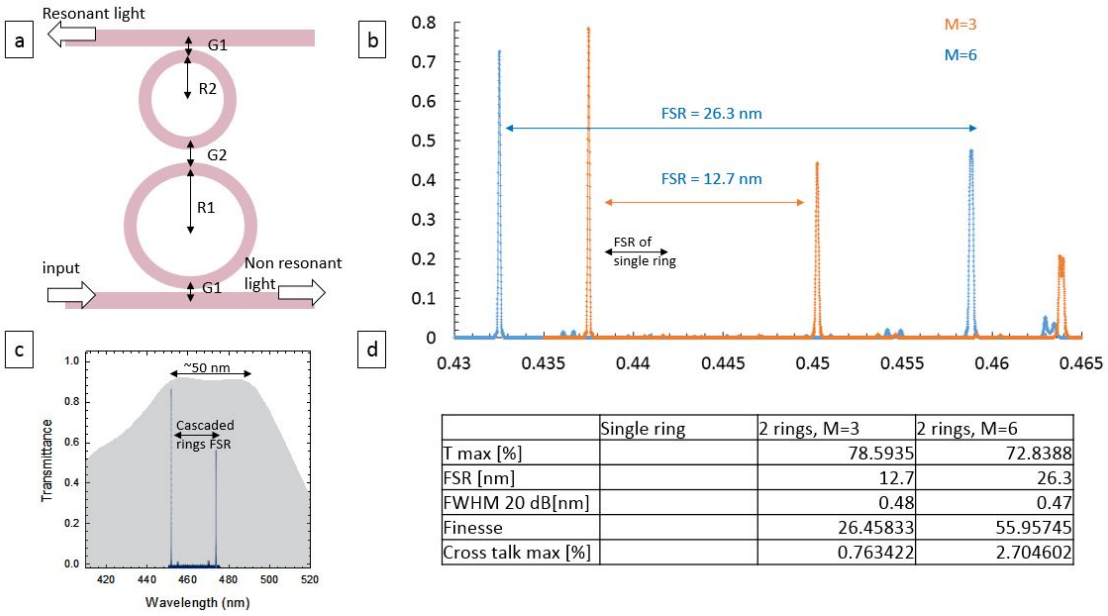

	Single ring	2 rings, M=3	2 rings, M=6
T max [%]		78.5935	72.8388
FSR [nm]		12.7	26.3
FWHM 20 dB[nm]		0.48	0.47
Finesse		26.45833	55.95745
Cross talk max [%]		0.763422	2.704602

Figure 50.1: Nanophotonics for dozens of light sources. (a): Cascaded ring resonators that use the Vernier effect to extend the ring FSR. (b): the extended FSR still lies in the maximum of absorption of the opsin ChR2. (c): 2D FDTD simulations of cascaded rings with M=3 and M=6 and comparison with single ring spectra. (d): table of extracted parameters, showing that cascaded rings can accomodate > 50 channels, minimum cross talk (<3%) and high transmission (>80%).

Our technology, thanks to the need of only one bus waveguide for multiple outputs, could be used to this end. At the moment, we designed four independently addressable light outputs, since we are limited both by our laser characteristics and by our ring resonator design.

Our laser's tunability range is 3.4 nm and the FWHM is 0.55 nm; by using a widely tunable laser (and filtering its bandwidth with an bandpass filter [117]) we could achieve a source tunability range > 50 nm and a FWHM below 1 nm, thus increasing the number of separate wavelength the laser can access.

Our ring resonator design is also limited by trade-offs between the maximum FSR (which increases by decreasing the ring radius) and the ring transmission. At the wavelength of 450 nm, curvature losses increase dramatically for ring radii below

2.8 um, and the resulting FSR is around 6 nm. Thus our current nanophotonic configuration can host a maximum of around 10 different rings having separate resonances within their FSR. However, as for the limits on the laser, we can design the rings to expand their FSR. To achieve this, we exploit the Vernier effect by series-coupling multiple rings (see Fig. 50.1 a) [9]. We start with the initial single ring, having radius R1, FSR1 and gap G1, and we extend its FSR by a factor M, which is arbitrarily chosen. Then we design the second ring by setting $M2 = M1 - 1$ and its cavity length $L2 = M1 * L1/L2$, such that it suppresses the interstitial peaks and double-peak resonances.

For example, by starting with a ring with fixed width (W=200 nm), G1=80 nm and R=3.75 μm, and resulting in a FSR1=4.23 nm, we can obtain FSR2 equal to 12.7 nm or 26.3 nm by choosing M1=3 or M1=6 and by setting R2=R1+1 um or 0.5 μm, respectively. The gap between the rings (G2=190 nm) should be designed to achieve critical coupling.

Figure 50.1 b shows three dimensional FDTD simulations of the wider FSRs, which still lies within the maximum absorption of the opsin ChR2, which is around 50 nm wide. Fig. 50.1 c,d shows an example of simulation of series-coupled resonators having a wide FSR (>20 nm), high transmission (>80%) and small interstitial peak values (<3%). Given the wide FSR of the cascaded ring, and by choosing a widely tunable and narrowband laser, a high number of channels (>50) can be achieved, as we show in Fig. 50.1 d.

Validation of carbon-based nanomaterials

Future work on the impedance decrease of carbon nano onions must be carried,

as well as test on the mechanical adhesion to the electrode and *in vivo* biocompatibility must be analysed.

Device applications for neuroscience experiments

The advancements reported in this thesis - and concerning the integration of nanocircuits and nanomaterials in micrometric neural probes - push the technological boundaries towards their scalability (in terms of implant size reduction, sensor and stimulation site numbers) and functionality (in terms of the optical excitation and/or inhibition of desired neurons with high speed and negligible tissue heating).

By the use of these devices, we expect to achieve an accurate neural network readout and control, by enabling an *in vivo* readout of a large number of neurons combined with the individual or simultaneous silencing or excitation of the desired neuron types in the desired locations. These future studies will thus aim at retrieving highly detailed information on the functioning of neurons inside networks for short term ($<$ 1 week) *in vivo* experiments. Long recordings (>weeks) are not explored in this thesis since we did not focus on the long term device biocompatibility.

A first experiment example is the inference of the cortical layers' function by detecting the signal propagation across the network and by selectively exciting or inhibiting desired layers. Similarly, the function of different neuron types can be interrogated by assigning different opsins to different neuron types and by exciting each with a color. Third, the previous experiments could be combined to selectively excite specific neuron types in desired cortical layers. Besides, these trials could be performed in behaving animals to detect associated behavioral changes. Furthermore, for future experiments, we will couple our neural probe to a high-speed

wavelength-tunable laser to study fast (ms) *in vivo* neural networks' dynamics. Apart from a high-resolution network interrogation, future experiments will allow us to validate the light spatial resolution (how close we can place light output gratings without them activating the same neurons), the capabilities of focusing gratings, and the carbon-based nanomaterial benefits.

Conclusions

In conclusion, we studied the integration of nanotechnologies in neural probes, which are invasive microdevices used to analyze *in vivo* neural networks. Probes have micrometric dimensions and were extensively studied and used in the last decades to read and manipulate neural activity using microsensors and micro stimulation sites (microwaveguides or micro light emitting diodes). Here, by the integration of nanophotonic circuits, nanofabrication techniques, and the use of nanomaterials, we pushed the technological boundaries to drastically scale these devices and increase their functionalities, towards a high-resolution study of neural networks *in vivo* (Fig. 51.1).

For example, a high-resolution manipulation of neurons inside a network requires the illumination of several selectable areas along the device, the integration of multiple sources to stimulate a high number of different cells, and the use of multiple wavelengths (i.e. blue 450 nm and red 650 nm) to simultaneously excite and/or inhibit the neurons or to manipulate desired types of neurons.

For the first time, we developed passive nanophotonic circuits that allow on-demand light delivery for multiple wavelengths and a high number of independently addressable outputs. We achieve this with the use of ring resonators as a strategy to locate light in the area of interest, and with the use of directional couplers to independently

assign wavelengths pertaining to the absorption of different opsins. We select the desired light output location and color by tuning the external laser's wavelength, thus avoiding any heat generation associated with the flowing of currents. Besides, our nanophotonics have a small lateral footprint, which, in contrast to other reported solutions, does not increase as a function of the number of output channels. We validated both *in vitro* and *in vivo* our photonics' capabilities to stimulate the neurons in the area of interest for a single color (blue wavelengths). Future experiments will use multiple colors (red and blue wavelengths) to stimulate distinct neuron types.

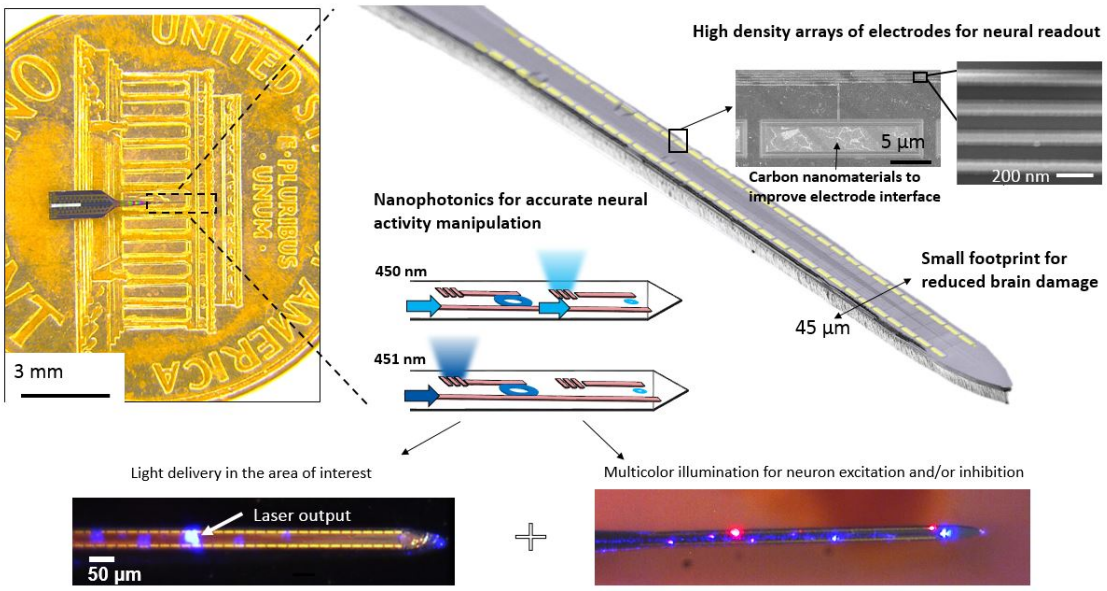

Figure 51.1: Project results, showing the successful integration of nanotechnologies in microprobes in the form of nanophotonics and low footprint interconnects and arrays of electrodes. (Left): device on a one-cent coin; Center: false-color SEM image of the insertion part of the device highlights its small width and thickness dimensions. (Top right): integration of carbon-based nanomaterials on microelectrodes. (Bottom): concept of the nanophotonic circuits to deliver light in the color and area of interest to excite or inhibit the desired neurons.

We made use of nanofabrication techniques (such as electron beam lithography) to integrate a massive numbers of sensors, so to detect several dozens of distinct

neurons. Optoelectrodes in literature have few sensing sites, due to limits of space in the placement of interconnects in the device, and to the presence of photonic circuits. Here, we overcome these limits by fabricating nanometric scale interconnections (120 nm wires, 450 nm pitch), and by stacking the interconnect and sensor layer in a three-dimensional configuration above the nanophotonic circuits. As a result, we fabricate probes embedding 64 readout electrodes and several light stimulation sites in a probe tip whose width is only 45 micrometers.

We further scale the tip thickness by the complete removal of the silicon substrate and leave only the functional layers embedding the nanophotonic and electrical circuits, thus obtaining 5 micron thick tips; such devices are able to correctly penetrate through the dura mater to perform in vivo experiments. Altogether, with the low footprint of our circuits, we obtained devices whose cross-sectional area (device cross section divided by the number of sensors and stimulation sites) is two orders of magnitude smaller than the state of the art optoelectrodes [63], demonstrating the scalability of our approach.

Finally, we developed fabrication techniques towards the integration of carbon-based nanomaterials on the sensors' interfaces, so to improve their biocompatibility and signal to noise ratio readout. We developed a wafer-level technique for the integration of graphene and the electrodeposition of carbon nano onions, which are concentric graphitic shells with a high area available towards charges in the neural extracellular environment. Future *in vitro* studies will validate the nano onion coating's benefits in terms of signal to noise ratio and biocompatibility.

From a neuroscience perspective, decoding the role of different neuron types and of groups of neurons in *in vivo* networks is challenging because current state of the art devices lack the capability of interfacing a large number of neurons and

have limited functionalities. By integrating nanotechnologies in microprobes, we overcome several technological bottlenecks and allow the experimenter to interface with a large number of neurons and to manipulate the desired types of neurons in the desired areas, thus paving the way towards high resolution studies of neural networks.

Author contributions

V. Lanzio was the leading researcher managing and working on the entire project (probes integrating electrodes and rings, couplers, oxide probes, carbon nanomaterial integration) and designed, simulated, fabricated, optimized, assembled and experimentally in vitro characterized the neural probes. The project (probe integrating rings and electrodes) was conceptualized by S. Cabrini, H. Adesnik and P. Denes; integration of carbon nanomaterials was conceptualized by A. Lamberti and F. Pirri. A. Koshelev conceptualized the ring resonator circuit and helped in initial testing. V. Lanzio conceptualized and managed the project for the integration of the directional coupler and the 5 µm thick oxide probes. S. Sassolini and M. West supervised the initial part of the project, while S. Cabrini, A. Lamberti and F. Pirri supervised the entire project on, respectively, the probe work (S. Cabrini) and the carbon nanomaterial work (A. Lamberti and F. Pirri). M. Lorenzon helped V. Lanzio in data analysis and discussion and manuscript writing. Optical simulations and testing was performed by V. Lanzio and P. Micheletti (supervised by V. Lanzio). G.Presti, E. D'Arpa, and P. De Martino helped optimize the fabrication processes, supervised by V. Lanzio. S. Dhuey performed the electron beam lithography steps. V. Lanzio optimized most of the fabrication processes and the process integration, device characterization, and assembly. E. D'Arpa integrated the graphene on electrodes, supervised by V. Lanzio, A. Lamberti and F. Pirri. Carbon nanomaterials were developed at Politecnico di Torino, by A. Lamberti and F. Pirri's groups. In vivo experiments and the corresponding data analysis was performed at Adesnik Lab (University of California, Berkeley) by G. Telian, supervised by H. Adesnik. Some in vitro experiments (photoelectric artefacts) were performed at Bouchard's Lab (Lawrence Berkeley National Laboratory). Work by

V. Lanzio was developed at the Department of Applied Science and Technology, Politecnico di Torino (carbon nanomaterials) and at the Molecular Foundry, Lawrence Berkeley National Laboratory (probe fabrication). Work at the Molecular Foundry was supported by the Office of Science, Office of Basic Energy Sciences, of the U.S. Department of Energy under Contract No. DE-AC02-05CH11231.

Main publications on the project:

1. Lanzio V, Telian G, Koshelev A, Micheletti P, Presti G, D'Arpa E, et al. Small footprint optoelectrodes for simultaneous readout and passive light localization by the use of ring resonators. Nature Microsystems and nanoengineering, Accpeted. Preprint: arXiv:200901387 [physics.bio-ph] [Internet]. 2020 Sep 2 [cited 2020 Sep 14]; Available from: http://arxiv.org/abs/2009.01387

2. Lanzio V, West M, Koshelev A, Telian G, Micheletti P, Lambert R, et al. High-density electrical and optical probes for neural readout and light focusing in deep brain tissue. J Micro/Nanolithography, MEMS, MOEMS. 2018;17(02):1.

3. Lanzio V, Lorenzon M, Dhuey S, Pirri CF, Lamberti A, Cabrini S. Scalable nanophotonic neural probes for multicolor and on-demand light delivery in brain tissue. Nanotechnology [Internet]. 2021 Jun 25 [cited 2021 May 11];32(26):265201. Available from: https://iopscience.iop.org/article/10.1088/1361-6528/abef2a

4. Lanzio V, Gutierrez V, Hermiz J, Bouchard K, Cabrini S, Neural probes merging the gap between silicon scalability and polymeric-like flexibility, In preparation.

Bibliography

[1] A. Taflove and S. C. Hagness. "Computational Electrodynamics: The Finite-Difference Time-Domain Method, 3rd ed." In: *Norwood, MA: Artech House* (2005). ISSN: 20413181. DOI: 10.1039/9781849732680-00147.

[2] H. Ahmad et al. "Novel D-shaped fiber fabrication method for saturable absorber application in the generation of ultra-short pulses". In: *Laser Physics Letters* 14.8 (2017). ISSN: 1612202X. DOI: 10.1088/1612-202X/aa7729.

[3] M.I. Alayo, I. Pereyra, and M.N.P. Carreño. "Thick SiOxNy and SiO2 films obtained by PECVD technique at low temperatures". In: *Thin Solid Films* 332.1-2 (1998), pp. 40–45. ISSN: 00406090.

[4] Per Andersen and Edvard I. Moser. "Brain temperature and hippocampal function". In: *Hippocampus* 5.6 (Jan. 1995), pp. 491–498. ISSN: 1050-9631. DOI: 10.1002/hipo.450050602. URL: http://doi.wiley.com/10.1002/hipo.450050602.

[5] Lucio Claudio Andreani et al. "Optimizing grating couplers for silicon photonics". In: *International Conference on Transparent Optical Networks*. Vol. 2016-Augus. IEEE Computer Society, Aug. 2016. ISBN: 9781509014675. DOI: 10.1109/ICTON.2016.7550565.

[6] Rachel Aronoff. "Layer- and column-specific knockout of NMDA receptors in pyramidal neurons of the mouse barrel cortex". In: *Frontiers in Integrative Neuroscience* 1.NOV (Nov. 2007), p. 1. ISSN: 1662-5145. DOI: 10.3389/neuro.07.001.2007. URL: http://journal.frontiersin.org/article/10.3389/neuro.07.001.2007/abstract.

[7] Tymon Barwicz et al. "Reconfigurable silicon photonic circuits for telecommunication applications". In: *Laser Resonators and Beam Control X*. Ed. by Alexis V. Kudryashov, Alan H. Paxton, and Vladimir S. Ilchenko. Vol. 6872. SPIE, Feb. 2008, 68720Z. DOI: 10.1117/12.772740. URL: http://proceedings.spiedigitallibrary.org/proceeding.aspx?doi=10.1117/12.772740.

[8] Bruce P. Bean. "The action potential in mammalian central neurons". In: *Nature Reviews Neuroscience* 8.6 (June 2007), pp. 451–465. ISSN: 1471003X. DOI: 10.1038/nrn2148.

[9] Robi Boeck et al. "Series-coupled silicon racetrack resonators and the Vernier effect: theory and measurement". In: *Optics Express* 18.24 (2010), p. 25151. ISSN: 1094-4087. DOI: 10.1364/oe.18.025151.

[10] W. Bogaerts et al. "Silicon microring resonators". In: *Laser and Photonics Reviews* 6.1 (2012), pp. 47–73. ISSN: 18638880. DOI: 10.1002/lpor.201100017.

[11] Edward S. Boyden et al. “Millisecond-timescale, genetically targeted optical control of neural activity”. In: *Nature Neuroscience* 8.9 (2005), pp. 1263–1268. ISSN: 10976256. DOI: 10.1038/nn1525. arXiv: 9809069v1 [gr-qc].

[12] Romain Brette et al. “Simulation of networks of spiking neurons: A review of tools and strategies”. In: *Journal of Computational Neuroscience* 23.3 (Dec. 2007), pp. 349–398. ISSN: 09295313. DOI: 10.1007/s10827-007-0038-6.

[13] Alessio Paolo Buccino et al. “How does the presence of neural probes affect extracellular potentials?” In: *Journal of Neural Engineering* 16.2 (2019). ISSN: 17412552. DOI: 10.1088/1741-2552/ab03a1.

[14] György Buzsáki et al. “Tools for probing local circuits: High-density silicon probes combined with optogenetics”. In: *Neuron* 86.1 (2015), pp. 92–105. ISSN: 10974199. DOI: 10.1016/j.neuron.2015.01.028.

[15] Dawen Cai et al. “Improved tools for the Brainbow toolbox”. In: *Nature Methods* 10.6 (2013), pp. 540–547. DOI: 10.1038/nmeth.2450.

[16] Maysamreza Chamanzar et al. “Ultracompact optoflex neural probes for high-resolution electrophysiology and optogenetic stimulation”. In: *Proceedings of the IEEE International Conference on Micro Electro Mechanical Systems (MEMS)*. Vol. 2015-Febru. February. Institute of Electrical and Electronics Engineers Inc., Feb. 2015, pp. 682–685. DOI: 10.1109/MEMSYS.2015.7051049.

[17] Byoung-Yong Chang and Su-Moon Park. “Electrochemical Impedance Spectroscopy”. In: *Annual Review of Analytical Chemistry* 3.1 (June 2010), pp. 207–229. ISSN: 1936-1327. DOI: 10.1146/annurev.anchem.012809.102211. URL: http://www.annualreviews.org/doi/10.1146/annurev.anchem.012809.102211.

[18] Christopher A. R. Chapman, Noah Goshi, and Erkin Seker. “Multifunctional Neural Interfaces for Closed-Loop Control of Neural Activity”. In: *Advanced Functional Materials* 1703523 (2017), p. 1703523. ISSN: 1616301X. DOI: 10.1002/adfm.201703523. URL: http://doi.wiley.com/10.1002/adfm.201703523.

[19] Chang Hao Chen et al. “An Integrated Circuit for Simultaneous Extracellular Electrophysiology Recording and Optogenetic Neural Manipulation”. In: *IEEE Transactions on Biomedical Engineering* 64.3 (Mar. 2017), pp. 557–568. ISSN: 15582531. DOI: 10.1109/TBME.2016.2609412.

[20] Ritchie Chen, Andres Canales, and Polina Anikeeva. “Neural recording and modulation technologies”. In: *Nature Reviews Materials* 2.2 (2017), pp. 1–16. ISSN: 20588437. DOI: 10.1038/natrevmats.2016.93. URL: http://dx.doi.org/10.1038/natrevmats.2016.93.

[21] Lukas Chrostowski and Michael Hochberg. *Silicon photonics design*. Cambridge University Press, Jan. 2015, pp. 1–418. ISBN: 9781316084168. DOI: 10.1017/CBO9781316084168. URL: https://www.cambridge.org/core/books/silicon-photonics-design/BF3CF13E8542BCE67FD2BBC7104ECEAB.

[22] T. Chung et al. “Electrode modifications to lower electrode impedance and improve neural signal recording sensitivity”. In: *Journal of Neural Engineering* 12.5 (2015). DOI: 10.1088/1741-2560/12/5/056018.

[23] Xinyan Cui and David C Martin. “Fuzzy gold electrodes for lowering impedance and improving adhesion with electrodeposited conducting polymer”. In: *Sensors and Actuators, A: Physical* 103.3 (2003), pp. 384–394.

[24] Lorenzo Pavesi David J. Lockwood. *Silicon Photonics II, Components and Integration*. Vol. 94. 2003, pp. 89–91. ISBN: 9783642105050.

[25] Meng Deng et al. “Sensors and Actuators B : Chemical Electrochemical deposition of polypyrrole / graphene oxide composite on microelectrodes towards tuning the electrochemical properties of neural probes”. In: *Sensors & Actuators: B. Chemical* 158.1 (2011), pp. 176–184. ISSN: 0925-4005. DOI: 10.1016/j.snb.2011.05.062. URL: http://dx.doi.org/10.1016/j.snb.2011.05.062.

[26] Hans Ulrich Dodt et al. “Ultramicroscopy: Three-dimensional visualization of neuronal networks in the whole mouse brain”. In: *Nature Methods* 4.4 (Apr. 2007), pp. 331–336. ISSN: 15487091. DOI: 10.1038/nmeth1036.

[27] Na Dong et al. “Opto-electro-thermal optimization of photonic probes for optogenetic neural stimulation”. In: *Journal of Biophotonics* 11.10 (Oct. 2018), e201700358. ISSN: 1864063X. DOI: 10.1002/jbio.201700358. URL: http://doi.wiley.com/10.1002/jbio.201700358.

[28] J. Du et al. “High-Resolution Three-Dimensional Extracellular Recording of Neuronal Activity With Microfabricated Electrode Arrays”. In: *Journal of Neurophysiology* 101.3 (2009), pp. 1671–1678. ISSN: 0022-3077. DOI: 10.1152/jn.90992.2008. URL: http://jn.physiology.org/cgi/doi/10.1152/jn.90992.2008.

[29] David J. Edell et al. “Factors Influencing the Biocompatibility of Insertable Silicon Microshafts in Cerebral Cortex”. In: *IEEE Transactions on Biomedical Engineering* 39.6 (1992), pp. 635–643. ISSN: 15582531. DOI: 10.1109/10.141202.

[30] Robert Egger et al. “Generation of dense statistical connectomes from sparse morphological data”. In: *Frontiers in Neuroanatomy* 8.November (Nov. 2014), p. 129. ISSN: 1662-5129. DOI: 10.3389/fnana.2014.00129. URL: http://journal.frontiersin.org/article/10.3389/fnana.2014.00129/abstract.

[31] Gaute T. Einevoll et al. “Modelling and analysis of local field potentials for studying the function of cortical circuits”. In: *Nature Reviews Neuroscience* 14.11 (2013), pp. 770–785. ISSN: 1471003X. DOI: 10.1038/nrn3599. URL: http://dx.doi.org/10.1038/nrn3599.

[32] Zoltan Fekete. “Recent advances in silicon-based neural microelectrodes and microsystems: A review”. In: *Sensors and Actuators, B: Chemical* 215 (2015), pp. 300–315. ISSN: 09254005. DOI: 10.1016/j.snb.2015.03.055. URL: http://dx.doi.org/10.1016/j.snb.2015.03.055.

[33] David J. Garrett et al. “Diamond for neural interfacing: A review”. In: *Carbon* 102 (June 2016), pp. 437–454. ISSN: 00086223. DOI: 10.1016/j.carbon.2016.02.059.

[34] *Gold Plating Solution . Neuralynx*. URL: https://neuralynx.com/hardware/gold-plating-solution.

[35] Frederic Grillot et al. “Size influence on the propagation loss induced by sidewall roughness in ultrasmall SOI waveguides”. In: *IEEE Photonics Technology Letters* 16.7 (July 2004), pp. 1661–1663. ISSN: 10411135. DOI: 10.1109/LPT.2004.828497.

[36] Logan Grosenick, James H. Marshel, and Karl Deisseroth. “Closed-loop and activity-guided optogenetic control”. In: *Neuron* 86.1 (Apr. 2015), pp. 106–139. ISSN: 10974199. DOI: 10.1016/j.neuron.2015.03.034.

[37] Hiroshi Hama et al. “Scale: A chemical approach for fluorescence imaging and reconstruction of transparent mouse brain”. In: *Nature Neuroscience* 14.11 (Nov. 2011), pp. 1481–1488. ISSN: 10976256. DOI: 10.1038/nn.2928.

[38] Xue Han. “In vivo application of optogenetics for neural circuit analysis”. In: *ACS Chemical Neuroscience* 3.8 (2012), pp. 577–584. ISSN: 19487193. DOI: 10.1021/cn300065j.

[39] Hermann A. Haus and Tymon Barwicz. “Three-Dimensional Analysis of Scattering Losses Due to Sidewall Roughness in Microphotonic Waveguides”. In: *Journal of Lightwave Technology, Vol. 23, Issue 9, pp. 2719-* 23.9 (Sept. 2005), p. 2719.

[40] R. G. Heideman et al. “TriPleXTM: The low loss passive photonics platform: Industrial applications through Multi Project Wafer runs”. In: *2014 IEEE Photonics Conference, IPC 2014* 3 (2014), pp. 224–225. DOI: 10.1109/IPCon.2014.6995329.

[41] Maxwell Henderson, Brigita Urbanc, and Luis Cruz. “A Computational model for the loss of neuronal organization in microcolumns”. In: *Biophysical Journal* 106.10 (May 2014), pp. 2233–2242. ISSN: 15420086. DOI: 10.1016/j.bpj.2014.04.012.

[42] D a Henze et al. “Intracellular features predicted by extracellular recordings in the hippocampus in vivo.” In: *Journal of neurophysiology* 84.1 (2000), pp. 390–400. ISSN: 0022-3077. DOI: 84:390-400. URL: http://www.ncbi.nlm.nih.gov/pubmed/10899213.

[43] David Grant Colburn Hildebrand et al. “Whole-brain serial-section electron microscopy in larval zebrafish”. In: *Nature* 545.7654 (May 2017), pp. 345–349. ISSN: 14764687. DOI: 10.1038/nature22356.

[44] Guosong Hong and Charles M. Lieber. *Novel electrode technologies for neural recordings*. June 2019. DOI: 10.1038/s41583-019-0140-6.

[45] Toshihiko Hosoya. “The basic repeating modules of the cerebral cortical circuit”. In: *Proceedings of the Japan Academy Series B: Physical and Biological Sciences* 95.7 (2019), pp. 303–311. ISSN: 13492896. DOI: 10.2183/pjab.95.022.

[46] Z. Josh Huang and Liqun Luo. “It takes the world to understand the brain: International brain projects discuss how to coordinate efforts”. In: *Science* 350.6256 (2015), pp. 42–44. ISSN: 10959203. DOI: 10.1126/science.aad4120.

[47] Fahmeed Hyder and Douglas L. Rothman. "Advances in Imaging Brain Metabolism". In: *Annual Review of Biomedical Engineering* 19.1 (June 2017), pp. 485–515. ISSN: 1523-9829. DOI: 10.1146/annurev-bioeng-071516-044450. URL: http://www.annualreviews.org/doi/10.1146/annurev-bioeng-071516-044450.

[48] Edward Jan et al. "Layered Carbon Nanotube-Polyelectrolyte Electrodes Outperform Traditional Neural Interface Materials". In: *Nano Letters* 9.12 (2009), pp. 4012–4018. DOI: 10.1021/nl902187z.

[49] J. H. Jang et al. "Direct measurement of nanoscale sidewall roughness of optical waveguides using an atomic force microscope". In: *Applied Physics Letters* 83.20 (Nov. 2003), pp. 4116–4118. ISSN: 00036951. DOI: 10.1063/1.1627480.

[50] Xingchen Ji et al. "Ultra-low-loss on-chip resonators with sub-milliwatt parametric oscillation threshold". In: *Optica* 4.6 (2017), p. 619. ISSN: 2334-2536. DOI: 10.1364/optica.4.000619.

[51] E. G. Jones. "Microcolumns in the cerebral cortex". In: *Proceedings of the National Academy of Sciences of the United States of America* 97.10 (May 2000), pp. 5019–5021. ISSN: 00278424. DOI: 10.1073/pnas.97.10.5019.

[52] James J. Jun et al. "Fully integrated silicon probes for high-density recording of neural activity". In: *Nature* 551.7679 (Nov. 2017), pp. 232–236. ISSN: 14764687. DOI: 10.1038/nature24636.

[53] Komal Kampasi et al. "Dual color optogenetic control of neural populations using low-noise, multishank optoelectrodes". In: *Microsystems and Nanoengineering* 4.1 (2018). ISSN: 20557434. DOI: 10.1038/s41378-018-0009-2. URL: http://dx.doi.org/10.1038/s41378-018-0009-2.

[54] Jonas Karlsson et al. "High Fidelity Visualization of Large Scale Digitally Reconstructed Brain Circuitry with Signed Distance Functions". In: *2019 IEEE Visualization Conference, VIS 2019*. Institute of Electrical and Electronics Engineers Inc., Oct. 2019, pp. 176–180. ISBN: 9781728149417. DOI: 10.1109/VISUAL.2019.8933693.

[55] Edward W Keefer et al. "Carbon nanotube coating improves neuronal recordings". In: *Nature Nanotechnology* 3.July (2008), pp. 1–6. DOI: 10.1038/nnano.2008.174.

[56] Christina K. Kim, Avishek Adhikari, and Karl Deisseroth. "Integration of optogenetics with complementary methodologies in systems neuroscience". In: *Nature Reviews Neuroscience* 18.4 (2017), pp. 222–235. ISSN: 14710048. DOI: 10.1038/nrn.2017.15. URL: http://dx.doi.org/10.1038/nrn.2017.15.

[57] Nathan C. Klapoetke et al. "Independent optical excitation of distinct neural populations". In: *Nature Methods* 11.3 (2014), pp. 338–346. ISSN: 15487105. DOI: 10.1038/nmeth.2836.

[58] E. Krook-Magnuson et al. "Cerebellar Directed Optogenetic Intervention Inhibits Spontaneous Hippocampal Seizures in a Mouse Model of Temporal Lobe Epilepsy". In: *eNeuro* 1.1 (2014). ISSN: 2373-2822. DOI: 10.1523/ENEURO.0005-14.2014. URL: http://eneuro.sfn.org/cgi/doi/10.1523/ENEURO.0005-14.2014.

[59] Duygu Kuzum et al. “Transparent and flexible low noise graphene electrodes for simultaneous electrophysiology and neuroimaging”. In: *Nature Communications* 5.May (2014), pp. 1–10. DOI: 10.1038/ncomms6259. URL: http://dx.doi.org/10.1038/ncomms6259.

[60] Vittorino Lanzio et al. “High-density electrical and optical probes for neural readout and light focusing in deep brain tissue”. In: *Journal of Micro/Nanolithography, MEMS, and MOEMS* 17.02 (2018), p. 1. ISSN: 1932-5134. DOI: 10.1117/1.jmm.17.2.025503.

[61] Aziliz Lecomte, Emeline Descamps, and Christian Bergaud. “A review on mechanical considerations for chronically-implanted neural probes”. In: *Journal of Neural Engineering* 15.3 (2018). ISSN: 17412552. DOI: 10.1088/1741-2552/aa8b4f.

[62] Scott F Lempka, Svjetlana Miocinovic, and Matthew D Johnson. “In vivo impedance spectroscopy of deep brain stimulation electrodes”. In: *Journal of Neural Engineering* 6.4 (2009), p. 046001. DOI: 10.1088/1741-2560/6/4/046001.

[63] Sarah Libbrecht et al. “Proximal and distal modulation of neural activity by spatially confined optogenetic activation with an integrated high-density optoelectrode”. In: *Journal of Neurophysiology* 120.1 (July 2018), pp. 149–161. ISSN: 15221598. DOI: 10.1152/jn.00888.2017. URL: https://www.physiology.org/doi/10.1152/jn.00888.2017.

[64] Chia-min Lin et al. “Flexible carbon nanotubes electrode for neural recording”. In: *Biosensors and Bioelectronics* 24.9 (2009), pp. 2791–2797. DOI: 10.1016/j.bios.2009.02.005.

[65] John Y. Lin. “A user’s guide to channelrhodopsin variants: Features, limitations and future developments”. In: *Experimental Physiology* 96.1 (2010), pp. 19–25. ISSN: 09580670. DOI: 10.1113/expphysiol.2009.051961.

[66] Ta Chung Liu et al. “Implantable Graphene-based Neural Electrode Interfaces for Electrophysiology and Neurochemistry in In Vivo Hyperacute Stroke Model”. In: *ACS Applied Materials and Interfaces* 8.1 (2016), pp. 187–196. ISSN: 19448252. DOI: 10.1021/acsami.5b08327.

[67] X. Liu, S. Ramirez, and S. Tonegawa. “Inception of a false memory by optogenetic manipulation of a hippocampal memory engram”. In: *Philosophical Transactions of the Royal Society B: Biological Sciences* 369.1633 (2013), pp. 20130142–20130142. ISSN: 0962-8436. DOI: 10.1098/rstb.2013.0142. URL: http://rstb.royalsocietypublishing.org/cgi/doi/10.1098/rstb.2013.0142.

[68] Jean Livet et al. “Transgenic strategies for combinatorial expression of fluorescent proteins in the nervous system”. In: *Nature* 450.7166 (Nov. 2007), pp. 56–62. ISSN: 14764687. DOI: 10.1038/nature06293.

[69] Víctor A. Lórenz-Fonfría and Joachim Heberle. *Channelrhodopsin unchained: Structure and mechanism of a light-gated cation channel*. 2014. DOI: 10.1016/j.bbabio.2013.10.014. URL: http://dx.doi.org/10.1016/j.bbabio.2013.10.014.

[70] Yichen Lu, Xin Liu, and Duygu Kuzum. "ScienceDirect Graphene-based neurotechnologies for advanced neural interfaces". In: *Current Opinion in Biomedical Engineering* 6 (2018), pp. 138–147. ISSN: 2468-4511. DOI: 10.1016/j.cobme.2018.06.001. URL: https://doi.org/10.1016/j.cobme.2018.06.001.

[71] Yichen Lu et al. "Flexible Neural Electrode Array Based-on Porous Graphene for Cortical Microstimulation and Sensing". In: *Nature Publishing Group* May (2016), pp. 1–9. DOI: 10.1038/srep33526. URL: http://dx.doi.org/10.1038/srep33526.

[72] Yi Lu et al. "Biomaterials Electrodeposited polypyrrole / carbon nanotubes composite fi lms electrodes for neural interfaces". In: *Biomaterials* 31.19 (2010), pp. 5169–5181. ISSN: 0142-9612. DOI: 10.1016/j.biomaterials.2010.03.022. URL: http://dx.doi.org/10.1016/j.biomaterials.2010.03.022.

[73] Xiliang Luo et al. "Biomaterials Highly stable carbon nanotube doped poly (3 , 4-ethylenedioxythiophene) for chronic neural stimulation". In: *Biomaterials* 32.24 (2011), pp. 5551–5557. ISSN: 0142-9612. DOI: 10.1016/j.biomaterials.2011.04.051. URL: http://dx.doi.org/10.1016/j.biomaterials.2011.04.051.

[74] Xiliang Luo et al. "Pure graphene oxide doped conducting polymer nanocomposite for bio-interfacing". In: *Journal of Materials Chemistry B* 1.9 (2013), pp. 1340–1348. DOI: 10.1039/c3tb00006k.

[75] Yu Ma. "In vivo 3D digital atlas database of the adult C57BL/6J mouse brain by magnetic resonance microscopy". In: *Frontiers in Neuroanatomy* 2.APR (Mar. 2008), p. 1. ISSN: 1662-5129. DOI: 10.3389/neuro.05.001.2008. URL: http://journal.frontiersin.org/article/10.3389/neuro.05.001.2008/abstract.

[76] Yuriko Maegami et al. "Spot-size converter with a SiO 2 spacer layer between tapered Si and SiON waveguides for fiber-to-chip coupling". In: *Optics Express* 23.16 (2015), p. 21287. DOI: 10.1364/OE.23.021287.

[77] Sasikanth Manipatruni, Long Chen, and Michal Lipson. "Ultra high bandwidth WDM using silicon microring modulators". In: *Optics Express* 18.16 (Aug. 2010), p. 16858. ISSN: 1094-4087. DOI: 10.1364/oe.18.016858. URL: http://www.shf.de/en/communication/products/rf_broadband_amplifier/40_gbps_rf_amplifier/.

[78] Michael L. Martini et al. "Sensor Modalities for Brain-Computer Interface Technology: A Comprehensive Literature Review". In: *Neurosurgery* 86.2 (2020), E108–E117. ISSN: 15244040. DOI: 10.1093/neuros/nyz286.

[79] Ludvik Martinu and Daniel Poitras. "Plasma deposition of optical films and coatings: A review". In: *Journal of Vacuum Science & Technology A: Vacuum, Surfaces, and Films* 18.6 (2000), pp. 2619–2645. ISSN: 0734-2101. DOI: 10.1116/1.1314395.

[80] Hisato Maruoka et al. "Lattice system of functionally distinct cell types in the neocortex". In: *Science* 358.6363 (Nov. 2017), pp. 610–615. ISSN: 10959203. DOI: 10.1126/science.aam6125.

[81] Niall McAlinden et al. “Thermal and optical characterization of micro-LED probes for in vivo optogenetic neural stimulation”. In: *Optics Letters* 38.6 (2013), p. 992. ISSN: 0146-9592. DOI: 10.1364/OL.38.000992. URL: https://www.osapublishing.org/abstract.cfm?URI=ol-38-6-992.

[82] Sanja Mikulovic et al. “On the photovoltaic effect in local field potential recordings”. In: *Neurophotonics* 3.1 (Jan. 2016), p. 015002. ISSN: 2329-423X. DOI: 10.1117/1.nph.3.1.015002. URL: https://www.spiedigitallibrary.org/terms-of-use.

[83] Aseema Mohanty et al. “Reconfigurable nanophotonic silicon probes for sub-millisecond deep-brain optical stimulation”. In: *Nature Biomedical Engineering* 4.2 (Feb. 2020), pp. 223–231. ISSN: 2157846X. DOI: 10.1038/s41551-020-0516-y. URL: https://www.nature.com/articles/s41551-020-0516-y.

[84] Carolina Mora Lopez et al. “A Neural Probe with Up to 966 Electrodes and Up to 384 Configurable Channels in 0.13 μm SOI CMOS”. In: *IEEE Transactions on Biomedical Circuits and Systems* 11.3 (June 2017), pp. 510–522. ISSN: 19324545. DOI: 10.1109/TBCAS.2016.2646901.

[85] Xin Mu et al. “A Compact Adiabatic Silicon Photonic Edge Coupler Based on Silicon Nitride/Silicon Trident Structure”. In: *2019 18th International Conference on Optical Communications and Networks, ICOCN 2019*. Institute of Electrical and Electronics Engineers Inc., Aug. 2019. ISBN: 9781728127644. DOI: 10.1109/ICOCN.2019.8934126.

[86] Xin Mu et al. “Edge couplers in silicon photonic integrated circuits: A review”. In: *Applied Sciences (Switzerland)* 10.4 (Feb. 2020), p. 1538. ISSN: 20763417. DOI: 10.3390/app10041538.

[87] *Nanophotonic FDTD Simulation Software - Lumerical FDTD*. URL: https://www.lumerical.com/products/fdtd/?utm_campaign=2028782350&utm_source=google&utm_medium=cpc&utm_content=356244346239&utm_term=%2Bfdtd%20simulation&adgroupid=73452698793&gclid=CjwKCAjwqJ_1BRBZEiwAv73uwJDTJgvWfPpVl7kJ5oSJe5BmV4WUuDQyO97XbWwS9CAUpHUIV-c2NRoCiDEQAvD_BwE.

[88] *nanoZ Kit . Neuralynx*. URL: https://neuralynx.com/hardware/nanoz-kit.

[89] Rajeevan T. Narayanan, Daniel Udvary, and Marcel Oberlaender. “Cell Type-Specific Structural Organization of the Six Layers in Rat Barrel Cortex”. In: *Frontiers in Neuroanatomy* 11 (Oct. 2017), p. 91. ISSN: 1662-5129. DOI: 10.3389/fnana.2017.00091. URL: http://journal.frontiersin.org/article/10.3389/fnana.2017.00091/full.

[90] *Nerve Cell Icon Flat Graphic Design, Neuron Logo Stock Vector - Illustration of human, science: 137469711*. URL: https://www.dreamstime.com/nerve-cell-icon-flat-graphic-design-neuron-logo-nerve-cell-icon-flat-graphic-design-neuron-logo-white-image137469711.

[91] Andrew M H Ng et al. “Biosensors and Bioelectronics Highly sensitive reduced graphene oxide microelectrode array sensor”. In: *Biosensors and Bioelectronic* 65 (2015), pp. 265–273. ISSN: 0956-5663. DOI: 10.1016/j.bios.2014.10.048. URL: http://dx.doi.org/10.1016/j.bios.2014.10.048.

[92] T D Barbara Nguyen-vu et al. “Vertically aligned carbon nanoflber arrays: An advance toward electrical-neural interfaces”. In: *Small* 2.1 (2006), pp. 89–94. DOI: 10.1002/smll.200500175.

[93] Ben Niu. *High efficiency edge coupler, novel nonlinear optical polymers with large Kerr-coefficient and automatic layout generation in silicon photonics*. Tech. rep. 2016. URL: https://docs.lib.purdue.edu/open_access_dissertations/1372.

[94] Marie Engelene J. Obien et al. *Revealing neuronal function through microelectrode array recordings*. Jan. 2015. DOI: 10.3389/fnins.2014.00423. URL: http://www.multichannelsystems.com.

[95] Jun Rong Ong et al. “Silicon nitride double-tip fiber-to-waveguide edge couplers at visible wavelengths”. In: *Optics InfoBase Conference Papers* Part F122-.1 (2017), pp. 2–4.

[96] Dong Wook Park et al. “Fabrication and utility of a transparent graphene neural electrode array for electrophysiology, in vivo imaging, and optogenetics”. In: *Nature Protocols* 11.11 (2016), pp. 2201–2222. ISSN: 17502799. DOI: 10.1038/nprot.2016.127. URL: http://dx.doi.org/10.1038/nprot.2016.127.

[97] Dong-wook Park et al. “Electrical Neural Stimulation and Simultaneous in Vivo Monitoring with Transparent Graphene Electrode Arrays Implanted in GCaMP6f Mice”. In: (2018). DOI: 10.1021/acsnano.7b04321.

[98] David Pech et al. “Ultrahigh-power micrometre-sized supercapacitors based on onion-like carbon”. In: *Nature Nanotechnology* 5.9 (2010), pp. 651–654. ISSN: 17483395. DOI: 10.1038/nnano.2010.162.

[99] I. Pereyra and M. I. Alayo. “High quality low temperature DPECVD silicon dioxide”. In: *Journal of Non-Crystalline Solids* 212.2-3 (1997), pp. 225–231. ISSN: 00223093. DOI: 10.1016/S0022-3093(96)00650-3.

[100] Carl C.H. Petersen. “Sensorimotor processing in the rodent barrel cortex”. In: *Nature Reviews Neuroscience* 20.9 (Sept. 2019), pp. 533–546. ISSN: 14710048. DOI: 10.1038/s41583-019-0200-y.

[101] Ferruccio Pisanello, Leonardo Sileo, and Massimo De Vittorio. “Micro- and nanotechnologies for optical neural interfaces”. In: *Frontiers in Neuroscience* 10.MAR (2016), pp. 1–9. ISSN: 1662453X. DOI: 10.3389/fnins.2016.00070.

[102] *Platinum Black Plating Solution . Neuralynx*. URL: https://neuralynx.com/hardware/platinum-black-plating-solution.

[103] Scott Pluta et al. “A direct translaminar inhibitory circuit tunes cortical output”. In: *Nature Neuroscience* 18.11 (Nov. 2015), pp. 1631–1640. ISSN: 15461726. DOI: 10.1038/nn.4123.

[104] R. Rao et Al. “Carbon Nanotubes and Related Nanomaterials: Critical Advances and Challenges for Synthesis toward Mainstream Commercial Applications”. In: *ACS Nano* 12.12 (2018), pp. 11756–11784. ISSN: 1936086X. DOI: 10.1021/acsnano.8b06511.

[105] Bogdan C. Raducanu et al. “Time Multiplexed Active Neural Probe with 1356 Parallel Recording Sites”. In: *Sensors* 17.10 (Oct. 2017), p. 2388. ISSN: 1424-8220. DOI: 10.3390/s17102388. URL: http://www.mdpi.com/1424-8220/17/10/2388.

[106] Michael W. Reimann et al. “A null model of the mouse whole-neocortex micro-connectome”. In: *Nature Communications* 10.1 (Dec. 2019), pp. 1–16. ISSN: 20411723. DOI: 10.1038/s41467-019-11630-x.

[107] Benjamin Richier and Iris Salecker. “Versatile genetic paintbrushes : Brainbow technologies”. In: *Wiley Interdisciplinary Reviews: Developmental Biology* 4.2 (2015), pp. 161–180. DOI: 10.1002/wdev.166.

[108] Gustavo Rios et al. “Nanofabricated Neural Probes for Dense 3-D Recordings of Brain Activity”. In: *Nano Letters* 16.11 (Nov. 2016), pp. 6857–6862. ISSN: 15306992. DOI: 10.1021/acs.nanolett.6b02673.

[109] David A. Robinson. “The Electrical Properties of Metal Microelectrodes”. In: *Proceedings of the IEEE* 56.6 (1968), pp. 1065–1071. ISSN: 15582256. DOI: 10.1109/PROC.1968.6458.

[110] Cyrille Rossant et al. “Spike sorting for large, dense electrode arrays”. In: *Nature Neuroscience* 19.4 (2016), pp. 634–641. ISSN: 15461726. DOI: 10.1038/nn.4268.

[111] Dheeraj S. Roy et al. “Memory retrieval by activating engram cells in mouse models of early Alzheimer’s disease”. In: *Nature* 531.7595 (2016), pp. 508–512. ISSN: 14764687. DOI: 10.1038/nature17172.

[112] Wesley D Sacher et al. “Beam-Steering Nanophotonic Phased-Array Neural Probes”. In: *Optics InfoBase Conference Papers*. c. OSA - The Optical Society, 2019, pp. 16–17. DOI: 10.1364/CLEO{_}AT.2019.ATh4I.4.

[113] Pranoy Sahu and Nirmal Mazumder. “Advances in adaptive optics–based two-photon fluorescence microscopy for brain imaging”. In: *Lasers in Medical Science* 35.2 (Mar. 2020), pp. 317–328. ISSN: 1435604X. DOI: 10.1007/s10103-019-02908-z.

[114] Massimo Scanziani and Michael Häusser. “Electrophysiology in the age of light”. In: *Nature* 461.7266 (2009), pp. 930–939. ISSN: 00280836. DOI: 10.1038/nature08540.

[115] Robert Scharf et al. “Depth-specific optogenetic control in vivo with a scalable, high-density μlED neural probe”. In: *Scientific Reports* 6.January (2016), pp. 1–10. ISSN: 20452322. DOI: 10.1038/srep28381. URL: http://dx.doi.org/10.1038/srep28381.

[116] Ronald V Schmidt and R O D C Alferness. “Directional coupler switches, modulators, and filters using alternating delta beta techniques.” In: *IEEE transactions on circuits and systems* CAS-26.12 (1979), pp. 1099–1108. ISSN: 00984094.

[117] Eran Segev et al. “Patterned photostimulation via visible-wavelength photonic probes for deep brain optogenetics”. In: *Neurophotonics* 4.1 (2016), p. 011002. ISSN: 2329-423X. DOI: 10.1117/1.NPh.4.1.011002. URL: http://neurophotonics.spiedigitallibrary.org/article.aspx?doi=10.1117/1.NPh.4.1.011002.

[118] Terrence J Sejnowski, Patricia S Churchland, and J Anthony Movshon. "Putting big data to good use in neuroscience". In: *Nature Publishing Group* (2014). DOI: 10.1038/nn.3839. URL: http://www.nih.gov/science/brain/2025/.

[119] Michael J. Shaw et al. "Fabrication techniques for low-loss silicon nitride waveguides". In: *Micromachining Technology for Micro-Optics and Nano-Optics III* 5720.January 2005 (2005), p. 109. ISSN: 16057422. DOI: 10.1117/12.588828.

[120] Shy Shoham, Daniel H. O'Connor, and Ronen Segev. "How silent is the brain: Is there a "dark matter" problem in neuroscience?" In: *Journal of Comparative Physiology A: Neuroethology, Sensory, Neural, and Behavioral Physiology* 192.8 (Aug. 2006), pp. 777–784. ISSN: 03407594. DOI: 10.1007/s00359-006-0117-6.

[121] Micha E. Spira and Aviad Hai. "Multi-electrode array technologies for neuroscience and cardiology". In: *Nature Nanotechnology* 8.2 (Feb. 2013), pp. 83–94. ISSN: 17483395. DOI: 10.1038/nnano.2012.265.

[122] Joseph M. Stujenske, Timothy Spellman, and Joshua A. Gordon. "Modeling the Spatiotemporal Dynamics of Light and Heat Propagation for InVivo Optogenetics". In: *Cell Reports* 12.3 (July 2015), pp. 525–534. ISSN: 22111247. DOI: 10.1016/j.celrep.2015.06.036.

[123] A. Z. Subramanian et al. "Low-Loss Singlemode PECVD silicon nitride photonic wire waveguides for 532-900 nm wavelength window fabricated within a CMOS pilot line". In: *IEEE Photonics Journal* 5.6 (Dec. 2013). ISSN: 19430655. DOI: 10.1109/JPHOT.2013.2292698.

[124] D. H. Szarowski et al. "Brain responses to micro-machined silicon devices". In: *Brain Research* 983.1-2 (2003), pp. 23–35. ISSN: 00068993. DOI: 10.1016/S0006-8993(03)03023-3.

[125] Martin Thunemann et al. "Deep 2-photon imaging and artifact-free optogenetics through transparent graphene microelectrode arrays". In: *Nature Communications* 9.1 (2018), pp. 1–12. ISSN: 20411723. DOI: 10.1038/s41467-018-04457-5.

[126] Hong-chang Tian et al. "Biomaterials Graphene oxide doped conducting polymer nanocomposite fi lm for electrode-tissue interface". In: *Biomaterials* 35.7 (2014), pp. 2120–2129. ISSN: 0142-9612. DOI: 10.1016/j.biomaterials.2013.11.058. URL: http://dx.doi.org/10.1016/j.biomaterials.2013.11.058.

[127] Ruben A. Tikidji-Hamburyan et al. "Software for Brain Network Simulations: A Comparative Study". In: *Frontiers in Neuroinformatics* 11 (July 2017), p. 46. ISSN: 1662-5196. DOI: 10.3389/fninf.2017.00046. URL: http://journal.frontiersin.org/article/10.3389/fninf.2017.00046/full.

[128] Carsten H. Tischbirek et al. "In Vivo Functional Mapping of a Cortical Column at Single-Neuron Resolution". In: *Cell Reports* 27.5 (Apr. 2019), pp. 1319–1326. ISSN: 22111247. DOI: 10.1016/j.celrep.2019.04.007.

[129] *Understanding the FDTD Method*. URL: https://www.eecs.wsu.edu/~schneidj/ufdtd/.

[130] Trevor J Vincent et al. “Longitudinal Brain Size Measurements in App/Ps1 Transgenic Mice”. In: *Magnetic Resonance Insights* 4 (2010), pp. 4–19. DOI: 10.4137/MRI.S5885. URL: http://www.la-press.com.http//www.la-press.com..

[131] Maria Vomero et al. “Highly Stable Glassy Carbon Interfaces for Long-Term Neural Stimulation and Low-Noise Recording of Brain Activity”. In: *Nature Publishing Group* December 2016 (2017), pp. 1–14. DOI: 10.1038/srep40332. URL: http://dx.doi.org/10.1038/srep40332.

[132] Jiangtao Wang et al. “Growing highly pure semiconducting carbon nanotubes by electrotwisting the helicity”. In: *Nature Catalysis* 1.5 (2018), pp. 326–331. ISSN: 25201158. DOI: 10.1038/s41929-018-0057-x. URL: http://dx.doi.org/10.1038/s41929-018-0057-x.

[133] N Winkin et al. “Nanomaterial-modified Flexible Micro-electrode Array by Electrophoretic Deposition of Carbon Nanotubes”. In: *Journal of Biochips and Tissue Chips* 6.1 (2016), pp. 1–6. DOI: 10.4172/2153-0777.1000115.

[134] Fan Wu et al. “An implantable neural probe with monolithically integrated dielectric waveguide and recording electrodes for optogenetics applications”. In: *Journal of Neural Engineering* 10.5 (2013). ISSN: 17412560. DOI: 10.1088/1741-2560/10/5/056012.

[135] Fan Wu et al. “Monolithically Integrated μLEDs on Silicon Neural Probes for High-Resolution Optogenetic Studies in Behaving Animals”. In: *Neuron* 88.6 (2015), pp. 1136–1148. ISSN: 10974199. DOI: 10.1016/j.neuron.2015.10.032.

[136] Jing Zhang et al. “Stretchable Transparent Electrode Arrays for Simultaneous Electrical and Optical Interrogation of Neural Circuits in Vivo”. In: *Nano Letters* 18.5 (2018), pp. 2903–2911. DOI: 10.1021/acs.nanolett.8b00087.

[137] Yongbin Zhang et al. “Cytotoxicity effects of graphene and single-wall carbon nanotubes in neural phaeochromocytoma-derived pc12 cells”. In: *ACS Nano* 4.6 (2010), pp. 3181–3186.

[138] Zhihao Zheng et al. “A Complete Electron Microscopy Volume of the Brain of Adult Drosophila melanogaster”. In: *Cell* 174.3 (July 2018), pp. 730–743. ISSN: 10974172. DOI: 10.1016/j.cell.2018.06.019.

[139] Haihan Zhou et al. “Acta Biomaterialia composite coatings for improving the stability of microelectrodes in neural prostheses applications”. In: *Acta Biomaterialia* 9.5 (2013), pp. 6439–6449. ISSN: 1742-7061. DOI: 10.1016/j.actbio.2013.01.042. URL: http://dx.doi.org/10.1016/j.actbio.2013.01.042.

[140] Tiecheng Zhu et al. “Ultrabroadband high coupling efficiency fiber-to-waveguide coupler using Si3N4/SiO2 waveguides on silicon”. In: *IEEE Photonics Journal* 8.5 (2016), pp. 1–12. DOI: 10.1109/JPHOT.2016.2600037.

[141] Xinpei Zhu et al. “Optical Brain Imaging: A Powerful Tool for Neuroscience”. In: *Neuroscience Bulletin* 33.1 (Feb. 2017), pp. 95–102. ISSN: 19958218. DOI: 10.1007/s12264-016-0053-6.

This Ph.D. thesis has been typeset by means of the TEX-system facilities. The typesetting engine was pdfLATEX. The document class was `toptesi`, by Claudio Beccari, with option `tipotesi=scudo`. This class is available in every up-to-date and complete TEX-system installation.